Persistent Phosphors for Smartphone-Based Luminescence Thermometry and Anti-Counterfeiting Applications

Zur Erlangung des akademischen Grades eines

Doktors der Ingenieurwissenschaften

(Dr.-Ing.)

von der KIT-Fakultät für Elektrotechnik und Informationstechnik

des Karlsruher Instituts für Technologie (KIT)

genehmigte

Dissertation

von

Ngei Katumo, M.Sc.

geboren in Makueni, Kenia

Tag der mündlichen Prüfung: 23.06.2022

Hauptreferent: Prof. Dr. Bryce Sydney Richards

Korreferentin: Prof. Dr. Claudia Wickleder

Kurzfassung

Leuchtstoffe anhaltender Lumineszenz im sichtbaren Spektrum eröffnen neue Möglichkeiten für Smartphone-basierte Anwendungen. Videoaufnahmen mit dem Smartphone mit 30 Bildern pro Sekunde können persistente Lumineszenzlebenszeiten einer Größenordnung von 100 ms und länger bestimmen. Die mit dem Smartphone aufgezeichneten Daten können benutzt werden um Anwendungen zu realisieren, die ansonsten nur für kurze Lebenszeiten möglich sind. Diese Alternative umgeht den Bedarf an teuren und relativ komplizierten Messinstrumenten, die für die Detektion von kurzen Lebenszeiten eingesetzt werden, wie zum Beispiel Multichannel scaling, Hochgeschwindigkeitskameras und Mikroskope zur Messung der Fluoreszenzlebenszeit. Diese Arbeit konzentriert sich auf die Detektion anhaltender Lumineszenz für Temperaturmessung und Anwendungen zur Fälschungssicherung mit dem Smartphone.

Für die Smartphone-basierte Temperaturmessung wurde ein optimierter Gd_2O_2S: Eu^{3+} als Leuchtstoff verwendet, der mithilfe einer UV-Quelle angeregt werden kann. Der Leuchtstoff zeigte eine temperaturabhängige Lumineszenz, die hell und lange anhaltend genug war, um mit einer Smartphone-Kamera mit 30 Bildern pro Sekunde aufgezeichnet zu werden. Der Leuchtstoff hat eine Photolumineszenz-Quantenausbeute von 65 % und seine Lebenszeit nimmt mit steigender Temperatur ab. Dies wurde beobachtet über einen Temperaturbereich von 270 K bis 338 K, in dem die Lebenszeit von 1107 ms bis auf 100 ms abfiel. Die Analyse der zeitintegrierten Emission mit dem Smartphone nach einer Anregung mit 375 nm zeigte, dass die Temperaturen im Bereich von 270 K bis 338 K präzise gemessen werden konnten mit einer Messungenauigkeit unter 2 K. Darüber hinaus wurde die Lebenszeitmessung nicht durch Hintergrundstrahlung beeinträchtigt und ermöglichte somit eine genaue Temperaturmessung auch bei einer Hintergrundbeleuchtungsstärke von bis zu 1500 lx.

Um eine Smartphone-basierte Fälschungssicherung zu realisieren wurden anhaltende Leuchtstoffe mit einstellbarer Lebenszeit bei Raumtemperatur benutzt, um dynamische, lumineszierende Etiketten zu entwickeln. Dynamische

Fälschungssicherung wurde mithilfe von Ti^{4+}-dotierten $Gd_2O_2S: Eu^{3+}$ realisiert, wobei die Ti^{4+}-Dotierung eine Kontrolle der Lebenszeit bei Raumtemperatur ermöglicht. Durch eine Veränderung der Kodotierung von 0 bis 0.09 mol% konnte die Lebenszeit von 1.17 ± 0.02 bis 5.95 ± 0.07 s durchgestimmt werden mit einer Anregung bei 375 nm. Durch eine Kombination von Leuchtstoffen mit verschiedenen Lebenszeiten konnten somit dynamische Etiketten zur Fälschungssicherung entwickelt werden. Die Lebenszeit der Leuchtstoffe für diese dynamischen Muster bestimmte dabei die Komplexität der Fälschungssicherung. Solche Muster, die aus einer Kombination von Leuchtstoffen mit großen Unterschieden in der Lumineszenzlebenszeit entwickelt wurden, konnten mit bloßem Auge beobachtet werden. Im Gegensatz dazu sind zeitliche Änderungen in Etiketten mit viel kürzerer Lebenszeit im Bereich von 0.2 s nur schwer mit bloßem Auge nachzuvollziehen. Mithilfe der Smartphone-Kamera mit einer Aufzeichnungsrate von 30 Bildern pro Sekunde können die versteckten Merkmale jedoch leicht entschlüsselt werden. In Hinblick auf die tatsächliche Anwendung am Verkaufsort, ist eine UV-Quelle einerseits normalerweise nicht vorhanden in einem Smartphone und andererseits stellt der Einsatz von UV-Strahlung für die Anregung der Leuchtstoffe eine Gesundheitsrisiko dar.

Um die Nutzung einer UV-Quelle gänzlich zu vermeiden, wurden zweifarbige dynamische Etiketten zur Fälschungssicherung entwickelt. Diese erlauben eine Anregung mithilfe eines herkömmlichen Smartphone-Blitzlichtes während die Emission einfach mit der Kamera aufgezeichnet werden kann. Zu diesem Zweck wurden grün emittierende ($SrAl_2O_4: Eu^{2+}$, Dy^{3+} (SAED)) und rot emittierende ($CaS: Eu^{2+}$ und $SrS: Eu^{2+}$) Leuchtstoffe entwickelt. Die Lebenszeit von SAED konnte variiert werden von 0.5 s bis 11.7 s durch Glühen des kommerziell erhältlichen Stoffes, was eine Verringerung der Störstellendichte im Material zur Folge hat. Die Lumineszenzlebenszeit von $CaS: Eu^{2+}$ und $SrS: Eu^{2+}$ konnte dagegen zwischen 0.1 bis 0.6 s und 150 bis 377 ms eingestellt werden mithilfe der Eu^{2+}-Dotierdichte.

Die Nutzung eines Smartphones ermöglicht nicht nur lebenszeit-basierte Temperaturmessungen ohne teure Messinstrumente, sondern eröffnet darüber hinaus eine kostengünstige Methode zur Authentifizierung von lumineszenzbasierten, dynamischen Markierungen zur Fälschungssicherung.

Abstract

Phosphors that exhibit persistent luminescence (PersL) open up new possibilities for smartphone-based sensing and anti-counterfeiting applications. With a smartphone video recording at 30 frames-per-second (fps), the lifetime of the PersL can be determined if it is greater than 100 ms. The smartphone-acquired data can then be used to realize applications otherwise reserved for phosphors that have a short lifetime. Lifetime images can be created from smartphone-acquired videos which typically needed complicated instrumentation for short lifetime detection and imaging such as multichannel scaling, high-speed cameras, and fluorescence lifetime imaging microscopes. This thesis is focused on smartphone-based detection of PersL for thermometry and anti-counterfeiting applications.

To establish smartphone-based PersL lifetime thermometry, a Gd_2O_2S: Eu^{3+} persistent phosphor, excitable with a UV source was synthesized, characterized, optimized, and applied. The Gd_2O_2S: Eu^{3+} phosphor exhibited a temperature-dependent PersL lifetime that was bright and long enough to be video recorded at 30 fps using a smartphone camera. The phosphor had a photoluminescence quantum yield of 65 %, and its PersL lifetime decreased with an increase in temperature from 1107 to 100 ms in the 270 – 338 K range. From the analysis of the integrated emission from the smartphone-acquired videos following 375 nm excitation, temperatures in the 270 – 338 K range could be accurately determined with a precision better than 2 K. Using spectral filters, this temperature determination could be done with bright background illumination up to 1500 lm/m^2.

To realize smartphone-based anti-counterfeiting, persistent phosphors with tunable PersL lifetime at room temperature were developed to make labels with dynamic luminescence. The PersL lifetime tuning was realized by co-doping Gd_2O_2S: Eu^{3+} phosphor with Ti^{4+} ions to tune the PersL lifetime at room temperature. By controlling the Ti^{4+} co-doping from 0 to 9 mol%, the PersL lifetime of these phosphors could be tuned from 1.17 ± 0.02 to 5.95 ± 0.07 s after 375 nm excitation. Dynamic anti-counterfeiting labels were then realized by making patterns using phosphors with different PersL lifetimes. The intricacy level of the

developed labels depended on the PersL lifetime of phosphors that were used to realize the dynamic patterns. Anti-counterfeiting patterns that were developed using persistent phosphors with large differences in their PersL lifetime were observable by the naked eye. In contrast, anti-counterfeiting patterns developed with phosphors with close PersL lifetime (0.20 s PersL lifetime difference) were difficult to differentiate by eye but the patterns could be easily decoded from an analysis of 30 fps videos acquired using a smartphone. From an application perspective, the use of UV excitation is not desirable as an illumination source not present in the smartphone is needed and UV radiation can pose health risks.

To eliminate the use of UV excitation, dual-color dynamic anti-counterfeiting labels that allowed the smartphone flashlight to act as the excitation source and the emission detected using its camera were developed in the final part of this thesis. In this direction, labels based on green-emitting $SrAl_2O_4$: Eu^{2+}, Dy^{3+} (SAED), and red-emitting CaS: Eu^{2+} and SrS: Eu^{2+} phosphors that allowed smartphone flashlight excitation and subsequent authentication from acquired video analysis were developed. The SAED persistent lifetime could be varied from 0.50 to 11.70 s by annealing the commercial material in the air to reduce the trap density. The persistent luminescence lifetime of the synthesized CaS: Eu^{2+} and SrS: Eu^{2+} could be varied from 0.10 to 0.60 s and 0.15 to 0.40 s respectively by varying the Eu^{2+} dopant concentration. Color tunability of the phosphors was achieved by blending the SAED and the red-emitting phosphors. Several sets of anti-counterfeiting labels based on seven-segment displays, 2D barcodes, and customizable labels were developed.

In summary, this thesis shows that tailored PersL phosphors allow the use of smartphones for lifetime determination. This not only surmounts the use of the expensive hardware for short lifetime thermometry applications but also opens an inexpensive route for authentication of luminescence-based dynamic anti-counterfeiting labels.

Table of Contents

Acknowledgments

I would like to express my profound gratitude to Prof. Bryce Richards for allowing me to pursue my Ph.D. in the “Advanced Materials and Optical Spectroscopy (AMOS)” group at the Institute of Microstructure Technology (IMT), at KIT via a DAAD scholarship. He walked with me during the initial proposal development stage for the DAAD scholarship application and has remained supportive of my research undertaking since I joined IMT. Thank you for the guidance, insightful feedback, and constructive engagement in all aspects of this work. I am deeply indebted to my immediate supervisor Dr. Ian Howard for his extensive support, guidance, and invaluable supervision. Your expertise, creativity, understanding, and willingness to push the boundaries sharpened my thinking and extensively improved the quality of my work.

Thumbs up Dr. Dmitry Busko, an extremely creative dude who takes a problem and converts it to solutions! I learned a lot from your creativity and hand-on-experience dealing with optics. Thanks for ensuring that the optics labs are always up and running. Special thanks to Dr. Guojuun Gao for the initial training on sample preparation and characterization.

Special gratitude goes to Karlsruhe School of Optics and Photonics (KSOP) for providing technical and interdisciplinary training through the now highly reputable Ph.D. program. The knowledge I gained through the MBA-fundamentals program is invaluable. Thanks for organizing the conferences, summer schools, and seminars even during the hard times of COVID 19. Special thanks to Dr. Franco Weth my KSOP mentor, Dr. Danays Kunka, Ms. Denica Angelova-Jackstadt, and the entire KSOP engagement office for the support.

This work was made possible through the financial support provided by the German Academic Exchange Service (DAAD) through their Ph.D. scholarship program. Special thanks go to Michael Alexander Hillenblink for the support when challenges arose during my research. I am also grateful to have been awarded the Amplify Scholarship for Black Scientists from OPTICA (formally Optical Society of America) to enhance my knowledge and visibility in optics and photonics.

I am also grateful to have made new friends who guided me in the new environment, helped me with initial instrument training, and introduced me to Ph.D. research life. Thank you, Dr. Efthymios Klampaftis, Dr. Andrey Tushartov, Dr. Damien Hurdy, Prof. Uli Paetzold, Dr. Gerardo Hernandez-Sosa, Dr. Guojun Gao, Dr. Reetu Elza Joseph, Dr. Stephan Dottermusch, Dr. Michael Adams, Dr. Marius Jakoby, Dr. Michael Oldenburg, Dr. Lwitiko Pholds, Dr. Nicolo Baroni, Dr. Hossain, Ihteaz Muhaimeen, Dr. Deski Beri, Dr. Chauhan Aditya, Dr. Jakob Kiran, Dr. Amjad Farooq, Dr. Hossein Nasrabadi, Milian Kaiser, Natalia Kiseleva, Vinay Kumar, Jan Fischer, Julie Roger, Roman Lyubimenko, Felix laufer, Roja Singh, Ritzer David, Pariya Nazari, Gota Fabrizio, Fernando Arteaga-Cardona, Sheying Li, Aiman Roslizer, Eduard Madirov, Luis Arturo Ruiz-Preciado and Isabel Allegro. Your moral support, advice, and engagements kept my spirits high. Special thanks to Reetu, and Jan for proofreading my thesis document.

I would also like to thank the entire IMT staff for providing a conducive research environment and helping whenever needed. Special thanks to Alexandra Möritz for helping me in the design and fabrication of my anti-counterfeiting label molds. I also very much appreciate the support provided by the International Student Office (IStO) KIT for their support during my stay. Special thanks to Hartmut Speck and Oliver Kaas for the advice, support, and guidance you provided.

I am extremely grateful to my dear family, my dear wife Jane Musyoka, my daughter Katrina Katumo (KK), and Leon Katumo (Leo). It is from you that I get the courage and energy to work hard. Thanks, Jane, your sacrifices, encouragement, support, love, and care are invaluable. Thanks for taking care of KK and Leo during my long working hours. I dedicate this work to you. Lastly, I would like to thank my parents, James Ngei and Rose, my brothers Sylvester Maingi and Charles Mutua, and my siz Winnie for the constant encouragement and support. I am forever grateful!

List of Publications

Patents:

1. **Katumo, N.,** Howard, I. A., Busko, D., Gao, G., Turshatov, A., Richards, B. S., Photonic Markers Enabling Temperature Sensing and/or Security Marking using Low Frame Rate Cameras (2021/6/30) EP 3842505A1 (19219261.5) (Patent pending).

2. Li, K., **Katumo, N.,** Howard, I. A., Busko, D., Turshatov, A., Richards, B. S., Photonic Markers Enabling Security Marking, Product Identification and Material Sorting using Low Frame Rate Cameras. 102021003206.3 (Patent pending).

First author publications:

3. **Katumo, N.,** Gao, G., Laufer, F., Richards, B. S., & Howard, I. A. (2020). Smartphone-Based Luminescent Thermometry via Temperature-Sensitive Delayed Fluorescence from Gd_2O_2S: Eu^{3+}. *Advanced Optical Materials*, *8*(19), 2000507.

4. **Katumo, N.,** Ruiz-Preciado, L. A., Kumar, V., Hernandez-Sosa, G., Richards, B. S., & Howard, I. A. (2021). Anticounterfeiting Labels with Smartphone-Readable Dynamic Luminescent Patterns Based on Tailored Persistent Lifetimes in Gd_2O_2S: Eu^{3+}/Ti^{4+}. *Advanced Materials Technologies*, *6*(7), 2100047.

5. **Katumo, N.,** Li, K., Richards, B. S., & Howard, I. A. (2022). Dual-color dynamic anti-counterfeiting labels with persistent emission after visible excitation allowing smartphone authentication. *Scientific Reports*, *12*(1), 1-14.

Co-authored publications:

6. Gao, G., Busko, D., **Katumo, N.,** Joseph, R., Madirov, E., Turshatov, A., ... & Richards, B. S. (2021). Ratiometric luminescent thermometry with excellent sensitivity over a broad temperature range utilizing thermally-assisted and multiphoton upconversion in triply-doped La_2nO_3: $Yb^{3+}/Er^{3+}/Nd^{3+}$. *Advanced Optical Materials*, *9*(5), 2001901.

7. Kumar, V., Dottermusch, S., **Katumo, N.,** Chauhan, A., Richards, B. S., & Howard, I. A. (2022). Unclonable Anti-Counterfeiting Labels Based on Microlens Arrays and Luminescent Microparticles. *Advanced Optical Materials*, 2102402.

List of Conference Contributions

8. **Katumo N.,** Bryce S. Richards, and Ian A. Howard. *Smartphone Authenticatable Dynamic Color-Tunable Anti-Counterfeiting Labels Based on Persistent Phosphors*, Karlsruhe Days of Optics & Photonics Best Poster Award 2021. Best poster award.

9. **Katumo N.,** Bryce S. Richards, and Ian A. Howard. Determination of delayed luminescence lifetimes of $Gd_2O_2S: Eu^{3+}/Ti^{4+}$ phosphors using smartphones; Applications to anti-counterfeiting. *KSOP-QMat Summer School.* 4-5 Sept. 2020. Karlsruhe, Germany. (Poster)

10. **Katumo N.,** Guojun Gao, Felix Laufer, Bryce S. Richards, and Ian Howard. Luminescence thermometer based on the thermal shifting of charge transfer band. *European Material Research Society (EMRS).* May 27th - 31st 2019. *Nice France.* (Poster)

11. **Katumo N.,** Bryce S. Richards, and Ian A. Howard. Thermometric-based Photonic-marking via thermally shifting charge-Transfer-Band in $Gd_2O_2S: Eu^{3+}$. *Karlsruhe days of Optics and Photonics*, 9-10 Sept. 2019. Karlsruhe, Germany. (Poster)

List of Abbreviations

ADC	Analog to digital converters
CB	Conduction band
CCD	Charge-coupled device
CMOS	Complementary metal oxide semiconductor
CTB	Charge transfer band
DC	Down conversion
DS	Downshifting
ED	Electric dipole
EQ	Electric quadrupole
FIR	Fluorescence intensity ratio
FLIM	Fluorescence lifetime imaging microscopy
ICDD	International center for diffraction data
ICSD	Inorganic crystal structure database
IMT	Institute of Microstructure Technology
IoT	Internet of things
KIT	Karlsruhe Institute of Technology
KSOP	Karlsruhe School of Optics and Photonics
LMCT	Ligand to metal charge transfer
MCS	Multi-channel scaling
MD	Magnetic dipole
PersL	Persistent luminescence
PLQY	Photoluminescence quantum yield
POS	Point-of-sale
PUF	Physical unclonable function
TCL	Thermally coupled levels
TCPSC	Time correlated single photon counting
TDPL	Temperature-dependent photoluminescence
UC	Upconversion
VB	Valence band

1

Introduction

Persistent luminescence (PersL) also known as afterglow or delayed luminescence and sometimes phosphorescence is a phenomenon in which luminescence continues (for several milliseconds to several hours) after the excitation source has been removed [1-5]. Their persistent nature of emission continues to amaze and fascinate people. Materials that exhibit PersL are referred to as persistent phosphors. Persistent phosphors derive their applications from their luminescence characteristics following excitation. In this thesis, persistent phosphors are used to realize smartphone readable luminescence thermometry and anti-counterfeiting.

Luminescence thermometry is the intentional exploitation of temperature-dependent luminescence properties such as lifetime, emission spectra, and spectral shifts to achieve spatial thermal sensing. It is of great importance to today's technological needs as it succeeds in areas where the existing thermometry techniques perform poorly, more so when the measuring scales are below 10 µm [6]. Some of the emerging technologies where luminescent thermometers are superior to existing techniques include hard-to-access areas in nanotechnology, biomedicine, optoelectronics, and analytical systems [6-9]. Therefore, there is a strong need to realize luminescence thermometry. A major challenge so far has been the luminescence-reading device that translates the temperature-dependent luminescence characteristic to an indicative temperature value. These include spectrometers, lifetime imaging instruments, and fast cameras, all of which are relatively expensive and in some cases not portable. To surmount this problem, a

smartphone is used to read (video-record) the temperature-dependent PersL lifetime of europium doped gadolinium oxysulphide ($Gd_2O_2S: Eu^{3+}$) following 375 nm pulsed excitation. From the analysis of the acquired videos, it is possible to determine the surface temperature and acquire 2D images of a surface coated with the phosphor. By extending the PersL of the $Gd_2O_2S: Eu^{3+}$ at room temperature it was also possible to realize smartphone readable dynamic anti-counterfeiting.

The problem of counterfeit products, bills, and documents is not a new one, but it is becoming a tremendous burden to society as it poses serious economic, health, social, and safety concerns. In the same instance, inferior counterfeit products violate intellectual property rights and destroy a brand's reputation. It is expected that the economic burden of counterfeiting and piracy in 2022 will drain over USD 4 trillion from the global economy at a cost of over 5 million legitimate jobs [10, 11]. The most serious health concerns are due to counterfeit pharmaceuticals. For example, close to a quarter of a million deaths occur each year due to counterfeit malaria and pneumonia medication [12]. Unfortunately, counterfeiting is increasing and eating into legitimate global trade.

An effective solution to minimize counterfeiting is to introduce opportunities for more effective anti-counterfeiting measures that are robust and easier to use in distinguishing fakes from genuine products. At the same time, the approaches should remain affordable and accessible to those who acquire the tagged products. A front-runner in the establishment of such anti-counterfeiting technologies is luminescence materials that display overt and covert features after appropriate excitation. In this thesis, persistent phosphors with tunable PersL lifetime readable from ordinary smartphones are used to realize dynamic anti-counterfeiting labels. The use of smartphones ensures inexpensive authentication while at the same time opening up extension possibilities of integrating the anti-counterfeiting technique with other product securing approaches.

The following section discusses the fundamentals of PersL. This is then followed by a discussion on smartphone-based PersL sensing and its applications in luminescence thermometry and anti-counterfeiting. Finally, an outline of the thesis is provided.

1.1 Fundamentals of PersL

Persistent phosphors have charge carrier trapping and charge recombination centers (activator centers) that are responsible for the PersL. When a persistent phosphor is appropriately excited (usually with visible light, ultraviolet (UV), X-rays, or gamma radiation), part of the excited charge carriers are trapped in the trap centers and others contribute to the instantaneous emission observed during excitation. After the excitation has ceased, the trapped charge carriers are thermally promoted to the activator centers leading to PersL. The trapping centers are either lattice defect centers, impurity centers, and self-trapping potential wells, in which the charge carriers (electrons and holes) are trapped for some time before being released to the activator ion [13, 14]. Once in the activator ion, the charge carriers can relax to the ground state radiatively leading to PersL or non-radiatively.

Figure 1.1 illustrates a general process of producing PersL in a persistent phosphor [14]. Following UV excitation, the emitter ions are excited from the ground state to an excited state near the conduction band (process 1). In this position, part of the excited electrons are trapped in the trap centers while others relax to the ground state radiatively or non-radiatively.

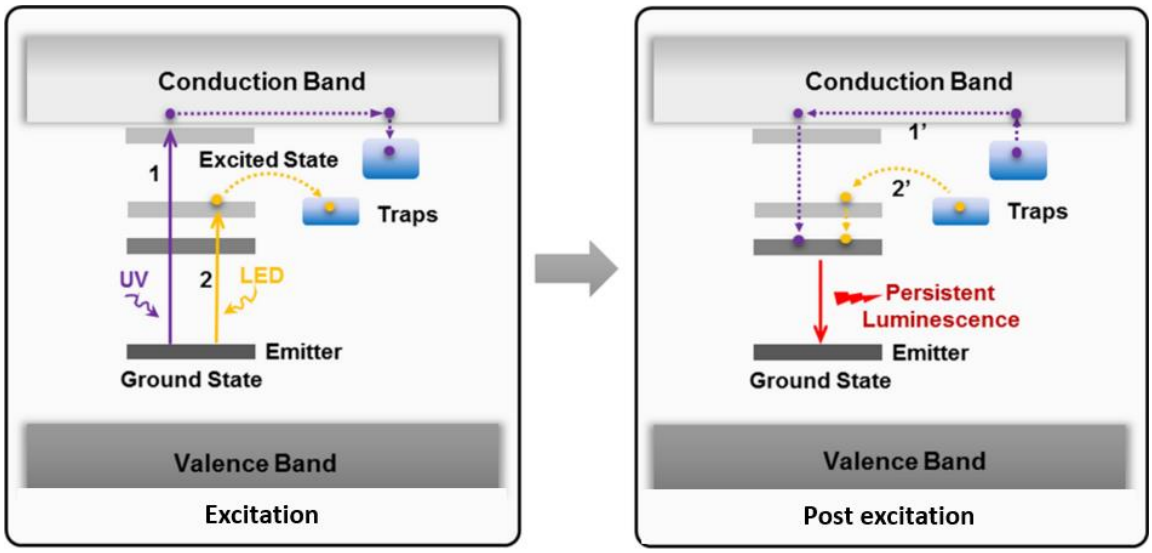

Figure 1.1. Schematic diagram of persistent luminescence under different excitation sources. Adapted from Liu et al.[14]. CC BY 4.0 license.

Once the excitation is ceased, the trapped electrons re-enter the conduction band (CB) (process 1') via various stimulation mechanisms such as thermal activation and then relax to the ground state [14]. Electrons that relax radiatively lead to the observed PersL. This is the dominant process of PersL and it is a downshifting process. Alternatively, following light-emitting diode (LED) excitation, electrons can also be excited to a corresponding excited state. Then some relax to the ground states and others are trapped in the trap centers via either a quantum tunneling process or exciton hopping. Again, upon ceasing the excitation, the trapped charge is thermally freed and can return to the activator leading to PersL (process 2') [14, 15].

The activator (also known as an emitter) ions are usually doped in the host at low concentrations. For inorganic phosphors, most of them are usually the rare-earth ions, from which the emission either stems from the 4f - 4f transitions or the 5d - 4f transitions or the transitional metals ions. In this thesis, the trivalent europium doped gadolinium oxysulphide, $Gd_2O_2S: Eu^{3+}$ is used for thermometry applications. Additionally, the PersL lifetime of the $Gd_2O_2S: Eu^{3+}$ is tuned by co-doping the optimized sample with various doping concentrations of Ti^{4+} ions. The phosphors are then used to realize dynamic luminescence anti-counterfeiting after UV excitation. in addition divalent doped calcium sulfide, $CaS: Eu^{2+}$, strontium sulfide, $SrS: Eu^{2+}$, and Strontium aluminate doped with europium and dysprosium, $SrAl_2O_4: Eu^{2+}, Dy^{3+}$ are also used to develop smartphone authenticatable of dual-color dynamic anti-counterfeiting labels. For these labels, the smartphone flashlight acts as the exciting source and the smartphone camera detects the dynamic PersL of the patterns. Therefore the Eu ion is the dominant emitter ion used to realize these applications in this thesis. The next section briefly discusses Eu activated PersL.

1.2 Europium Activated PersL

Photoluminescence (PL) in Eu - activated phosphors emanate either from the 4f - 4f transitions in Eu^{3+} ions or from the allowed 5d - 4f transitions of divalent Eu^{2+} ions. In both Eu^{3+} and Eu^{2+} activated persistent phosphors, the trap levels are usually due to intrinsic defects such as oxygen vacancies, impurities, and lattice distortions [16]. More so, the addition of co-dopants such as Nd^{3+}, Ti^{4+}, and Dy^{3+}

has been demonstrated to significantly enhance the PersL by creating more trapping centers [1]. Note that one possible cause of the enhancement of the trapping centers is due to the charge imbalance of these ions when they replace the host ion. Other factors that affect PersL include the method of phosphor synthesis, the concentration of the dopants, and the reductive atmosphere utilized during phosphor synthesis [16]. Typical host materials for Eu^{3+} activated persistent phosphors include but are not limited to lanthanide oxysulphides (Ln_2O_2S) for Ln = (Gd, Y, La, Lu) [8, 11, 17], also SnO_2 [18], and Ca_2SnO_4 [19]. For Eu^{2+} doped hosts, the alkaline earth aluminates, silicates, and sulfide-based hosts are the most efficient and most explored materials for PersL. The $SrAl_2O_4$: Eu^{2+}, Dy^{3+}, $Sr_4Al_{14}O_{25}$: Eu^{2+}, $Dy^{3+,}$ and $CaAl_2O_4$ Eu^{2+}, Nd^{3+} are among the most studied and most efficient materials [20].

For efficient PersL, the persistent phosphor should have strong absorption bands to allow efficient ‘charging’ during excitation. Unfortunately, the Eu^{3+} the 4f - 4f forbidden transition probabilities are not high enough to ensure strong absorption. These transitions are typically narrow sharp spectral lines and thus not efficient in absorption during excitation [21]. Alternative charging of the persistent phosphor has to be sought. Luckily, Eu^{3+} is the most oxidizing of the lanthanide trivalent ions and establishes charge-transfer bands (CTB) that have very strong absorption, especially in the UV region [21]. The CTB acts as antennas that absorb light and then transfer the energy to the Eu^{3+} ion. A good example of a persistent phosphor used in this thesis is the Gd_2O_2S: Eu^{3+} which has a broad absorption ranging from 400 - 250 nm [8]. To increase its trap density and enhance or tune the PersL, co-dopant ions such as Ti^{4+}, and Mg^{2+} are used [11, 22, 23]. All Eu^{3+} activated phosphor emissions stem from the parity forbidden 4f - 4f transitions that are well shielded from the crystallographic environment and independent of the host. These transitions lead to typically sharp spectral lines that are roughly constant from host to host.

The Eu^{2+} ion is the ‘workhorse’ of persistent phosphors and still is the custodian of the best persistent phosphors known to date, the $SrAl_2O_4$: Eu^{2+}, Dy^{3+} (SAED) developed by Matsuzawa in 1996 [1, 4, 24]. Contrary to the 4f - 4f transitions that are well shielded from the crystallographic environment, the 5d - 4f transitions of Eu^{2+} are strongly affected by the crystallographic and chemical environment of the

host. As a result, the absorption and emission that emanate from Eu^{2+} are tunable in a broad range of wavelengths from UV to near-infrared (NIR) [25, 26]. Note that the Eu^{2+} (5d - 4f transition) is a parity-allowed transition by Laporte's rule, and acts ideally as the excitation band [27]. Again, for $Eu^{2+,}$ activated persistent phosphors, an appropriate co-dopant ion such as Dy^{3+} is used as it enhances the PersL by increasing the trap density.

1.3 Applications of PersL

PersL applications can be broadly classified into either display-and-lighting or biological applications. The applications mostly utilize the PersL property of the persistent phosphors which are usually dispersed in various media. Among the applications; luminous paints are the most commercialized lighting and display applications in safety signs, lighting sources, road traffic signs architecture decorations and glow watches, and luminous fibers [28]. The historical applications of PersL materials include glow-in-the-dark paints, toys, and watch dials [28].

Recently, there has been an interest to develop glow in the dark roads whose glow guides road users in the dark by making the trajectory of the line visible as shown in Figure 1.2. These roads are charged during the day and store the optical energy which they slowly release at night [29].

Figure 1.2. Glow in the dark roads near Oss in the Netherlands. The road marking absorb light during the day and emit the green glow at night providing visible trajectory lines to road users. Adapted from Scott [29]. Copyright 2022, National Public radio NPR.

Alternatively, lighting from vehicle headlights 'recharges' the phosphor-based marking hence making them visible all night. Another fascinating application that has been explored in the recent past is anti-counterfeiting. Classically, fluorescence steady-state-based anti-counterfeiting techniques have been the dominant technique in phosphor-based anti-counterfeiting labels even to date.

However, the temporal domain of luminescence has gained a lot of interest as it provides a wider library of ensuring high security of anti-counterfeiting labels compared to the steady-state. As a result, there has been increased interest from the scientific community to develop anti-counterfeiting labels based on PersL. Some of the contributions are presented as primary work in this thesis. Figure 1.3 shows a composite image of the use of PersL phosphors for safety signage and also anti-counterfeiting applications [30].

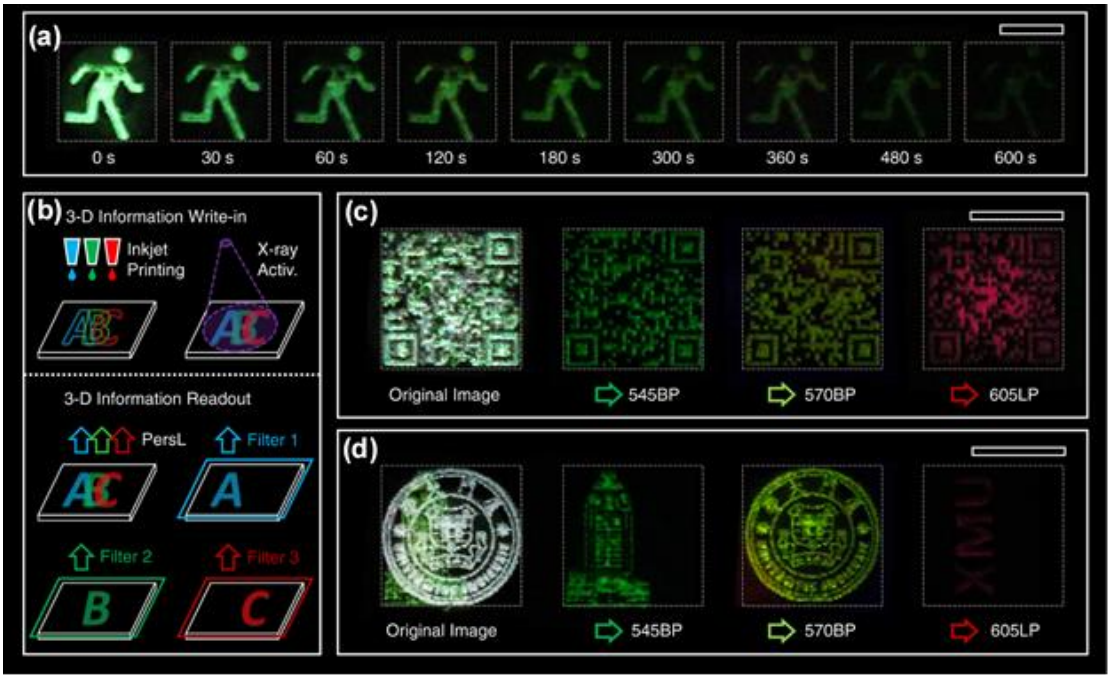

Figure 1.3. a) PersL based on $NaYF_4:Tb^{3+}$@NaYF4 inks showing images of an emergency exit sign with a delay time of up to 600s. b) Schematic illustration of developing anti-counterfeiting labels based on PersL inks. The upper and lower figures illustrate the information write-in and readout processes, respectively. The patterns are designed in an overlapping manner and the encrypted message is red by reading the persistent luminescence with specific band pass filters, 545BP, 570BP, and 605LP filters as shown in (c) and (d). Adapted from Zhuang et al. [30] CC BY 4.0 license.

In Figure 1.3a, a safety sign with a delay of up to 600 s is demonstrated. These safety signs guide those exiting buildings in case of emergencies such as blackouts. With the same persistent phosphors, anti-counterfeiting labels can be developed as shown in Figure 1.3b where different markers are inkjet printed in an overlapping manner. The readouts after excitation of the labels are shown in Figure 1.3c where the encrypted information can be read in the temporal domain while utilizing appropriate optical bandpass filters. Persistent phosphors that strongly absorb in the UV region where solar cells show inadequate absorption and emit in the visible region where solar cells have adequate absorption are also used as spectral converters. Most solar cells have a poor spectral response in the UV region and therefore converting the UV photons to visible photons enhances their performance [31]. In addition, the luminescence downshifting (LDS) layer in front of some solar cells such as those based on perovskites has been reported to also enhance their photostability [32].

Persistent phosphors are widely used for in vivo and in vitro bio-imaging applications [28, 33]. Since there are capable of sustained emission, real-time background-free monitoring of biological processes is possible. The use of PersL materials in bio-imaging allows the excitation of the species before imaging and permits detection and imaging without external illumination. This process ideally produces better resolution images compared to the use of fluorescence probes which suffer from background noise since imaging is done after excitation and not simultaneously. Other applications include molecular sensing and molecular detection through fluorescence energy transfer mechanisms [28, 34].

When the intensity of the PersL is strong and tailorable, it is possible to extend the applications beyond the ones already discussed. More so, it is possible to quantify the PersL lifetime from inexpensive and portable devices such as smartphones as opposed to expensive instrumentation such as streak cameras, fluorescence imaging microscopes (FLIM), and time-correlated single-photon counting (TCSPC). In this thesis, persistent phosphors that emit in the visible region are used to demonstrate smartphone-based applications in thermometry and anti-counterfeiting. Ideally, the smartphone acts as the PersL detector by video-recording the emission at 30 frames-per-second (fps) following excitation of the

phosphor. Various applications are then realized from the analysis of the acquired video frames.

1.4 Smartphone-Based PersL Sensing

Smartphones are everywhere across the globe, helping in communication, leisure (games and social media), photography, and handling of our financial transactions among many other applications. Their strong hardware and extensive software capabilities have always opened doors for new applications otherwise initially dedicated to sophisticated or specialized devices. In the field of luminescence, the smartphone has acquired numerous sensor applications. These include but not limited to PersL imaging [8, 11, 35-38], bio-sensing applications [39-41], internet-of-Things (IoT) health applications [42, 43], chemical [44] and radiation detection [45]. Most of these applications utilize the smartphone camera in conjunction with other accessories and supporting software.

The smartphone camera is based on complementary metal-oxide-semiconductor (CMOS) photodiodes. While the CMOS can detect up to 1100 nm, the bandgap of the silicon, the smartphone cameras are equipped with NIR filters to only detect 400 -700 nm [46]. This visible detection range is intentionally designed for photography so that the captured images mimic that observed by the eye. The CMOS camera photosites are also covered with color filters in a Bayer series array to allow the realization of colored images that mimic human observation [41, 47]. In a Bayer series, 50% of the photosites in the CMOS sensor are green-covered 25% are blue-covered and the last 25% are red-covered. After each image is acquired, a demosaicing algorithm interpolates the RGB channels of the photosites into one colored super-pixel [41]. Each photosite contributes a single 8-bit grayscale intensity (2^8 = 256; 0 - 255 levels) and thus each channel in a colored image has 255 levels. Once acquired, the images or videos are displayed on the smartphone and can be extracted for further analysis. Another important feature of the smartphone camera is the standard 30fps video-recording rate. This limits the smartphone to only acquire the PersL (PersL lifetimes >100 ms) and not the very fast component of the emission in luminescence phosphors. Finally, to use the smartphone camera in dynamic lighting environments, manual control is necessary to lock the frame rate, exposure, ISO, and shutter speed. For most android-based

smartphones, this is achieved through the camera-2-application interface (Camera 2API) [48]. Iphones also allow for manual control of the shutter speed, sensor sensitivity (ISO), and exposure compensation in their camera applications. With all the smartphone camera settings in order, one can acquire the persistent emission by directly video recording the persistent emission.

Afterward, the PersL of each frame in the video is converted to a PersL decay curve in Matlab program as shown in Figure 1.4 in the case of the Gd_2O_2S: $0.06Eu^{3+}$. The smartphone-derived data is in agreement with the photon counting (multi-channel scaling, (MCS)) acquired PersL lifetime data. A complete description of the video-to-decay lifetime conversion is presented in the methods chapter sections 3.4.2 of this thesis.

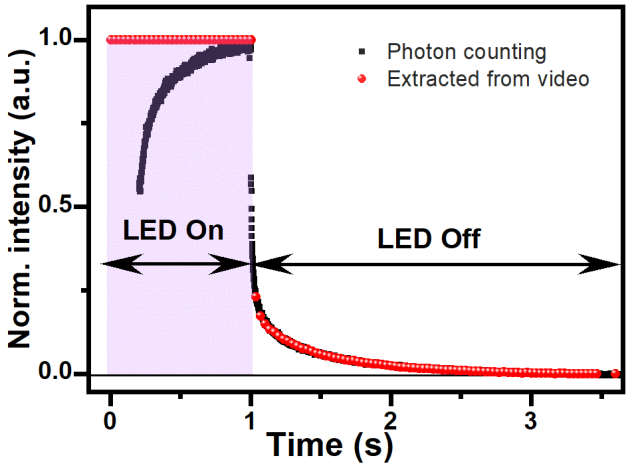

Figure 1.4. Normalized PersL lifetime of the $^5D_0$ state of Eu^{3+} in Gd_2O_2S: $0.06Eu^{3+}$ during and after excitation with 375 nm LED. The photon counting process is indicated in black while the computation from smartphone-acquired video is in red and does not show the raise time of the phosphor when the LED is on.

The very first component of the persistent decay is not captured owing to the 30 fps limitation of the smartphone camera. There is also a clear difference in the data acquired when the LED is turned on since the smartphone channels are saturated as opposed to the rise time observed in the spectral-specific photon counting process. For clarity purposes, the integral emission when the LED is off is the PersL representing the continued release of trapped charge carriers. Now, this data is obtained with a smartphone only, without any integrated accessories. Due to the

30 fps and saturation of the sensors during excitation, a realistic offset of 0.2 s is allowed after the excitation is ceased. It is also possible to determine shorter lifetimes. However, one has to incorporate other accessories to compensate for the low fps as demonstrated by Zhu using a miniaturized smartphone-based system with a motor to rotate the sample [49]. The added accessories help create a streak image across the phone sensor and allow spatial information to be translated into faster temporal information.

To acquire the PersL lifetime using only a smartphone (without other performance-enhancing accessories such as lenses), the persistent phosphors used have to meet several conditions. Firstly, the PersL emission must be in the visible region (400 - 700 nm) due to the NIR filters incorporated in the CMOS sensors. Secondly, the PersL must be bright enough to be captured by the smartphone camera. This is related to the external photoluminescence quantum yield (PLQY), of the phosphor. The PLQY is the ratio of the number of photons emitted to the number of photons absorbed. Finally, the PersL of the phosphor must be greater than 100 ms. The lower limit is due to the low frame rate which excludes the smartphone camera from capturing the very fast component of fluorescence. In addition, it is also practical to give an allowance for the saturated pixels to settle after saturation during excitation. Some of the phosphors used in this thesis fulfilling these conditions are the Gd_2O_2S: Eu^{3+} and Gd_2O_2S: Eu^{3+}, Ti^{4+} phosphors which are UV excitable down-shifting (DS) materials. It would also be interesting if the smartphone would serve as both the exciting device using its flashlight and as the detecting device using its camera. For this, the persistent phosphors should also absorb and emit in the visible region. In this thesis, $SrAl_2O_4$: Eu^{2+}, Dy^{3+} (SAED), CaS: Eu^{2+}, and SrS: Eu^{2+} persistent phosphors have been used to demonstrate smartphone excitation and detection for dynamic and color-tunable anti-counterfeiting [35].

1.4.1 Applications in Luminescence Thermometry

Luminescence thermometers provide contactless and noninvasive temperature sensing in areas where traditional thermometers are impractical to use. The operating principle is based on monitoring the temperature-responsive parameter and mapping it to the calibrated temperature. The applications areas in which

luminescence thermometers would provide solutions over the traditional thermometers include micro-scale areas in microelectronics, micro-optics, microfluidics, and nano-medicine [7]. The three main approaches used in luminescence thermometry include; 1) spectral shifting of emission spectra in response to temperature, 2) emission intensity measurements (either a single emission or a pair of emission transitions: - also known as the fluorescence intensity ratio (FIR) method) and 3) luminescence lifetime measurements [7]. In the three luminescence thermometers, thermal quenching of the luminescence underpins the main mechanism of thermometry and results from the temperature dependence of the non-radiative transitions rate [50]. The lanthanides are the most notably used luminescence centers for thermometry applications.

The FIR method is by far the most explored approach to inferring temperature from luminescence spectroscopy. Thermometry calibration is achieved by taking the ratio of intensities of two thermally coupled levels. For the FIR method, the Er, Yb lanthanide ion pairs with Er being the activator ion and Yb the sensitizer are by far the most explored in various host matrices such as in $NaYF_4$ [7, 51]. However, the intensity-based approach is prone to background radiation, a factor that limits its applications beyond laboratory settings in the case where emission is in the visible region. The alternative, which is the use of temperature-induced changes in the emission lifetime, is less sensitive to environmental variables such as the scattering of the luminescence emission after excitation and background radiation [8]. However, compared to the intensity methods, the lifetime-based approach requires expensive high-speed imaging equipment to capture the microseconds lifetime in materials [8]. Moreover, the process is more time-consuming and complex relative to the FIR methods [7]. More information on the fundamentals of luminescence thermometry including figures of merit is covered in section 2.4.1 of the background chapter.

In this thesis, a PersL thermometer based on $Gd_2O_2S: Eu^{3+}$ phosphor that allows the determination of temperature in the 270 - 338 K range from the analysis of smartphone acquired videos post UV excitation is demonstrated [8]. The $Gd_2O_2S: Eu^{3+}$ persistent phosphors PersL is temperature sensitive and decreases as the temperature increases. Therefore, videos of the PersL emission were acquired for each set temperature using a smartphone from which the PersL

lifetime was derived and mapped to the indicative temperature. These PersL lifetimes provide a calibration curve with the PersL lifetime from other surfaces that can be mapped to and the temperature determined. The developed luminescent thermometer had a relative sensitivity greater than 3.1% K^{-1} across its measuring range and good precision better than 2 K in the 270 - 320 K range [8]. Owing to the insensitivity of the lifetime-based luminescence thermometry approach to background illuminance, temperatures in the range of 270 – 320 K could be determined with a temperature resolution better than 2 K, even at bright ambient light levels of 1500 lm/m^2. Inspired by this work, and the power of the smartphone in the IoT efforts are in progress to realize IoT platforms for temperature monitoring [36]. Additionally, the coupling of temperature sensing with other applications such as smartphone-based anti-counterfeiting [37], internet (e-heath) [42], and bio applications [40] remains an active field of research.

1.4.2 Applications in Anti-Counterfeiting

Counterfeiting of products, documents, and bills is a global problem with far-fetching negative consequences to the economy, health, and safety of consumers. It is regarded as a serious crime in both developing and developed countries due to not only the widespread forgery of currency bills and certificates but also the loss of revenue brand reputation and legitimate jobs. To mitigate these negative effects, considerable efforts have been devoted to the design and implementation of brand-proof anti-counterfeiting technologies [52]. Of particular importance for these technologies are the continuous improvements of anti-counterfeiting technologies to keep counterfeiters at bay. This is because the whole industry of anti-counterfeiting and counterfeiting is usually a ‘cat and mouse game’ where it is usually a matter of time before a new anti-counterfeiting technology is cloned. It is therefore an ever-evolving field.

The most common established technologies used to safeguard products include watermarks [53], holograms [54], barcodes (2-3D), digital and smart signatures [55], plasmonic labels [56], physical unclonable functions (PUFs) [57-59], and luminescence tags [11, 60]. These anti-counterfeiting labels are attached to the products and authenticated during transactions either in the logistical chain or in the point-of-sale (POS) terminals. Alternatively, the anti-counterfeiting features are

embedded in the products in the case of bills and certificates. While the dominant high-level anti-counterfeiting technology is the holograms, in the last decade several companies have ramped up new technologies based on luminescence tagging. Some of these companies include Authentic Vision [61], Systech [62], Zortag [63], and Bosch [64], and optically code the anti-counterfeiting features for smart authentication with available devices such as smartphones and digital readers. Irrespective of the technology integrating the anti-counterfeiting feature, luminescence tags are of particular interest for preventing counterfeiting due to their unique yet tailorable optical properties and ease of integration with other technologies such as barcodes [55], PUFs [57], holograms [65], and security threats.

Luminescence-based anti-counterfeiting labels exploit the excellent optical properties of luminescence materials to provide overt and covert features in the labels. The most exploited optical properties in these labels include their high emission intensity, tunable color emission, tunable PersL lifetimes, and various emission modes such as photoluminescence, chemiluminescence, and mechanoluminescence [66]. The current research on luminescence anti-counterfeiting can be broadly divided into two major classes unique and interchangeable labels.

The unique labels class is devoted to developing PUFs, for which each label is unique and requires complete verification of the authenticating parameters [58, 59, 67, 68]. For these labels, the gold-standard security feature is therefore the unique physical aspects acquired during the stochastic label development process that limits other manufacturing techniques from making exact replicas of each label. Nevertheless, even reproducing a single label is not a worthy investment as labels are not interchangeable but unique from one another. Despite providing the highest security, there are significant overheads associated with their implementation in real life as each unique label has to be characterized and its verification features stored in a database to allow authentication [68]. This process is both time-consuming and costly and thus its market is selective to brands that are willing to pay for the overheads [59].

Interchangeable luminescence anti-counterfeiting labels, on the other hand, are similar across a brand. That is to mean that all the tags securing a certain brand of product look alike. These interchangeable labels are broadly classified into single-level, dual-level, or multi-level according to the level of security the label provides [66]. The single-level anti-counterfeiting labels are classically the oldest. The most common labels in this class are the labels that reveal the patterns when illuminated with ultra-violet (UV) light [11]. Examples of such labels include the use of invisible full-color anti-counterfeiting patterns which reveal the security features upon 254 nm excitation as demonstrated by Andres *et al*. [60].

Dual-level luminescence anti-counterfeiting tags display both covert and overt features following the appropriate stimulation that can be parameterized and quantified during authentication [66]. For these labels, the normal naked eye observation after stimulation is always not enough to authenticate the tagged product and more than one step must be undertaken for the authentication. These labels are realized through either regulating the excitation sources (e.g. dual-mode excitations and different excitation wavelengths) [52, 69-71] or co-regulating the excitation source with other parameters such as the luminescence lifetime [70, 72-76], along with thermal [69], mechanical, and color tuned emissions [77-83], and chemical response of the labels [66]. A good example of double-level anti-counterfeiting tags is the work of Yang *et al*. based on $MAl_{12}O_{19}:Cr^{3+}$ (M = Ca and Sr) persistent phosphors with deep red/NIR emissions and PersL lifetime. In this case, the NIR intensity could be the pattern carrier but is only visible when the deep red emission is filtered after excitation [84]. In addition, the PersL lifetime after UV excitation could also be tailored via Ti^{4+} co-doping and utilized for anti-counterfeiting [84].

Multilevel luminescence anti-counterfeiting is the highest level mode and labels in this category employ more than two dimensions of authentication/verification [66]. A good example of multilevel anti-counterfeiting labels are the ones developed by Zhang *et al.* $NaNbO_3:Pr^{3+}$, Er^{3+} luminescent microparticles [85]. For these labels, multilevel anti-counterfeiting was realized through superior color integration matrix (red-orange-yellow-green), bi-temporal (fluorescence and PersL), and tetra-modal (Thermo-/mechano- and upconversion and downshifting) emission using the $NaNbO_3:Pr^{3+}$, Er^{3+} microparticles [85].

Cutting across all the various categories of luminescence-based anti-counterfeiting is the hardware required for label authentication. The ideal label-authenticating device ought to be easily available, and cheap and should verify the labels in a non-sophisticated manner. Unfortunately, this is not usually the case, especially for the verification of covert features in the labels. For instance, PUFs authentication involves a wide range of sophisticated authenticating devices ranging from Raman mapping [86, 87], fluorescence imaging and reflection [59], confocal imaging [88], and spectrally resolved imaging techniques [89]. These authenticating devices and techniques are not only expensive to implement in point-of-sale terminals but also impractical for ordinary products. They only would make sense if the trade is of precious high-price products worth the investment.

In the same line of argument, some of the interchangeable labels also require sophisticated authenticating devices that are impractical at point-of-sale terminals. For instance, labels that exploit the temporal domain of luminescence but their phosphors have a short lifetime require sophisticated instrumentation such as TCSPC and FLIM setups. An example of this is the work by Kalytchuk *et al.* who utilized carbon dots with 4.4 ns and 6.1 ns to demonstrate dynamic anti-counterfeiting using a FLIM setup [90]. Similarly, Lu *et al*. developed $NaYF_4$:Yb, Tm nanocrystals labels in the micro-second range for which the lifetime was read using a time-resolved confocal scanning microscope [75]. Again, these sophisticated instrumentations are hard to realize in point-of-sale terminals.

For these technologies to be realized in point-of-sale terminals there is a need for alternative authentication hardware that is cheap, ubiquitous, and straightforward. Smartphone has many potential features and their low cost and ease of availability to end-users make them a prime candidate for authenticating labels. Currently, a lot of effort is geared towards realizing smartphone-based authentication luminescence labels. Research on smartphone-based authentication of PUFs where end-users at point-of-sale terminals could use their smartphone to acquire images and compare them to the verification database is of great interest [57, 68]. For instance, Kumar *et al.* also demonstrated the use of smartphones to authenticate anti-counterfeiting labels based on microlens arrays and luminescent microparticles [91].

In this thesis, the use of smartphones as the authentication devices of dynamic luminescence anti-counterfeiting labels is established. By using phosphors with different persistent lifetimes, covert features concealed in the temporal domain of luminescence can be decoded from the analysis of videos acquired with smartphones post excitation. The first work on anti-counterfeiting utilized Gd_2O_2S: Eu^{3+}, Ti^{4+} persistent phosphors to realize smartphone-readable dynamic anti-counterfeiting patterns for which the Ti^{4+} co-doping regulated the PersL lifetime after UV excitation [11]. Further, the use of UV light source was eliminated by developing visibly excitable labels based on $SrAl_2O_4$: Eu^{2+}, Dy^{3+} (SAED), CaS: $Eu^{2+,}$ and SrS: Eu^{2+} for which the smartphone flashlight would excite the phosphors after which its camera would capture the dynamic pattern change [35]. By doing so, the smartphone could be used alone in a similar manner to other technologies such as digital fingerprint-based PUFs.

1.5 Outline

This chapter presented a broad perspective of the work on smartphone-based applications using PersL phosphors. The basics of PersL were also discussed. A brief overview of the smartphone's CMOS sensor was also presented. Chapter 2 presents the background of this thesis. This includes an extensive review of lanthanide spectroscopy, PersL, and state-of-the-art applications of PersL. The chapter also briefly reviews the use of smartphones in the lab with a special focus on the coupling of smartphone cameras as data acquisition hardware.

In Chapter 3, the phosphor synthesis procedures, experimental set-ups, and methods used throughout this thesis are discussed. This includes the phosphor verification techniques such as X-Ray diffraction and morphological studies with a scanning electron microscope. The methods of determining the PersL using the smartphone are extensively covered. The comparative method of determining the PersL using the multi-channel scaling technique is also covered. The experimental designs for determining the Photoluminescence quantum yield (PLQY) the PL and PLE are covered as well.

Chapters 4 to 6 present the results of the thesis research. In chapter 4, the results of smartphone-based luminescence thermometry based on Gd_2O_2S: Eu^{3+} phosphors are presented. The desire to extend the PersL of Gd_2O_2S: Eu^{3+} led to

the creation of a persistent lifetime palette with room temperature tunable persistence via controlled Ti^{4+} doping. These phosphors were ideal for the development of dynamic anti-counterfeiting labels readable with smartphones following UV excitation and the results are presented in chapter 5. Inspired by the use of a smartphone to read the anti-counterfeiting labels, chapter 6 presents the results on dual-color dynamic anti-counterfeiting labels with persistent emission that could be excited with a smartphone flashlight and decoded from the analysis of the smartphone acquired video post excitation.

Chapter 7 provides a summary of the findings in this thesis and gives an outlook and potential future work that would see the findings explored in this thesis implemented in business settings. Possibilities for expanding the library of PersL-based phosphors for anti-counterfeiting and other applications such as chemical sensing are outlined. Furthermore, the label development used in this thesis is suitable for proof-of-concept, but not ideal for practical business applications. Ideas to realize commercially viable label printing options are pointed out.

2

Background

This chapter provides an overview of the fundamental concepts of lanthanide spectroscopy and the applications used in this work. It starts with an introduction to the photophysics of lanthanide materials based on the quantum mechanics of lanthanide ions and their energy states. Thereafter, a discussion on lanthanide luminescence and persistent luminescence processes is given. The chapter further discusses luminescence thermometry and luminescence-based anti-counterfeiting in general before narrowing it down to state-of-the-art applications utilizing smartphones.

2.1 Introduction to Lanthanide Spectroscopy

In this section, a discussion on the concept of lanthanide spectroscopy from the multi-electron systems in quantized states point of view is covered. Thereafter, the discussion explores the unique energy states of ions based on orbital theory for the ground state and excited states of ions. Consequently, the energy level splitting of Ln ions in hosts under the influence of the electric field produced by the crystalline environment is discussed in detail. Finally, the theoretical review establishes an understanding of the energy-level structures and selection rules of electronic transitions.

2.1.1 The Electron Configuration of Atoms

The arrangement and energies of electrons in an atom can be described using a quantum mechanical model [92]. The quantum mechanical model describes an electron with a specific quantum of energy in relation to certain parameters of its wavelike motion according to the Schrödinger equation (SE);

$$\mathcal{H}\Psi_n = E_n\Psi_n \tag{2.1}$$

where H is the Hamiltonian operator (sum of kinetic and potential energy), Ψ_n is the set of all wave functions and is dependent on the coordinate system and time. The E_n is the total quantified energy associated with the wave function (normally referred to as Eigenvalues of Ψ_n). While Ψ_n is not directly observable, its square, $(\Psi_n)^2$ gives the probability of finding a particle/electron in the position given by the coordinates. Each solution to the SE gives an energy state of the electron associated with a given orbital.

An electron in an atom is defined by a set of four quantum numbers of which the first three describe its orbit in terms of size (energy), shape, and orientation in space while the fourth describes the spin of the electron itself [93]. These numbers are the principal quantum number, (n), the angular momentum quantum number (ℓ), and the magnetic quantum number (m_ℓ). The fourth quantum number, spin quantum number (m_s) specifies the orientation of the spin axis of an electron following the Pauli Exclusion Principle [93]. The Pauli Exclusion Principle states that no more than two electrons can occupy the same orbital and the two electrons in the same orbital must have opposite spins [94].

The principal quantum number, *n,* is an integer (1, 2, 3 …) and specifies the energy of an electron and the orbital size. It provides approximations of the relative distance from the nucleus and thus as it increases so does the energy level. The angular momentum quantum number, ℓ, is also an integer that ranges from 0 to (n-*1*) and provides information about the shape of the orbital. The angular momentum quantum number is also called the azimuthal quantum number. To distinguish the numbers from n, a letter code (*s, p, d, f, g* …) is used to describe the subshells as shown in table one. The magnetic quantum number, m_ℓ, is an integer from $-\ell$ to $+\ell$ and sets the limit on the magnetic quantum number, m_ℓ, by providing the orientation in space of an orbital for a given energy *n* and shape, ℓ. This number divides

the sublevels into individual orbitals that hold the electrons as described in table 2.1. Finally, the spin quantum number provides the two possibilities in which an electron can spin and takes values of ±1/2.

The quantum numbers described in table 2.1 are usually assigned specific terms to fully describe the position of the electron in an atom according to the energy level, (or shells) described by n, the sublevels (subshells) described by ℓ, and the possible number of orbitals in the subshell defined by the *s, p, d, f, g, …* notation.

Table 2.1 Quantum numbers of electrons in an atom.

Name	**Symbol**	**Value range**	**Property**
Principal quantum number	n	$1 \leq n$	Orbital size (shell)
Azimuthal quantum number	ℓ	$0 \leq \ell < n$	Orbital shape (s, p, d, f, g, … values representing sub-shells)
Magnetic quantum number	m_ℓ	$-\ell \leq m \leq n$	Orbital orientation
Spin quantum number	m_s	$\pm\frac{1}{2}$	Spin direction

The atom has a nucleus at its center, which contains protons and neutrons. The central structure is then surrounded by either an electron in the case of hydrogen or multiple electrons in the case of the other elements. The quantum numbers define the distribution of electrons in an atom. For many-electron systems, the number of electrons that can occupy an orbital is limited, and the orbitals are filled in order of increasing energy ($n+\ell$) according to the Aufbau principle [93].

The Aufbau principle and Pauli's exclusion principle, which states that no two electrons in the same atom have the same four quantum numbers form the basis of filling the periodic table [93, 95]. Note that the spin quantum number differentiates two electrons in the same orbital by fulfilling the exclusion principle. For orbitals of equal energy, the order of filling of electrons is executed according to Hund's rule,

where the electron configuration of lowest energy is assigned to the maximum number of unpaired electrons with parallel spins. In the periodic table, this holds up to period three since from periods 4 - 7 other effects come into play to distort this order.

In the periodic table, period four contains the first series of the transition elements in which the *d* orbitals start to fill. Three major factors affect the filling pattern in periods 4 – 7 and include: 1) Effects of shielding and penetration on the orbital energy, 2) Filling order of the 4s and 3d orbitals. 3) Stability of half-filled and filled orbitals [93]. The effect of shielding and penetration on the orbital energy leads to the 4s orbitals filing first before the 3d orbitals fill. As a result, the 4s occupying electrons penetrate closer to the nucleus while the probability of finding the 3d occupying electrons outside the inner $n = 1$ and $n = 2$ levels is high. This automatically makes the 4s orbital have lesser energy while the electrons occupying the 3d orbital become shielded from the nuclear charge. Thus, the ns sublevel in this period fills before the *(n-1) d* sublevel, the remainder from the *(n-1) d* sublevel then fills the *(n-2) f* and np for the lanthanides and the actinides. The general sequence for filling electrons in these periods is thus, *ns*, first of the *(n -1) d,* all *(n-2) f*, the remainder of the *(n-1) d*, and *np*. The electron filling usually proceeds one electron at a time for the d orbitals and p orbitals. This is true for most of the elements except for chromium (Cr; Z = 24; [Ar] $4s^1 3d^5$) and copper (Cu, Z = 29) because of the increased stability of half-filled sublevels and filled sublevels [93]. For Cr, the half-filled 4s orbital together with a half-filed 3d orbital is much more stable than if the 4s were to be filled. In the same argument, Cu is more stable (low in energy) by having filled 3d orbitals and half-filled 4s orbitals [93].

2.1.2 Coupling of Angular Momentum and Spectroscopic Terms

So far, we have a description of the electronic configuration of an atom in the ground state. The effects and interactions of the orbital angular momentum and the spin are revealed when the atom interacts with another species (atom, ion, photon, etc). When a photon interacts with an atom, either one of two main processes would occur depending on the energy of the incident photon. If the photon energy is more than the work function of the electron in the atom, emission of photoelec-

trons as described by the photoelectric effect occurs. This makes the atom a positive ion. However, if the photon energy is not sufficient to eject the electron from the force of the binding nucleus, the electron remains under the influence of the nucleus but moves to a higher excited state. These excited states are sets of quantized energy levels that are regulated by the interaction of orbital angular momenta and electron spin. The fine splitting of such energies occurs due to the coupling of the electron spin and the orbit of a single electron or due to Coulomb forces resulting from multi-electron interaction of the orbital angular momenta. The type of coupling is dependent on the atomic number (heaviness of the atom), with those atoms having (Z < 40) exhibiting what is termed as L - S coupling (also called Russel-Saunders coupling (R - S)). The heavier elements (Z >= 40) are described by J - J coupling.

For L-S coupling, the net angular momentum, J, can be computed from the sum of the total spin angular momentum from all intrinsic spins and the sum of orbital angular momentum.

$$J = L + S = \sum_i l_i + \sum_i s_i \tag{2.2}$$

The first summand in equation 2.2 denotes the total orbital angular momentum while the second summand denotes the total spin angular momentum. The values of the total orbital angular momentum, L = 0,1,2,3,4,5, … are spectroscopically noted with the letters S, P, D, F, G, H, I, …. Note that values in which L > 20 are not used, and apart from the first four spectroscopic notations S, P, D, F that derive their names from spectroscopic lines; Sharp, Principal, Diffuse and Fundamental, the others are designated capitalized alphabetical letters after F, that is G to Z except for J. From equation 2.2 and the notations of L, we can now define the term symbol (also called the Russel-Saunders term symbol) associated with the energy level of the atom.

$$^{2s+1}L_J \tag{2.3}$$

where the superscript term 2S+1 is the multiplicity of the terms, S is the total spin angular momentum and J is the total angular momentum. The magnitude of *J* varies from |L+S| and |L-S|, since L and S must have an intersection (not parallel) as

schematically described in Figure 2.1 [96]. For this coupling, *the Spin-Spin coupling>orbit-orbit coupling>spin-Orbit coupling.*

In J-J coupling, the L and S moments of each electron are first coupled to form the total angular momentum J. These individual results are then summed up to obtain the net angular momentum of the system as shown in equation 2.4. The approach is not simple and requires computational techniques to identify the energy levels and sublevels [97].

$$\begin{array}{ccc} L_1 + S_1 & = & J_1 \\ \downarrow & & \downarrow \\ L_2 + S_2 & = & J_2 \end{array} \qquad leading\ to\ J\ = \sum_i J_i \tag{2.4}$$

While the J-J coupling would be ideal for describing the energy levels in heavy atoms, the L - S coupling has remained the scheme of choice for the lanthanide series and is widely used to describe their energy level splitting [98].

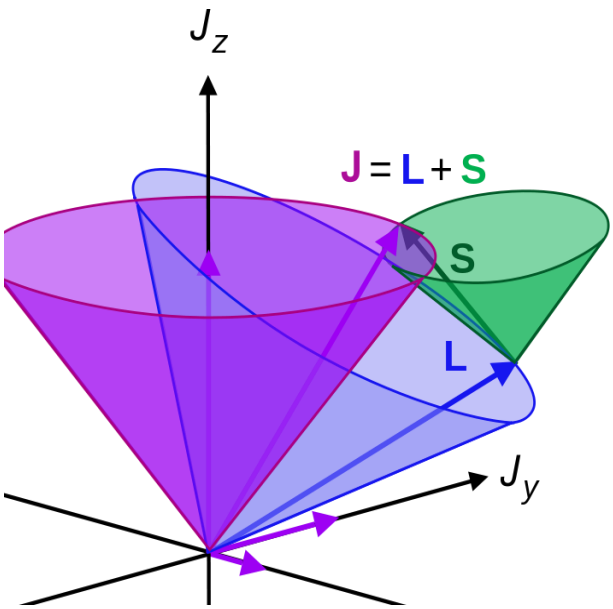

Figure 2.1. Vector addition of total orbital moment, L in blue and spin orbital moment S in green to give the resultant total angular momentum J, in purple. Reproduced from Maschen [96]. CC-BY license.

The energy levels that arise from the LS coupling are further split due to the presence of a magnetic field, a phenomenon usually referred to as the Zeeman effect [99]. These atomic terms usually referred to as spectroscopic sub-levels

(microstates), represent the splitting of the orbitals due to orbital-orbital coupling that arises due to the presence of an intense magnetic field (such as polarized light) [99]. The number of microstates possible for a given spectroscopic level can be calculated from the formula:

$$Number\ of\ microstates = \frac{r!}{n!\,(r-n)!} \tag{2.5}$$

where *r* is two times the number of orbital positions, *n* is the number of valence electrons to be placed in *r,* and ! represents the factorial operator. Whenever a photon that has less energy than the work function of the atom interacts with the electrons, it excites the electrons to these energy levels after which they undergo either radiative transitions or non-radiative transitions or a combination of both, to get back to their ground state. To demonstrate the application of the Spectroscopic levels (microstates), we use europium (Eu^{3+}) as a demonstration atom. However, before we cover this, we first discuss the lanthanides for which Eu^{3+} is a member [100].

2.1.3 The Lanthanides

The lanthanides were first discovered in 1787 when an unusual black mineral, named Gadolinite, containing several lanthanides was discovered in Ytterby, a small village in Sweden [101]. Subsequent separation of the mineral and discovery of other elements lead to what is now known as the lanthanide series. The lanthanides are a group of 15 elements, ranging from lanthanum (La, Z = 57, [Xe] $5d^1 6s^2$) to Lutetium (Lu, Z = 71, [Xe] $4f^7 5d^1 6s^2$) in the periodic table. The symbol Z represents the atomic number. The elements are arranged based on their atomic number, and due to the filling pattern being affected by factors described in section 2.1.1 the filling of the $4f^n$ is not chronological [102, 103].

Most of the lanthanides form stable +3 oxidation state which has the [Xe] $4f^n$ (for n= 0-14 for La^{3+} to Lu^{3+} respectively) electronic configuration [102]. Exceptions include Eu^{2+}, Sm^{2+}, Yb^{2+}, Ce^{4+}, and Tb^{4+} due to the presence of a half-filled 4f shell (for Eu^{2+}) and a full-filled 4f shell (for Yb^{2+}) that translates to a mild reduction of their potentials [102]. The divalent Sm^{2+} is considered the extreme boundary for divalent lanthanide ions and the most reducing ion of the three divalent lanthanide

ions [104]. The Ce^{4+} and Tb^{4+} tetravalent ions are formed due to the stability provided by the fully-filled shells and the half-filled shell respectively [102].

The 4f and 5d electrons determine the fascinating spectroscopic and magnetic properties of the lanthanides [102, 103, 105, 106]. In addition, the 5d and 6s valence electrons are greatly influenced by the chemical environment of the host [102, 103, 105, 106]. The three types of transitions involving the lanthanide ions include the sharp intra-configurational 4f-4f transitions, the broader 4f - 5d transitions, and broad charge transfer mediated transitions [92]. The 4f-4f transitions are discussed in this section, while the broader 4f-5d transitions and the broad charge-transfer-states-based transitions are discussed later in section 2.2.

The triply doped lanthanide ions have unique spectroscopic properties, specifically absorption and photoluminescence due to the 4f-f transitions [92, 107]. The absorption and emission of light in the trivalent lanthanides are promoted by operators linked to the nature of light: the odd-parity electric dipole (ED) operator, the even-parity magnetic dipole (MD) operator, and electric quadrupole (EQ) operators [21, 92]. For ED transitions, Laporte's parity selection rules imply that states with the same parity cannot be connected by ED transitions [92]. Consequently, ED transitions are forbidden by the ED mechanism and become partially allowed by either mixing with charge-transfer states of neighboring ligands or by mixing with the 5d orbitals [105]. To cater for this relaxation, the ED transitions are referred to as induced (or forced) ED transitions. The intensities of ED transitions are described using the Judd-Ofelt (J-O) theory. Some of the induced ED transitions such as $^5D_0 \rightarrow {}^7F_0$ transition in Eu^{3+} are hypersensitive [21]. The MD transitions are allowed, but their intensity is weak [21, 92]. The EQ transitions are also parity allowed but are much weaker than the MD transitions and therefore rarely observed [21, 92].

When the crystal environment allows for 4f-f transitions, the characteristic absorption and emission spectra of lanthanides in the near ultraviolet, visible, and infrared regions are observed following appropriate excitation. Of course, the observed emission and absorption states are a mere part of the total number of possible microstates for atoms with the $4f^n$ configuration (see equation 2.5). For the $4f^n$ configuration, with the azimuthal quantum number $\ell = 3$, the total degeneracy D, is given by:

$$D = \frac{(4\ell + 2)!}{(4\ell + 2 - \mathrm{n})!\,\mathrm{n}!} = \frac{14!}{(14 - \mathrm{n})!\,\mathrm{n}!} \quad (2.6)$$

where n is the number of 4f electrons in the outermost shell of the lanthanide ion in consideration. For instance, n = 6 for Eu^{3+} and therefore the total degeneracy, D of the [Xe]$4f^6$ electronic configuration of Eu^{3+} is 3003.

The emission spectra, for Ln^{3+}, are usually unique sharp-spectral lines for each of the elements and vary in strength depending on various factors including the nature of transition, the host material, and the synthesis process among other environmental factors [105]. These $4f^n$ energy level levels in the lanthanides are normally represented using a Dieke diagram (energy level diagram) shown in Figure 2.2. The energy levels demonstrated in Figure 2.2 are for $LaCl_3$ and the energies are up to 40,000 cm^{-1} (250 nm) [108]. The name is coined from the name of the first author and an interested reader can check the work by Dieke [108] and the subsequent work by Peijzel *et al.* [108]. The Dieke diagram provides an overview of the energy levels of the $4f^n$ configuration of trivalent lanthanides.

Not all the transitions depicted in the Dieke diagram in Figure 2.2 between the $4f^n$ and $4f^n$ levels are observed [109-111]. One of the main reasons for this is that the strong $4f^n$ - $4f^{n-1}5d$ absorption usually obstructs the weak $4f^n$ - $4f^n$ transitions, especially in the ultraviolet (UV) region making them non-observable [109, 110]. Additionally, transitions involving larger changes in J > 6 with respect to the ground state are forbidden [110]. Emission occurs from certain energy levels whose gap to the next lower level is more than four or five times the maximum phonon energy of the host lattice [110]. Smaller energy gaps do not lead to emissions as they are bridged via multi-phonon relaxation. The semi-circles in Figure 2.2 indicate the levels under emissions have been observed [111].

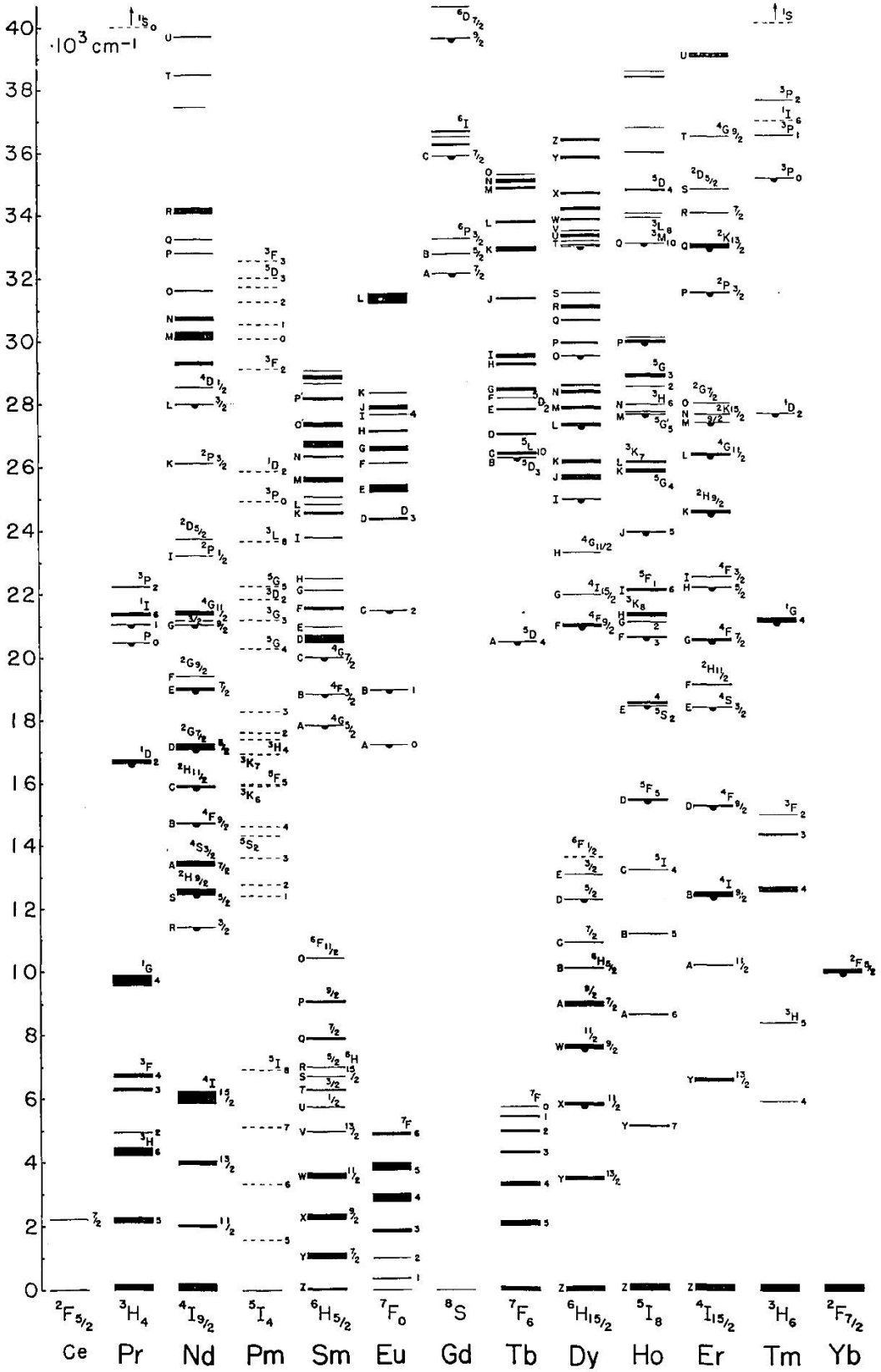

Figure 2.2. The energy level diagram (Dieke diagram) of the trivalent lanthanides. The semicircles indicate where emission are mostly observed. Reproduced with permission from Carnall et al. [111].

2.1.4 Energy States of Trivalent Lanthanides

The electronic configuration for the trivalent lanthanides (Ln^{3+}) is [Xe] $4f^n$ where n varies from zero to 14 for La^{3+} to Lu^{3+}. For each of the Ln^{3+} elements, it is possible to calculate the total number of possible microstates according to equation 2.6. The total number of microstates is referred to as the total degeneracy and expresses the total number of possible unique electronic configurations of the electrons [21]. It was demonstrated in the previous section that the Eu^{3+} has 3003 microstates from the calculations using equation 2.6. The degeneracy of the $4f^n$ configuration is either partly or totally lifted by several perturbations acting on the Ln^{3+} ion. These perturbations include; electron repulsion (terms), spin-orbit coupling (levels), crystal-field perturbation (sub-levels), and the Zeeman effect [21].

In this work, the Eu^{3+}, [Xe] $4f^6$ is used to demonstrate the degeneracy and splitting of energy levels and emphasize the naming of the spectroscopic terms denoting transitions in the Dieke diagram. It is selected because it is the main Ln^{3+} ion used in most of the phosphors in this thesis. While we have already noted that the total degeneracy of Eu^{3+} ion is 3003, only the ground level notations for which absorption and emission is observed are demonstrated.

Firstly, the energy levels of Eu^{3+} conforming to the $^{2s+1}L_J$ notation described in equation 2.3 that is indicated in the Dieke energy level diagram in Figure 2.2 is defined. Since the Eu^{3+} ion has 60 electrons; 54 electrons form a xenon closed-shell electronic configuration, and the remaining 6 electrons occupy the 4f orbital. The $4f^6$ degeneracy is lifted partly or totally by several perturbations acting on the Eu^{3+} ion: electron repulsion, spin-orbit coupling, the crystal field perturbation, and finally the Zeeman Effect as shown in Figure 2.3. The electron repulsion effect, the electrostatic interaction between the different electrons in the 4f shell, leads to 119 $^{2s+1}L_J$ terms for Eu^{3+} ion. These terms are further split into 295 $^{2s+1}L_J$ levels via spin-orbit interaction [21, 112]. The spin-orbit interaction results from the influence of the spin magnetic moment of the electron and the magnetic field created by the movement of the electron around the nucleus of the atom [21]. When the Eu^{3+} ion is in a chemical environment (doped into a host) the degeneracy is further lifted by the crystal-field effect to form the irreducible representation of the energy levels, normally referred to as the spectroscopic levels [112]. The splitting is usually due

to the interactions of the 4f electrons with ligand electrons. The levels that remain after lifting due to crystal-field splitting are further split by the Zeeman Effect, which is the splitting of the energy levels by an external magnetic field.

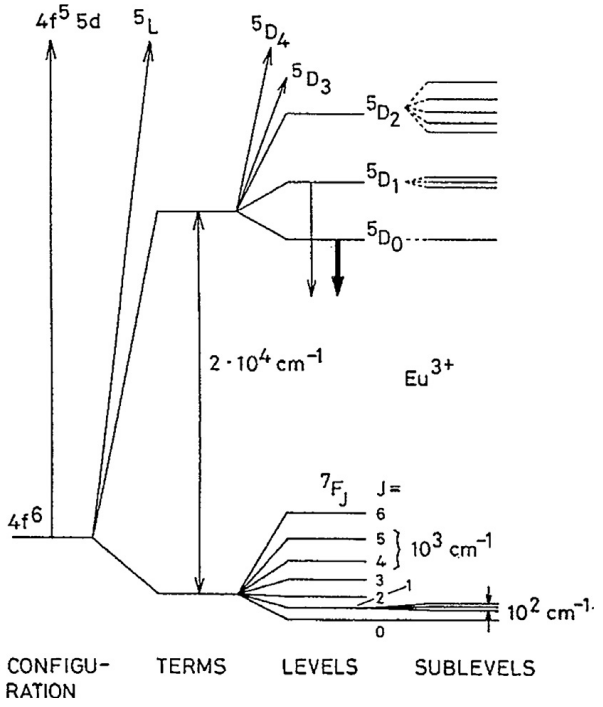

Figure 2.3. The partial energy configuration of Eu^{3+} [Xe] $4f^6$ showing the effects of perturbations due to electronic repulsion (terms), spin-orbit coupling (levels) and crystal-field effects (sublevels). Emission usually comes from the sublevels with the downward pointing arrows. Reproduced with permission from Jean-Claude [112].

Having demonstrated the energy level splitting criteria, it is time to introduce the criteria of how the states are named. Hund's rules are now applied to derive the name of the ground state of the $4f^6$ electrons of Eu^{3+} following equation 2.3. Firstly, the total spin quantum number S of $4f^6$ electrons of Eu^{3+} is S = [½ + ½ + ½ + ½ + ½ + ½] = 3 and therefore we obtain the first superscript term 2S + 1 = 7. The nomenclature for the spin multiplicity is singlet, doublet, triplet, quartet, quintet, sextet, and septet for 2S + 1 = 1, 2, 3, 4, 5, 6, 7, respectively and the selection is based on Hund's 1st rule. A corollary of 1st rule is that the spin multiplicity must be as large as possible for the ground state [21, 112]. The total angular momentum L, given by the first summand in equation 2.2, is calculated to be, L = [(+3) + (+2) + (+1) + 0 + (−1) + (−2)] = 3 and corresponds to F in the S (L=0), P (L=1), D (L=2), F

(L=3) notation. Note that in the L values the letter J is omitted as it represents the total angular quantum number [21, 112]. Accordingly, Hund's 2nd rule demands that in cases where there are more than one term with the same spin multiplicity, the one with the highest total angular momentum (L value) is the ground state, and therefore ^7F is the ground-term for Eu^{3+}. The possible values of J for the $4f^n$ electrons in trivalent lanthanides are J = |L-S| for less than half-filled subshells and L+S for more than half-full. For the ^7F ground term of Eu^{3+} the L= 3 and S = 3 so the possible combinations for J are L + S, L + S-1, L + S-2 . . ., |L-S| leading to 6, 5, 4, 3, 2, 1, 0. Now the term can be defined as ^7F_J for J = 0, 1, 2, 3, 4, 5, 6. To identify the ground state, Hund's 3rd rule is applied. The 3rd rule states that for shells that are less than half-filled the ground state has the lowest possible J value, and for more than half-filled shells, the ground state has the highest possible J value. [20] The consequence is that the $^7F_0$ becomes the ground state for Eu^{3+} ions and the order of increasing energy of the ^7F terms becomes $^7F_0 < {}^7F_1 < \cdots < {}^7F_6$.

The characteristic energy levels usually reveal themselves as spectroscopic lines upon being directly excited or via energy transfer as shown in Figure 2.4 for $Ba_3Y_4O_9$: Eu^{3+} phosphor material [113]. Note that it is a generally accepted convention that the emitter and co-doped donor species be written after the host material chemical composition as $Ba_3Y_4O_9$: Eu^{3+}. This convention provides instant guidance to the donor /emitter centers. The process begins by excitation into the charge-transfer band ($O^{2-} \rightarrow Eu^{3+}$) from which the absorbed energy is transferred to the $^5H_3$ state Eu^{3+} ion as shown in Figure 2.4. Consequently, part of the energy quickly settles at radiative levels lower in energy as denoted by the dotted vertical lines. It is from these points that the excitons relax to the ground state leading to emission (denoted by the downward pointing arrows) in the 419 nm to 656 nm range. To describe the transitions leading to emission, one states the high energy $^{2s+1}L_J$ state and uses an arrow to point to the final state. For example, the transition leading to 583 nm emission in Figure 2.4 is $^5D_0 \rightarrow {}^7F_0$.

The emissions emanating from the transitions shown in Figure 2.4 and other Ln^{3+} emitter-based transitions differ in intensities depending on several factors which include the nature of dipole transition, whether they are allowed or forbidden according to Judd-Ofelt (J-O) theory, the host-crystal perturbations (J - mixing

effects), and local symmetry of the emitting Eu^{3+} ion. The allowed and forbidden ED transitions are briefly reviewed according to J-O theory hereafter.

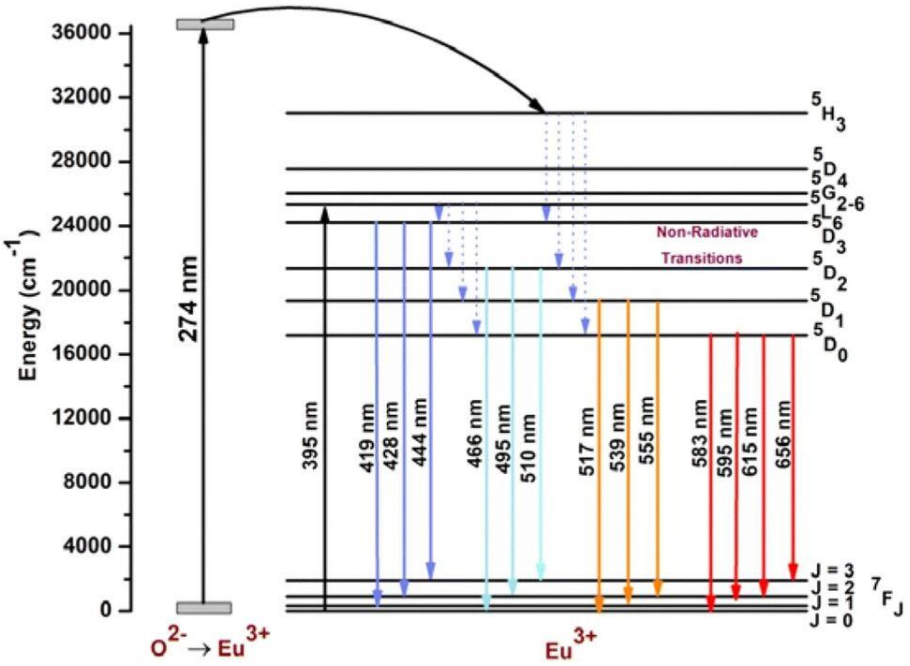

Figure 2.4. The energy level diagram for trivalent europium ion doped $Ba_3Y_4O_9$ nanophosphor showing the levels which lead to radiative emissions. Reproduced with permission from Hooda et al. [113]. Copyright 2019 Springer Nature.

2.1.5 Judd Ofelt Theory

The J-O theory is used in lanthanide spectroscopy to express the ED intensity of the $4f^n$ - $4f^n$ transitions as a function of three parameters (Ω_λ):

$$S_{ED} = e^2 \sum_{\lambda=2,4,6} \Omega_\lambda \langle \psi || U^{(\lambda)} || \psi' \rangle^2 \tag{2.7}$$

Where S_{ED} is the electric dipole line strength of the transitions between ψ and ψ' coupled-multiplets expressed in 10^{36} debye^2 units, e is the electric charge of the electron and $\langle ||U^{(\lambda)}|| \rangle^2$ is the squared reduced matrix elements of the unit tensor operator [92, 114]. The J-O parameters are experimentally estimated from the absorption spectrum $\varepsilon(\bar{\nu})$ via the least squares method [92]. Experimentally, the dipole strength is defined as:

$$S_{(Exp.)} = \frac{10^{36}}{108.9 \bullet \mathrm{X}_A(T)} \bullet \left((2J+1)\frac{9n}{(n^2+2)^2}\right) \int \frac{\varepsilon(\bar{\nu})}{\bar{\nu}}\, d\bar{\nu} \tag{2.8}$$

Where X_A is the fractional population of the initial state, at a temperature T (in kelvin), n is the refractive index, $\varepsilon(\bar{\nu})$ is the molar absorption coefficient in unit $mol^{-1}cm^{-1}$ and $\bar{\nu}$ is the wavenumber in cm^{-1}. The $\frac{9n}{(n^2+2)^2}$ term involving n is known as Lorentz's local field correction [115]. The term (2J+1) is the degeneracy of the initial state. Note that in equation 2.8, the absorption measurement is the last summand involving the integral as a function of wavelength.

In practice, the J-O phenomenological parameters ($\Omega_{\lambda=2,4,6}$) are obtained by fitting the experimental absorption data in equation 2.8 using the least-squares method with the J-O expression in equation 2.9. The minimized expression is:

$$RMS_{Rel} = \left[\frac{1}{n-p}\sum_{i=1}^{n}\left(\frac{S_i^{Exp.} - S_i^{Calc.}}{S_i^{Exp.}}\right)^2\right]^{1/2} \tag{2.9}$$

where n is the number of experimental oscillator strengths and p is the fitting parameter (usually p = 3) used in the relative RMS fitting [115].

After obtaining the J-O parameters, the radiative transition probabilities $A(\psi J, \psi' J')$ for all the excited states can be obtained from the equation:

$$A(\psi J, \psi' J') = \frac{64\,\pi^4 \bar{\nu}^4}{3h(2J+1)}\left[\frac{(n^2+2)^2}{9}\, S_{ED} + n^3 D_{MD}\right] \tag{2.10}$$

where h is the Planck constant, n is the refractive index, and $(2J+1)$ is the degeneracy of the initial state [21, 115, 116].

Finally, the relative intensities of the transitions (the branching ratios) are calculated from the equation [21]:

$$\beta_R(\psi J, \psi' J') = \frac{A(\psi J, \psi' J')}{\sum_{\psi' J'} A(\psi J, \psi' J')} \tag{2.11}$$

The results from Equation 2.11 provide the relative intensity of the transitions in the luminescence spectrum. Another important application of the J-O theory is the calculation of the radiative lifetime τ_{rad} of the excited level J from equation 2.10.

The radiative transition probabilities presented via equation 2.10 also involve the magnetic dipole (MD) transition in the last summand of the equation. The MD transitions are allowed by the Laporte selection rules, however, their intensities are usually low relative to those of ED transitions [21]. The MD transitions are largely independent of the crystal-field wave functions, and in most instances considered constant [21]. They are caused by the interaction of the lanthanide ion with the magnetic field components in the exciting radiation. For ED transitions, $|\Delta S| = 0, |\Delta L| \leq 6, |\Delta J| \leq 6 \text{ and } |\Delta J| = 2,4,6 \text{ if J} = 0 \text{ or J}' = 0$ as in the case of Eu^{3+}. For the MD transitions $|\Delta S| = 0, |\Delta L| = 0, |\Delta J| = 0, \pm 1$ with 0↔ 0 transition being forbidden [21, 117].

2.2 Lanthanide Luminescence

Lanthanide luminescence can broadly be classified into three categories depending on the energy transfer mechanism upon excitation namely, downshifting (DS), and down-conversion (DC) also sometimes known as quantum cutting (QC), and Upconversion (UC). The two former cases are linear optical processes independent of the incident excitation power while UC is a non-linear optical process.

The UC process is a non-linear anti-stokes optical process in which low-energy photons are sequentially absorbed and subsequently emitted as high-energy photons [118-120]. The UC process in Ln^{3+} based phosphors is due to well-defined ladder-like energy states that facilitate the combination and radiative relaxation of energy [119]. The UC process first involves initial absorption to create an intermediate excited state from which the neighboring ions transfer their energies between each other via various processes until one ion reaches a metastable state. These processes are well defined and explored in literature. They include the energy transfer upconversion (ETU) process, ground-state absorption (GSA)/excited state absorption (ESA), cooperative sensitization (CS), and cross-relaxation (CR) processes [119-121]. The radiative relaxation from the metastable state results in UC [119]. The most-reported UC process is based on the Yb^{3+}/Er^{3+} pair and the emission centers depend on the host crystal lattice [119]. The Yb^{3+} ion, in this case, serves as a sensitizer in lieu of its unique energy level ($^2F_{5/2}$) at ~980 nm while Er^{3+} acts as the activator. The energy difference between most of

the ladder-like energy states of the activator ion is multiple the energy difference between the first excited state $^2F_{5/2}$ and the ground state $^2F_{7/2}$ of the Yb^{3+} ion [119]. Besides having the right pair of sensitizer-activator ions, efficient UC also requires that the host matrix have low phonon energy [119, 122-124]. One superior host material is the hexagonal sodium yttrium fluoride (β-$NaYF_4$) [122, 123, 125] that has a phonon energy of <350 cm^{-1} [126].

Downconversion is a linear optical process that has its roots in 1957 when Dexter postulated the possibility of luminescence quantum yields greater than unity [127]. The yield of two photons per incident higher energy photon is quantitative as the emitted photons are low in energy. The process was first experimentally demonstrated in 1974 using yttrium fluoride doped with praseodymium (YbF_3:Pr^{3+}) [128]. The DC entails converting high-energy photons to two low-energy photons for applications in TV cathode rays-based screens, lasers, and mercury-free fluorescence tubes [129-131]. The phosphors used then dissipated roughly 50% of the energy as heat [131]. Nowadays research in DC is focused on down-converting the UV light (where most solar cells have very poor absorption) to the visible region where they optimally absorb in what is termed a spectral modification [132-134]. The maximum possible efficiency for DC is the one to two conversion ratio, i.e. 200%, and records of 194% for BaF_2:Gd, Eu phosphor [135], and 190% for $LiGdF_4$: Eu^{3+} phosphor has already been achieved [129].

Downshifting (DS) involves the conversion of one high-energy photon to one lower energy photon and therefore has a sub-unity efficiency. Luminescence DS has historically been an approach for which the short-wavelength UV and near UV photons are converted into visible spectrum photons [136-138]. The name DS was coined from the work of Weber *et al.* in 1976 and Hovel *et al.* in 1979 about luminescence solar concentrators via shifting the short-wavelength through having a DS layer on top of the photovoltaic (PV) cell to enhance spectral response in the UV region [138, 139]. The DS process is however centuries-old as it is the basic process of photoluminescence in lanthanides. Initially, most of the applications of DS focused on improving the performance of solar cells in the UV regions by spectral conversion to the visible [140-143]. Nowadays, DS including visible to NIR and NIR to NIR based DS has been realized and utilized for diversified applications including surface lighting and display applications [144, 145], thermometry [8, 146],

anti-counterfeiting [11, 147], and bio-imaging [77, 148]. For tailored applications such as bio-imaging, NIR to NIR-based DS is advantageous over the traditional UV-based excitation as it provides low photodamage, deep tissue penetration, and also low interference from visible lighting [149]. This thesis broadly deals with DS phosphors, with tailored applications for surface thermometry and anti-counterfeiting applications. The fundamentals of luminescence are discussed in the next section.

2.2.1 Emitter Sensitization: A Downshifting Perspective

Several optical processes occur whenever a phosphor material is irradiated with light, namely, absorption, scattering, reflection, refraction, and emission. For targeted efficient emission, the reflection, and scattering ought to be minimized. In addition, the phosphor emits a large portion of the absorbed energy (note that having high absorption does not translate to high photoluminescence). For a simple system, absorption occurs when the incident radiation matches with the bandgap of two energy states of the optical material. Complex systems usually involve absorption due to the presence of ligands and charge-transfer states [21]. In a simple system, the absorption of a photon must obey the following equation:

$$h\nu = E_2 - E_2 \tag{2.12}$$

where E_1 is the ground state and E_2 is the excited state, h is the Planck constant and ν is the photon frequency. The excess energy of the incident radiation is released into the system as heat.

Figure 2.5 shows a simple model representation of the process of persistent luminescence indicating the three key steps namely ionization, transportation, and liberation after sufficient excitation of the host [28]. Upon photon irradiation, ionization, the generation of charge carriers, occurs. As mentioned earlier, these charge carriers can be subsequently trapped in impurity levels through quantum tunneling or via the conduction band. The trapped charge carriers are gradually released to the activation ion leading to PersL. The most efficient way to trap electrons is usually through conduction band (CB) excitation or emitter excitation in states above the conduction band. In addition, energy hoping or quantum tunneling from the emitter is also possible. After the excitation is ceased, the

charge carriers in the trap centers can thermally be promoted to the activator ion or tunnel back to the activation ion leading to PersL as depicted by processes b and c in Figure 2.5

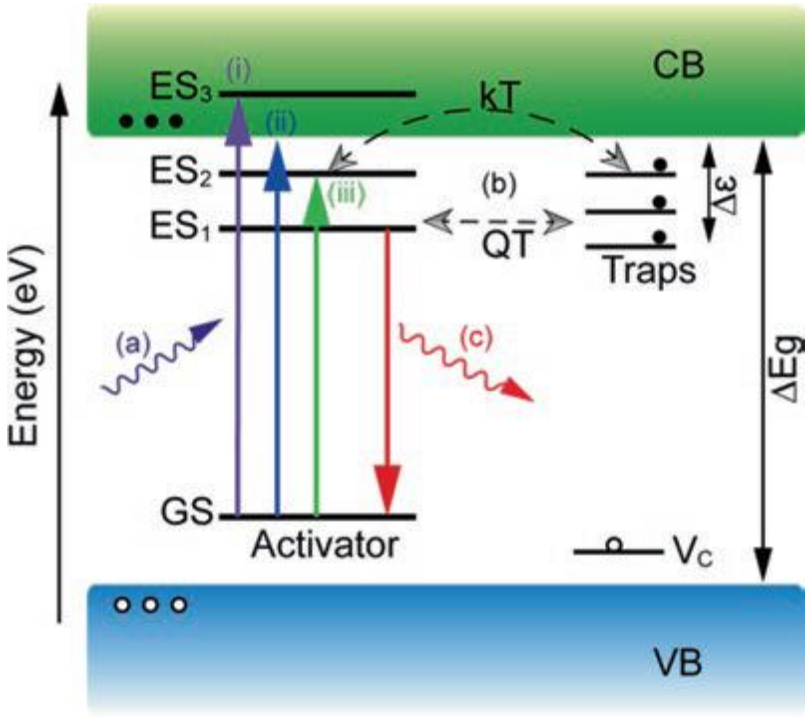

Figure 2.5. Schematic diagram of PersL. CB and VB are the conduction band and valence band of the host. GS and Es indicate the ground state and excited state, ΔEg is the bandgap of the host and T is temperature, k is Boltzmann constant and QT represents quantum tunneling. Steps (a), (b), and (c) represent the absorption, electron trapping, and emission processes. The upward and downward arrows represent photon excitation and emission processes, respectively. Reproduced with permission from Wu et al. [28]. Copyright 2017, Springer International Publishing.

Both the processes are broadly referred to as downshifting as they involve the absorption of high-energy photons and subsequent emission of lower energy photons. The presence of these two radiative channels invalidates absorption as a fundamental quantifier of the efficiency of photoluminescence as the absorbed energy can be dissipated either radiatively or non-radiatively. The absorption usually takes place in the sensitizer (host material), which then transfers the energy to the activator ion for emission. The sensitizer should have an appropriate

absorption cross-section as a first requirement to accumulate enough energy such that as much energy as possible can be transferred to the activator ion.

Now, having laid the foundation for PersL, the focus shifts to the Eu^{2+} and Eu^{3+} activator ions in downshifting hosts. The main optical transitions that lead to emission in a DS perspective in lanthanides involve four typical absorption transitions. Firstly, there are inter-band transitions between the valence band and conduction band defined by the bandgap of the host [150]. These transitions appear as a strong cut-off in the photoluminescence excitation (PLE) spectra or very strong absorption from diffuse reflectance spectra (DRS) of the un-doped host as shown in Figure 2.6a. Secondly, the $4f^n$-$4f^n$ transitions also show weak absorption cross-section, as they are narrow and parity forbidden [150]. We use the PLE spectra of Gd_2O_2S: Eu^{3+} to demonstrate these weak absorption cross-sections in Figure 2.6a. Thirdly, we have the charge-transfer states (densely packed states are also referred to as charge transfer bands) that are between the lanthanide ion state and the host band state and provide >1eV excitation band [21, 150].

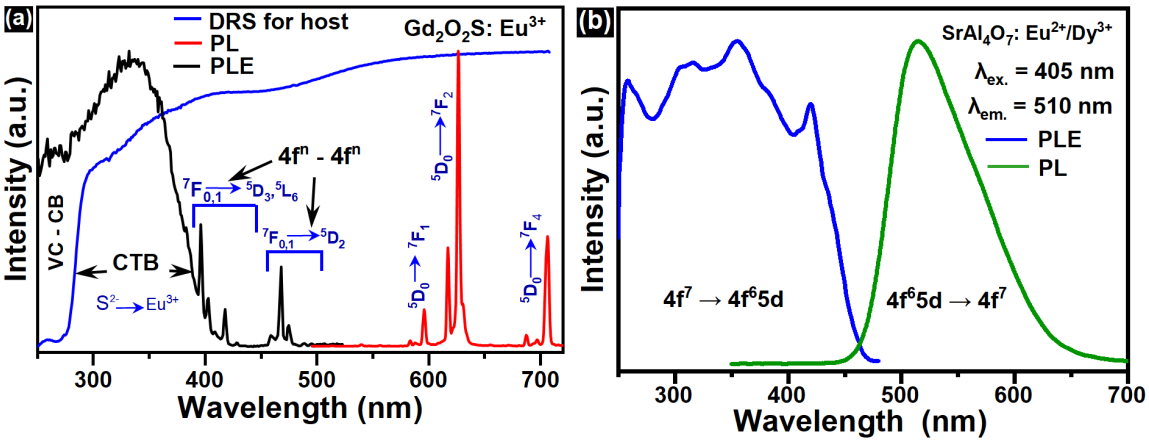

Figure 2.6. a) The diffuse reflectance spectra (DRS) of Gd_2O_2S host, the photoluminescence excitation (PLE, monitored at 626 nm) spectra and PL emission spectra after 735 nm excitation of Gd_2O_2S: Eu^{3+} phosphor. The inter-band transition (VC-CB), the charge transfer band (CTB) based states and the $4f^n$-$4f^n$ transition are observed in the PLE spectra. (b) The PLE (200-450 nm) of $SrAl_4O_7$: Eu^{2+}/Dy^{3+} showing the broadband absorption based on the $4f^7$- $4f^65d$ transition. Excitation in this band with 405 nm LED leads to the broadband emission centered at 510 nm.

These transitions are best depicted in Figure 2.6b using $SrAl_4O_7:Eu^{2+}/Dy^{3+}$ phosphor. Excitation to the broadband leads to the broadband $4f^65d \rightarrow 4f^n$ based Eu^{2+} emission. Note that in most cases the absorptions usually involve overlaps of the VB-CB, CTB, and the $4f^n$ state such as the case in Figure 2.6a.

2.3. Persistent Luminescence

PersL is a process by which a phosphor material continues to emit light after the excitation source has been removed. This self-sustained emission can last from several milliseconds to hours post excitation with high energy sources such as X-rays, ultraviolet (UV), and visible light in some cases [3-5]. The PersL is also referred to as afterglow and long-lasting phosphorescence (LLP) in literature [4]. The term PersL is nevertheless used in this work. In practice, the term afterglow is particularly used when the PersL is short, typically not more than a few seconds [151]. In this section, a brief review of the history of persistent luminescence (PersL) is provided together with an overview of the underlying mechanism of PersL. Specifically, the DS mediated PersL mechanism for which the Eu^{2+} ion is the emitter is mentioned.

2.3.1 History of PersL

The history of PersL is disputed, with different authors in Europe and Asia quoting diversified historical dates. According to Chiatti *et al.* PersL has been known for several centuries, with the so-called Bologna Stone containing barium sulfide with copper impurities (Cu^+) being the first record of PersL in the seventeenth century in Italy [3, 152-154]. On the Asian side, the story is different, with claims that PersL can be traced back as early as 1000 years ago, described in a note called '*Xiang Shan Ye Lu*' written by Y. Wen [155]. The note is published in the ancient Song dynasty (960-1279 A.D.) and contains the painting of a cow that remained visible at the night [155]. While this sounds like a mythical fairy tale, and only scanty literature is available, it still has its place in the history of PersL. Several authors have also quoted it as the first evidence of PersL [155-157]. Nevertheless, most authors agree that the discovery of the Bologna Stone at the beginning of the seventeenth century (1602) in Bologna, Italy is the first scientific evidence of PersL [154].

In the late 19th century, green-emitting zinc sulfide (ZnS) doped with Cu^{+} and later cobalt (Co^{2+}) was synthesized via the sublimation method by T. Sidot in 1866 [152, 155]. This phosphor attracted wide applications such as glow-in-the-dark luminous paints, watch-dials, toys, etc [4, 155]. This was closely followed by the development of other alkaline earth sulfides; CaS: Eu^{2+}, CaS: Bi^{3+}, SrS: Eu^{2+} PersL phosphors [151, 152, 155]. The synthesis route and lack of pure materials made the emission intensities of these phosphors too low, necessitating doping them with radioactive materials such as radium (Ra), promethium (Pm), or tritium (^{3}H) to yield an acceptably bright PersL [4]. As time progressed, there was an increased public concern and opposition due to the severe health and environmental pollution caused by these radioactive elements in the 1990s [152, 155].

These two issues, low intensity, and doping with radioactive components were addressed in 1996 when Matsuzawa *et al*. published an article on doped strontium aluminate doped with divalent-europium and dysprosium ($SrAl_2O4$: Eu^{2+}, Dy^{3+}) PersL phosphor [24]. This phosphor continued to emit bright light for several hours after the excitation (UV and visible light) was removed. The $SrAl_2O4$: Eu^{2+}, Dy^{3+} phosphor, henceforth referred to as SAED in this thesis presented ideal optical features to take over the market as glow-in-the-dark material in watches and provided a new avenue for applications. Such properties include: (i) the bright and long PersL extending to over a day, (ii) an ideal emission peak (520 nm) close to the maximum sensitivity of the human eye of ~550 nm, and a broad absorption band (450 - 250 nm) suiting both sunlight and various home-based light sources [155]. The development of the SAED phosphor renewed research interest in PersL phosphors and as of 2021, more than 250 phosphor materials that exhibit PersL have been developed for various applications [152].

2.3.2 Ln - Doped PersL Phosphors

In Ln-doped persistent phosphors, the PersL mainly occurs from the d-f transitions of Eu^{2+}, Cr^{3+} ions, the shielded 4f - 4f transitions in Eu^{3+}, Pr^{3+}, Tb^{3+}, Sm^{3+}, Tm^{3+}, Gd^{3+}, and Dy^{3+} ions or from the coupling arrangement of the Ln ions and charge states in the hosts [5]. This thesis focuses on persistent phosphors containing either Eu^{2+} or Eu^{3+} ions as the emitter centers and thus this section focuses on these two. For a reader interested in extensive PersL phosphor literature, a

comprehensive list of PersL can also be found in the works of Li *et al*. and Kang *et al.* who have done reviews on PersL phosphors [5, 158].

Phosphor materials doped with Eu^{2+} ions can exhibit broad-range PersL ranging from the visible to NIR region depending on the chemical micro-environment that the d-f ions experience [5]. The 5d orbitals interact directly with the ligand orbitals and therefore the location of the absorption band and emission spectra differ immensely from hosts. The majority of the very long PersL phosphors are aluminate and alkaline metal-based phosphors, most of which have Eu^{2+} as the emitter. A co-dopant is usually added to increase the trap density and structural defects. In most cases, either trivalent dysprosium, Dy^{3+} or neodymium, Nd^{3+} ions are used as in the case of $SrAl_2O_4$: Eu^{2+}, Dy^{3+} (SAED) [159]. The SAED emits in the green and its PersL is highly dependent on the method of synthesis and excitation time. For the europium-and dysprosium-doped strontium aluminate phosphors, we note that the Sr/Al ratio influences the wavelength of the $4f^6 5d^1 \leftrightarrow 4f^7$ emission with $Sr_4Al_{14}O_{25}$: Eu^{2+} emitting in the blue region while $SrAl_2O_4$: Eu^{2+} emitting in the green region [160-162].

The other Eu^{2+}-based PersL phosphors used in this work are the SrS: Eu^{2+} and CaS: Eu^{2+}. These phosphors have their absorption bands extending to the visible region and emitting in the red region. For these phosphors, the absorption and emission are dominated by the $4f^6 5d^1 \leftrightarrow 4f^7$ transition of Eu^{2+} ions [5, 26]. To activate the $4f^6 5d^1 \leftrightarrow 4f^7$ transition in Eu ions, the phosphors have to be prepared in a reductive environment (N_2+H_2, or Ar+H_2 and CO atmosphere) to reduce the Eu^{3+} to Eu^{2+}.

PersL phosphors based on the Eu^{3+} have characteristic persistent emission lines corresponding to the 4f-4f transition of the Eu^{3+} ion. The emission spectra are independent of the crystal lattice environment as the 4f orbitals are well shielded. Since the 4f-4f transition in Eu^{3+} is narrowband-based, absorption is majorly mediated through charge transfer states and inter-band transitions (see Figure 2.6a). Some emission bands of the Eu^{2+} such as the $^5D_0 \rightarrow {}^7F_2$ electric dipole transition are hypersensitive, as they are affected by the nature of the ligand field [163]. The charge transfer states have broad absorption bandwidth and thus ensure enough absorption to sustain the PersL. In this work, Gd_2O_2S: Eu^{3+} which

has a relatively short PersL time has been used for smartphone-based luminescence thermometry [8]. The absorption in Gd_2O_2S: Eu^{3+} is based on the charge transfer band (CTB, also denoted as LMCT) (see Figure 2.6a) [21]. The position of the CTB depends on the nature of the ligand and the optical electronegativity of the ligand [21]. It is also strongly temperature-dependent and therefore exploited herein for surface thermometry via CTB quenching [8]. Similar to the case of Eu^{2+}, to enhance the PersL of the phosphor, co-doping to enhance trap density is always undertaken. For instance, co-doping the Gd_2O_2S: Eu^{3+} with Ti^{4+}, enhanced the PersL and provided intentional tuning applicable for dynamic luminescence anti-counterfeiting [11]. In the next section, the underlying mechanism of PersL is discussed.

2.3.3 PersL Mechanism: Charge Carrier Trapping and Detrapping

The mechanism of PersL in inorganic materials has remained debatable, with new experimental data always disputing/improving on previous theories [17, 155, 164-168]. While the PersL mechanism in literature is disputed, it is agreeable that PersL always involves the thermal release and subsequent recombination of trapped charge carriers, i.e., an electron or a hole, from defects/traps in the phosphor [155, 167, 168]. The PersL occurs when sufficient energy liberates the charge carriers and helps them recombine in a luminescent center. The distribution of trap states is quantified in terms of depth and density.

This trap depth also referred to as the activation energy, is the energy difference between the trap center and the conduction band or valence band in the case of an electron trap or a hole, respectively. A shallow trap in either way results in very short PersL while a very deep trap, or rather, a trap site far away from the conduction or valence band makes it hard for the charge carrier to escape. Raising the temperature (activation energy) will however liberate the charge carriers and lead to PersL. For room temperature PersL, a trap depth of 0.6 – 0.7 eV is usually required for most PersL phosphors [168, 169]. Apparently, the trap depth gradually increases as the PersL-time increases, meaning that deeper traps recombine later while shallow traps recombine early. This observation is consistent with the observation of the initial high-brightness of long PersL phosphors immediately after the excitation source is removed, when the shallow traps (< 0.6 eV) empty fast,

which is then followed by the slow decay process characterized by the weak but sustained PersL.

The trap density on the other hand is the total number of trapped charge carriers after excitation [170]. For a PersL material having a trap depth of 0.6 – 0.7 eV, a high trap density would translate to a very effective PersL. The quantified trap densities for effective PersL are of the same order of magnitude as the number of dopants for doped PersL phosphors [1]. For other self-activated PersL phosphors, (without dopants or co-dopants), the traps are ascribed to intrinsic defects i.e., vacancies and lattice defects [1]. Nevertheless, these vacancies and lattice defects have to be sufficiently large in number to sustain PersL.

A general model showing the trapping and de-trapping of charge carriers is shown in Figure 2.7. The excitation of the PersL material leads to the filling of the trap centers, which then release the trapped electrons/holes long after the excitation source is, removed leading to PersL. The model shown in Figure 2.7 is a general model, with several models being developed for various phosphors. For instance, the RE_2O_2S: Ln^{3+} (RE = La, Gd, Y and Lu; and Ln = Eu^{3+} and Ti^{4+}) based PersL mechanism is best described by the vacuum referred binding energy (VRBE) diagram developed by Dorenbos and team [17].

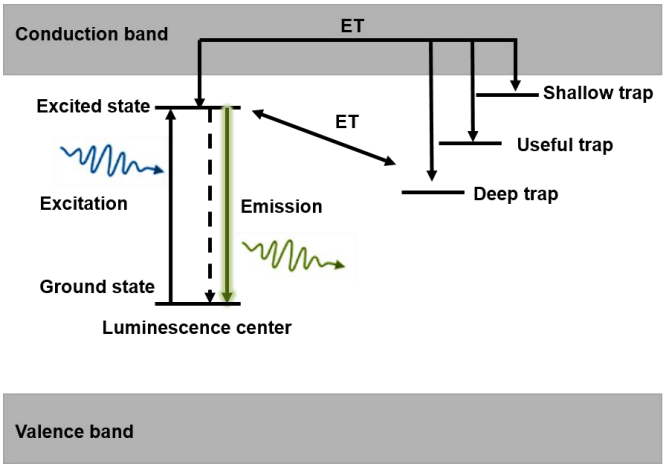

Figure 2.7. PersL mechanism model showing the trapping and de-trapping process leading to PersL. Following excitation, the excited state fills the trap centers (defect centers) which then empty after the excitation source is removed.

The VRBE is defined as the energy needed to bring an electron to a vacuum outside the sample from its level. Its energy at rest in the vacuum level is defined as energy zero [17]. The VRBE for instance explains why the persistent luminescence of $Gd_2O_2S: Eu^{3+}$ is enhanced when the Ti^{4+} ions are co-doped.

2.4 State-of-the-Art

The previous sections discussed the basic photophysics of lanthanide-based materials and the optical properties of PersL materials. The unique, yet tailorable optical properties of lanthanide-based phosphors permit a wide variety of applications. In this thesis, we demonstrate how we can measure the spatial temperature of a surface by exploiting the optical properties of $Gd_2O_2S: Eu^{3+}$. In addition, we also demonstrate smartphone-based anti-counterfeiting applications based on tuned PersL of $Gd_2O_2S: Eu^{3+}$, $Gd_2O_2S: Eu^{3+}/Ti^{4+}$, $CaS: Eu^{2+}$, $SrS: Eu^{2+}$, and SAED. We therefore briefly discuss luminescence thermometry and anti-counterfeiting in the next sections, which are the main applications mentioned in further chapters of this thesis.

2.4.1 Luminescence Thermometry

Temperature is a thermodynamic property and one of the fundamental units of measurement that can be qualitatively defined as the ‘degree of hotness or coldness.’ The practice of temperature measurements is referred to as thermometry. Temperature is of great importance because it not only is something that we feel but it also affects the smallest aspects of our lives, the performance of our gadgets, the weather and climate, chemical reactions, and so on. Of course, the temperature measurement in most of these aspects is accomplished with established thermometers such as liquid-in-glass thermometers, thermocouples, fiber optic thermometers, manometric thermometers, and resistance thermometers, quartz, ultrasonic thermometers, and infrared thermometers among many others [7, 50]. However, temperature measurement in emerging environments (nano/microscale, intracellular, microelectronics) is difficult to accomplish with these traditional methods, and that's where lanthanide thermometry comes in [7, 8, 50].

Lanthanide thermometry exploits the temperature dependence of optical properties of lanthanide materials to 'read' the temperature of a target surface. The most exploited optical property for lanthanide thermometry is luminescence, whose characteristics, such as emission intensity, decay and rise time, band position, and width are sensitive to temperature [50]. Temperature-induced changes in emission intensity (intensity ratio between two peaks) and temperature-induced changes in emission lifetime are the most explored [8]. The PL emission intensity following depopulation of excited states reduces with an increase in the temperature of the material due to quenching. Temperature quenching of luminescence forms the basis of luminescence thermometry [50]. In order to understand this phenomenon in detail, consider that following excitation of a phosphor the number of populated states is N. These excited states depopulate radiatively and non-radiatively with time such that, $dN\ \alpha\ Ndt$. The temporal evolution is described by formulating both the radiative (k_r) and non-radiative (k_{nr}) transition rates, $dN = -(k_r + k_{nr})Ndt,$ where photon emissions are created by the radiative de-excitation pathways while the non-radiative pathways lead to the release of vibrational energy. The electron depopulation and the luminescence intensity therefore exponentially decay with a time constant,τ commonly referred to as the lifetime of the excited state:

$$\tau = \frac{1}{k_r + k_{nr}} \tag{2.13}$$

The inverse of the radiative transition rate is referred to as the radiative lifetime and is independent of temperature. On the contrary, the non-radiative transitions (vibrational energy) are temperature-dependent and affect the luminescence emission intensity, as described in equation 2.14:

$$I(T) = C.k_r.\tau(T) = A.\frac{1}{k_r + k_{nr}(T)} \tag{2.14}$$

where *C* is a constant representing several physical parameters in both the measuring instrumentation and the material under investigation and does not change with temperature [50]. The non-radiative transition rate increases with temperature and the expression for temperature dependence lifetime is as given by equation 2.15;

$$(T) = \frac{1}{k_r + A.\exp(E_a/K_B T)} \tag{2.15}$$

where A is a pre-exponential constant, K_B is the Boltzmann constant, T is the temperature on Kelvin scale and E_a represents the apparent activation energy of the process. Simple lifetime fitting of luminescence decays of the form $\tau(T) = A\,exp(E_a/K_B T)$ using Gd_2O_2S: Eu^{3+} is part of the work covered in this thesis and demonstrates temperature read-out using a smartphone [8]. The obtained temperature-dependent lifetimes are plotted against the measured temperature and fitted to provide a calibration file from which lifetime data of the same material can map the surface temperature.

The FIR method typically relies on a pair of thermally-coupled levels (TCLs) in a lanthanide ion in which the emission from the higher TCL to the lower TCL varies with temperature due to the Boltzmann distribution [171, 172]. The Boltzmann equation for the FIR based thermometer is:

$$\mathrm{FIR} = A.\exp\left(\frac{-\Delta E}{K_B T}\right) \tag{2.16}$$

where A is an invariant constant, which depends on the host, ΔE is the separation between the pair of energy levels, K_B is Boltzmann constant and T Is temperature in kelvin.

The performance of the thermometers is estimated by the absolute (S_a), relative sensitivities (S_r), and temperature resolution (ΔT). These terms are also referred to as figures-of-merit for the thermometers. The S_a is defined as the rate of change of the thermometric parameter in response to the variation of the temperature in kelvin [6, 173, 174] and is expressed as:

$$S_a = \left|\frac{dQ}{dT}\right| \tag{2.17}$$

where Q is a parameter indicating temperatures such as FIR, or the lifetime. The relative sensitivity is defined as the ratio of the absolute sensitivity to the value indicating the temperature. It indicates the percentage change in the value indicating temperature per kelvin change in temperature [6, 8, 174]. It is expressed as:

$$S_r = \left|\frac{1}{Q} \times \frac{dQ}{dT}\right| \times 100\% \tag{2.18}$$

The temperature resolution (δT) is also an important figure of merit for luminescence thermometers and indicates the smallest change in temperature that causes a perceptible change in the indication value [174] and is defined as:

$$\delta \mathrm{T} = \frac{\sigma}{S_a} = \frac{\sigma_r}{S_r} \tag{2.19}$$

where σ_r, is the relative standard error or uncertainty in the measurement. Other figures of merit include repeatability and spatial resolution. Repeatability is the precision achieved by the thermometer in replicating the same temperature measurements under the same conditions. The spatial resolution defines the minimum distance between the points of measurement under which the temperature can be resolved from the indication value.

Having established an understanding of the fundamentals of luminescence thermometry and figures of merit, the focus is now shifted to a review of materials used for lifetime-based luminescence thermometry. Some of the state-of-the-art lifetime-based luminescence thermometer figures of merit, together with the detection range are shown in table 2.2. An interested reader is welcome to read more in the following reviews [50, 175]. As observed the minimum possible temperature for the lifetime thermometry approach is around the 273 K regime. This is because the methods are heavily reliant on thermal quenching (non-radiative relaxation). With a few exceptions, the detection range is also usually limited compared to the FIR method. The relative sensitivities are broad, ranging from 1 - 12.2 $\%K^{-1}$. The smartphone-based PersL thermometry registered a relative sensitivity of 4.5 $\%K^{-1}$ at 273 K [8]. This value lies on the higher side of lifetime-based thermometers.

Besides temperature detection, it is possible to read the temperature distribution on a surface from the apparatus by reading the lifetime in some instances [183]. This is accomplished by having a TCSPC instrument, usually attached to a confocal port or a non-descanned microscope for which it determines the time, t, of the photon within the laser pulsed sequence.

*Table 2.2. A summary of phosphors used in thermometry based on the lifetime of downshifting emission showing the synthesis route, the emitter ion, the temperature detection range, and relative sensitivity (S_R). * denotes smartphone-based PersL thermometry.*

Material	Ion	Synthesis method	Sensitivity range (K)	Sr ($\%K^{-1}$)	Ref.
$GdAlO_3$	Eu^{3+}	Solid state	620-793	2.28 @793K	[176]
TiO_2	Eu^{3+}	Sol-gel	307-500	2.43 @400K	[177]
$BaMg_2Al_{10}O_{17}$	Eu^{2+}	Commercial	500-700 700-1300	5ns at 700 K 1 µs -10 ns	[178]
TiO_2	Sm^{3+}	Sol-gel	300-370	10.15@340K	[179]
$La_2Mo_3O_{12}$	Yb/Er	Solid-state	303 - 573	0.28 @ 303 K	[180]
β-Li_2TiO_3	Mn^{4+}	Solid-state	10-350	3.21 @332 K	[181]
Zn_2GeO_4	Mn^{2+}	Solid-state	250-420	12.2 @370 K	[182]
Gd_2O_2S	Eu^{3+}	Solid-state	273-338	4.5 @273 K	[8]*

The data, taken together with the pixel, line, and frame clock signals accumulate the scanning area for which point-based lifetime and images are generated [183]. The procedure is more promising in biological applications for which the spatial temperature is mapped at specified cell locations.

An example of this is the work of Gao and colleagues demonstrated fluorescence lifetime imaging microscopy (FLIM) using biocompatible butter that exhibited phase change close to human body temperature tagged with an aggregated-induced emission dye that acted as the signal reporter shown in Figure 2.8 [184]. As observed the fluorescence color codes change with temperature change with fluorescence lifetime change from 0.83 to 1.45 ns. In addition to the temperature mapping, the microscope also provides temporal images ideal for continuous monitoring.

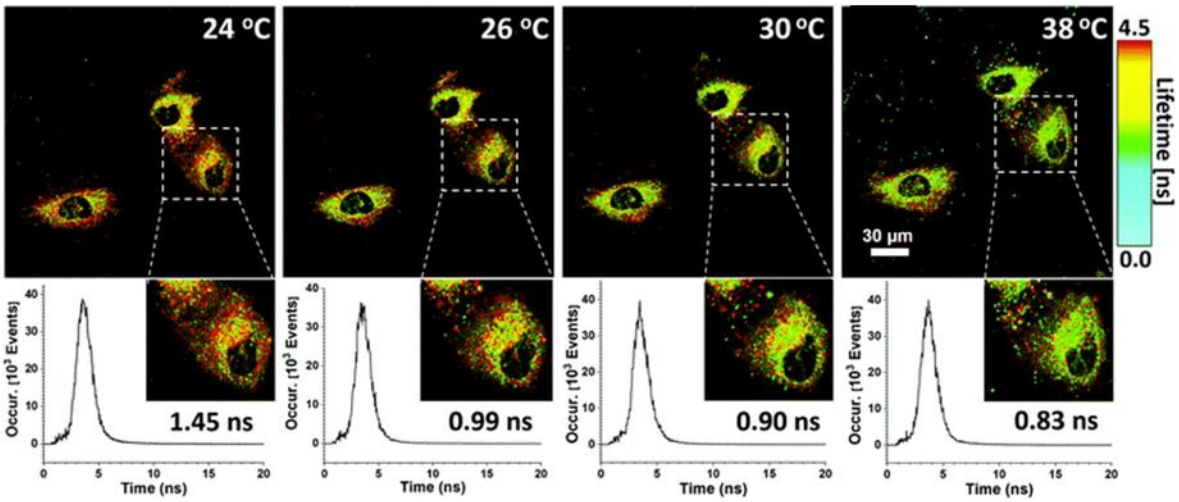

Figure 2.8. In vitro FLIM images and corresponding fluorescence decay curves of cells were measured at the indicated temperature. To distinguish the lifetimes, the pseudo-color format is used. Reproduced from Gao et al. [184]. CC BY-NC 3.0 license.

The same concept of generating thermal images can be realized using smartphones and a PersL phosphor whose luminescence change as a function of temperature [8]. Following appropriate phosphor excitation, the smartphone video records the PersL from which temporal images are generated. In addition, location-specific PersL lifetime can be extracted from the analysis of the pixels at ROI as a function of time [8]. Application areas for this smartphone-based approach reported in this thesis include hard-to-access areas in analytical systems, electronics, and general surfaces that ideally can be coated with persistent phosphors. The use of PersL phosphors and smartphones significantly reduces the cost factor brought about by FLIM or other imaging devices such as NIR cameras.

2.4.2 Dynamic Luminescence Authentication

Luminescence anti-counterfeiting is the intentional use of luminescence-based authenticating labels on genuine products to prevent product forgery. The anti-counterfeiting features include covert and overt features that are verified during the authentication process. These covert and overt features of the anti-counterfeiting labels are realized by tailoring the changeable luminescence behavior of the materials under the regulation of various external stimuli [66]. Broadly, luminescence anti-counterfeiting is realized either by exploiting the use of static

luminescence (steady-state PL) or the time decays following external stimuli or a combination of both. The various categories and classifications of luminescence anti-counterfeiting tags have extensively been discussed in chapter one section 1.4.2. In this section, a special focus on the detecting approaches is provided.

The major drawback in realizing luminescence-based anti-counterfeiting tags is the costs brought about by the authentication devices in the case of covert features. For instance, in the case of physical unclonable functions (PUFs), one has to characterize each label and implement a database for authentication [68]. Besides, the authentication devices for this kind of label are sophisticated and may include advanced confocal microscopes [89], fluorescence imaging devices, integrated charge-coupled devices [12] and Raman spectroscopy [86]. Similarly, some of the interchangeable luminescence-based labels also require sophisticated instrumentation for authentication. Notable work in the exploitation of temporal domain started with a demonstration of proof-of-concept in the sub-nanosecond PL lifetime following UV excitation for which a TCSPC [185].

In this category of short lifetimes, for instance, Kalytchuk *et al.* demonstrated dynamic anti-counterfeiting using two carbon dots that had either 4.4 ns or 6.1 ns fluorescence lifetime upon 365 nm UV excitation as shown in Figure 2.9 [90]. A FLIM system was required to acquire these patterns realized using these carbon dots [90]. Two CDs, one with a short lifetime of 4.4 ns and the other with 6.1 ns are used for anti-counterfeiting label development. The labels could be directly handwritten on paper, inkjet-printed, or transfer printed on non-luminescent paper. The authors demonstrated the performance of FLIM in anti-counterfeiting by printing the symbol ‘R’ as part of 35 separate pixels on a non-luminescent commercial paper. Following 365 nm excitation with a UV lamp, the labels showed intense blue emission, with no possibility of visually decoding the ‘R’ pattern by eye as shown in *Figure 2.9*. Interestingly, when FLIM has been applied the fluorescence decay of each pixel point can be extracted that points to the ‘R’ pattern. To implement the set-up Kalytchuk and colleagues proposed integrating the FLIM apparatus into a multiwell-plate reader. This would ideally add to the overhead cost of establishing the authentication setup.

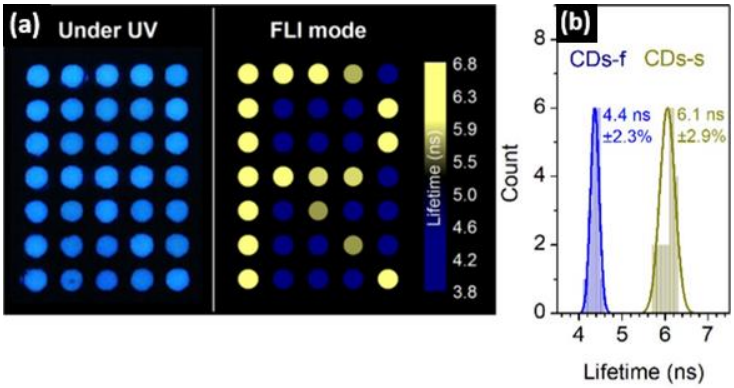

Figure 2.9. Fluorescence lifetime imaging microscopy (FLIM) for anti-counterfeiting using carbon dots. a) Uniform blue pattern is observed under UV excitation while under FLIM mode the covert letter 'R' is observed. b) The lifetime of the two CDs used. Adapted with permission from Kalytchuk et al. [90]. Copyright 2018 Americal chemical Society.

A similar concept, this time integrated into 2D barcodes which rely on FLIM has also been demonstrated using lifetime-tunable lead-halide perovskite nanocrystals as shown in Figure 2.10 [186]. The printed unicolor label before exposure is shown in Figure 2.10a. In their work, a portable cost-effective time-of-flight FLIM prototype was used to decode the 6.5 ns and 9.5 ns lifetimes to covertly reveal the hidden barcode using TCSPC-FLIM pseudo color image as shown in Figure 2.10b.

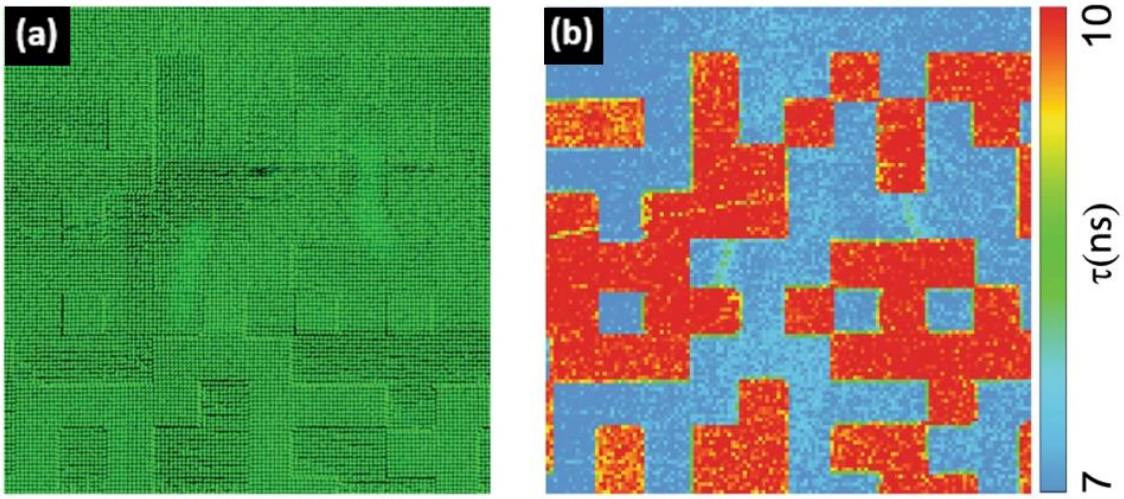

Figure 2.10. a) A zoomed-in image of a unicolor printed anti-counterfeiting label established with two perovskite-based inks with a different lifetime. b) The same image under TCSPC-FLIM pseudo color showing a 2D barcode differentiated by the lifetime of the inks. Adapted from Yakunin et al. [186]. CC BY 4.0 license.

These amazing results show the intricacy level of the temporal domain despite the application challenges faced by the authenticating device [186]. In the same line of research, Lu *et al.* made a significant step in utilizing longer PL phosphors with a lifetime in the 29-662 µs range for optical coding [75]. Despite the significant step in the use of relatively longer lifetimes, a single-pixel fast detector or an expensive high-speed camera was still required in reading the anti-counterfeiting labels. Besides the expensive and sophisticated instrumentation required to read these very short lifetimes of the labels, an expert is required due to the complications that arise during the authentication process. Consequently, these two challenges make it kin to impossible to implement anti-counterfeiting labels with a short lifetime in point-of-sale terminals.

However, these two fundamental problems can be solved by developing labels with a persistent lifetime in the 100 ms to 10 s range that are also emitted in the visible region. This would allow the use of smartphones as authentication devices. As such, the cost of a sophisticated authentication device would be eliminated. The lower limit is due to the low frame rate (ideally 30 fps), found in most smartphones for video recording the signal from the labels [8, 11, 187]. On the other hand, the upper limit provides a practical and realistic time for the authentication of the labels.

To eliminate the challenges of expensive authentication hardware most of the luminescence-based anti-counterfeiting approaches have focused on labels that allow the use of smartphones as the authentication device. This is because once tailored to the specific function, the smartphones are efficient, reliable, and robust in terms of authentication. For instance, the PUFs, which are known to rely on sophisticated systems for authentication are exploiting the use of smartphones too. The work of Vinay et al. for instance demonstrated the use of a smartphone to decode PUF patterns based on random bright points generated through micro-lenses focusing on microparticles upon UV excitation [188]. Other explored options include adding accessories to the smartphone camera sensor and miniaturized optoelectronics devices to enhance its functionality [68, 189]. This has been for instance demonstrated by Quan *et al*. using scattered core-shell nanoparticles scattered on various metal electrodes. The smartphone in this case could ideally detect the patterns, and color of the patterns [189].

Similarly, there has been a shift towards the use of smartphones as anti-counterfeiting hardware in the other categories of anti-counterfeiting labels. For example, Jose *et al.* demonstrated smartphone readable single-level anti-counterfeiting labels whose QR codes could be read using smartphones upon UV excitation [190]. Similar QR codes with dual-level anti-counterfeiting features were also demonstrated using optical nanomaterials by Wei *et al.* from which the patterns were read with a smartphone after either UV or NIR illumination [191]. Ideally, smartphone use, therefore, cuts across all the levels of visible region luminescence-based anti-counterfeiting.

While the use of smartphones for authentication of luminescence-based anti-counterfeiting labels is speedily catching up, there are some boundary conditions for which these labels have to satisfy. The first boundary condition is that the emission upon excitation should be in the visible region (400 - 700 nm). This is imposed by the smartphone camera acquisition range of 400 - 700 nm ideally imposed with a NIR filter for photography applications [192]. The second boundary condition is that the emission intensity must be high enough to be detectable with the smartphone camera ideally in a darkened environment. Extensions to these two conditions also include visible absorption of the phosphors used in developing the labels if the smartphone flashlight is to be used as the excitation source.

In this thesis, the smartphone is used as the main device for authenticating most of the dynamic anti-counterfeiting labels. Firstly, labels based on Gd_2O_2S: Eu^{3+}/Ti^{4+} persistent phosphors that can be excited with 375 nm UV LED are demonstrated. The dynamic images were read after the excitation was ceased and covert features were decoded from the smartphone-acquired videos. This technique was further extended to allow the use of only a smartphone as both the illumination and authentication device by using SAED, CaS: Eu^{2+}, and SrS: Eu^{2+} persistent phosphors. The absorption bands of these phosphors allow visible light excitation, like the one found in smartphone flashlight, and emit in the visible region for the CMOS camera on the smartphone to capture the images. Blending the phosphors allowed the realization of dual-color dynamic anti-counterfeiting patterns that changed upon ceasing the smartphone flashlight excitation. The trend to use smartphones is also motivated by their compatibility with IoT, their portability, real-time tracing, and tracking capacity.

2.5 Smartphone in the Lab: A Leap Towards the Future

The smartphone is arguably the most recent technological innovation that has achieved a broad transformative effect in virtually every sphere of life. It is a modern-day technological pet that some people cannot live without [193]. The smartphone has two unique features that make it fundamentally a human companion:1) Its strong hardware capabilities and 2) it's extensive software capacity that supports the IoT and multimedia functionalities. By exploiting the potential functionalities of smartphones, scientists have been able to push forward applications that otherwise are performed with sophisticated instrumentation.

Some of the notable research on the use of smartphones in the lab include research on climate change and weather [194, 195], bio-imaging and point-of-care testing [196, 197], thermometry [6, 8], anti-counterfeiting [11, 37, 191], radiation detection [198, 199], and big-data [194]. Broadly speaking, the use of smartphones in the lab, provides for miniaturization of the instrumentation used in the labs by replacing them with the ubiquitous smartphone. This is usually accompanied by reduced implementation costs and time while ensuring a global reach of the functionality under consideration.

2.5.1 Smartphone Camera Sensor

In this thesis, the smartphone camera, based on a CMOS sensor is used for detecting the emissions of the phosphors used for tailored applications in anti-counterfeiting and luminescence thermometry. The CMOS sensor captures incident photons and converts them to electrons based on the photoelectric effect. The electrons are then converted to a voltage from which a pixel value is obtained [200]. Figure 2.11 shows the schematic of a typical CMOS image sensor depicting the photon capture and subsequent electron generation, electron to voltage conversion, amplification, and digital conversion [201].

In a CMOS sensor, the charge from the photosites is converted to a voltage, and the signal is multiplexed as rows and columns by the analog to digital converters (ADCs) on-chip. Each photosite contains a photodiode, microlens, and three transistors that perform the functions of resetting, activating the photosite, and charge conversion, selection, and multiplexing [201].

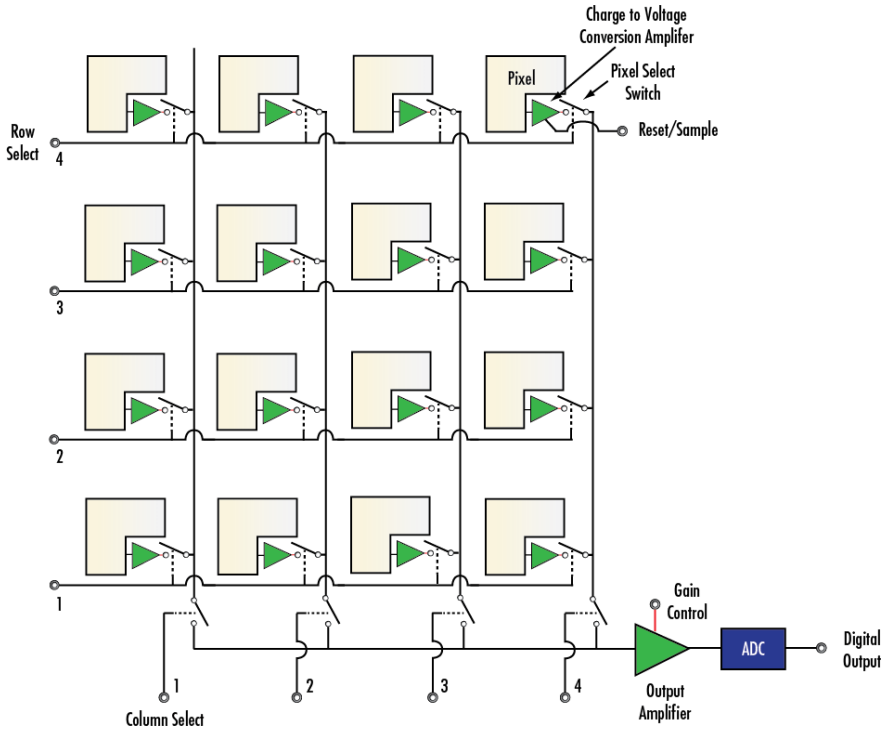

Figure 2.11. Block diagram of a complementary metal oxide semiconductor (CMOS). Reproduced from Edmund Optics [201].

The multiplexing in the CMOS is coupled with an electronic rolling shutter for exposure timing. Now, for smartphone cameras, the CMOS camera captures colored images. This is realized by covering the CMOS photosites with first NIR filters and secondly covering the photosites with color filters in a series called the Bayer series. The NIR filter is used to cut off the NIR region which the human eye does not detect as the camera is used to capture images mimicking human observation [47]. To realize colored images, a filter (e.g. Bayer filter array) is placed in front of each photosite to allow it to capture either red, green, or blue colors. Figure 2.12 shows the arrangements of the photosites forming the pixel [202]. The arrangement is such that there are twice as many green photosites compared to red and blue photosites which mimic the resolving power and greater sensitivity of the green light to the human eye [47]. An algorithm interpolates the RGB channels of the photosites into one colored pixel. The RGB values obtained from the sensor are usually interpolated based on neighboring pixels using the YUV4:2:2 sampling technique to save on bandwidth [47]. The term YUV defines the color space where Y, stands for intensity components (ranging from black to white), and U for blue projection, and V for red projection respectively. Due to this, the spatial resolution is slightly compromised. In this work, Samsung Galaxy A5(2017) is mostly used for imaging. It uses a Samsung S5K3P8 CMOS sensor in which the photosites are covered using the Bayer filter array manner to form a pixel.

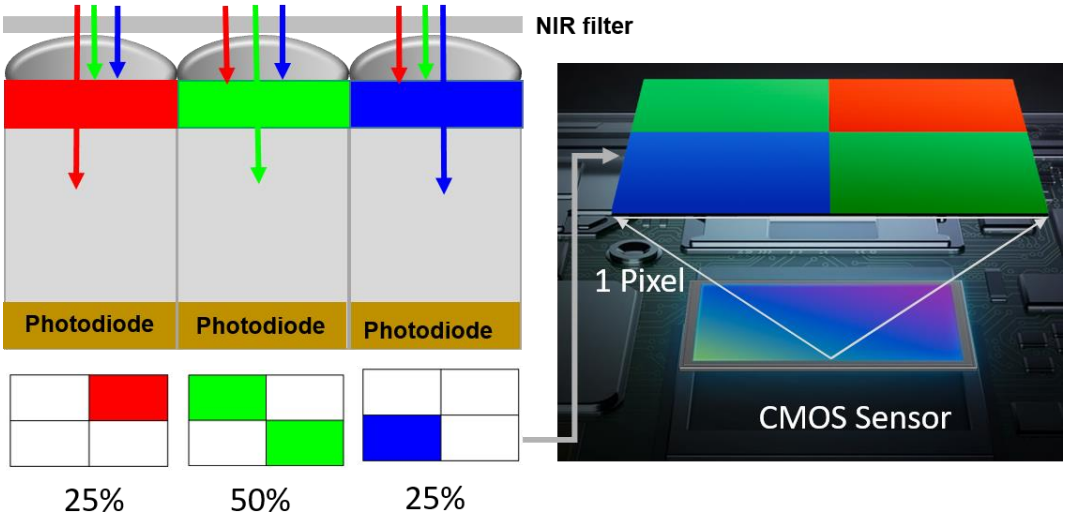

Figure 2.12. Schematic of the Bayer filter array on the photosites forming the colored pixel. In the Bayer series, 50% of the photosites are green, 25% are blue, and 25% are red. A NIR filter is placed in front of the micro lenses to block NIR radiation. Note that for simplicity purposes, the optical focusing due to the micro lenses is ignored in the figure. Adapted from Samsung Electronics [202].

2.6 Summary

Lanthanides, part of the rare-earth elements, although not as scarce as the name suggests are elements whose atomic numbers range from 57 to 71. These elements exist in nature as sparsely distributed compounds in minerals. The optical properties of these materials make them ‘special’ in spectroscopy-based applications. This chapter has laid the foundation of the photophysics of lanthanides from the orbital theory perspective. The fundamentals of luminescence and potential applications of PersL in thermometry and anti-counterfeiting using a ubiquitous smartphone are presented. This chapter forms the base for the results of chapters.

3

Methods

This chapter covers the material synthesis process, material characterization techniques, measurement systems, and the design and development of anti-counterfeiting labels, utilized throughout the research.

3.1 Material Synthesis

The phosphor materials used in this thesis are Gd_2O_2S: Eu^{3+}, Gd_2O_2S: Eu^{3+}, Ti^{4+}, CaS: Eu^{2+}, SrS: Eu^{2+} and $SrAl_2O_4$: Eu^{2+}, Dy^{3+} abbreviated as (SAED). The Gd_2O_2S: Eu^{3+} and Gd_2O_2S: Eu^{3+}, Ti^{4+} were synthesized in an oxidizing environment while the CaS: Eu^{2+} and SrS: Eu^{2+} were synthesized in a reductive environment. All the phosphors were synthesized via the solid-state reaction method. The Gd_2O_2S: Eu^{3+}, Gd_2O_2S: Eu^{3+}, Ti^{4+} were synthesized using the thermal concept muffle furnace shown in Figure 3.1a. The $SrAl_2O_4$: Eu^{2+}, Dy^{3+} phosphor was commercially acquired from (Sigma Aldrich) and was annealed in the air in the muffle furnace to tune the persistent luminescence. The CaS: Eu^{2+} and SrS: Eu^{2+} persistent phosphors were synthesized using the GSL-1500X tube furnace under Ar/H2 gas (95/5%) reducing environment.

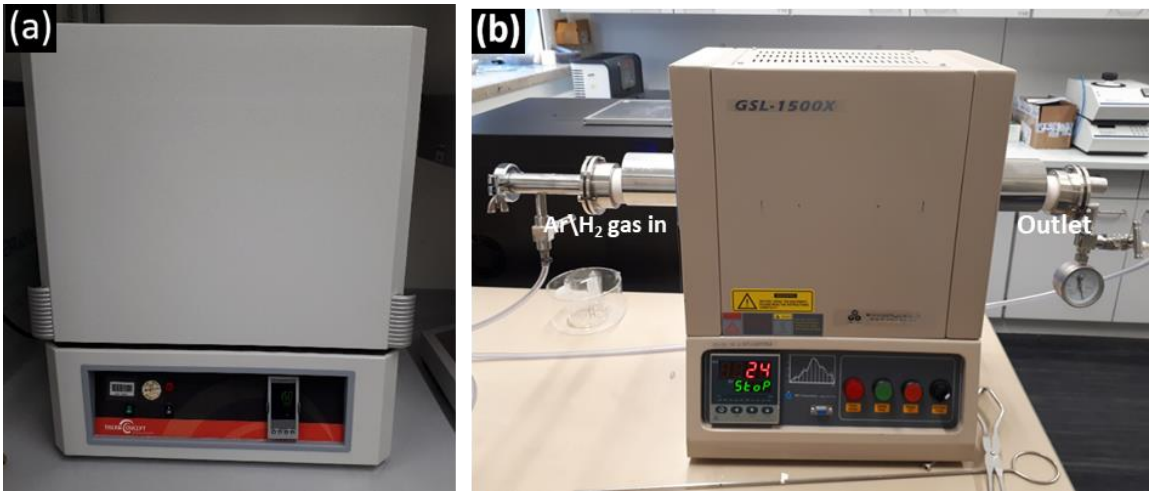

Figure 3.1. (a) The muffle furnace use in material synthesis. The furnace maximum operating temperature is 1300 ^{o}C (b) The GSL-1500X tube furnace with Ar/H_2 gas inlet. It has a maximum of 1500°C.

3.1.1 Synthesis of $Gd_2O_2S: Eu^{3+}$

The starting materials for preparing $Gd_2O_2S: Eu^{3+}$ were Gd_2O_3, (ChemPur, purity 99.9%) Eu_2O_3 (ChemPur, purity 99.9%), and sulfur (S), (ChemPur, purity 99+ %), with Na_2CO_3 (ChemPur, purity 99+ %) and K_3PO_4 (ChemPur, purity 99+ %), used as a flux. Samples composed of $(Gd_{1-x}Eu_x)_2O_2S$ for ($0 \leq x \leq 0.13$) molar ratio, were weighed and then ground with a mortar and pestle for 15 minutes. The experimental molar ratio used was for example; 0.95: 3: 0.05 for Gd_2O_3: S: Eu_2O_3 with the flux ratio maintained at 3:1 for Na_2CO_3: K_3PO_4 for preparing the $Gd_2O_2S: 0.005Eu^{3+}$. In a typical preparation using these ratios, the $Gd_2O_2S: 0.005Eu^{3+}$ would be realized by mixing 2.75 g of Gd_2O_3, 0.14 g of Eu_2O_3, 0.77 g of S, 1.27 g of Na_2CO_3, and finally 0.85 g of K_3PO_4 all together and then, thoroughly grinding them for 15 minutes using mortar and pestle. At the end of grinding, the composite mixture was thoroughly mixed till it turned pale-yellow. The composite mixture was then transferred into covered alumina crucibles and annealed at (1000 – 1250 ^{o}C) for 1 h at a ramping rate of 8 ^{o}C/min. The phosphors were left to cool in the furnace to room temperature. They were then washed with deionized water five times via centrifuging to remove the excess water-soluble salts, excess sulfur, and water-soluble impurities.

3.1.2 Synthesis of Gd_2O_2S: Eu^{3+}, Ti^{4+}

From the previous synthesis of Gd_2O_2S: xEu^{3+}, the phosphor performing optimally is observed to be Gd_2O_2S: $0.06Eu^{3+}$, and it registered a PLQY of 65% following 375 nm excitation. The sample was then co-doped with Ti^{4+} ions to form Gd_2O_2S: $0.06Eu^{3+}$, yTi^{4+} for ($0 \leq y \leq 0.24$) mol. The starting materials used were Gd_2O_3, (ChemPur, purity 99.9%) Eu_2O_3 (ChemPur, purity 99.9%), TiO_2, (Sigma Aldrich, 99.9%), and sulfur (S), (ChemPur, purity 99+ %), with Na_2CO_3 (ChemPur, purity 99+ %) and K_2CO_3 (ChemPur, purity 99+ %), as flux. The experimental molar ratio used is 0.85: 0.06: 0.09: 3 for Gd_2O_2S: Eu_2O_3: TiO_2 with the flux ratio maintained at 2:3 for K_2CO_3: Na_2CO_3 for preparing a typical Gd_2O_2S: $0.06Eu^{3+}$, $0.09Ti^{4+}$ phosphor. Excess sulfur was used to ensure the complete formation of the oxysulphide. The weighed materials were thoroughly ground using a mortar and pestle for 15 min., transferred in covered alumina crucibles, and annealed at a ramping rate of 8 ^oC/min. to high temperatures (1000-1250 ^0C) for 1 h. After the annealing, they were let to cool to room temperature in the furnace (the furnace automatically shut off after sintering the phosphor materials for 2 h). They were then washed with deionized water for five minutes via centrifuging to remove excess salts, excess sulfur, and water-soluble contaminants and dried at 150 ^oC for 2 h.

3.1.3 Synthesis of CaS: Eu^{2+}

The raw materials used for the synthesis of CaS: Eu^{2+} include $CaSO_4.2H_2O$ (VWR - Alfar Aesar, purity < 99%,), Eu_2O_3 (Sigma Aldrich, purity 99.99%,), pure ethanol (Sigma Aldrich, <= 100%) and activated carbon (C). The materials were used without further purification. A series of CaS: xEu^{2+} ($0.0005 < x < 0.015$ mol) phosphors were prepared via the solid-state reaction method in a reductive atmosphere (Ar: H_2 = 95:5) in a tube furnace. First, the molar ratio of the materials was weighed and thoroughly grounded for 15 minutes using a mortar and pestle. During the mixing process, appropriate amounts of pure ethanol and 2 mol (to the weighed ratio) of activated carbon were added to enhance the mixing of the raw materials and the formation of the pure phase of the material, respectively. Activated carbon was added to enhance the reduction process. After grinding, the materials were then let to dry in air and then transferred to a benchtop vacuum and

atmosphere tube furnace (MTI Corporation, GSL1500X) and annealed at 1200 ^{o}C for three hours in a reductive atmosphere (Ar: H_2 = 95:5) at a ramping rate of 5 ^{o}C/min. To preserve the Ar: H_2, the sintering was done towards the end of the day. The Ar: H_2 flow was then stopped in the morning when the furnace had cooled to room temperature. The annealed phosphors cooled down to room temperature in the furnace and then were ground to form powders for subsequent crystallographic and morphological verification.

3.1.4 Synthesis of SrS: Eu^{2+}

The raw materials used for the synthesis of SrS: Eu^{2+} include $SrSO_4.2H_2O$ (VWR - Alfar Aesar, Purity 99%), Eu_2O_3 (Sigma Aldrich, purity 99.99%,), activated carbon (C), and pure ethanol (Sigma Aldrich, <= 100%). The materials were used without further purification. The series of SrS: xEu^{2+} ($0.0005 < x < 0.015$ mol) was prepared via the solid-state reaction method in a reductive atmosphere (Ar: H_2 = 95:5) using a benchtop tube furnace (MTI Corporation, GSL1500X) with a vacuum sealing assembly. First, the molar ratio of the materials was weighed and activated carbon was added (2 molar units of the measured ratio). The species were then thoroughly grounded for 15 minutes using a mortar. During the mixing, appropriate amounts of pure ethanol were added to enhance the mixing of the materials. The mixture was left to dry (till ethanol is evaporated), after which the dried mixture was transferred to alumina crucibles for calcination at 1200 ^{o}C for 3 h in a reductive atmosphere (Ar: H_2 = 95:5) at a ramping rate of 5 ^{o}C/min. The phosphors were let cool to room temperature and then crushed to form powders for subsequent crystallographic and morphological verification.

3.1.5 Persistent Lifetime Tuning of $SrAl_2O_4$: Eu^{2+}, Dy^{3+}

The $SrAl_2O_4$:Eu^{2+}, Dy^{3+} (SAED), commercial phosphor was annealed in air under various temperatures (700 ^{o}C, 800 ^{o}C, 810 ^{o}C, 820 ^{o}C, 830 ^{o}C, 840 ^{o}C, 850 ^{o}C, 860 ^{o}C, and 900 ^{o}C) in order to tune the persistent luminescence lifetime. The annealed samples were labeled according to the annealing temperature in the air; SAED (700), SAED (800) SAED (810), SAED (820), SAED (830), SAED (840), SAED (850), SAED (860) and SAED (900) for phosphors annealed in air at 700 ^{o}C, 800 ^{o}C, 810 ^{o}C, 820 ^{o}C, 830 ^{o}C, 840 ^{o}C, 850 ^{o}C, 860 ^{o}C, and 900 ^{o}C, respectively.

The commercial phosphor was labeled as SAED (Ref.). During the air-annealing process, the ramping rate was maintained at 8 ^{o}C/minute for all the samples after which the phosphors were let to cool to room temperature.

3.2 Material Characterization

Before the photophysical characterization of the phosphor materials, X-Ray diffraction (XRD) and scanning electron microscope (SEM) was done to investigate the crystal structure and morphology of the samples respectively. These techniques are introduced briefly hereafter.

X-ray diffractometry is a non-destructive technique used to verify the crystal structure, material phases, and phase purity of bulk samples and films. The XRD works under the principle of diffraction whereby monochromatic X-rays are directed towards the sample via a slit and interact with the atomic planes of the sample. The interaction leads to either elastic or inelastic scattering of the X-rays. For elastic scattering, the energy of the scattered wave does not change, while for inelastic scattering the energy and momentum change. The elastic scattering formula is the basis of diffraction according to Bragg's law [203]. Bragg's law states that an incident X-ray on a crystal surface with a glancing angle, θ will be reflected with the same angle θ. If another x-ray (of the same phase and wavelength) is scattered in the same direction (it traverses a longer path of *2dsinθ*), constructive interference occurs when the length is equal to an integer multiple, *n* of the wavelength of the incident radiation, λ. For a diffraction peak to be observed, the constructive interference condition has to be precisely met, which is given by;

$$\mathrm{n}\lambda = \mathrm{AB} + \mathrm{BC} \tag{3.1}$$

Mathematically, as derived from Figure 3.2 and equation 3.1 Braggs law is then expressed as;

$$\mathrm{n}\lambda = 2d\sin\boldsymbol{\theta} \tag{3.2}$$

When constructive interference from many rows occurs, Bragg's peaks (diffraction peaks) become very sharp with mostly destructive interference in between [203]. The elastic scattered X-rays are collected by the detector after which the signals are converted into XRD patterns.

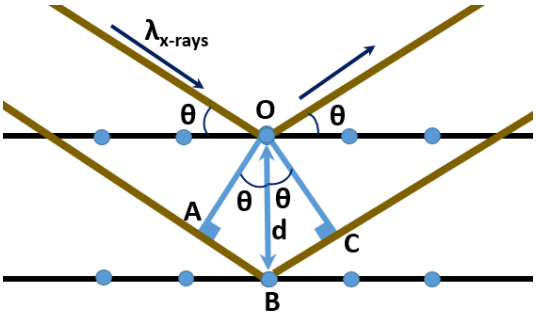

Figure 3.2. Reflection geometry for deriving Bragg's law. The incident X-ray has wavelength λ, the glancing angle (incidence angle is the angle to the surface normal) is θ, and d is the interplanar distance (path difference here is 2dsinθ). The dots represents atoms in the planes that are separated by a distance, d.

In this thesis, an X-ray powder diffractometer (Bruker, D2 Phaser) equipped with Cu Kα radiation (1.5405 Å), with a 1 mm divergent slit was used for sample analysis. An image of the D2 Phaser XRD is shown in Figure 3.3**.** To make the measurement, the powdered phosphors were first loaded in sample holders and flattened with a glass slide.

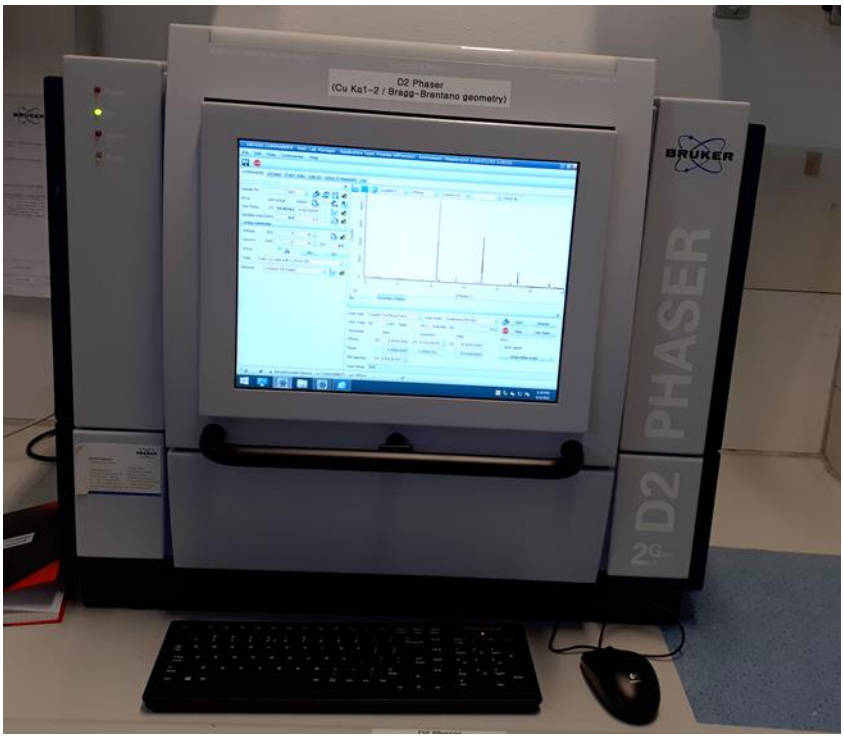

Figure 3.3. The benchtop D2 Phaser X-ray diffraction equipment in Bragg-Brentano geometry.

They were then loaded into the sample chamber, and the software was made to run for the desired 2θ degree. The patterns were then directly indexed using DIFFRAC.EVA software and compared using the Inorganic crystal structure database (ICSD) database and the international center for diffraction data (ICDD).

The SEM is a powerful tool for analyzing a sample's size and morphology. As the name suggests, it utilizes an electron beam to resolve small features of target samples even to one nm under optimal conditions [204]. Electrons have a much shorter wavelength than visible light, and the images are produced by probing the sample with a focused primary electron beam that is accelerated with high voltage (1kV to several kV). The focused beam then collides with the sample leading to the emergence of several emissions that include the low-energy secondary electrons (SEs), high-energy backscattered electrons (BSE), light emission (cathodoluminescence), and X-rays [204]. The SE is usually observed on the top surface of the sample and is mostly collected for image formation. If the SEM is equipped with an X-ray beam detector, it is possible to do an energy-dispersive X-ray (EDX) analysis. The morphology data of the phosphors used in this thesis were obtained using (Zeiss, Supra 60 VP) whose image is shown in Figure 3.4.

Figure 3.4. Image of the SUPRA 60VP scanning electron microscope (SEM).

3.2.1 Crystal Structure and Morphology of Gd_2O_2S: Eu^{3+}

The XRD patterns of Gd_2O_2S: x Eu^{3+} microcrystals are provided in Figure 3.5. The XRD patterns are consistent with ICSD call code 167755 for Gd_2O_2S and were mapped to the P-3m1 (164) space group of a trigonal crystal system. The XRD patterns did not change after the Gd_2O_2S was doped with Eu^{3+} ions as further shown in Figure 3.5b. No special peaks arose due to doping the sample with Eu^{3+}.

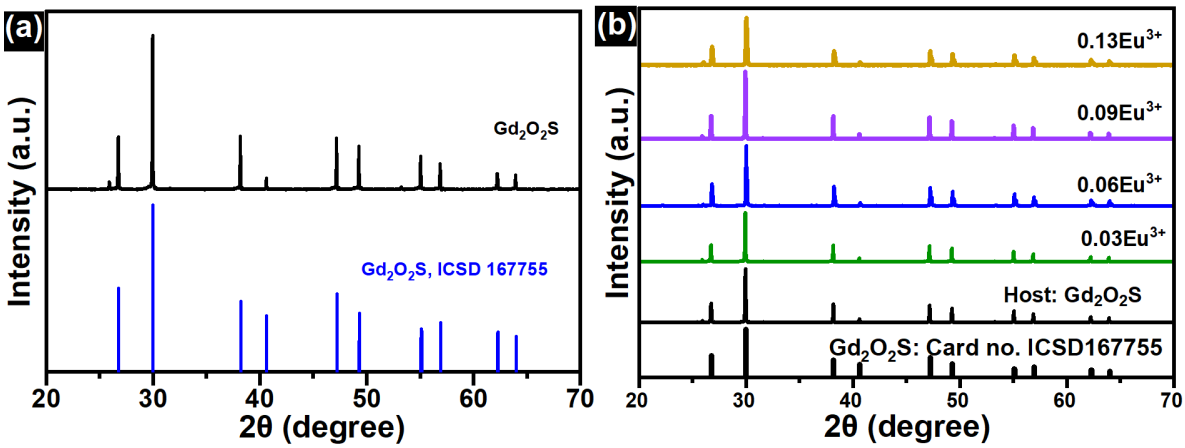

Figure 3.5. XRD patterns of the synthesized Gd_2O_2S and Gd_2O_2S: Eu^{3+}. (a) XRD patterns of synthesized Gd_2O_2S alongside XRD intensity patterns of ICSD 167755. (b) XRD patterns of the synthesized Gd_2O_2S: Eu^{3+} showing no change in XRD patterns of Gd_2O_2S with Eu^{3+} doping.

The SEM images of the Gd_2O_2S: Eu^{3+} microcrystals obtained using the SEM (Zeiss, Supra 60 VP) are provided in Figure 3.6. The particles were observed to be quasi-spherical and had sizes in the range of 1-10 µm. No major agglomerates were observed in the pure microcrystals.

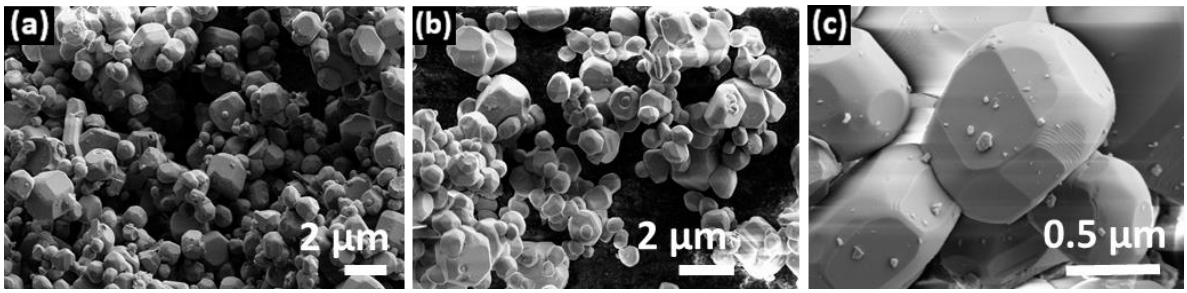

Figure 3.6. The SEM images of Gd_2O_2S: $0.005Eu^{3+}$ at; (a) 4000x (b) 8000x, and (c) 16000x showing quasi-spherical particles with minimal agglomeration.

3.2.2 Crystal Structure and Morphology of Gd_2O_2S: Eu^{3+}, Ti^{4+}

The XRD patterns shown in Figure 3.7 indicate that these phosphors retained the trigonal crystal structure of Gd_2O_2S even after doping with Eu^{3+} and Ti^{4+}. However, above 0.12 Ti^{4+} co-doping, peaks arising due to traces of $Gd_2Ti_2O_7$ that were mapped to ICSD 167918 were observed. Nevertheless, co-doping with Ti^{4+} up to 0.24 mol did not lead to significant changes in the crystal structure.

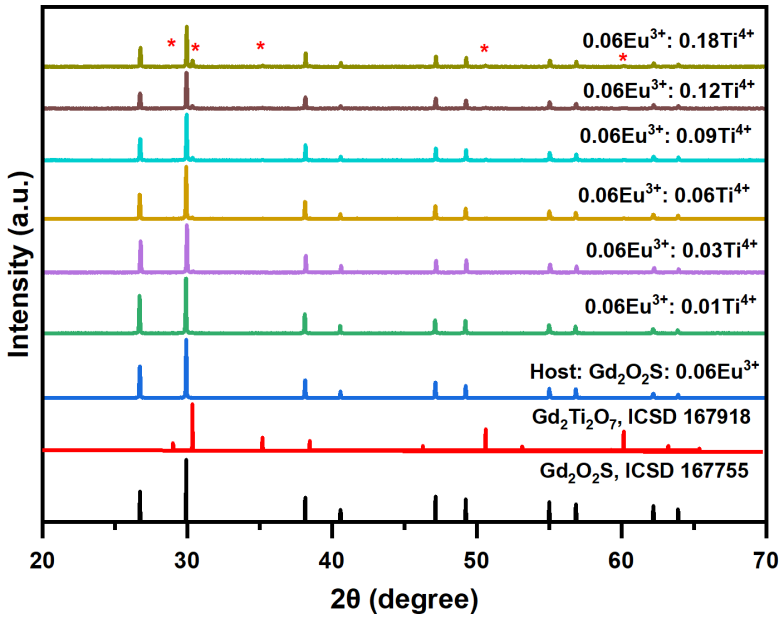

Figure 3.7. The XRD patterns of Gd_2O_2S: 0.06Eu^{3+}, yTi^{4+} phosphors. The XRD patterns are in agreement with the ICSD call code 167755 of Gd_2O_2S. For above 12% Ti^{4+} co-doping, traces of $Gd_2Ti_2O_7$ that can be mapped to ICSD 167918 are observed.

The SEM images of Gd_2O_2S: 0.06Eu^{3+}, 0.09Ti^{4+} are shown in Figure 3.8. The images reveal that the phosphor had quasi-spherical shapes and broad particle distribution (0.1-5 µm), a characteristic of the solid-state-reaction method. However, not all the particles were quasi-spherical as some with block-like structures were also present.

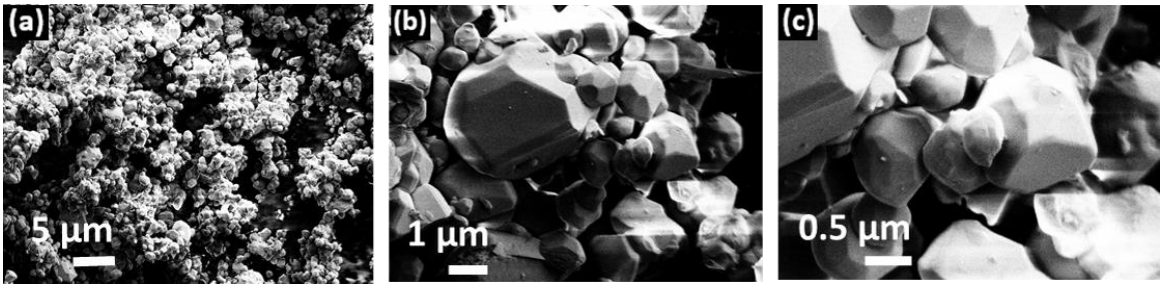

Figure 3.8. The SEM images of Gd_2O_2S: 0.06 Eu^{3+}, 0.09Ti^{4+} at (a) 1000x (b) 5000x, and (c) 15000x. The images reveal that the particle were quasi-spherical shaped with a broad distribution of ~ 0.1 – 5 µm. The images also reveal the presence of large non-quasi spherical large particles and clustering.

3.2.3 Crystal Structure and Morphology of CaS: Eu^{2+}

The XRD patterns of the CaS: Eu^{2+} phosphors showing that the phosphors were crystalline and had no special features are shown in Figure 3.9. The effect of doping with Eu^{2+} is also not observable from the XRD patterns, denoting that the cubic lattice structure remained unchanged after doping. The XRD patterns were mapped to JCPDS card no. 75-0893.

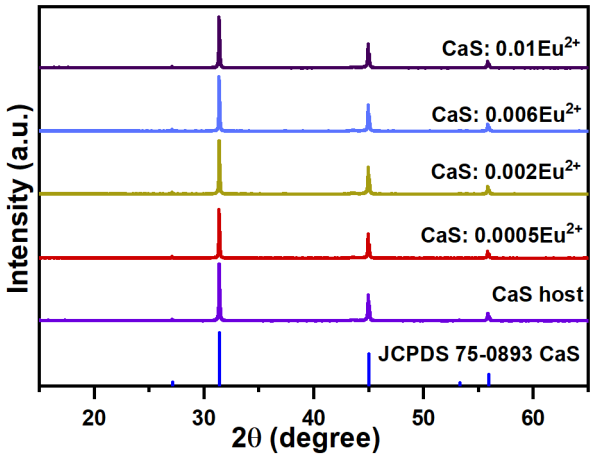

Figure 3.9. The XRD patterns for CaS: Eu^{2+} phosphors. No special peaks arising from increased Eu^{2+} doping are observed.

The morphology of the CaS: Eu^{2+} is shown in Figure 3.10. From the images, it is revealed that the phosphors agglomerated to form large grains. Most of the individual grains were in the range of 1-10 µm.

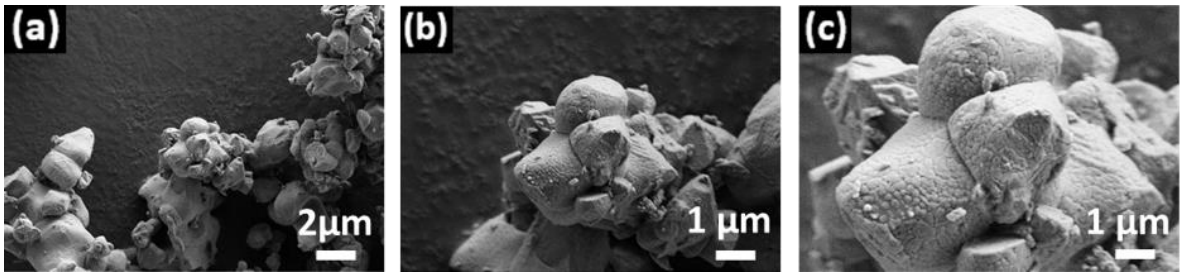

Figure 3.10. The SEM images of CaS: Eu^{2+} at a magnification of (a) 10,000x (b) 25,000x, and (c) 50,000x. The quasi-spheres have very high agglomeration that distorts their shapes. The particle size is >1 µm.

3.2.4 Crystal Structure and Morphology of SrS: Eu^{2+}

Figure 3.11 shows the XRD patterns of the synthesized SrS: Eu^{2+} phosphors. All the samples had a cubic lattice structure. The XRD patterns can be mapped to JCPDS card number 08-0489 and no special peaks are observed with an increase in the Eu^{2+} doping.

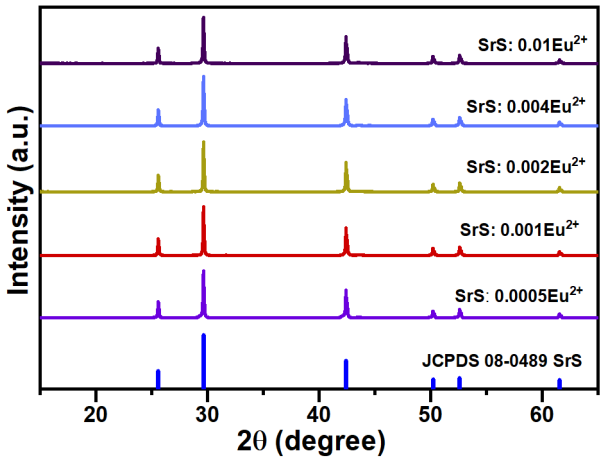

Figure 3.11. The XRD patterns for SrS: Eu^{2+} phosphors. No special peaks arising from increased Eu^{2+} doping is observed.

The SEM images of SrS: Eu^{2+} reveal the presence of quasi-spherical and quasi-cubic particles that mostly agglomerated to form big particles as illustrated in Figure 3.12. Small particles on the surface of the agglomerates were formed because of particle crushing during the grinding process for powder formation after annealing.

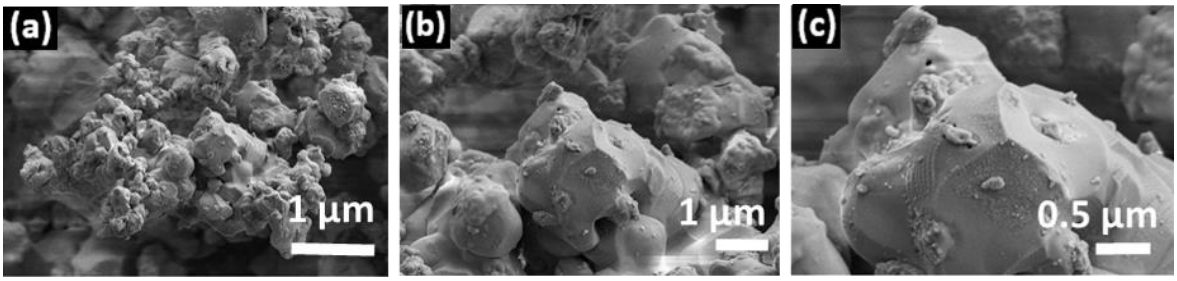

Figure 3.12. The SEM images of SrS: Eu^{2+} phosphors at a magnification of; (a) 1000x (b) 25,000x and (c) 50,000x. A mixture of quasi-spherical and quasi-cubic particles agglomerate to form big particles.

3.2.5 Crystal Structure and Morphology of $SrAl_2O_4$: Eu^{2+}, Dy^{3+}

Figure 3.13 shows the XRD patterns of the SAED phosphors. The XRD patterns were mapped to PDF number 00-034-0379. The patterns conform to that of a monoclinic crystal structure with the space group P121 (4). From the patterns, it is clear that the particles are polycrystalline. No new peaks or peak shifting is observed because of the annealing of the phosphors in the air. The peak intensity however reduced as the annealing in air temperature was increased.

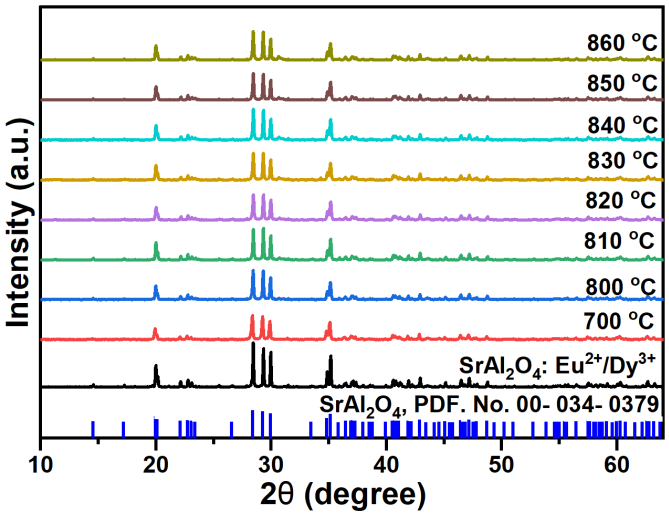

Figure 3.13. The XRD patterns for SAED phosphors. There are no special peaks that arise as a result of the annealing in air.

The SEM images of SAED (ref) are shown in Figure 3.14. The particles were irregular-shaped and with a broad particle distribution (5-100 µm) with a rough

surface texture. Besides the large grains, there was a significant number of small-sized irregular particles that seemed to have detached from the large particles.

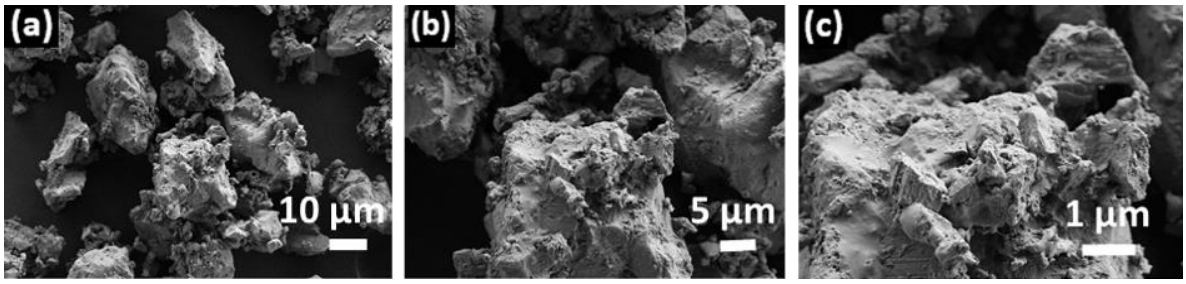

Figure 3.14. The SEM images of SAED (Ref.) phosphor at a magnification of; (a) 1000x (b) 2500x and (c) 5000x. The particles composed of large irregular shaped grains sieved with 100-µm sieve.

3.3 Steady-State Spectroscopy

Steady-state photoluminescence (PL) spectroscopy is the study of the emission and excitation spectra when phosphor materials are excited with continuous-wave radiation. The PL emission and excitation spectra are acquired when the exciting source is continuously shining on the sample. The absorption is in most cases based on the characteristic states of absorption of the ions in the host, charge-transfer states (ligand-metal charge transfer states), and location of localized trap centers/defect centers [21]. This thesis deals with PL emission of lower energy compared to the excitation source, through the downshifting process. The downshifting concept is already extensively discussed in the background chapter in section 2.2. The spectroscopic properties of the samples were investigated by undertaking diffuse reflectance spectra, PL emission via appropriate excitation, and PL excitation by monitoring the emission spectra. These processes are discussed hereafter.

3.3.1 Diffuse Reflectance Spectra

Diffuse reflectance spectroscopy (DRS) is a subset of absorption spectroscopy for powdered samples for which direct spectral absorption cannot be easily measured [205]. It involves directing the incident radiation towards the sample and collecting only the diffracted (scattered) light. Note that, when light is incident on the sample

(densely packed powdered sample), a combination of reflection, refraction, diffraction, and absorption occurs. To obtain an estimate of the scattered light, the detector is usually located away from the specular reflectance path that is directed towards an absorber outside the collecting integrating sphere through an opening. By eliminating the specular reflectance, the detector provides spectral information on the absorption regimes together with the scattering information within the spectra [205]. Note that this process is used herein as a probing technique for identifying the absorption band for excitation, as even the opening to exclude all the specular reflectance does not fully eliminate all specular reflectance. This is because the particles have different orientations. Nevertheless, the technique provides a good starting point for probing the spectroscopic lines and bands present in the phosphor material [205].

To obtain the DRS, a spectrophotometer (PerkinElmer, LAMBDA 950 UV/Vis/NIR) equipped with an integrating sphere (150 mm diameter) coated with Spectralon was used [206]. Spectralon is a broadband diffuse reflecting material produced by Labsphere Inc. used for coating integrating spheres. The excitation source used is either deuterium (for the UV range >319 nm) or a tungsten halogen lamp for the UV-NIR region. The two light sources are coupled to a double monochromator for selectively scanning the wavelength. The incident beam is usually split into a reference and a sample-probing beam by a rotating reflective chopper wheel that allows compensation of light fluctuations. The sample-probing beam is directed through the beam opening of the integrating sphere to hit the sample placed on the opposite side of the integrating sphere. Before any DRS measurement, alignments are made to the sample beam to ensure that the specular reflectance is out-coupled from the sphere via the reflectance opening. The reference beam does not directly hit the sample as it is off-centered and therefore only scattered light from this beam hits the sample via the surface of the integrating sphere. Two detectors are placed inside the integrating sphere: a photomultiplier tube (PMT) detector that detects 200 – 860 nm and an InGaAs detector that detects 860 – 2500 nm. The DRS data was collected in the 250-800 nm range. An exemplary image of the DRS of Gd_2O_2S host material and a Eu^{3+} doped one is shown in Figure 3.15. note that the strong absorption in the host corresponds to the bandgap of the host, 4.6 eV, and is denoted by the sharp decrease in diffuse reflection. Upon introducing Eu^{3+}

ions in the host, a stronger charge transfer band is formed and the sharp decrease in reflection is shifted to a higher wavelength. The weak reflection in the UV region denotes increased absorption and represents the appropriate excitation band of the material.

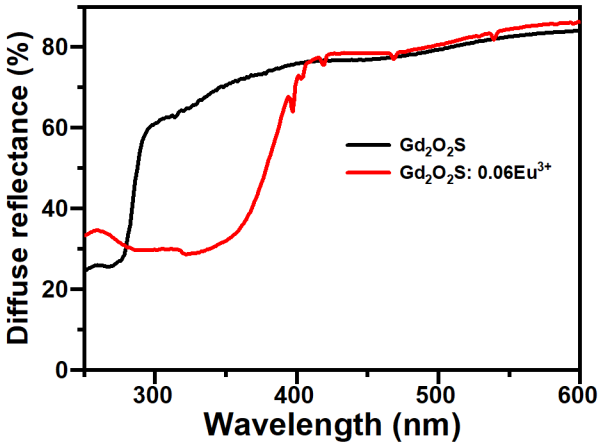

Figure 3.15. The DRS of Gd_2O_2S host material and Gd_2O_2S:0.06Eu^{3+}. The weak reflection in the 270 nm region coincides with the bandgap of the material while the broad absorption following Eu^{3+}doping indicates formation of another absorption band.

3.3.2 Photoluminescence Excitation Spectra

The PL excitation spectra were recorded using a spectrofluorometer (Varian, Cary 50 Eclipse) [207]. For the measurements, the powdered phosphor samples are placed inside quartz cuvettes and placed between the optical path of the two monochromators in the spectrofluorometer. One monochromator is coupled to a xenon flash lamp and acts as the excitation source and the other is coupled to the PMT and acts as the signal detector. For the PL excitation spectra, the PL of the sample at a specified wavelength is tracked as a function of excitation wavelength. The excitation monochromator is therefore not fixed as it continuously calibrates the xenon flash lamp to scan the desired excitation range. The monochromator coupled to the PMT is fixed to the PL emission wavelength whose excitation is being tracked. The PL excitation spectra trend is closely related to the DRS spectra as shown in Figure 3.16. Notice that the PLE provides more refined spectra than DRS and can resolve weak absorption bands otherwise observed as weak in DRS

measurements. In the case of Gd_2O_2S: Eu^{3+} the absorption bands due to the Eu^{3+} ions can be resolved.

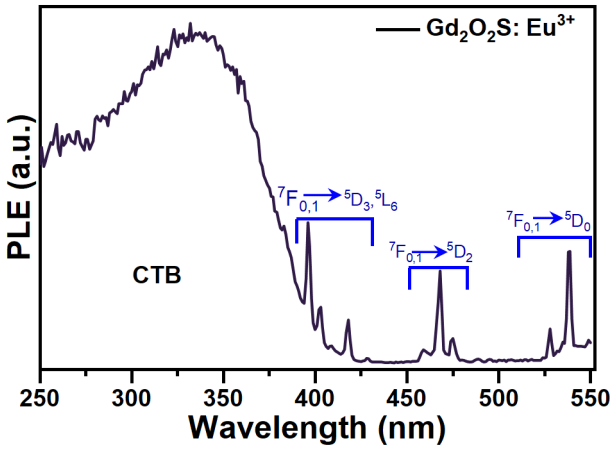

Figure 3.16. The PLE of Gd_2O_2S:Eu^{3+} tracked from 626 nm excitation. The spectra consists of a broad charge transfer band (CTB) and minor sharp absorption peaks ascribed to Eu^{3+} transitions.

3.3.3 Photoluminescence Emission Spectra

The PL emission spectra were recorded using the spectrofluorometer (Varian, Cary 50 Eclipse). To acquire the PL emission, the monochromator coupled to a xenon flash lamp is set to the desired excitation wavelength, while the monochromator coupled with the PMT scans the spectral emission range of the sample. Note that the excitation slit and detection slits of the monochromator in the spectrofluorometer can be varied from a fraction of a nanometer to several nanometers of wavelength depending on the desired excitation, detection modes, and the strength of the signal generated from the sample following excitation [207]. In most cases, when the excitation and detection wavelengths have to be maintained with higher precision by using smaller slit widths, the voltage gain of the PMT has to be adjusted accordingly.

An example of the PL emission spectra of Gd_2O_2S: Eu^{3+} following 375 nm excitation is shown in Figure 3.17. The emission spectra are composed of the Eu^{3+} transitions with the $^5D_0 \rightarrow {}^7F_2$ being the dominant transition. As a result, the phosphor looks red during excitation.

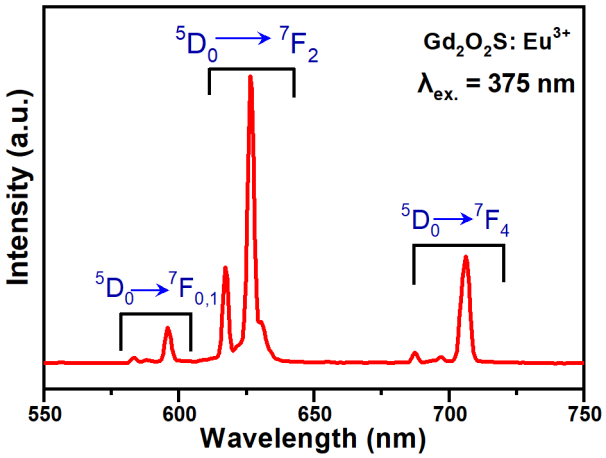

Figure 3.17 The PL emission of $Gd_2O_2S: Eu^{3+}$ following 375 nm excitation. The Eu^{3+} transitions are shown alongside.

Alternatively, the PL emission is recorded by exciting the samples with an external source such as a light-emitting diode (LED) or a laser diode, and then the emission is collected using a fiber-coupled spectrometer. Figure 3.18. Scheme of the experimental configuration of obtaining the steady-state photoluminescence and the photoluminescence quantum yield of a sample. Figure 3.18 gives a scheme of how the PL emission is acquired using this method. The exciting source, e.g. a LED 375 nm (Roithner LaserTechnik, XSL 375) controlled using a laser driver controller (Thorlabs, ITC4001) is first directed towards a collimating lens (Thorlabs, AC254-030-AB), then to a plano-convex lens (Thorlabs, LA1433) with a focal length of 150 mm that focuses the beam into the integrating sphere of diameter 4 inches (Labsphere, 3P-LPM-060-SL) in which the sample is placed. These optical collimating and focusing lenses can be changed to suit the experiment under consideration.

Following excitation, the emission is collected through the exit port of the integrating sphere, usually equipped with a baffle in the detection port to inhibit the direct excitation from going through to the spectrometer as this would likely destroy the pixels of its charge-coupled device (CCD) sensor. For downshifting measurements, a long-pass filter (e.g. FEL450, Thorlabs) is placed immediately after the exit port, whereas for upconversion measurements, where the excitation is for instance 980 nm, a short-pass filter (e.g. FES 950, Thorlabs) is placed after the exit port. Note that the selection rule for the optical filter is that it should always block the wavelength of the excitation source while allowing the

photoluminescence emission to be collected by the fiber cable to the spectrometer. The fiber optic cable (Thorlabs, FP1000URT) is coupled to a CCD spectrometer with integrated cooling (Avantes, AvaSpec-ULS2048x64TEC) to collect the emission. While most of the PL emission spectra can be obtained using this method, the same setup is mostly used for determining the PLQY of samples as discussed in the next section. The power of the excitation beam is also recorded by reflecting a known fraction of the line beam to a photodiode power sensor.

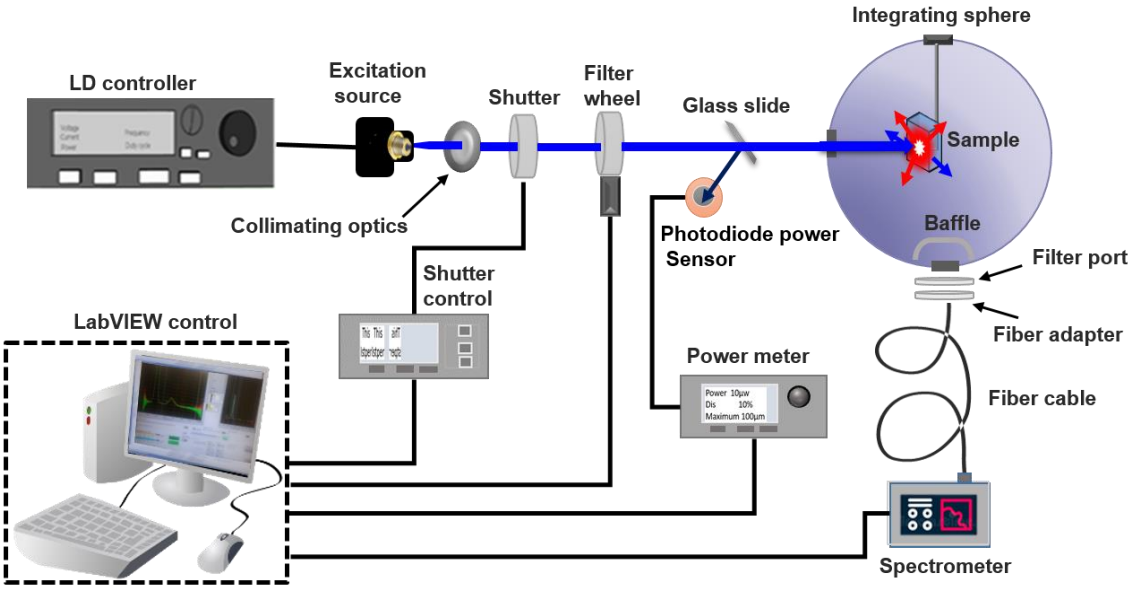

Figure 3.18. Scheme of the experimental configuration of obtaining the steady-state photoluminescence and the photoluminescence quantum yield of a sample.

3.3.4 Photoluminescence Quantum Yield

The PLQY indicates the efficiency of the PL process [208]. The PLQY also provides insights into the photophysical behavior of the phosphors as it is involved in the calculation of quenching-rate constants, energy transfer, lasing ability, and radiative and non-radiative constants [209]. The determination of PLQY is realized through either a relative or an absolute measurement technique [208, 210]. The relative technique entails comparison-computations of a well-known phosphor to another phosphor with similar photoluminescence characteristics [208]. The most relied approach for relative PLQY measurement entails a comparison of the integrated emission spectra of the phosphor to a standard sample obtained under

identical conditions. These conditions include but are not limited to temperature, humidity, absorption factors, excitation wavelength, and power of excitation [208]. These requirements possess a fundamental challenge as slight spectral changes in the PL requires a new reference. Despite this challenge, such a measurement only requires a conventional absorption spectrometer and a fluorescence spectrometer to determine the required PLQY calculation parameters.

On the other hand, the absolute approach, used throughout this thesis, does not require a standard reference. Instead, the sample to be measured is placed in an integrating sphere where the excitation source is directed via an opening as already illustrated in Figure 3.18. The emission signal is collected via an opening in the integrating sphere equipped with a baffle to prevent direct illumination by the incident flux [211, 212]. This technique ensures that all the light emitted from the excited sample is captured from all possible solid angles, as the integrating sphere collects the entirety of the emissions [208, 213]. In addition, the properties of the excitation beam such as the excitation power density are also recorded. This value is important for power-dependent emission, especially for upconversion [214].

The radiation exchange and interaction within the integrating sphere consider both the direct illumination from incident radiation and the subsequent diffuse reflection processes. The radiance L of the initial input flux $\emptyset$ in the diffusing surface of the sphere is given by:

$$L = \frac{\emptyset\rho}{\pi A} \tag{3.3}$$

where ρ is the reflectance, A is the illuminated area and π is the total projected solid angle from the sphere surface. Equation 3.3 is then modified to accommodate the subsequent multiple surface reflection and losses through the port opening. First, by taking the consideration of the port openings for the incident and output radiation, we modify equation 3.3 to:

$$L = \frac{\emptyset\rho}{\pi A(1-f)} \tag{3.4}$$

where $A(1-f)$ denotes the total area of the sphere minus the area of the port openings. By using an infinite power series, the expression for reflectance inside

the integration sphere again taking into account the reduction in area due to the port openings becomes:

$$\frac{\emptyset\rho(1-f)}{1-\rho(1-f)} \tag{3.5}$$

Combining equation 3.4 and equation 3.5 leads to a sphere surface radiance given by:

$$L_s = \frac{1}{\pi A(1-f)} * \frac{\emptyset\rho(1-f)}{1-\rho(1-f)} \tag{3.6}$$

which then simplifies to:

$$L_s = \frac{\emptyset}{\pi A} * \frac{\rho}{1-\rho(1-f)} \tag{3.7}$$

The first part of the above equation is an estimation of the radiance of the diffuse surface while the second part is referred to as the sphere multiplier, *M*, and depends on the opening port fraction,f, and the sphere surface reflectance.

$$M = \frac{\rho}{1-\rho(1-f)} \tag{3.8}$$

To account for all the sphere openings and reflections in an integrating sphere, the equation above can be generalized to:

$$M = \frac{\rho_i}{1-\rho_w(1-\sum_{i=0}^{n} f_i) - \sum_{i=0}^{n} \rho_i f_i} \tag{3.9}$$

Incorporating the generalized sphere multiplier in equations 3.9 to 3.7 leads to:

$$L_s = \frac{\emptyset_i}{\pi A_s} * \frac{\rho_i}{1-\rho_w(1-\sum_{i=0}^{n} f_i) - \sum_{i=0}^{n} \rho_i f_i} \tag{3.10}$$

where Φi is the input flux, ρ_0 is the initial incident flux reflectance, A_s is the inside surface area of the integrating sphere, ρ_w the reflectance of the sphere wall, ρ_i is the reflectance of the port opening and f_i the fractional area of the port opening given by

$$f_i = \frac{\sum_{i=1}^{n} A_i}{A_s} \tag{3.11}$$

where A is the area of the port opening. The experimental setup of the sphere during the measurement is shown in Figure 3.18.

The value of L_s, the radiance from the integrating sphere is then computed spectrally to collect the lasing spectra and the PL spectra for calculation of the PLQY. The absolute measurement allows for either two measurements (2M) or three measurements (3M) from which the internal PLQY of a sample can be determined. It is however a convention that in most cases these two measurements are done simultaneously as they share a lot of similarities as far as the acquired signals are concerned.

To determine the PLQY, a CCD spectrometer (Avantes, AvaSpec-ULS2048X64TEC) coupled to a spectralon coated integrating sphere (Labsphere, 3P-LPM-060-SL, 15 cmϕ) using an optical fiber (Thorlabs, FP1000URT) was used to acquire the signal following excitation. The coupled system was pre-calibrated using a calibration lamp (Ocean Optics, HL-3P-CAL). A scheme of the experimental configuration of the integrating sphere for determining the PLQY of the samples is shown in Figure 3.19. In practice, initialization measurements (dark counts) for the laser output and photoluminescence output are first measured. This acts as the zero-reference point. This is then followed by an Empty Sphere (ES) measurement where the laser is turned on, and a measurement is taken as shown in Figure 3.19 experiment A. The sample is then placed inside, in the path of the direct excitation beam and the spectrum is measured with one segment of the spectrum being registered in the laser emission segment and referred to as laser direct (LD) and the other emission corresponding to PL emission being registered in the PL side as photoluminescence direct (PD). This scheme is shown in Figure 3.19 experiment B. After this measurement, the sample is rotated away from the direct beam position such that only the reflections of the incident beam coming from the surface of the sphere hit the sample.

A spectrum is then acquired at this position, again in two parts, with the photoluminescence portion being the photoluminescence indirect (PI) and the laser section being Laser indirect (LI) as shown in Figure 3.19 experiment C. With these measurements, (3 measurements with six output integral spectra) one can

calculate the PLQY using either the 3M measurement where all the spectra are utilized or use the first two to calculate the PLQY based on the 2M method. The 2M method provides a simple way of estimating the PLQY, by utilizing measurements A and B shown in Figure 3.19.

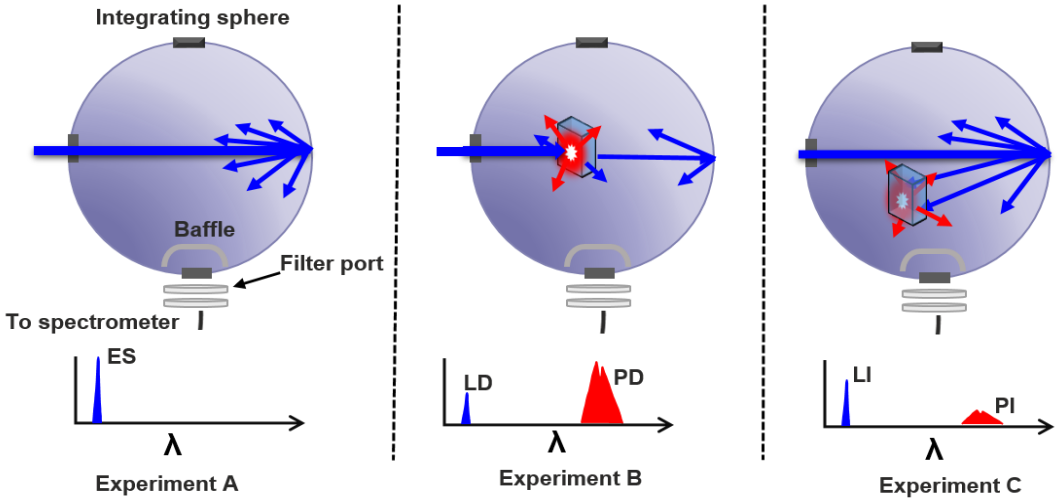

Figure 3.19. Scheme illustrating the three experiments required for PLQY measurement of a sample. In experiment A the excitation radiation is collected for an empty sphere (ES). In experiment, B the sample is placed inside the sphere in direct excitation to the incoming radiation. The spectra obtained contains both the laser radiation signal following the direct excitation and scattering light excitation of the sample (LD) together with the resulting total emission from the sample PD. In experiment C, the sample is placed in indirect position of the incoming laser radiation. The spectra collected contains the laser radiation signal after indirect excitation (LI) and the emission resulting from the indirect excitation of the sample PI.

From these data, the number of emitted photons is given by PD, while the total number of photons absorbed by the sample under direct flux is obtained by calculating the spectral difference between ES and LD. The PLQY is then estimated by the equation:

$$PLQY_{2m} = \frac{N_{em}}{N_{abs}} \approx \frac{PD}{ES - LD} = \frac{\int I_{em}(\lambda)d\lambda}{\int I_{laser,\,empty}(\lambda)d\lambda - \int I_{laser,\,sample}(\lambda)d\lambda} \quad (3.12)$$

The 3M method for PLQY estimation utilizes all the three measurements shown in Figure 3.19. It considers a single interaction of the sample with the excitation light and therefore eliminates the emission events due to the absorption of photons that have previously been scattered. The fraction of photons absorbed due to the direct flux hitting the sample can be estimated to be:[213]

$$A = 1 - \frac{LD}{LI} \tag{3.13}$$

From measurement C in Figure 3.19, the signal detected by the spectrometer due to this indirect excitation is simply the scattered laser radiation and light emitted from the sample following absorption of scattered incident radiation. By assuming that the initial scattering point of scattering is inconsequential, the contribution of the scattered radiation in experiment C can be expressed as:

$$(1 - A)(LI + PI) \tag{3.14}$$

The total photons detected by the detector from experiment B can therefore be expressed as:

$$PD + LD = (1 - A)(LI + PI) + \eta \cdot ES \times A \tag{3.15}$$

where the second term on the right represents the sample emission due to direct excitation. The term η represents the PLQY. Rearranging equation 3.15 to make η the subject of the formula and using equation 3.13 leads to the PLQY as determined by the 3 M method as:

$$PLQY_{3m} = \eta = \frac{PD - PI(1 - A)}{ES \cdot A} \tag{3.16}$$

both the 2M and 3M PLQY methods have experimentally been shown to yield similar results despite their underlying theoretical differences [210]. The excitation sources used for determining the PLQY in this thesis are a 375 nm LED (Roithner LaserTechnik, XSL 375), and a 450 nm (Thorlabs, M450LP1 – 450 nm) continuous wave (CW) laser diode controlled using a benchtop Laser Diode/TEC Controller (Thorlabs, ITC4001).

3.3.5 Temperature-dependent Photoluminescence

Temperature-dependent photoluminescence (TDPL) measurements probe the PL emission behavior of a phosphor material as a function of the temperature. The TDPL is obtained using a temperature-controlled thermal stage (Microptik, MHCS622-V/G) integrated with a high-resolution temperature controller (Microptik, MTD600) and an excitation setup as shown in Figure 3.20. To acquire the TDPL, the thermal stage was connected to a liquid nitrogen cooling system (Microptik, LN_2SYS) and a vacuum pump was connected to the sample stage to suck out air and moisture. The sample chamber has a glass window through which the excitation and emission are collected. The phosphor samples are placed in small alumina crucibles inside the sample chamber of the thermal stage. Light from a 375 nm LED excitation source (Roithner LaserTechnik, XSL 375) was first collimated using a collimating lens (Thorlabs, AC254-030-AB) focused using a plano-convex lens (Thorlabs, LA1257, focal length 75 nm) onto the sample surface.

The emission is filtered by a 450 nm long-pass filter (Thorlabs, FEL0450) and then collected with an optical fiber of 0.6 mm diameter (Newport, P/N78277) coupled with a spectrometer (Thorlabs, CCS200). Before data collection, an allowance of approximately five minutes was given to actualize the set temperature. The collecting fiber optics were aligned out of the specular reflection region of the excitation source to avoid direct illumination via reflection. Other excitation sources used for the TDPL measurement in this thesis include continuous wave (CW) laser diode excitation 300 nm (Thorlabs, M300L4), and 450 nm (Thorlabs, M450LP1) controlled by a Benchtop Laser Diode/TEC Controller (Thorlabs, ITC4001). The excitation power of the collimated LED was determined using a power meter (Thorlabs, PM100D).

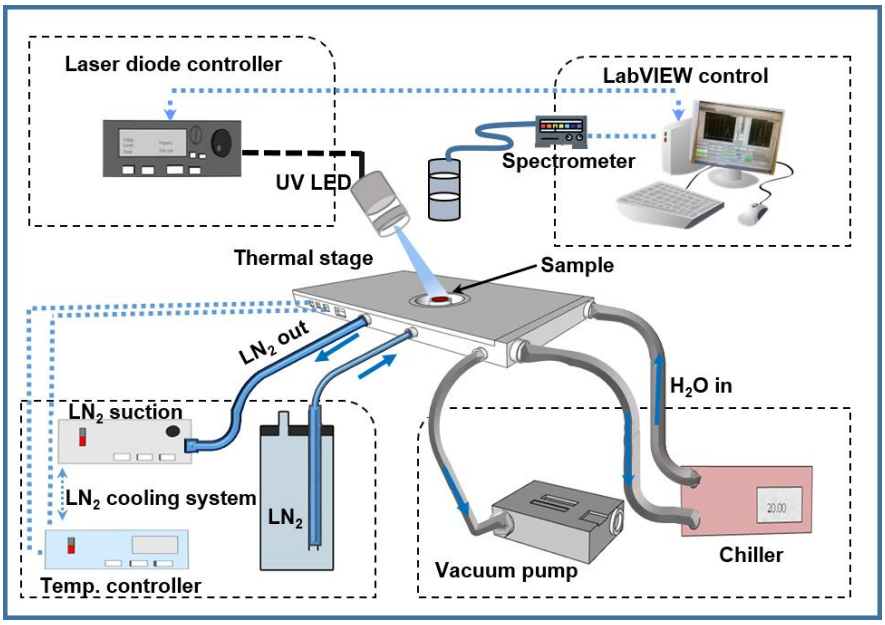

Figure 3.20. Schematic of the experimental setup for temperature dependent photoluminescence and PersL lifetime. The laser diode controls the excitation sources, the spectrometer captures the emission and the liquid nitrogen together with the temperature controller controls the temperature set value. The vacuum pump removes condensed air and moisture while the chiller maintains the temperature of the non-heating elements at the set temperature.

3.4 Time-Resolved Spectroscopy

Time-resolved spectroscopic methods provide information about the molecular processes of an excited state following excitation with appropriate radiation. This technique differs from steady-state spectroscopy in that, it accumulates the photon counts as a function of time. Another difference is that in steady-state spectroscopy the excitation is a continuous wave, whereas, in time-resolved spectroscopy, the excitation is pulsed.

In this work, time-resolved measurements to determine persistent decay profiles of phosphors were accomplished using two different setups: 1) using the multichannel scaling technique and 2) using smartphone cameras. While the multichannel scaling technique is an established technique, it usually involves expensive and non-portable instrumentation, whereas using the smartphone is ideal due to portability and the ubiquitous nature of smartphones. The portability,

availability, ease of use, and potential diversification of applications in smartphones are major motivations in this work.

3.4.1 PL Lifetime with PMT/ Multichannel Scaling Method

Emission from phosphors after excitation is usually a random process, with several exciting states emitting their photons at the instance of the pulse and others emitting the photons after the excitation source is exhausted. The luminescence lifetime is the average value of time an ion spends in an excited state before going back to the ground state. The statistical distribution of the emission after the excitation source is removed leads to the formation of a decay curve from which the lifetime can be estimated and fitted with mono, double, or triple exponential functions. In this thesis, long-lived persistent phosphors were used and therefore multichannel-scaling (MCS) was used to determine the lifetime. The MCS method is closely related to the TCSPC method but in the TCSPC the detection rate is as low as one photon per 100 excitation pulses and is only ideal for very short lifetimes. Data acquisition time using TCSPC would thus have been unrealistic for persistent phosphors.

A schematic of the PL decay measuring system based on MCS is provided in Figure 3.21. For the acquisition of lifetime data, the sample is excited using the desired excitation wavelength, power density, period, and pulse width. In most instances, however, the optimal period and pulse width are determined through a series of optimization during the initial set up as demonstrated later herein. The excitation power can be controlled by adjusting the current driving the LED in the laser diode controller. Since the internal trigger pulse generator of the laser diode controller is limited to a maximum pulse width of 1 s and a maximum repetition rate of 1 kHz, longer pulse widths (>1 s) and repetition rates below 0.2 Hz are coupled to the controller using a wave function generator (Agilent, 33220A-20MHz), acting as an external trigger source. The trigger signal generated by the wave function generator is connected to the MCS card Picoquant, TimeHarp 260 NANO) for synchronization. This trigger signal to the MCS is integrated with a microcontroller (Arduino, UNO) based delay generator to provide a delay of (~10 µs) that accounts for the electronic delays in the signal.

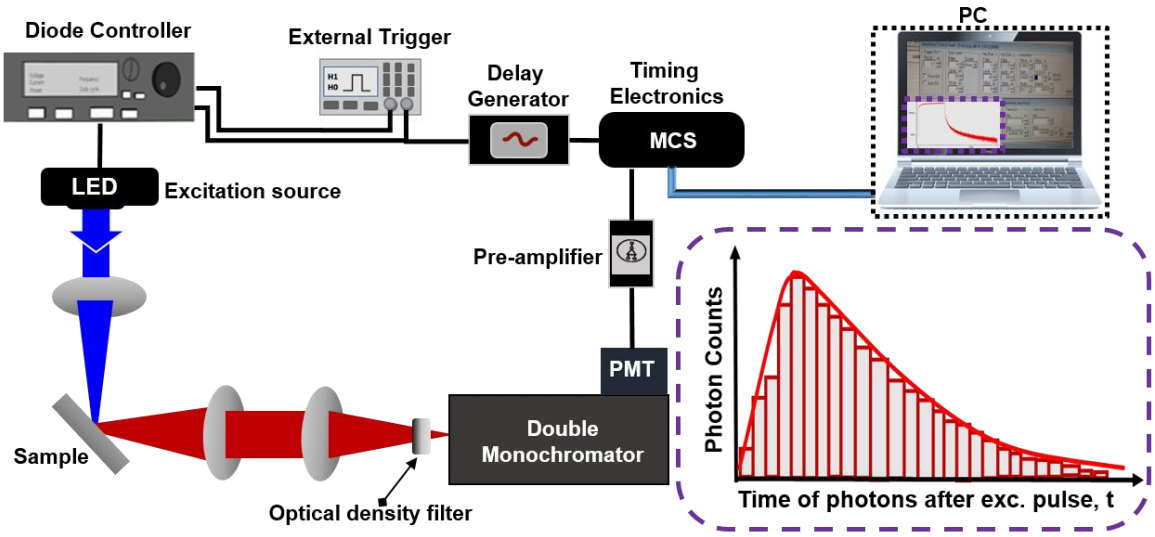

Figure 3.21. The experimental setup for photoluminescence lifetime determination using multichannel scaling. The emission from the sample following excitation is directed to the monochromator for wavelength selection after which a PMT captures the signal. The signal is then amplified before being fed to the multichannel scaling card. The obtained signal is synchronized to the trigger level using a microcontroller (Arduino, UNO) with an appropriate delay of 10 µs at the MCS. The signal is then displayed in the computer (PC) using a TimeHarp software, where histograms of the emission are displayed as a function of time.

The excitation source is then made to shine on the sample using a collimating lens (Thorlabs, AC254-030-AB) and a focusing plano-convex lens (Thorlabs, LA1433). The pulsed excitation leads to emissions from the samples that fluctuate from maximum intensity immediately following excitation and decays to zero before the next pulse hits the sample. Appropriate adjustments to the pulse width and period are made for obtaining the optimum signal. It was important to ensure that the excitation pulse drives the emission of the sample to a maximum steady-state and that before the next pulse all the emission is exhausted. The sample emission was directed toward the slit opening of a double monochromator (Bentham, DTMS300) using two lenses. A filter port, where neutral density filters can be inserted to decrease the intensity of the incoming emission is strategically placed in front of the double monochromator to avoid over saturation. The monochromator isolates the selected wavelength for which the lifetime is to be measured and transmits it to the detectors. For the UV- visible region (185 - 900 nm), a circular cage PMT

(Hamamatsu, R928P) was used as the detector. For NIR (900 - 1700 nm) measurements, the second outlet of the double monochromator is connected to an InGaAs/InP avalanche photodiode-based single-photon detector (ID Quantique, ID220) (not included in Figure 3.21). The output signal of the cooled PMT is then amplified using a pre-amplifier module (Picoquant, PAM-102) that provides a signal gain up to 25 dB. The amplifier then passes the amplified signal to the MCS card connected to the PC. The cooled NIR single-photon detector is usually directly connected to the MCS without additional pre-amplifiers. The MCS (Picoquant, TimeHarp 260-NANO) has an ultra-short dead time of <2 ns with 32768 histogram channels [215]. The lifetime decay data is acquired from the system using the TimeHarp software, where histograms of the emission are displayed as a function of time. A scheme of the histograms formed after many repeated measurements is shown in Figure 3.21. During the data acquisition process, the detected signal counts can also be regulated using the PMT voltage controller. This must be done carefully ensuring that the PMT is not driven to saturation and not damaged with very high voltage. The typically used voltage is 900 - 1050 volts. High voltage also may lead to overheating of the PMT, compromising the signal-to-noise ratio. Due to the sensitivity of the PMT, and the desire for high-accuracy data, the data collection is done in a dark environment (caged system). The data is then extracted, binned to the timescale, and fitted using an appropriate exponential function.

3.5 Smartphone-based PersL Lifetime Sensing

The MCS method described above is an established technique for determining the PL lifetime of phosphor materials. It is usually an extension of the TCSPC technique and therefore capable of measuring PL lifetime in the range of nanoseconds to milliseconds [216]. However, the MCS is not ideal for very long lifetimes in the range of hundreds of milliseconds to several seconds as in the case of persistent luminescence and phosphorescence. This is because the histogram build-up would require an unrealistic time for acquiring the signal for one decay curve. It is due to this reason, together with the inexpensiveness and portability of the ubiquitous smartphone, that we developed a method of determining the PersL lifetime above 100 ms to several seconds using videos acquired from a

smartphone. In this thesis, the PersL lifetime acquired from the analysis of a smartphone video is used to demonstrate surface thermometry and anti-counterfeiting.

3.5.1 Calibration of Smartphone Cameras: The Exposure Triangle

In smartphone cameras, the exposure triangle is based on three parameters, namely aperture, ISO, and shutter speed [217, 218]. The three parameters are balanced to capture the right moment in photography or to take the right videos with respect to lighting conditions. The ISO refers to the camera's sensitivity to light, or simply the signal gain of the camera's sensor. For a digital camera, the ISO is an amplification of the signal gained by the photosite of the camera sensor. It is therefore a post-acquisition adjustment (analog and digital amplification) after the camera photosites have already acquired the image. In manually controlled cameras, the ISO setting should only be changed at last after alternatives from the shutter speed and aperture are exhausted. The ISO should be kept as low as possible (base ISO) to ensure the highest image quality. This is however not always possible, especially when working in low-lighting conditions requiring one to brighten the image by increasing the ISO. Higher ISO settings however lead to noise (grains in the images) and distortion of the signal. Typical values of ISO in smartphones range from 50 to 3200. When all other camera parameters are held constant, every time the ISO is doubled, the brightness of the acquired image is also doubled. The increase in ISO is associated with a loss of image quality (image noise).

The camera shutter speed (sensor exposure time) dictates how long the camera sensor remains open (exposed to light) per second when taking a photo or a video. In digital cameras, the shutter is an electronic switch that switches the photosites on and off at the defined frequency. Slow shutter speed means longer exposure time and high shutter speeds mean shorter exposure time of the photosites. Ideally, if the shutter speed is low, the aperture opening needs to be larger, or else the ISO must be increased. On the other hand, when the shutter speed is high, the aperture needs to be closed (to allow a small opening) or the ISO is reduced.

Finally, the aperture is the hole in the lens through which light travels to the camera sensor. The aperture is expressed in f-numbers, also referred to as f-stops. The f-

numbers are expressed as fractions of the focal ratio of the lens focal length to the diameter of the aperture. For example, the aperture of the Samsung Galaxy A5 (2017) is f/1.89. This rear camera has a fixed focal length of 3.60 mm. The focal ratio, F is obtained by dividing the fixed focal length, by the denominator 1.89 to get F1.9.

The relationship between the ISO, shutter speed and aperture of a camera is expressed in the form of an exposure triangle as illustrated in Figure 3.22. Considering that the aperture of the smartphone camera is fixed in most cases, the ISO and shutter speed play an important role in adjusting the camera settings to capture the desired image/video. So, the order of operations in optimizing the camera settings usually begins by identifying the aperture size, then adjusting the shutter speed accordingly.

In ideal lighting conditions, this is usually enough to capture good images and videos, however, in a darkened environment, even the lowest shutter speed might not be enough to capture the desired image. This necessitates the adjustment of the ISO appropriately. In Figure 3.22 this order of operations is denoted with the clockwise arrow. However, too much increase in the ISO also leads to low-quality images and videos with grains.

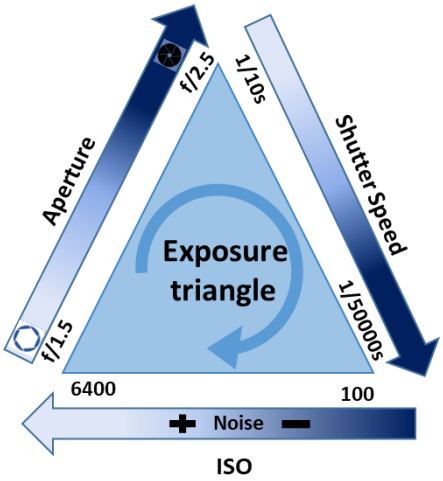

Figure 3.22. The camera exposure triangle. For most smartphones, the aperture is fixed and therefore the shutter speed and ISO becomes the dominant control parameters.

3.5.2 Smartphone Camera Acquisition Settings

The first step towards determining PL lifetime using a smartphone is to have absolute control of the camera settings by enabling the Camera 2 API. The term API stands for Application Programming Interface (API) and when camera 2 API is enabled it allows the user to have advanced access to manually control the exposure triangle settings [48, 219]. It is possible to turn the Camera 2 API feature on in several phone brands running on the Android Operating system (OS) (lollipop and android 6 Marshmallow or any other recent OS release as of 2021) such as Samsung, Google Pixel, Lenovo, and Xiaomi. Google *Play Store* offers an app *Camera2 probe* that probes if a smartphone has a camera 2 API support.

With the *camera 2 API* enabled, an open-source camera app by Mark Harman (camera HD (Open Camera V1.0, Code 1 © 2013-2016) in Galaxy store and named Open Camera (v1.48.1 Code: 77) in Google Play store is used. The spatial resolution is set to 1920×1080 pixels and the frame rate is set to *30 fps* (shutter speed 1/33 s^{-1}). The white balance is set to *fluorescent*, the color effect to *none,* and then the auto level to *unchecked*. The ISO is manually set to 1200, (this could be varied depending on the selected shutter speed), and the exposure time to 1/100 s and locked. All these settings are then saved in the app's settings manager and could be retrieved for re-use at a future time in the app. The app is used with android phones that include Samsung Galaxy (Samsung Electronics, A5 (2017), Samsung Galaxy A21S (Samsung Electronics), and Xiaomi (Redmi Note 4). For these phones, the Camera 2 API functionality is tested on-site.

For iPhone cameras (iPhone XR and iPhone 8 plus) a third-party app, *pro movie recorder version 1.10* is used to manually control the camera settings. This app can be downloaded in the app store. The camera settings are adjusted as follows: The shutter speed is set to 1/100s, and the ISO is set to 800. The white balance is set to fluorescent, the fps set to 30, and the focal distance set to 0.1 m. The settings were maintained and used during the measurements.

3.5.3 Smartphone PersL Lifetime Data Acquisition

To determine the PL lifetime, also referred to as PersL lifetime or afterglow of the phosphors, three excitation sources are used in this work: 1) an external LED of

375 nm (Roithner LaserTechnik, XSL 375), 2) an LED of 450 nm (Thorlabs, M450LP1) both controlled using a benchtop laser diode/TEC controller (Thorlabs, ITC4001) externally modulated using a function generator (Agilent, 33220A-20MHz) and 3) the smartphone flashlight. The smartphone flashlight has a peak emission at 450 nm and a broadband emission extending up to 750 nm [220].

In a typical experiment, to acquire the PL lifetime of the Gd_2O_2S: Eu^{3+} sample at room temperature, the sample was placed in alumina crucibles and excited with the 375 nm LED controlled with the laser diode controller and externally modulated with the function generator. A 5 s pulse was used for all the measurements. The smartphone video-recorded the emission at a distance of 5 - 10 cm after which the video is analyzed in MATLAB to extract the persistent decay curves. The flow chart for determining the persistent decay is shown in Figure 3.23. The acquired video is first cropped to specified pixels in a region of interest, then split into the red, green, and blue channels for further processing.

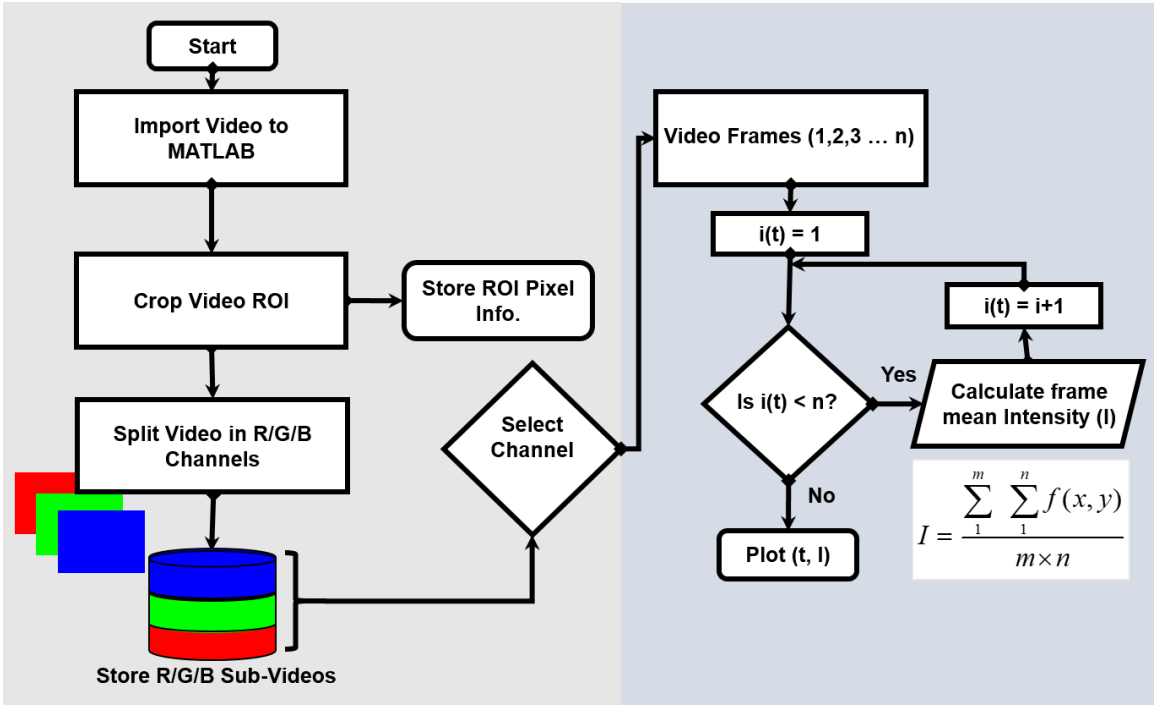

Figure 3.23. The flow chart for determining the persistent decays of persistent phosphors using smartphone acquired videos.

The PersL lifetime is then computed according to the desired RGB channel. The data is then saved and fitted in O*rigin*. The PersL lifetime data of CaS: 0.0005Eu^{2+} computed using the same procedure from videos acquired using the Samsung Galaxy A5(2017) is shown in Figure 3.24a. The PersL lifetime data used in this thesis is fit in a region of interest t_1-t_2 using either a single or multiple exponential fit shown in equation 3.17.

$$I = I_o + A_1 \exp(-t/\tau_1) + A_2\, exp\,(-t/\tau_2) \tag{3.17}$$

where τ_1 andτ_2 are the characteristics lifetime, A_1 and A_2 are their respective coefficients and I_o is an offset. Depending on the profile of the fit, one can fit either a single exponential or a double exponential in the t_1-t_2 selected ROI. For a single exponential such as the case of CaS: 0.0005Eu^{2+}, only the first two summands in equation 3.17 are needed. For this fitting, zero time is defined by the term t_0 as the zero time and t_1 is exactly 0.2 s after t_0 for all the measurements. The second value, t_2 is the time at which 90% of the total delayed emission has been collected. This time is identified by computing the integral emission area starting at t_1 as shown in Figure 3.24b. This value varies from phosphor to phosphor and must therefore be calculated for each phosphor material. The PersL lifetime from the smartphone is fitted using a single exponential function and an average lifetime of 593 $\pm$ 9 ms was registered.

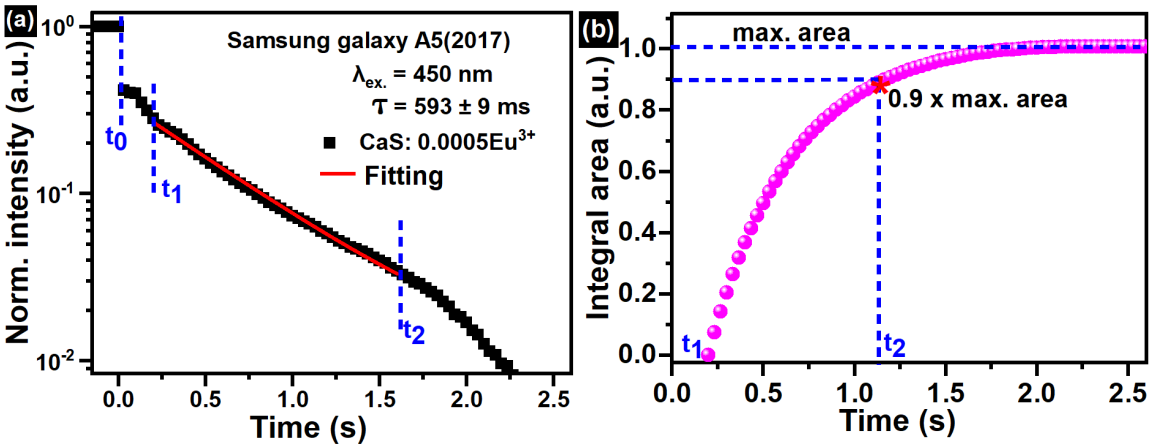

Figure 3.24. a) PersL lifetime of CaS: 0.0005Eu^{2+} following 450 nm excitation. b) Computed integral area of the delayed persistent emission of delayed emission of CaS: 0.0005Eu^{2+} as a function of time to identify boundary time t_2 *at 90% emission exhaustion.*

The same procedure was repeated using three other smartphones, namely iPhone XR, iPhone 8 plus, and Xiaomi (Redmi Note 4). These results are shown in Figure 3.25(a-c). The PersL decay curve has the same trend and the PersL lifetime fitting registered from each smartphone was within an acceptable margin. Figure 3.25d shows the summary of the obtained PersL lifetime from the four smartphones. The PersL lifetime registered for CaS: 0.0005Eu^{2+} with Samsung Galaxy A5(2017), iPhone XR, iPhone 8 plus, and Xiaomi (Redmi Note 4) are 593 ± 9 ms, 586 ± 11 ms, 598 ±13 13 ms, and 589 ±9 ms respectively. The PersL lifetime data shows that it is possible to obtain PersL lifetime using various smartphones. The rest of PersL lifetime data is presented using Samsung Galaxy A5(2017) due to it being available throughout the years of research.

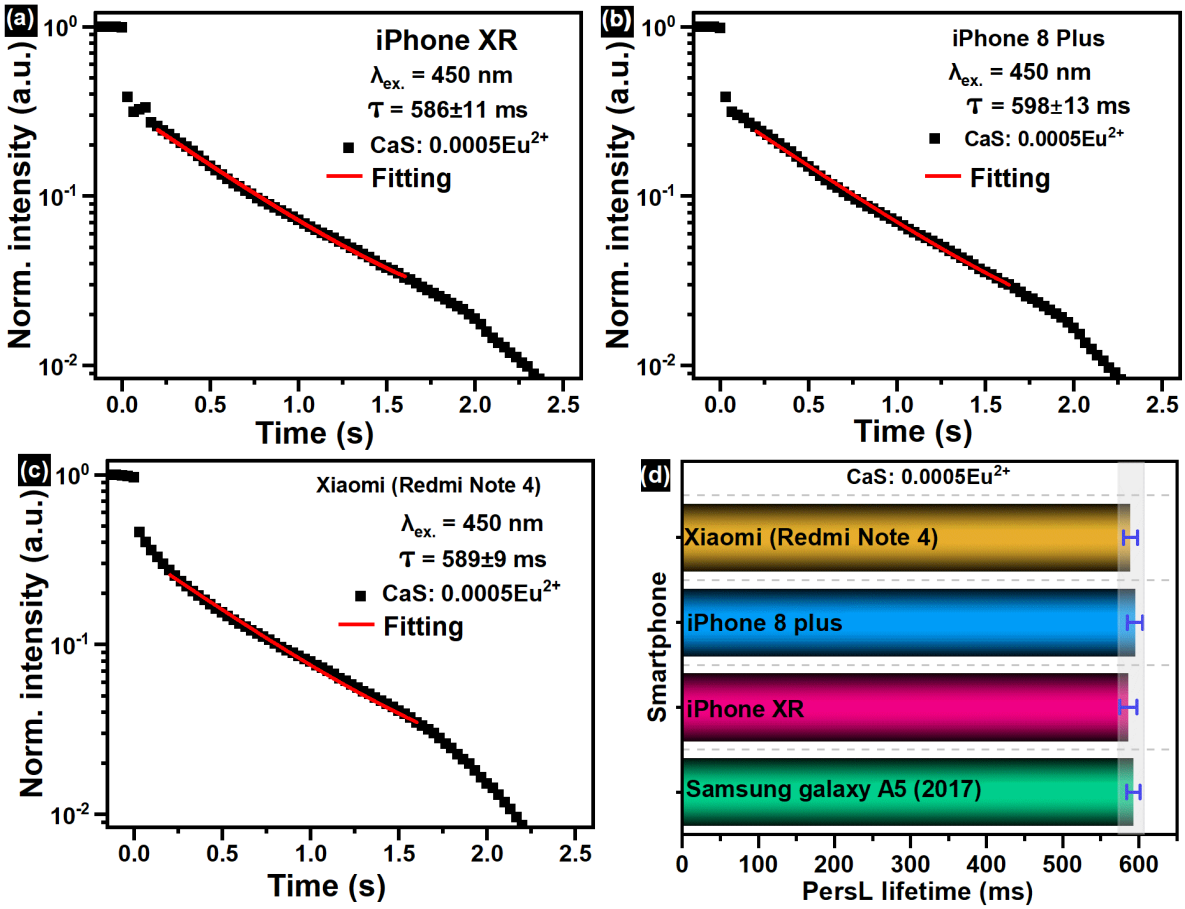

Figure 3.25. PersL lifetime of CaS: 0.001Eu^{2+} under 450 nm derived from videos acquired using: a) Samsung galaxy A5(2017) that registered a PersL lifetime value of 598 ms, b) iPhone XR that registered a PersL lifetime value of 586 ms c) iPhone 8 Plus that registered a PersL lifetime value of 601 ms and d) Xiaomi (Redmi Note 4) that registered a PersL lifetime value of 589 ms.

3.5.4 Boundary Conditions for Smartphone PersL Lifetime

Spectral Range Constraints: Smartphone cameras are designed to mimic the human eye as they are designed for consumer-based applications; therefore, their response is limited to the visible region. Note that although the sensor chip is fabricated using silicon, which can detect up to the NIR region (~1100 nm), an infrared filter (IR) filter usually limits the spectral detection range to between 400-700 nm [41, 199]. As a result, we can only use it to determine the persistent luminescence in the visible region.

Frame Rate Constraints: Most smartphone cameras acquire videos at 30 frames-per-second (30 fps) although it is possible to have 60 fps up to 960 fps but with very compromised video resolution, and also for a limited amount of time [221]. Nevertheless, high frame rate smartphone cameras are not common and as well are expensive. As a result, it is not possible to detect the very short persistent luminescence lifetime (<100 ms) because of two factors: 1) a very short lifetime demands synchronization of the excitation pulse with the detector to ensure that the zero time is exactly the time at which the pulse ceased. Using a smartphone this time has a dead-gate time of 33 ms. 2) The 30 fps also means that the data points captured for a very short fluorescence lifetime would be limited. The 30 fps imposes the lower limit of a PersL lifetime that can be determined using a smartphone at 100 ms [11]. The first few frames of the videos acquired using a smartphone camera immediately after the excitation source is turned off are also not reliable. This is due to the initial saturation of the pixels caused by the scattered light of the excitation. Higher frame rates would enable us to measure the short PersL lifetime in the future. Alternative methods of using smartphones to measure very low lifetime, even up to 22 µs, have also been demonstrated by exploiting the electronic rolling shutter of the CMOS camera together with an integrated microcontroller [222].

Pixel Sensor Size Constraints: Most smartphones feature a small sensor typically 1-2 µm pixel size and therefore their optical resolution is limited [223]. In addition, the pixels are grouped in Bayer configuration further reducing the effective pixel size. For a Bayer series, a pixel is composed of 4 photosites from which 2 are green, 1 is blue and 1 is red [224]. On the contrary, spectrometers have pixel sizes

ten times more than that of an average smartphone. For example, the pixel size of the CCS 200 spectrometer and Avantes spectrometer used in this work is 14 µm, representing up to 6 pixels per nanometer [225]. The anode patterns in PMTs have pixel sizes hundreds of times larger, a typical values range from 2 to 9 mm [226].

The 8-bit Color System Constraint: The images/videos acquired using smartphones cameras with 24-bit RGB images (8-bit for each color) meaning that for each RGB channel there are 255 shades. The 8-bit system constraint is disadvantageous for detecting very bright emissions, as after a certain threshold the channels saturate at 255. This is ideally not a large number compared to distributing emission intensity. However, note that most phosphors lose the majority of the emission that can saturate the sensor immediately after the exciting source is removed.

3.6 Development of Anti-counterfeiting Labels

In this work, several anti-counterfeiting labels were developed to demonstrate the luminescence-based security features that can be utilized from the persistent phosphors. Three label development processes which include inkjet printing, drop-casting, and mold-pattern filling were used.

3.6.1 Inkjet Printing

An inkjet printer Dimatix Materials Printer (Fujifilm, DMP-2831) equipped with a 10 pl cartridge (21 µm nozzle) was used to print anti-counterfeiting labels based on Gd_2O_2S: $0.06Eu^{3+}$, $0.03Ti^{4+}$ or Gd_2O_2S: $0.06Eu^{3+}$, $0.09Ti^{4+}$ persistent phosphors. To print the labels, the printer jetting frequency was set at 5 kHz, the printer drop spacing was set at 20 µm and the print head temperature was set at 40^{o}C. The labels were printed on a glass substrate (Borofloat Schott) which was set at 28 ^{o}C. The inks were developed by first mixing Gd_2O_2S: $0.06Eu^{3+}$,$0.03Ti^{4+}$ or Gd_2O_2S: $0.06Eu^{3+}$,$0.09Ti^{4+}$ at 20 mg/ml in Terpineol and are then ultra-sonicated for 1 h to enhance particle distribution. The inks were then filtered with 10, 5, and then 2.7 µm syringe filters. The final product after filtration was loaded into the cartridge for printing. A two-step pattern deposition is used to print the desired pattern. First, the Gd_2O_2S: $0.06Eu^{3+}$, $0.09Ti^{4+}$ ink was used to print the pattern letters “I M T” (denoting the Institute of Microstructure Technology of the KIT). A

composite pattern of printed dots forming a rectangle is then realized by printing the other dots using Gd_2O_2S: $0.06Eu^{3+}$, $0.03Ti^{4+}$ based ink. The printed patterns are dried at 120 ^oC for 5 minutes.

3.6.2 Drop Casting Deposition

Dynamic anti-counterfeiting labels based on Gd_2O_2S: Eu^{3+}, Ti^{4+}, CaS: Eu^{2+}, SrS: Eu^{2+} and $SrAl_2O_4$: Eu^{2+}, Dy^{3+} (SAED) together with some SAED: CaS: Eu^{2+} and SAED: CaS: Eu^{2+} blends are drop-casted in glass slides to make anti-counterfeiting labels. The suspensions were created by first dissolving 5 grams of polyvinylpyrrolidone (PVP) in a 20 ml mixture of ethanol and water (ethanol: deionized water at 30:70 wt%) and stirring with a magnetic stirrer for 1 h until the fluid is clear. This solution was then used as the binding agent to the phosphors during the casting. Appropriate amounts of the Gd_2O_2S: Eu^{3+}, Ti^{4+}, blends of SAED (820): CaS: $0.001Eu^{2+}$ (95:5 wt%) and SAED (900): CaS: $0.008Eu^{2+}$ were mixed with the PVP solution to form the casting suspension. For the SAED: CaS: Eu^{2+} and SAED: CaS: Eu^{2+} blends, a typical suspension was prepared as follows. One gram of the blended phosphor, SAED (820): CaS: $0.001Eu^{2+}$(95:5 wt%) was placed in the 15 ml of dissolved PVP and magnetically stirred for 30 minutes at 50 ^oC until the mixture gained homogeneity. For the SAED (900): CaS: $0.008Eu^{2+}$ a typical 5 ml suspension was prepared by adding to it 0.33 grams of the blend and magnetically stirred for 30 minutes to obtain a homogeneous mixture. The blended phosphors were then drop cast freehand on glass slides that are maintained at 50 - 60 ^oC on hot plates to speed up the drying process.

3.6.3 Seven-Segment Display Mold

Four-digit seven-segment displays made of PMMA sheets were developed in-house using an ultra-precision milling machine. The display numbers were designed using SURFCAM traditional software. The segment dimensions for all the segments were 10 mm by 3 mm and each segment had a depth of 0.5 mm. The edges of each segment are maintained at 90^o, and a boundary of 0.5 mm is maintained between each segment. To demonstrate anti-counterfeiting using the seven-segment display, the selected phosphors based on Gd_2O_2S: xEu^{3+},yTi^{4+},

and SAED: CaS: xEu^{2+} and SAED: SrS: xEu^{2+} (95:5 wt%) blended phosphors embedded in the segments to form the display segment.

3.6.4 Optical Barcode Development

Optical barcodes based on SAED, CaS: Eu^{2+}, SrS: Eu^{2+} and SAED: CaS: xEu^{2+} and SAED: SrS: xEu^{2+} (95:5 wt %) blended phosphors were developed by filling 1 mm diameter glass tubes with the phosphors and respective phosphor blends. The ends of each of the filled glass tubes were sealed using a sealant after filling. They were then aligned in a 1 mm spacing by fixing a blank glass tube in-between them in glue-taped black paper to form the dynamic barcodes.

4

Smartphone-Based Luminescence Thermometry

This chapter presents the results of the use of a smartphone to determine the temperature of a 2D surface via the PersL of $Gd_2O_2S:Eu^{3+}$. It is based on the following first author publication and a submitted patent:

***Katumo, N.,** Gao, G., Laufer, F., Richards, B. S., & Howard, I. A. (2020). smartphone-based luminescent thermometry via temperature-sensitive delayed fluorescence from $Gd_2O_2S:Eu^{3+}$. Advanced Optical Materials, 8(19), 2000507 [8].*

***Katumo, N.,** Howard I.A., Gao G., Busko D., Turshatov, A., Richards B.S., 'Photonic markers enabling temperature sensing and security marking using low frame rate cameras.' Patent application No.EP3842505A1 (Patent Pending) [227].*

The idea of the publications was conceived by the author, Ian. A. Howard and Bryce S. Richards after the first author realized that the intense bright emission

from $Gd_2O_2S: Eu^{3+}$ could be video-recorded using a smartphone camera and the PersL lifetime could be derived by analyzing the video. The phosphors were prepared by the first author under the guidance of Guojun Gao, who further undertook morphological studies and X-ray diffraction together with the first author. Dmitry Busko, Ian Howard, and Felix Laufer cooperatively worked with the first author in setting up measurement systems for determining the PLQY and time-resolved photoluminescence (PL) measurement. The steady-state and time-resolved measurements at various temperature variations were done by the author. All the authors helped in interpreting the results and developing the text for the publications.

4.1 Luminescence Thermometers

Non-contact-based luminescence thermometers are important in precisely determining the temperature of hard-to-access locations in biological and analytical systems with nano/micro-sized dimensions [7, 8, 50]. To spatially map the temperature in the submicron scale, or the distribution of temperature on a surface, camera-based imaging techniques can reliably be used to generate thermographic images. On the contrary, contact-based thermometers are not able to make accurate and precise temperature readings when the spatial resolution decreases to the sub-micron scale [7, 8, 50, 174].

The major approaches to determining the temperature via luminescence are the fluorescence intensity ratio (FIR) of two thermally coupled transitions and the emission lifetime method as they are considered self-referencing techniques [8, 228]. The FIR method is however sensitive to environmental variables such as background radiation and scattered light.[5] These shortcomings can be easily overcome in a lab setting using a microscope setup. But such a setting is not easily achievable in everyday situations [8, 227]. On the contrary, the emission lifetime method is virtually unaffected by environmental variables. Regardless, the FIR method has been widely used as compared to the emission lifetime method as most of the existing material systems have lifetimes in the nano-micro regime whose acquisition requires expensive high-speed imaging equipment and infrastructure. This challenge can be solved by developing material systems that have long PersL lifetimes (milliseconds to seconds).

Herein, we present the results of a Gd_2O_2S: Eu^{3+} phosphor synthesized with long enough PersL lifetimes that can be used to produce 2D temperature images. The PersL lifetime can even be captured by a 30 fps camera, such as those found in ordinary smartphones. Most smartphone cameras are based on time-gated CMOS sensors. By capturing the PersL of the phosphor following excitation, it is possible to reconstruct the PersL decay in the region of interest (ROI), which is usually the region of phosphor emission. Now, by analyzing the PersL lifetime reconstructed from the smartphone-acquired thermal images of a surface coated with the Gd_2O_2S: Eu^{3+} phosphor, it is possible to determine the temperature in the range 270-338 K with a precision of more than 2 K. This result acts as a proof-of-principle indicating that the temperature can be determined using a smartphone even in bright background illuminance up to 1500 lm/m^2, further emphasizing the stability of the measurements in the presence of background light.

4.2 Photophysical Properties of Gd_2O_2S: Eu^{3+} Phosphor

First, the photophysical properties of Gd_2O_2S: Eu^{3+} phosphors were investigated as part of the phosphor optimization process via diffuse reflectance analysis, PL excitation, emission spectra, and PLQY. Figure 4.1 shows the DRS of Gd_2O_2S: $x$$Eu^{3+}$ phosphor (for x = 0 - 0.13 mol). The un-doped sample shows deep UV absorption with a cut-off at ~269 nm that coincides with the 4.6 eV bandgap of Gd_2O_2S. When Gd_2O_2S is doped with Eu^{3+} ions, a CTB representing enhanced absorption develops in the 200 – 400 nm range.

The deep UV absorption is usually due to the host excitation by charge transfer from $O^{2-}\rightarrow Eu^{3+}$ with minor contributions from $Gd^{3+}\rightarrow Eu^{3+}$ and $S^{2-}\rightarrow Eu^{3+}$ energy transfers [229, 230]. The $S^{2-}\rightarrow Eu^{3+}$ charge transfer dominates beyond 269 nm [230]. The increase in Eu^{3+} doping continuously increases the absorption of the phosphor material. Apart from this CTB, other weak and narrow bands of absorption are also observed in the spectra from the 390 – 600 nm region. These narrowband peaks are discussed in the next paragraph. These spectroscopic absorption bands are best described from the PL excitation (PLE) spectra taken from the 626 nm emission of Gd_2O_2S: Eu^{3+} shown in Figure 4.2. The PLE spectra show the broadband CTB from 250 – 400 nm that arises due to the O^{2-}/S^{2-}/Gd^{3+} → Eu^{3+} energy transfer [229, 230].

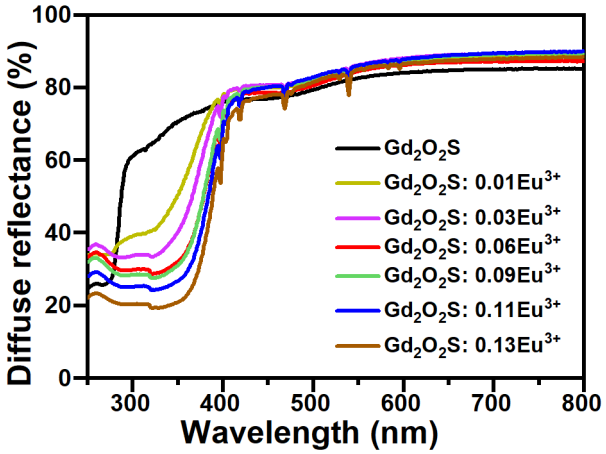

Figure 4.1. The diffuse reflectance spectrum of $Gd_2O_2S:xEu^{3+}$ phosphors showing broadband absorption due to the CTB (200 - 400 nm). The absorption onset of the un-doped sample at 269 nm corresponds to a bandgap of 4.6 eV. Adapted from Katumo et al. [8]. CC BY-ND 4.0 License.

Apart from the CTB, other narrowband transitions that correspond to $^7F_{0,1}\rightarrow{}^5D_3$, $^5L_6$ (396 – 418 nm), $^7F_{0,1}\rightarrow{}^7D_2$ (468 nm), and $^7F_{0,1}\rightarrow{}^7D_0$ (538 nm) transitions of the Eu^{3+} are also observed. These narrow band absorption corresponds to direct Eu^{3+} excitation and have weak absorption compared to the CTB whose transitions are allowed by the Larpote selection rule.

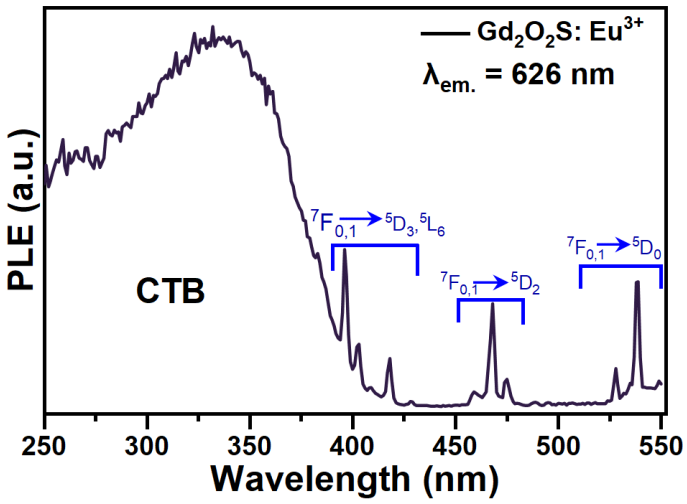

Figure 4.2. The PL excitation spectra for Gd_2O_2S: Eu^{3+} (tracked at 626 nm). The spectrum consists of a CTB in the range 250 - 400 nm due to $O^{2-}/S^{2-}/Gd^{3+}\rightarrow Eu^{3+}$ energy transfer and sharp bands common in Eu^{3+} intra-configurational transitions. These bands correspond to $^7F_{0,1}\rightarrow{}^5D_3$, $^5L_6$ (396 nm), $^7F_{0,1}\rightarrow{}^7D_2$ (468 nm) and $^7F_{0,1}\rightarrow{}^7D_0$ (538 nm), respectively.

The Eu^{3+} transitions in the UV region also overlap with the strong CTB absorption and therefore seem weak relative to the strong CTB absorption [21]. The CTB excitation is therefore preferred for sensitization of Eu^{3+} as it acts as an antenna that absorbs light and then efficiently transfers it to the Eu^{3+} emitter [21]. Upon excitation of the Gd_2O_2S: $0.06Eu^{3+}$ phosphors in the CTB with 375 nm LED, the $^5D_0 \rightarrow ^7F_j$ (j = 0, 1, 2, and 4) transitions of Eu^{3+} are observed as shown in Figure 4.3. The emission spectrum is dominated by the hypersensitive $^5D_0 \rightarrow ^7F_2$ ED transition of the Eu^{3+} centered at 626 nm with a shoulder at 616 nm. This pronounced transition was responsible for the typical red emission observed following excitation of the phosphor in the CTB. The $^5D_0 \rightarrow ^7F_4$ ED transition of the Eu^{3+} centered at 704 nm is also observed as well as the $^5D_0 \rightarrow ^7F_0$ ED and $^5D_0 \rightarrow ^7F_1$ MD transitions centered at 584 nm and 596 nm respectively.

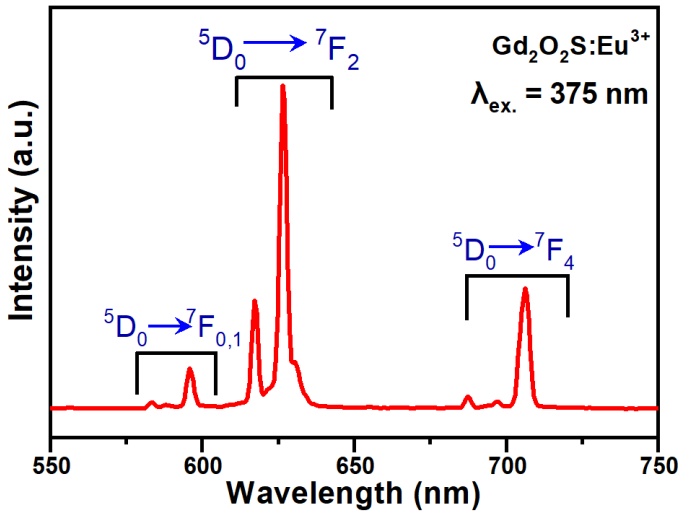

Figure 4.3. The PL emission spectra of Gd_2O_2S: 0.06Eu3+ under 375 nm excitation at room temperature. The emission spectra consists of 5D0→7Fj (for j = 0, 1, and 4) Eu3+ transitions with the dominant emission 5D0→7F2 (626 nm) with a left shoulder at 616 nm. The other emission band centers are $^5D_0 \rightarrow ^7F_{0,1}$ (595 nm) and $^5D_0 \rightarrow ^7F_4$ (704 nm). Reproduced from Katumo et al. [8]*. CC BY-ND 4.0 License.*

The PLQY of the Gd_2O_2S: xEu^{3+} (for x = 0.01 - 0.13) phosphors under 375 nm excitation at room temperature are shown in Figure 4.4. The PLQY increases with an increase in Eu^{3+} doping from 38 ± 1% for Gd_2O_2S: $0.01Eu^{3+}$ to 65 ± 1% for

Gd_2O_2S: $0.06Eu^{3+}$. Further Eu^{3+} doping leads to a decrease in the PLQY with the Gd_2O_2S: $0.13Eu^{3+}$ registering a PLQY value of 32 ± 1%.

The initial increase in PLQY is due to the optimization of the formation of the optimal radial distance of Eu^{3+} emitting centers to the absorbing matrix in the host. As the doping concentration of Eu^{3+} increases, the distances decrease, leading to efficient energy transfer of the absorbed energy to it. However, this happens until it reaches a point where Eu ↔ Eu self-quenching (concentration quenching) sets in. In this case, beyond $0.06Eu^{3+}$ doping, the concentration quenching effects (non-radiative de-excitation) drastically reduce the PLQY. The experimentally found optimal doping concentration leading to maximum PLQY is in agreement with previous reports on Gd_2O_2S: Eu^{3+} phosphors [229-231]. Similar results have also been reported for $Ca_{19}Mg_2(PO_4)_{14}$: $0.06Eu^{3+}$ where $0.06Eu^{3+}$ is found to be the optimal concentration [232]. The Gd_2O_2S: $0.06Eu^{3+}$ sample was therefore selected for thermometry, as it not only has the highest PLQY but also, the longest PersL [8].

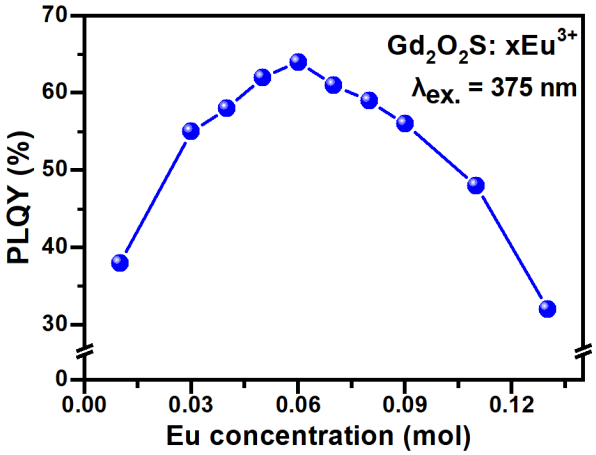

Figure 4.4. The photoluminescence quantum yield (PLQY) parameters of the Gd_2O_2S: xEu^{3+} phosphor (x = 0.01 - 0.13) under 375 nm excitation. The line is used simply as a guide for the eye. Adapted from Katumo et al. [8]. CC BY-ND 4.0 License.

4.2.1 Temperature-Dependent Charge Transfer Model

The position of the CTB and its luminescence-quenching behavior is strongly dependent on temperature [21]. At a given temperature, excitations to the CTB

rapidly thermalize to the bottom of the charge transfer states and then feed the 4f states via resonance crossovers. To develop a temperature-dependent charge transfer (TDCT) model, first, the effect of temperature on the integrated emission of Gd_2O_2S: $0.06Eu^{3+}$ under 470 nm, 375 nm, and 300 nm excitations were evaluated [8]. Figure 4.5 shows the normalized integrated emission of $^5D_0$ emissions of Gd_2O_2S: $0.06Eu^{3+}$ into the 4f states in the 100 - 900 K temperature range. For 470 nm and 375 nm excitation, the integral emission of Gd_2O_2S: $0.06Eu^{3+}$ increases as the temperature was increases from 100 K to 373 K, respectively. Further increase in temperature leads to a decrease in the integrated emission due to thermal quenching.

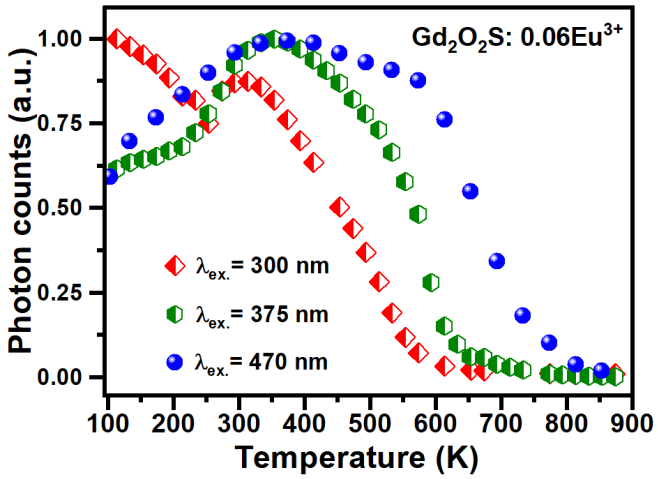

Figure 4.5. Normalized temperature dependence of the integrated $^5D_0$ emissions of Gd_2O_2S: $0.06Eu^{3+}$ into the 4f states under various excitation wavelengths for temperatures in the range 100 – 900 K. Adapted from Katumo et al. [8]. CC BY-ND 4.0 License.

The scenario under 300 nm excitation is a little different, as initially, the integrated emission decreases as the temperature increase up to 253 K and then begins to increase and reaches a maximum at 313 K. Further increase leads to a decline in the integrated emission. The initial decrease in integrated emission under 300 nm excitation up to 253 K shows the distinct Arrhenius behavior. We hypothesize that the initial decrease is due to resonances of the charge transfer states feeding higher-level Eu^{3+} states efficiently as compared to the feeding from the thermalized electrons in the conical base of the CTB to the ^5D_j (j= 0-2) states of Eu^{3+}. The subsequent increase in integrated emission is therefore due to the CTB being in

resonance with the ^5D_j (j= 0-2) states of Eu^{3+}, making this feeding the dominant mechanism above 253 K. A similar observation, for which the CTB becomes the dominant relaxation channel above 270 K has also been reported for Eu $(thd)_3$ crystal [233]. The increase in integrated emission under all excitation conditions can be thus attributed to enhanced feeding of the ^5D_j (j = 0 - 2) emitting states by the CTB as it traverses them. In addition, it is expected that if the CTB falls below the thermal activation energy of the $^5D_0$state, it quenches the emission to the ground state.

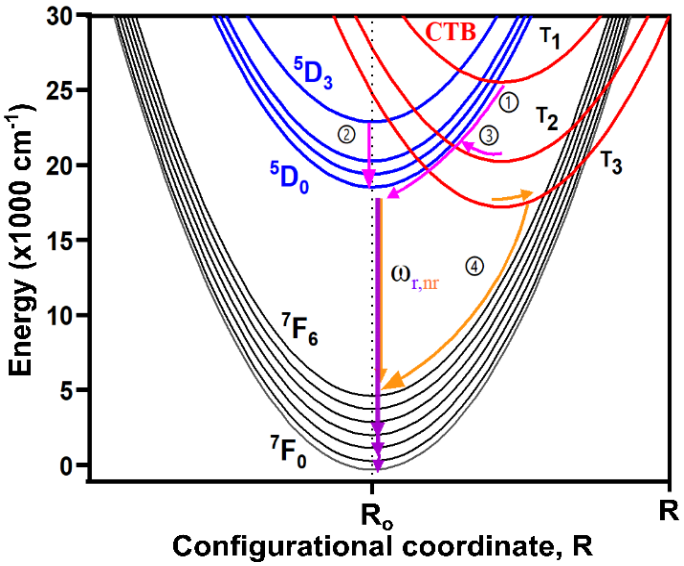

Figure 4.6. A temperature-dependent charge transfer (TDCT) model indicating the thermal shift of the CTB in Gd_2O_2S: Eu^{3+} as the temperature increases. The intra-configurational coordinates are of the Eu^{3+} ion up to the $^5D_3$ state. As the temperature increases fromT_1 to T_3, such that $T_1 < T_2 < T_3$, the CTB shifts to lower energy. The notations ①,② and ③denote the channels through which the $^5D_0$ state is fed through the CTB as it shifts due to change in temperature. The notation ④ denotes the quenching pathway that dominates at higher temperatures when the CTB is at lower energies relative to the $^5D_0$ state. The photons that feed the $^5D_0$ state of Eu^{3+} in this configuration from any of the possible channels can either relax radiatively or non-radiatively to the ^7F_j (j = 0 - 4)state via the $\omega_{r,nr}$ relaxation channel. Reproduced from Katumo et al. [8]. CC BY-ND 4.0 License.

The atypical behavior of the temperature-dependent emission can fully be described using a temperature-dependent charge transfer (TDCT) model that explains the observed trend in the integrated emission as a function of temperature as shown in Figure 4.6 [8]. At low temperatures, the location of the CTB is at a high-energy position (~T_1) and hence its excitation rapidly settles to the base followed by instantaneous feeding of the $^5D_0$ state via ① and ②. These two channels feed the $^5D_0$ efficiently and therefore at lower temperatures no PersL is observed. As the temperature increases, the CTB lowers to the ~T_2 position whereupon excitation of the $^5D_0$ state is either rapidly fed via ① and ② or a delayed feed through pathway ③. The delayed feed via pathway ③ leads to the observed PersL in the 273 k regime. In this regime, the conical base of the CBT acts as a temporal-photonic battery that slowly feeds the $^5D_0$ state of Eu^{3+} leading to the observed PersL. The observed PersL then begins to tail off as the temperature is further increased, due to the increased feeding efficiency of the $^5D_0$ state by the CTB established at resonance energies. At the same time, due to the resonance of the conical base with the $^5D_0$ state, the instantaneous PL intensity increases. Further increase in temperature shifts the CTB to ~T_3, a position that is lower in energy than the emitting $^5D_0$ state of Eu^{3+}. In this position, excitations either feed the $^5D_0$ state through ② or are quenched to the ^7F_j ground states via ④. The electrons fed to the $^5D_0$ state from all the possible channels relay to the ground state either radiatively or non-radiatively ($\omega_{r,nr}$) to the ^7F_j ground states. This model further explains why the dominant quenching mechanism at a higher temperature is via the CTB for Gd_2O_2S: Eu^{3+}. To summarize, the model explains the initial increase in instantaneous PL emission and build-up of PersL as the temperature is increased as the CTB traverses the $^5D_0$ state, before providing a route needing lower energy, for quenching to the ^7F_j ground states [8].

The TDCT model sufficiently explains the sustained integrated emission of Gd_2O_2S: Eu^{3+} under 470 nm excitation relative to the other excitations shown in Figure 4.5. The sustained integrated emission is due to: (1) the majority of the 470 nm (21276 cm^{-1}) excitation photons directly feeding the ^5D_j (j = 0, 1, 2, and 3) states of the Eu^{3+} state whose thermal quenching is via the ω_{nr} channel shown in Figure 4.6. (2) When the CTB is around the T_2 position and under the 470 nm excitation, the CTB is in resonance with the $^5D_0$ state and thus crossover feeding

is enhanced over a large regime of temperature. Similar phenomena of thermal quenching via CTB have been presented for various materials [234-236].

4.2.2 The PersL Lifetime of $Gd_2O_2S: Eu^{3+}$ using a Smartphone

Figure 4.7a shows the PersL of $Gd_2O_2S: Eu^{3+}$ at room temperature measured using single-photon counting and multichannel scaling together with the PersL lifetime data acquired using a smartphone (Samsung Galaxy, A5(2017)). For the PersL lifetime determined from the analysis of the smartphone acquired video, the persistent decay was acquired in the following fashion: For each frame of the red channel, an ROI in which the sample emission occurs was selected and all the pixels were averaged and then time-mapped to the relevant frame with respect to the 30 fps rate. The computed intensity values for the PersL decay plotted in the time scale are presented in that data, extracted from the video in Figure 4.7a. In the same plot, the PersL lifetime measurement using the MCS technique (photon counting) is also shown for comparison. To define the PersL lifetime fitting region, several times of interest, for which the PersL lifetime region is fitted, are also named in Figure 4.7a. The first frame, after which the 375 nm UV excitation is turned off, is found by searching the maximum difference between the subsequent two frames.

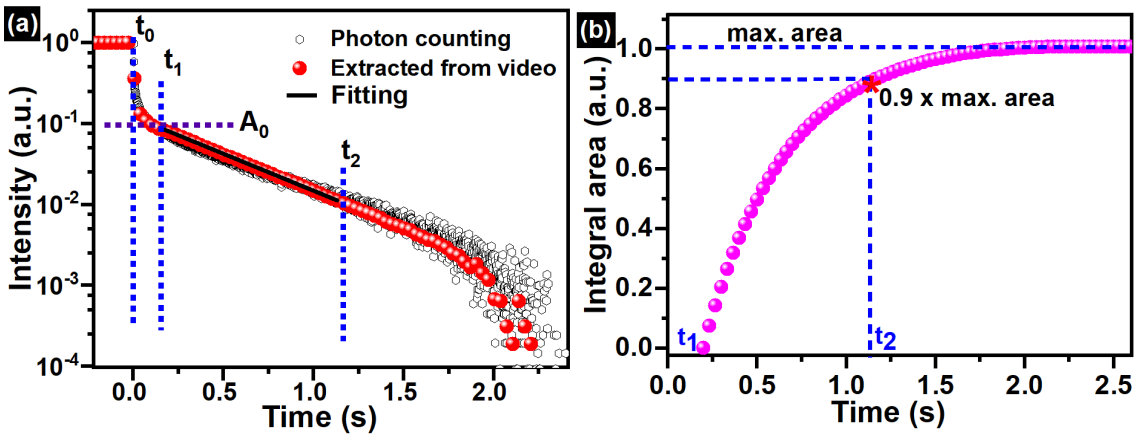

Figure 4.7. a) The delayed luminescence lifetime of $Gd_2O_2S: 0.06Eu^{3+}$ at 293 K extracted from a smartphone video compared to reference data taken by conventional single-photon counting with a multichannel scaler. b) Integrated area of the delayed emission (starting from 221 ms) as a function of time. The time t_2, is identified by computing 90 % of the maximum integrated area.

This frame was labeled t_0 and represents time zero. The first boundary value t_1 is a constant offset from t_0 and was universally set to 221 ms. This offset allowed for the settling of the instrument response of the camera system from the rapid decrease in the prompt response. The second value, t_2 is the time at which 90% of the total delayed emission has been collected. This value, therefore, varies for every level of Eu^{3+} doping and also every PersL lifetime computed at different temperatures. Systematically, the point t_2 is identified by computing the integral emission starting from t_1 and then finding the 90% position relative to the maximum as shown in the case of Gd_2O_2S: $0.06Eu^{3+}$ at room temperature. The procedure is then repeated for all the other samples at room temperature and various temperatures during temperature mapping. The PersL lifetime(s) are fitted using a single exponential function shown in equation 4.1.

$$I = A \times \exp\left(\frac{-t}{\tau}\right) \tag{4.1}$$

where A is the amplitude and τ the lifetime. At 293 K the PersL lifetime extracted from the smartphone video-recorded PL emission was 475 ± 13 ms while the lifetime determined using the single-photon counting, MCS process was 484 ± 4 ms. The PersL lifetime extracted from the smartphone video in the fitting region thus had an uncertainty of roughly a factor of three greater than the one determined via the single-photon counting process. The relative uncertainty of the PersL lifetime measurements taken using the smartphone was ~3% at room temperature. The PersL lifetime decay curves of Gd_2O_2S: xEu^{3+} (x = 0.01 – 0.13 mol) fitted in the determined ROI are shown in Figure 4.8. By visual inspection, the PersL lifetime first increases with an increase in Eu^{3+} doping up to $0.06Eu^{3+}$, as shown in Figure 4.8a. Further increase in Eu^{3+} doping beyond 0.06 Eu^{3+} leads to a gradual decrease in the PersL lifetime as shown in Figure 4.8b.

A summary of the PersL lifetime values for the various Eu^{3+} doping concentrations at room temperature (~293 K) alongside the already reported PLQY is shown in Figure 4.8c. The PersL lifetime increases from 220 ± 5 ms to 475 ±13 ms as the Eu^{3+} doping is increased from 0.01 to 0.06 mol. Further increase in Eu^{3+} doping leads to a gradual decrease of the PersL lifetime with Gd_2O_2S: 0.13 Eu^{3+} registering a PersL lifetime of 150 ± 7 ms. Note that, as also shown in Figure 4.8c

the PLQY values also have a similar trend in response to the Eu^{3+} doping. The initial increase is usually attributed to an optimization step in which an initial increase in Eu^{3+} ions leads to an increase in PersL lifetime and PLQY, as their doping concentration is increased up to an optimum point beyond which Eu ↔ Eu quenching starts to dominate the relaxation process. This is a characteristic phenomenon for which a CTB is involved in the transfer and emission via an Ln^{3+} emitter and is sometimes referred to as self-quenching [237]. The Gd_2O_2S: $0.06Eu^{3+}$ thus has the best PLQY and highest PersL lifetime (see Figure 4.8c) and is therefore selected and used for smartphone-based luminescence thermometry applications.

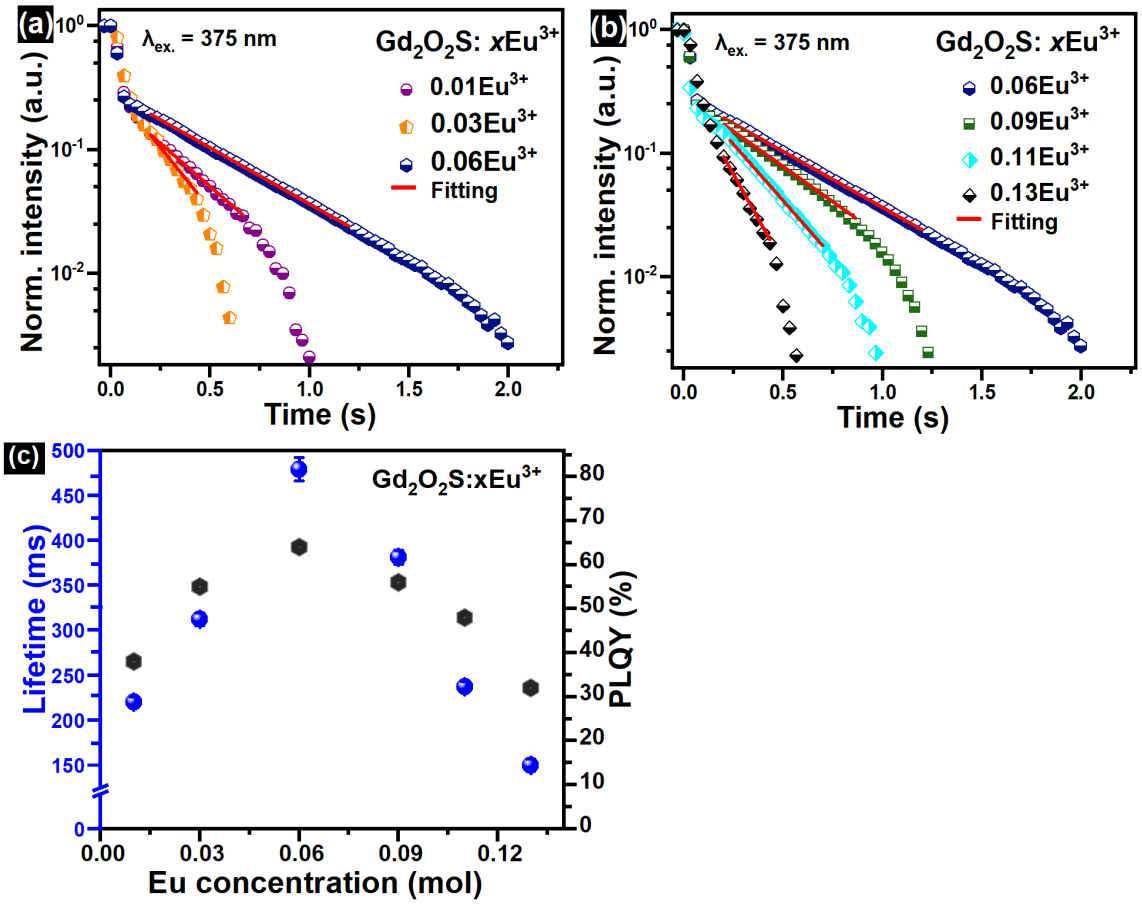

Figure 4.8. PersL decay curves of Gd_2O_2S: xEu^{3+} for a) x = 0.01, 0.03 and 0.06 mol and b) x = 0.06, 0.09, 0.11, and 0.13 mol following 375 nm excitation. c) The PersL lifetime and PLQY values of Gd_2O_2S: x Eu^{3+} for x = 0.01- 0.13 mol.

4.3 Smartphone-Based PersL Thermometry using Gd_2O_2S: Eu^{3+}

The effect of temperature in the 273 to 333 K-temperature range on the PersL of Gd_2O_2S: $0.06Eu^{3+}$ is illustrated in Figure 4.9. Zero time denotes the time at which the excitation source (375 nm LED) was switched off. At lower temperatures, the PersL is observable by the naked eye even after 1.2 s. The emission fades more quickly at higher temperatures. As the temperature of a phosphor is increased, the non-radiative recombination rates increase leading to a decrease in PLQY and lifetime.

However, as already discussed, the PersL of Gd_2O_2S: Eu^{3+} phosphor relies on the thermal promotion of excitons held in a long-lived CTB to the $^5D_0$ state of the Eu^{3+} ion. As such, both the CTB-mediated radiative and non-radiative pathways are temperature sensitive. As a result, the PersL decay behavior depends on the location of the CTB, the emitting $^5D_0$ state of Eu^{3+}, and the influence of activation energies. As a result, the PLQY is reduced less than it would be due to the temperature contribution towards radiative relaxation via the CTB. Ideally, the PLQY reduces as the temperature is increased in most phosphors due to the non-radiative rates of activation. The phosphors, therefore, remain bright enough for PersL lifetime to be measured from the analysis of videos acquired with a smartphone.

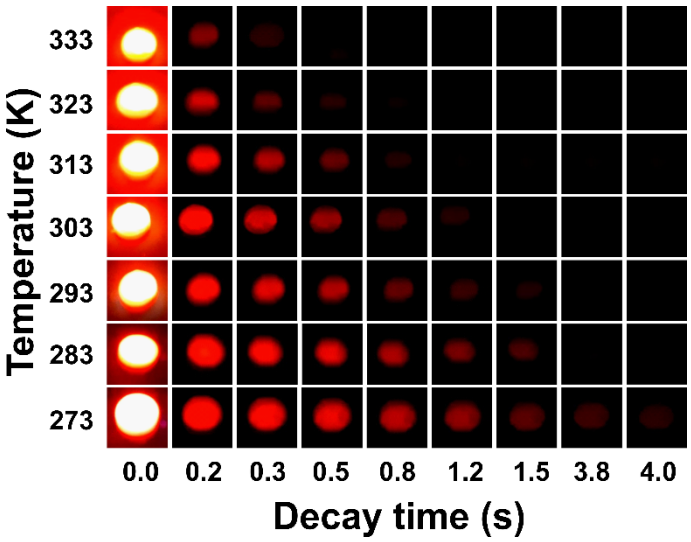

Figure 4.9. Individual frames extracted from videos of Gd_2O_2S: $0.06Eu^{3+}$ as a function of temperature. Reproduced from Katumo et al. [8]. CC BY-ND 4.0 License.

The PersL lifetime data of the temperature-dependent emission of Gd_2O_2S: $0.06Eu^{3+}$ extracted from the videos acquired with a smartphone is shown in Figure 4.10. The PersL lifetime data follows the same trend as the decay observed in the frames shown in Figure 4.9. The PersL lifetime decreases as the temperature increases from 273 to 333 K.

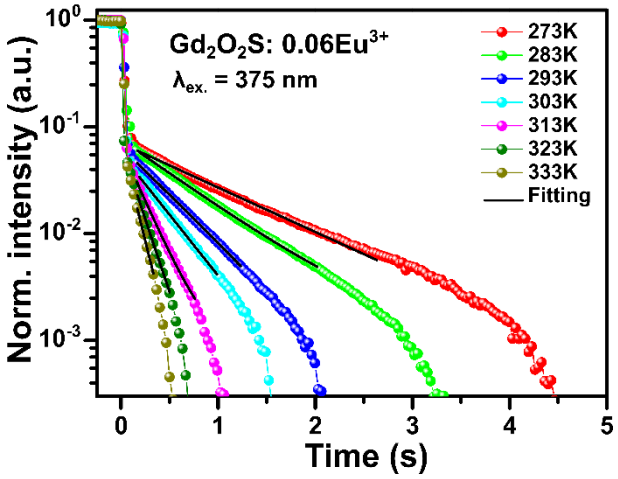

Figure 4.10. Emission intensity (normalized) as a function of time extracted from smartphone acquired videos of emission of Gd_2O_2S: $0.06Eu^{3+}$after pulsed UV LED excitation (375 nm) for the 273-333 K temperature range. Reproduced from Katumo et al. [8]. CC BY-ND 4.0 License.

Again, by fitting the PersL lifetime in the ROI analogous to the one in Figure 4.7b using equation 4.1, we obtain the PersL lifetime as a function of temperature as shown in Figure 4.11. At 273 K, the PersL lifetime registered by the phosphor from the analysis of the smartphone-acquired videos was 1107± 29 ms. The PersL lifetime gradually reduced an increase in temperature with the PersL lifetime registered at 333 K being 115 ± 7 ms.

The plot in Figure 4.11 forms the fundamental basis under which the PersL lifetime thermometry is established, as it provides the calibration curve from which other lifetimes can be mapped and translated to temperature values. To obtain the calibration curve, the PersL lifetime shown in Figure 4.11 was fitted using a single exponential equation of the form:

$$\tau(T) = A * \exp\left(\frac{E_a}{k_B T}\right) = 0.00439 * \exp\left(\frac{3390}{T}\right) \quad (4.2)$$

where k_B is the Boltzmann constant, E_a is the apparent activation energy for the radiative and non-radiative rate and was determined to be 0.29 ± 0.01 eV, T is the absolute temperature in Kelvin, and A is a prefactor constant that was found to be (4±1) $\times 10^{-3}$.

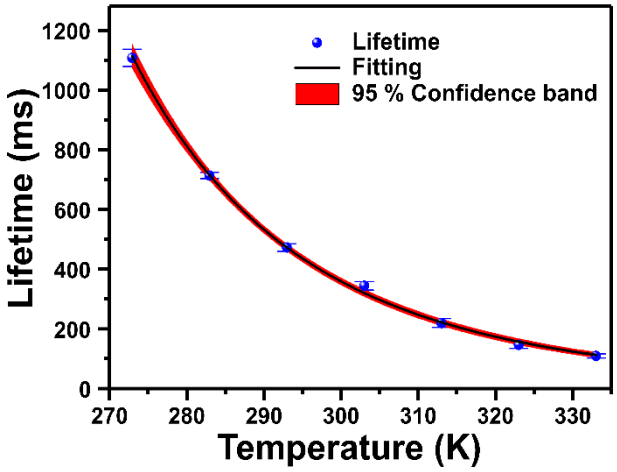

Figure 4.11. Variation of the PersL lifetime as a function of temperature in the 273 - 333 K range for $Gd_2O_2S:Eu^{3+}$. Reproduced from Katumo et al. [8]. CC BY-ND 4.0 License.

From equation 4.2, it is possible to calculate the temperature of the surface by obtaining the PersL lifetime indicative value and mapping it to the representative temperature. Alternatively, by moving T to the right-hand side of equation 4.2, one has to just feed in the obtained PersL lifetime in the equation to know the temperature in equation 4.3:

$$T = \frac{E_a}{k_B(Ln(\tau) - Ln(A))} = \frac{0.29}{k_B(Ln(\tau) - Ln(4.4 \times 10^{-3}))} \quad (4.3)$$

Note that for this work, equations 4.2 and 4.3 provide the calibration curve of the thermometer, other equations are also used by other authors. Ideally, the equation that best fits the data is used and as such even straight-line equations have been in the work of Gharouela *et al*. using $M^{I}(Na, Li, K)Pr(PO_3)_4$ and PrP_5O_{14} hosts

doped with praseodymium [238]. Other authors have also used the modified Arrhenius equation to fit the lifetimes as a function of temperature [233, 239-241].

4.3.1 Thermometer Figure-of-Merit

Several figures of merit are used to evaluate the performance and characteristics of the luminescence thermometers to provide a basis for comparing them with existing results [50]. These figures of merit include the absolute and relative sensitivity, the temperature range and temperature resolution, temperature acquisition time, and reproducibility test. From the PersL lifetime data, the thermometer could accurately map temperature in the 270 - 338 K range. The temperature acquisition time for lifetime measurements is dictated by the amount of time for which the lifetime is acquired. As a result, a period of 5 s, including the excitation and PersL decay acquisition using a smartphone is a realistic approximation for the longest PersL lifetime at 273 K. This time would decrease as the temperature increases, due to a decrease in the PersL decay. The computation of the acquired data should ideally be instantaneous compared to the data acquisition time. Due to the longer data acquisition times compared to the LIR methods, the lifetime-based thermometry approaches fall short of dynamic temperature mapping [50, 242].

Figure 4.12 shows the dependence of relative sensitivity (Sr) as a function of temperature in the 273 – 333 K range. The relative sensitivity values are calculated according to equation 4.4:

$$S_r = \left| \frac{1}{\tau_T} * \frac{\partial(\tau_T)}{\partial T} \right| * 100\% = \frac{E_a}{k_B T^2} * 100\% \quad (4.4)$$

The parameters used in equation 4.4 are derived from fitting equation 4.2 and the specific lifetimes that are determined from equation 4.1. The obtained values decrease from 4.5% K^{-1} at 273 K to 3.1%K^{-1} at 333 K. The relative sensitivity is highest for the low temperatures due to the large gradient change in the PersL lifetime with small temperature changes compared to high temperatures. To put this in context, a 20 ms change in PersL lifetime at 273 K translates to a 0.5 K change while the same 20 ms change in PersL lifetime at 320 K translates to a 3.5 K change. The higher the relative sensitivity the better the luminescence

thermometer. Therefore, it is desirable to use luminescence thermometers in thermal ranges for which they exhibit the highest relative sensitivities.

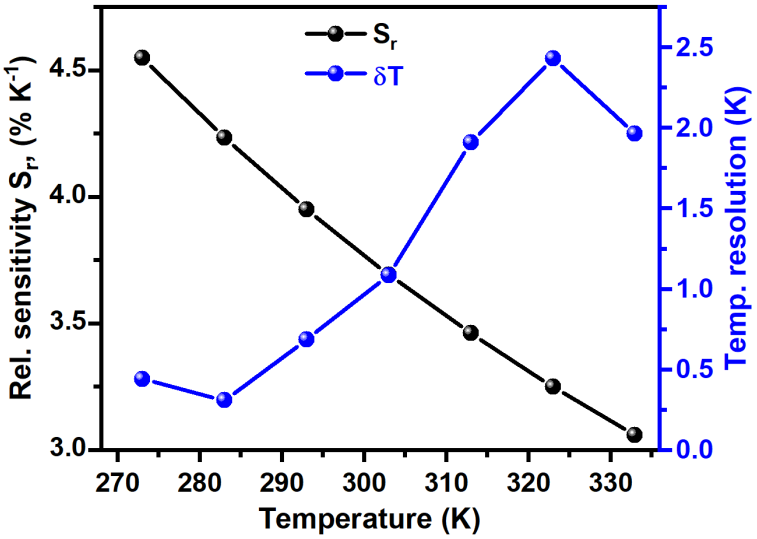

Figure 4.12. The relative sensitivity and temperature resolution of the luminescence thermometer. Reproduced from Katumo et al. [8]. CC BY-ND 4.0 License.

The temperature resolution (δT) was computed using equation 4.5:

$$\delta T = \frac{1}{S_r} \times \frac{\delta\tau}{\tau} \tag{4.5}$$

Where $\delta\tau/\tau$ is the relative standard error given by;

$$\frac{\delta\tau}{\tau} = \left| \frac{\sqrt{\frac{\sum(\tau_i - \tau_{mean})^2}{N}}}{\tau_{(T)}} \right| * 100\% \tag{4.6}$$

The relative standard error for five measurements was determined to be 2.6, 1.4, 2.7, 4.0, 6.7, 7.9, and 6.0% for 273, 283, 293, 303, 313, 323, and 333 K respectively. For temperatures below 300 K, the thermometer could resolve the temperature to more than 1 K but the resolution decreases to 2.5 K at around 333 K. The relatively poor resolution in the 333 K is due to the short PersL lifetimes for these temperatures that are at the boundary limit of the 30 fps smartphone cameras. A practical limit of 100 ms for the PersL lifetime detection using a smartphone video camera was established. This PersL lifetime value translated to

a temperature of 338 K for our phosphor. For temperatures higher than 338 K, the PersL lifetime would fall below 100 ms making it hard to accurately determine the PersL lifetime from a 30 fps smartphone camera.

The maximum relative sensitivity of 4.5% K^{-1} at 273 K is comparable with other results obtained in this temperature regime. Some of the Eu^{3+} based thermometers with comparable relative sensitivities include SrY_2O_4: Eu^{3+} with S_r of 5.55% K^{-1} at 473K, [243] ZrO_2: Eu^{3+} with S_r of 1.8% K^{-1} at 293 K [244] and $LiTaO_3$:Ti^{4+}, Eu^{3+}@PDMS with S_r of 3.637% K^{-1} at 300 K [245]. More details on the comparison of the relative sensitivity of lifetime-based thermometers can be found in the works of Brites, and Carlos [173, 174] besides these references [239, 245].

4.3.2 Spatial Temperature Mapping

To test the accuracy and practicality of the luminescence thermometer to spatially map temperature, an inhomogeneous temperature gradient was set using a metal bar attached to two heating/cooling stages as shown in Figure 4.13.

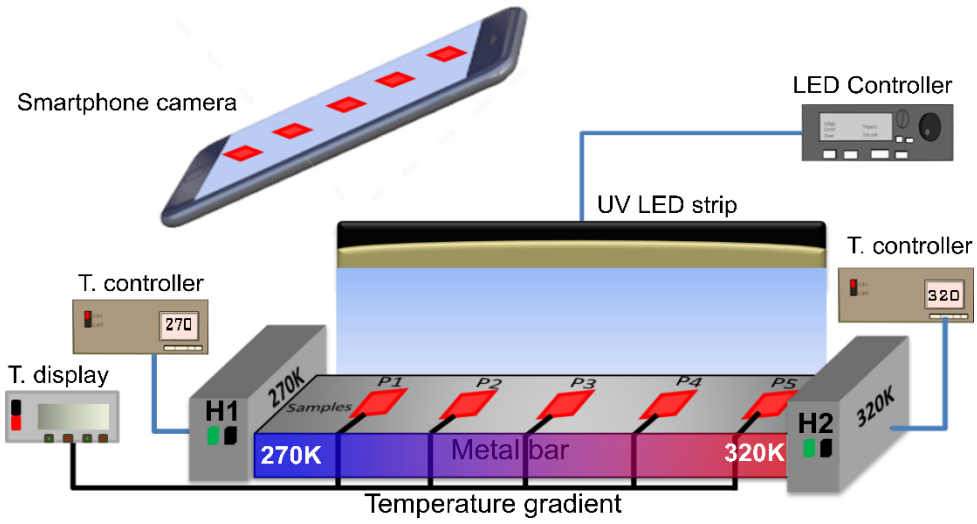

Figure 4.13. Experimental set-up of apparatus for establishing a temperature gradient from 270 to 320K along a metal bar. The five patches in the metal bar containing the $Gd_2O_2S:Eu^{3+}$ phosphor material are marked P1-P5. An in-house made UV (375 nm) LED strip illuminates the bar uniformly with pulses as the smartphone camera video records the emission. Reproduced from Katumo et al. [8]. CC BY-ND 4.0 License.

The metal bar had five patches along with the plate where a thin layer of the Gd_2O_2S: $0.06Eu^{3+}$ phosphors was pressed onto the bar. For each patch, a thermocouple probe was attached at the patch center to provide an independent reference. One end of the bar was maintained at 270 K while the other end was maintained at 320 K.

Figure 4.14a shows frames selected from the ROI extracted from the smartphone video of the metal strip after UV excitation with time zero being the last frame for which the LED strip was on. The initial frames indicate that the instantaneous emission from the five patches immediately after the LED strip goes off is almost similar.

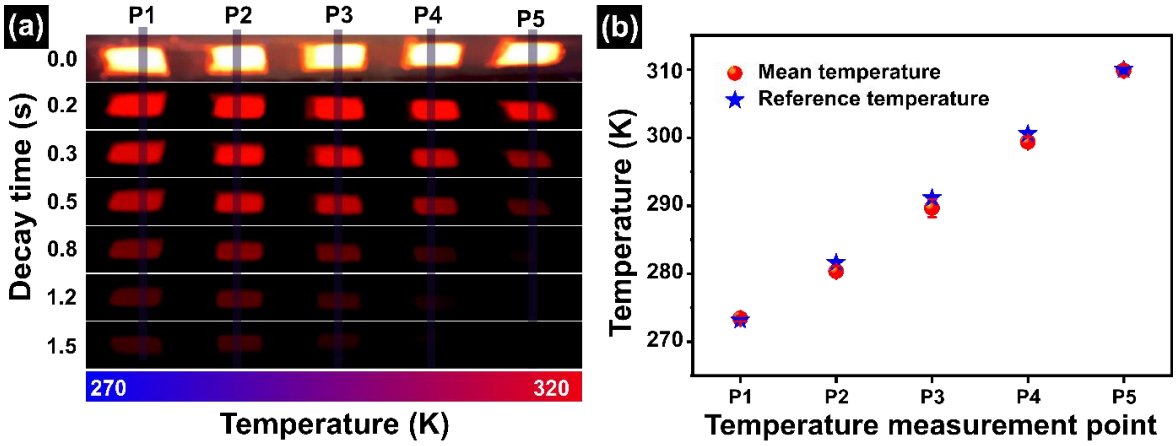

Figure 4.14. a) Individual frames from an exemplary smartphone video showing that the PersL is visible from the cold side of the bar much longer than it is from the hot side of the bar. b) The temperatures estimated from the smartphone-estimated lifetime are shown for each of the five points on the metal bar (the red circles represent mean temperature extracted from lifetimes of several individual videos). The derived temperature is in agreement with the reference value read from the thermocouple at that location (blue star). Adapted from Katumo et al. [8]. CC BY-ND 4.0 License.

In contrast, the later frames show that the emission from the hotter side faded away rapidly relative to the emission from the cooler side of the metal bar. Again, by integrating the emission intensity over each patch containing the Gd_2O_2S: 0.06 Eu^{3+} phosphor, the specific PersL lifetime for each patch (representing different temperature readouts) could be computed from a single video. To check

repeatability and reproducibility, five videos are acquired using the same fashion and the PersL lifetime is computed and the representative temperature is determined using equation 4.3. The as determined temperatures were then compared to the thermocouple read-out temperatures for the five patches shown in Figure 4.13. The comparative results are shown in Figure 4.14b. The reference temperatures lie within the error margins of the measured temperatures. This confirms the accuracy of the method in determining the spatial temperature from PersL through analysis of a single smartphone acquired video. The average resolution in the derived temperature, that is, temperature determined from the analysis of PersL lifetime data at each patch, was 0.9 K. This value is in agreement with the temperature resolution results shown in Figure 4.12. The average deviation of the derived temperature values to the thermocouple readings was 0.6 K. These results validate the accuracy of the technique as the derived temperature not only agrees with the performance parameters of the PersL thermometer but as well as to the reference temperature.

The spatial temperatures determined in the previous case are based on pure Gd_2O_2S: $0.06Eu^{3+}$ phosphors embedded on the five patches. However, in many instances, it is the norm that the phosphor is blended with a binding matrix for coating the surfaces for which the temperature is to be determined [245]. A non-optically sensitive binder was used to demonstrate minimal phosphor loading which would nevertheless lead to the same temperature reading for a surface as compared to the pure surfaces (without binder). Figure 4.15(a-d) shows the PersL lifetime plots for 4 wt%, 6 wt%,10 wt%, and 20 wt% concentration of Gd_2O_2S: $0.06Eu^{3+}$ in a binder which registered PersL lifetime values of 443 ms, 460 ms, 442 ms, and 434 ms at 295 K. The measured PersL lifetime translates to an average temperature of 294.5 K and has a standard deviation of 0.6 K. At very low concentrations of the phosphor in the binding matrix, <4 wt%, it is not possible to accurately determine the PersL lifetime as the emission signal from the scattered phosphor particles is too low.

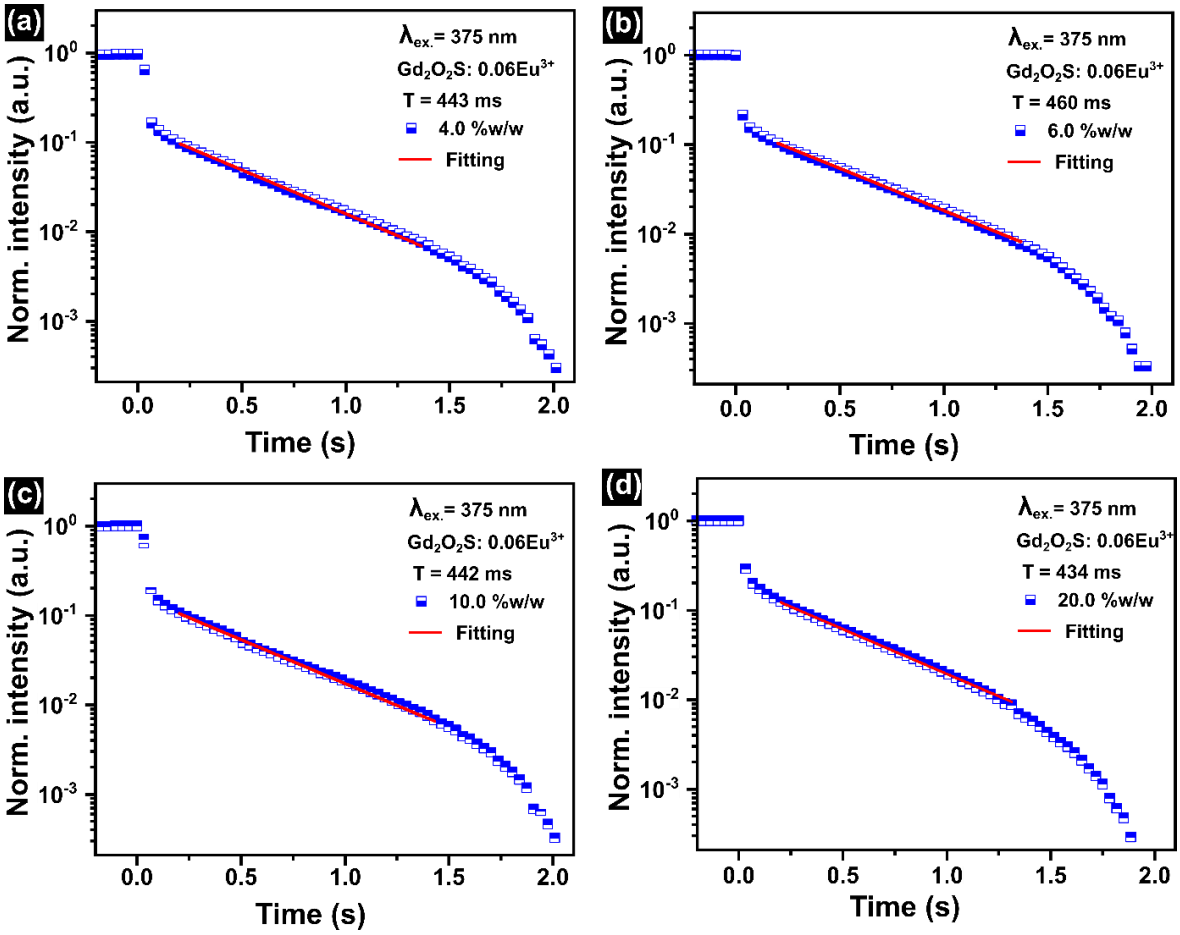

Figure 4.15. The PersL lifetime of Gd_2O_2S: $0.06Eu^{3+}$ at 295K as a function of concentration in %wt with a non-optically sensitive binder. a) 4 wt%, b) 6 wt%, c) 10 wt% and d) 20 wt%. Adapted from Katumo et al. [8]. CC BY-ND 4.0 License.

4.3.3 Temperature Sensing in Ambient Lighting

The effect of background photon noise on luminescence thermometers is usually a major concern. The effect is more pronounced in intensity ratio-based methods and less severe for the lifetime-based approaches [7]. To quantify the effect of background illumination on the technique, the room lighting conditions were varied using white light LED bar as the measurements were acquired. The spectrum of the white LED bar is shown in Figure 4.16 and is composed of a sharp band centered at 450 nm and a broadband emission extending from 500 nm to the near-infrared region. The emission centered at 450 nm is usually from an indium gallium nitride LED [246]. The broadband emission extending to the near-infrared region is a downshifted conversion of some of the blue light by phosphors in the coating

of the LED. The illuminance was adjusted from 0 to 1500 lm/m^2 and was measured using a digital lux meter (AP-881D, AOPUTTRIVER) placed adjacent to the phosphor sample.

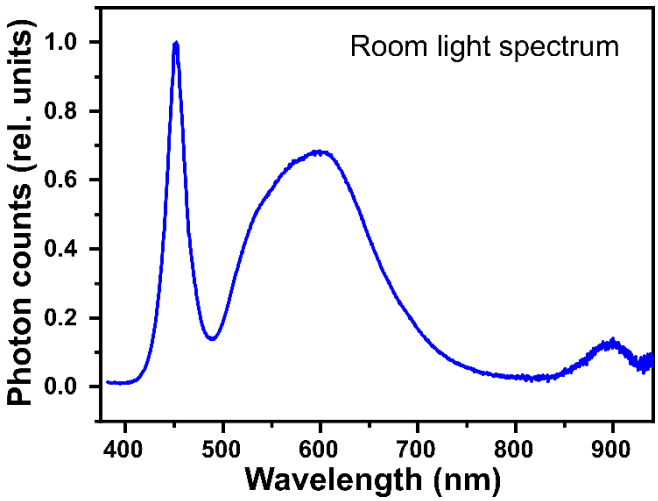

Figure 4.16. Room light (cool white light LED) spectrum. The room lighting spectrum usually has a sharp peak in the blue region (450 nm) and a broad emission extending from 500 nm to the near-infrared region.

To acquire the PersL signal, the bandwidth of the background illumination was suppressed by introducing a 650 nm short-pass filter (FESH0650, Thorlabs) and a 600 nm long-pass filter (FELH0600, Thorlabs) in front of the smartphone video camera.

To determine the PersL lifetime, the acquired videos are cropped in the ROI, and the PL intensity average of each frame is determined as a function of time from the video. These data, normalized to the value when the LED was on, are shown for 0 lm/m^2, 500 lm/m^2, 1000 lm/m^2, and 1500 lm/m^2 in Figure 4.17. The background luminance as observed in the raw videos increases with an increase in the background illumination. The increase in background noise was identified by acquiring the video before the 375 nm excitation when the LED lighting was turned on and reached a maximum value of 0.431 at 1500 lm/m^2. By doing so, it is easy to subtract the background luminance from the raw data.

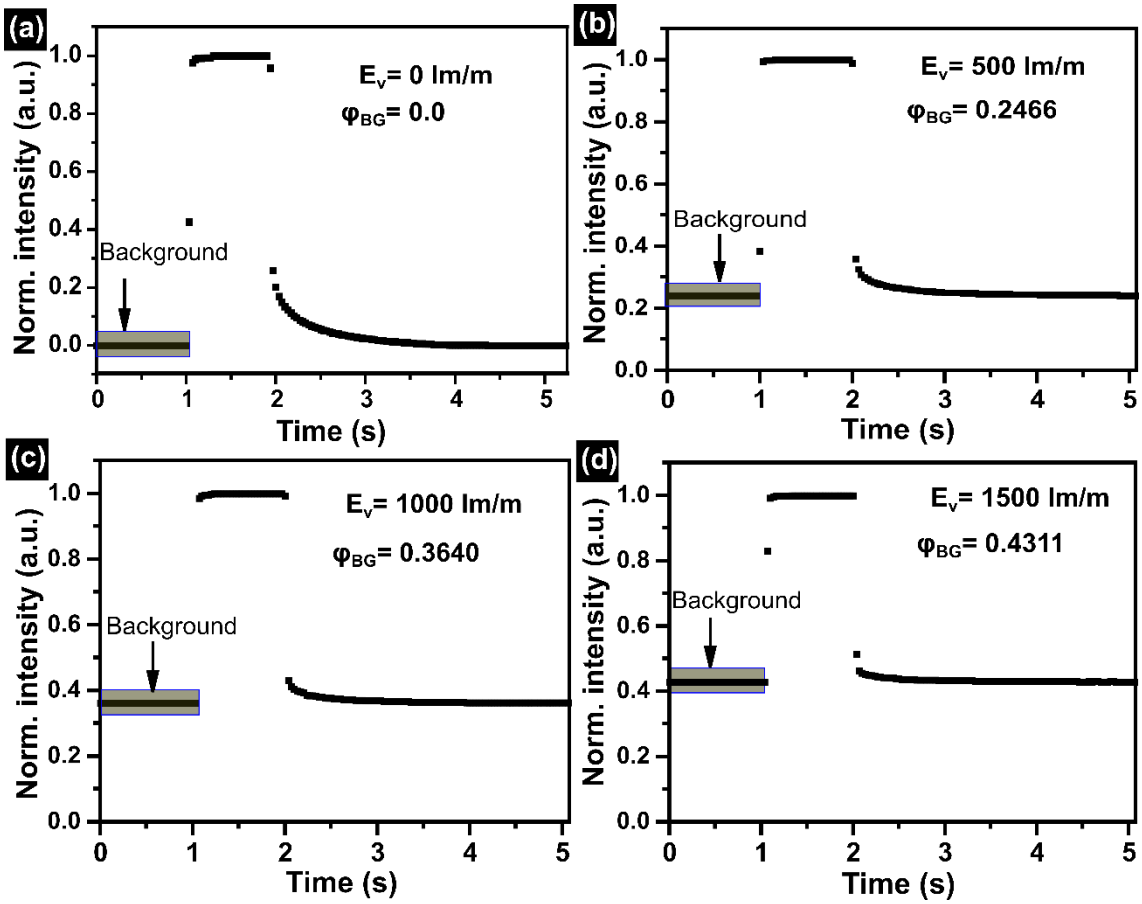

Figure 4.17. Raw PersL lifetime data extracted from region of interest in the videos showing the background, excitation pulse and subsequent decay of the phosphor post excitation at 293 K for a) sample in the dark, E_v = 0 lm/m², b) E_v = 500 lm/m², c) E_v = 1000 lm/m² and d) E_v = 1500 lm/m².The background signal (φ_{BG}) increases with increase in illuminance relative to the maximum signal from zero in the dark to 0.4311 under 1500 lm/m². Adapted from Katumo et al. [8]. CC BY-ND 4.0 License.

Before subtracting the background signal, the photon shot noise, the standard deviation of the background noise, and response to the luminance were evaluated by computing the standard deviation of the background region of the raw data. These results are shown in Figure 4.18. The photon short noise ideally increases with the square root of the luminance, which it roughly does. The noise at the highest luminance levels is in the order of 4×10^{-4} whereas the PersL decay signal height is on average around 1×10^{-2}. As a result, it is possible to accurately extract the PersL lifetime due to the high signal-to-noise ratio.

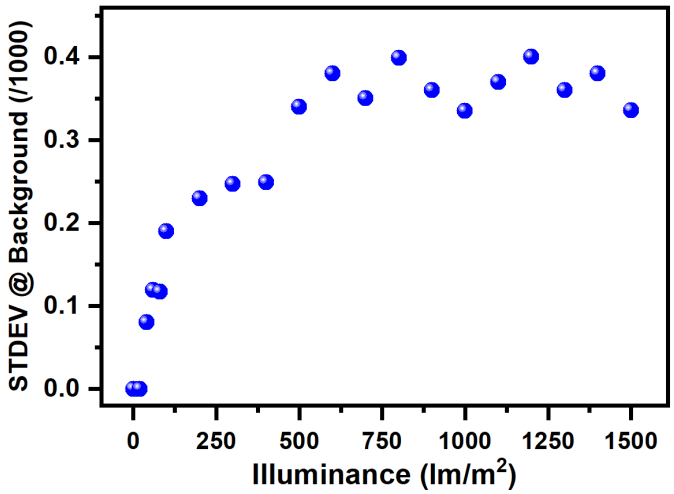

Figure 4.18. Standard deviation (STDEV) of background signal as a function of illuminance. The STDEV increases with increase in illumination in an exponential growth manner and stabilizes around $4x10^{-4}$. Reproduced from Katumo et al. [8]. CC BY-ND 4.0 License.

The PersL lifetime data with the background noise subtracted is shown in Figure 4.19. For these four plots taken at 0, 500, 100, and 1500 lm/m^2 the average lifetime registered are 470 ± 5 ms. These values are in agreement with the data taken in the dark and lie well within the margin of 475 ± 13 ms for several measurements taken in the dark. From the plots, one can however notice the difference in the PersL decay after the fitting region, with the data acquired at zero lm/m^2 having less noise while the data acquired at 1000 lm/m^2 and 1500 lm/m^2 having higher levels of noise. The fitting region t_1 - t_2 was however outside the noisy region.

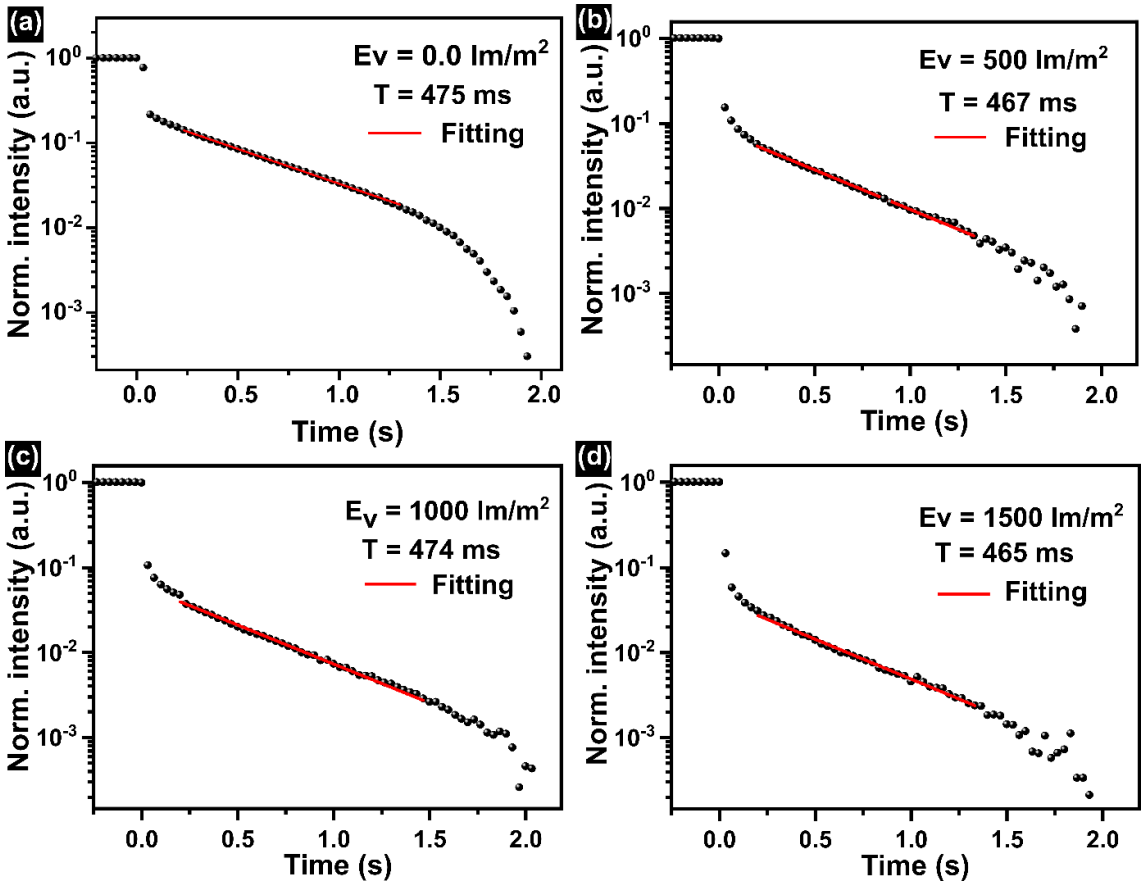

Figure 4.19. PersL lifetime processed from the raw data at 293 K with end of pulse excitation shifted to zero-time for a) sample in the dark, E_v = 0 lm/m², b) E_v = 500 lm/m², c) E_v = 1000 lm/m² and d) E_v = 1500 lm/m². Reproduced from Katumo et al. [8]. CC BY-ND 4.0 License.

Figure 4.20 shows a summary of the PersL lifetime and the indicative temperature when the ambient lighting illumination is increased from 0 to 1500 lm/m2. The mean PersL lifetime and standard deviation of data from all of the different illumination conditions is 477±13 ms. This corresponds to a relative error of 2.7% for measurements made in ambient lighting. Temperature-wise, these PersL lifetime data corresponds to 292.9 ± 0.7 K, which is well in agreement with the room temperature of 293 K.

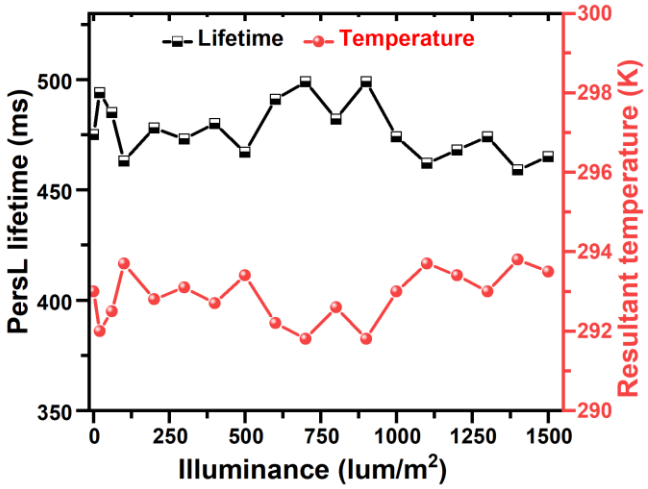

Figure 4.20 Summary of PersL lifetime (black) and indicative temperature (red) as a function of illuminance (0 – 1500 lm/m²). The resulting average lifetime is 477±13 ms and translates to a mean temperature of 292.9 ± 0.7 K. Reproduced from Katumo et al. [8]. CC BY-ND 4.0 License.

4.4 Introduction to Dynamic Photonic Markers

Dynamic photonic markers, in which the persistent luminescence decay is tunable after excitation are desirable for anti-counterfeiting applications [227]. The persistent tunability of the Gd_2O_2S: Eu^{3+} with respect to the Eu^{3+} doping allows for the development of photonic markers readable from videos acquired using ordinary smartphone cameras as shown in Figure 4.21. The frames of interest shown as a function of time demonstrate that it is possible to develop dynamic anti-counterfeiting patterns. The use of smartphone cameras away from complicated and specialized detectors such as high-speed cameras highly reduces the cost of implementing smartphone-based photonic marking for security/anti-counterfeiting applications.

For the provided frames based on Gd_2O_2S: Eu^{3+}, the persistent lifetime is short as already discussed in Figure 4.8 but feasible for dual dynamic patterns via the use of the longest persistent decay provided by Gd_2O_2S: $0.06Eu^{3+}$ and a short persistent phosphor such as Gd_2O_2S: $0.13Eu^{3+}$. Indeed to have more patterns the tunability of the phosphors must be broadened to provide a larger pallet of persistent luminescence. The next chapter reports on the realization of a broader

pallet based on extended persistent luminescence of Gd_2O_2S: Eu^{3+} via co-doping with Ti^{4+} ions [11].

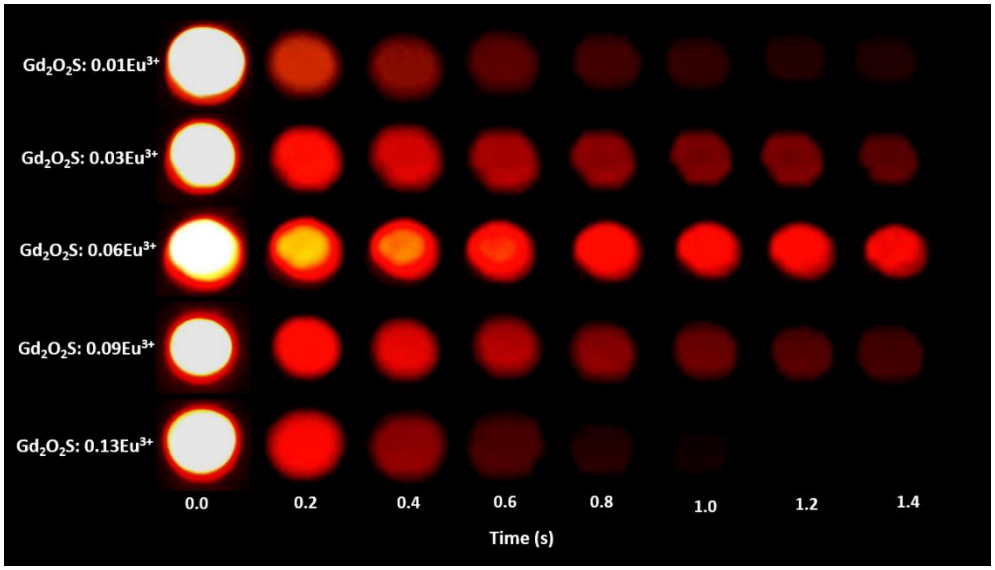

Figure 4.21. Video frames extracted from videos of Gd_2O_2S: x Eu^{3+} (x= 0.01 - 0.13 mol) showing a pallet of emission as function of Eu doping following 375 nm excitation.

4.5 Summary

To summarize, the results presented in this chapter demonstrated smartphone-based luminescence imaging in the 273 - 333 K range based on the PersL of Gd_2O_2S: Eu^{3+} phosphor. First, a performance optimization step to develop a phosphor with the longest PersL lifetime and highest PLQY was undertaken. For this step, varying the Eu^{3+} doping from 0.01 to 0.13 mol led to the identification of Gd_2O_2S: $0.06Eu^{3+}$ as the best optically performing phosphor under 375 nm excitation. As the intent of the phosphor was thermometry applications, studies on the temperature-dependent PL under various excitation conditions were undertaken to provide additional data on top of the photophysical data following excitation to model the energy transfer mechanism. From the results, it was possible to develop a TDCT model which explained the energy transfer mechanism in the Gd_2O_2S: Eu^{3+} phosphor.

The Gd_2O_2S: $0.06Eu^{3+}$ phosphor was then used for luminescence imaging in which the emission following 375 nm excitation was captured with the smartphone

camera and then analyzed to map the surface temperature. Using the phosphor, a smartphone and a 375 nm LED, temperatures in the range of 270-320 K could be determined with a temperature resolution better than 2 K even at an ambient lighting level of 1500 lm/m^2. Note that the short range of temperature detection (270 - 320 K) is a characteristic of the lifetime technique as the technique employs the quenching mechanism of the phosphor [7]. Taken as a single system, the thermometer has a maximum relative sensitivity of 4.5% K^{-1} at 273 K reduced to 3.1%K^{-1} at 333 K. The temperature resolution was better than 1 K for temperatures below 300 K.

In addition to luminescence imaging, by utilizing the different PersL of the various Eu^{3+} doped samples, it was possible to demonstrate photonic markers whose PersL decay varied between 150 - 475 ms at room temperature. Note that for these photonic markers, the dynamic change would however be fast and not observable by the naked eye but can only be estimated via the analysis of the acquired videos. The idea of dynamic photonic markers for anti-counterfeiting application is explored in the next chapters in depth.

5

Smartphone-Readable Dynamic Anti-Counterfeiting Labels

This chapter deals with the results of anti-counterfeiting labels that are excited using UV radiation and the persistent emission read-out using a smartphone. The labels are based on $Gd_2O_2S: Eu^{3+}$, Ti^{4+} persistent phosphors. The results discussed herein are based on the following first-author publication:

***Katumo, N.,** Ruiz-Preciado, L. A., Kumar, V., Hernandez-Sosa, G., Richards, B. S., & Howard, I. A. (2021). Anti-counterfeiting labels with smartphone-readable dynamic luminescent patterns based on tailored persistent lifetimes in $Gd_2O_2S: Eu^{3+}/Ti^{4+}$. Advanced Materials Technologies, 2100047 [11].*

The idea was an extension of the previous thermometry work to extend the persistent lifetime of the $Gd_2O_2S: Eu^{3+}$ at room temperature and was conceived by the first author in close coordination with Dr. Ian Howard and Prof. Bryce Richards. Further optimization of the $Gd_2O_2S: Eu^{3+}$ from the previous work only led to a PersL lifetime of up to 1.17 s. This PersL lifetime was further enhanced up to 5.95 ± 0.02 s by co-doping with Ti^{4+} ions. The first author prepared the $Gd_2O_2S: Eu^{3+}$, Ti^{4+} phosphors at IMT, and undertook the subsequent characterization, including the XRD, PLQY, PL, PLE, and PLQY measurements. Vinay Kumar, a co-

author of the manuscript helped in acquiring PersL spectra post excitation of the phosphors. Afterward, the selected phosphors were used to develop dynamic anti-counterfeiting patterns that change after the excitation source is removed. Further exploration to have printed dynamic anti-counterfeiting labels using an inkjet printer was accomplished in the Innovation Lab at Heidelberg with the help of Ruiz-Preciado, and Dr. Hernandez-Sosa. All the authors participated in the discussion and writing of the manuscript.

5.1 Introduction

The luminescence anti-counterfeiting labels presented in this chapter have dual-level security. In principle, this means the labels contain at least one covert feature that has to be decoded from the analysis of its luminescence properties. While the overt features can uniquely be identified either via naked eyes, the covert features can only be decoded from either the analysis of their PersL lifetime or from binary images of acquired video frames following UV excitation [11]. Anti-counterfeiting labels in which the covert features are in the temporal domain have interesting inception. Investigations on the temporal domain began by either utilizing the very short fluorescence lifetime and later on relatively long PersL lifetime. For reasons of clarity, and to better demonstrate the convergence of the two approaches, this work focuses on PersL labels with a PersL lifetime greater than 100 ms but below 10 s. A straightforward reason behind this ‘sweet spot’ region of PersL lifetime will resolve in the next sections.

Early works on anti-counterfeiting based on luminescence lifetime are based on very short fluorescence lifetimes. Unfortunately, to capture the fluorescence lifetime, ideally less than a few milliseconds, expensive instrumentation such as fast cameras, FLIM, and TCSPC to resolve the lifetimes. These expensive instrumentation compromise the practical application of such labels in POS terminals besides does not make economic sense. Examples of such labels are the ones developed by Kalytchuk *et al.* based on two different sets of carbon dots with fluorescence lifetimes of 4.4 ns and 6.1 ns, respectively after 365 nm UV light excitation [90]. By using a FLIM apparatus, patterns developed using the two sets of carbon dots could be distinguished [90]. Similar experiments but with longer lifetimes in the range of 26 - 662 ms have also been demonstrated by Lu *et al.*

based on $NaYF_4$: Yb^{3+}, Tm nanocrystals dispersed in cyclohexane [75]. Sun *et al.* also demonstrated multi-level anti-counterfeiting in the nanosecond range using iridium (III) complexes [52]. Again, to verify the very short milliseconds lifetime, a single-pixel fast detector or an expensive high-speed camera is required to encode the anti-counterfeiting patterns. In principle, it is clear that the cost and sophistication of the measurement systems act as major limiting factors which inhibit the realization of anti-counterfeiting labels exploiting the time domain of luminescence.

Alternatively, researchers have also developed persistent phosphors with very long PersL after excitation for applications in dynamic anti-counterfeiting. For these labels, overt features dominate the labels' authentication process. Additionally, a combination of accessories in the authentication set-up allows covert features to be coded in the labels. For instance, Long *et al.* designed quasi-layered structured $Ca_3Ga_4O_9$:Bi^{3+} phosphors that had unique charge carrier trapping features [247]. The traps are filled by UV excitation (254 nm or 365 nm) and the afterglow is then photo-stimulated via 980 nm excitation. For these labels, instead of quantifying the PersL lifetime, band-pass filters are used to realize anti-counterfeiting post excitation. Closely related approaches have also been reported by Sang and coworkers who combined PersL and mechanoluminescence in Niobate structures based on $LiNbO_3$:Re^{3+}, RE^{3+} = Pr^{3+}, Tm^{3+}, $Er^{3+,}$ and Yb^{3+}) for photo-stimulated luminescence anti-counterfeiting with tunable colors [78]. In the same line of research, Pei *et al.* also developed anti-counterfeiting labels based on $NaCa_2GeO_4F$: Tb^{3+} that could be tuned by controlling the Tb^{3+} doping after 375 nm UV excitation. Unfortunately, the PersL was very long, in the range of hours 5.6 – 7 hours [248]. This made the anti-counterfeiting labels impractical for real-time anti-counterfeiting applications. Nevertheless, these contributions laid the ground for the use of color tuning and PersL lifetime for anti-counterfeiting.

The two challenges, the first one being, a very short fluorescence lifetime requiring expensive and sophisticated instrumentation and the other being impractically long PersL lifetimes infeasible for realistic applications are surmounted in this thesis. This is accomplished using Gd_2O_2S: Eu^{3+}, Ti^{4+} persistent phosphors to realize smartphone-readable anti-counterfeiting labels after UV excitation. For these labels, the PersL lifetime is tunable in the 1.17 ± 0.03 – 5.95 ± 0.07 s range via Ti^{4+}

co-doping concentration variation. At the same regime of PersL lifetime, the PLQY remains relatively constant, allowing for uniform initial brightness following illumination. Therefore, the dynamic patterns revealing the anti-counterfeiting aspects are realized after the UV excitation source is removed and either verified by naked eyes or from the analysis of the smartphone acquired videos after UV excitation. The use of smartphones for such applications is of course a front-runner as it is economical and easy to realize in various settings. In the next sections, first, the photophysical properties of the Gd_2O_2S: 0.06 Eu^{3+}, Ti^{4+} are explored, then anti-counterfeiting labels are demonstrated.

5.2 Photophysical Properties of Gd_2O_2S: Eu^{3+}, Ti^{4+} Phosphor

To exhibit a wider pallet of PersL decays at room temperature, the Gd_2O_2S: 0.06 Eu^{3+} phosphors were co-doped with Ti ions. Controlled co-doping with Ti^{4+} ions provides for controlled trap density and depth in the host allowing the PersL lifetime to be tuned [17, 249]. Figure 5.1 displays a smartphone-video-recorded PersL decay of Gd_2O_2S: 0.06Eu^{3+}, Gd_2O_2S: 0.03Ti^{3+}, and Gd_2O_2S: 0.06Eu^{3+}, 0.03Ti^{4+} upon 375 nm UV excitation for 10 s. The Gd_2O_2S: 0.006Eu^{3+} shows a relatively short PersL that is observable up to around 4 s after the 375 nm UV excitation has been switched off.

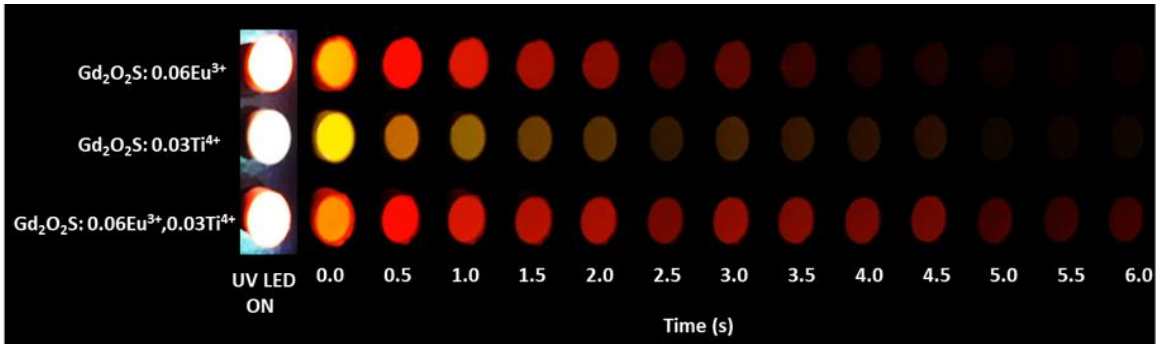

Figure 5.1. Video frames extracted from videos of luminescence of Gd_2O_2S: 0.06Eu^{3+}, Gd_2O_2S: 0.03 Ti^{4+}, and Gd_2O_2S: 0.06Eu^{3+}, 0.03Ti^{4+} for 10 s after UV excitation under $\lambda_{ex.}$ = 375 nm showing the PersL as a function of time. The Ti^{4+} co-doped sample has the longest PersL. Adapted from Katumo et al. [11]. CC BY-ND 4.0 license.

On the other hand, the Ti^{4+} mono-doped gadolinium oxysulfide phosphor - Gd_2O_2S: $0.03Ti^{3+}$ shows longer PersL observable beyond 5 s. Unfortunately, the PL is rather very low in intensity and yellowish-white in color. On the contrary, the Gd_2O_2S: $0.06Eu^{3+}$, $0.03Ti^{4+}$ synergistically demonstrates the strengths over the individually doped phosphors by demonstrating relatively longer PersL with very strong PL intensity. Its PersL emission extends beyond 6 s hence trumping over the others. Part of the reasons for the synergetic influence is decoded from the PL, PLE, and PersL decay analysis discussed in the next sections.

Figure 5.2 illustrates the PL excitation spectra of Gd_2O_2S: $0.06Eu^{3+}$, Gd_2O_2S: $0.03Ti^{3+,}$ and Gd_2O_2S: $0.06Eu^{3+}$, xTi^{4+}. All the excitations are tracked at 626 nm, the maximum emission point. The Gd_2O_2S: $0.03Ti^{3+}$ phosphor shows a weak CTB in the lower energy region of 420 – 280 nm but sharp peaks in the 280 - 250 nm region that coincides with the host material bandgap of 4.8 eV [250, 251]. A relatively weak absorption band in the 420 – 280 nm is also present and is attributed to $S^{2-}/O^{2-} \rightarrow Ti^{3+}$ energy transfer [8].

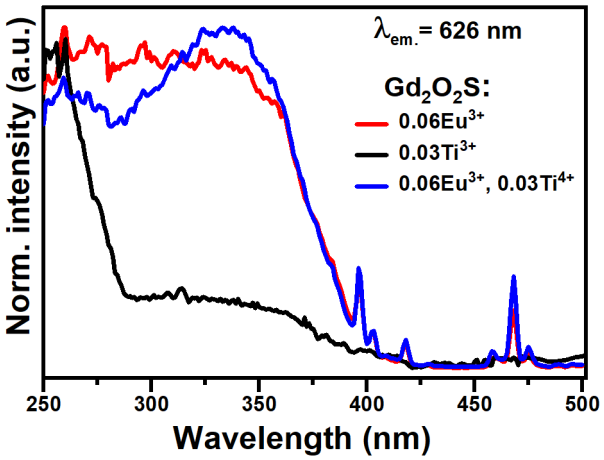

Figure 5.2. The PL excitation spectra of Gd_2O_2S: $0.06Eu^{3+}$, Gd_2O_2S: $0.03Ti^{3+}$ and Gd_2O_2S: $0.06Eu^{3+}$, $0.03Ti^{4+}$ tracked at $\lambda_{em.}$ = 626 nm. Reproduced from Katumo et al. [11] CC BY-ND 4.0 license.

As discussed in the previous chapter, the Gd_2O_2S: $0.06Eu^{3+}$ base sample exhibits a strong charge transfer extending from the 420 – 250 nm range [8]. Interestingly, when Gd_2O_2S: $0.06Eu^{3+}$ is co-doped with the Ti^{4+} ions, the very strong CTB in the

420 – 250 nm is maintained, analogous to that of the Gd_2O_2S: $0.06Eu^{3+}$ phosphor [8]. This strong CTB is attributed to the $S^{2-}/O^{2-} \rightarrow Eu^{3+}$ and partially to $S^{2-}/O^{2-} \rightarrow Ti^{n+}$(n = 3 and 4) charge transfer [252, 253]. Energy transfer from the host material via $Gd^{3+} \rightarrow Eu^{3+}/Ti^{4+}$ in the bandgap vicinity is also expected to contribute to the strong absorption in the bandgap region.

Absorption bands based on the Eu^{3+} intra-configurational 4f transitions, such as $^7F_{0,1} \rightarrow {}^5D_3$, $^5L_6$ (396 – 418 nm) and $^7F_{0,1} \rightarrow {}^7D_2$ (468 nm) are also observed in the Gd_2O_2S: $0.06Eu^{3+}$ and Gd_2O_2S: $0.06Eu^{3+}$, $0.03Ti^{4+}$ PLE spectra [8, 21, 229, 250]. The broad and strong CTB in the Eu^{3+} and Eu^{3+}, Ti^{4+} allows for a cheaper and safer UVA excitation with a 375 nm excitation source. The PL Gd_2O_2S: $0.06Eu^{3+}$, Gd_2O_2S: $0.03Ti^{4+}$, and Gd_2O_2S: $0.06Eu^{3+}$, $0.03Ti^{4+}$ following CTB excitation using a 375 nm LED are displayed in Figure 5.3. The Gd_2O_2S: $0.03Ti^{4+}$ PL emission is characterized by a broad emission band in the 900 – 500 nm region centered in the 626 nm region.

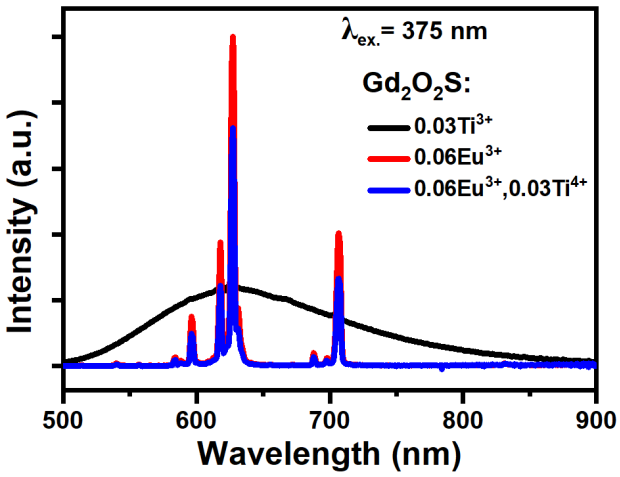

Figure 5.3. The PL emission spectra of Gd_2O_2S: $0.06Eu^{3+}$, Gd_2O_2S: $0.03T^{3+}$ and Gd_2O_2S: $0.06Eu^{3+}$, $0.03Ti^{4+}$ under 375 nm excitation. The emission spectra of Gd_2O_2S: $0.06Eu^{3+}$ and Gd_2O_2S: $0.06Eu^{3+}$, $0.03Ti^{4+}$ consists of then typical Eu^{3+} transitions while the PL emission of Gd_2O_2S: $0.03Ti^{4+}$ exhibits a broadband emission. Adapted from Katumo et al. [11]. CC BY-ND 4.0 license.

This broad emission explains the yellowish-white emission observed in the PersL emission (see Figure 5.1) and is due to the ($^2E \rightarrow {}^2T_2$) transition of the Ti^{3+} ion [253]. The energy level transitions during excitation entail the excited Ti^{4+} ion quickly capturing an electron forming an excited $Ti^{3+\bullet}$ ion that then combines with

a hole leading to the observed broadband emission [253, 254]. On the other hand, after 375 nm excitation, the Gd_2O_2S: $0.06Eu^{3+}$ and Gd_2O_2S: $0.06Eu^{3+}$, $0.03Ti^{4+}$ display the typical Eu^{3+} emission spectra with no trace signal of the broad emission of Ti^{4+} mono-doped phosphor. This feature is observed both for the steady-state and PersL as shown later.

For the Eu^{3+} PL emission, the $^5D_0 \rightarrow {}^7F_2$ (626 nm) Eu^{3+} ED hypersensitive transition with a shoulder at 617 nm is the dominant emission. The other emission centers are the $^5D_0 \rightarrow {}^7F_{0,1}$ (596 nm) MD transition, and the $^5D_0 \rightarrow {}^7F_4$ (704 nm) ED transition of the Eu^{3+}. Although the data provided up to now is not conclusive, it is clear that the Ti^{4+} transfers its charge carriers to the Eu^{3+}, which is the dominant emitting center in all the Eu^{3+}, Ti^{4+} doped samples.

Figure 5.4 shows the steady-state PLQY as a function of Ti^{4+} co-doping up to 0.24 mol. Note that the isolated red-point, with a PLQY of 65% is the optimized Gd_2O_2S: 0.06 Eu^{3+} sample. Upon Ti^{4+} co-doping, the PLQY reduced to 46 ± 3% for Ti^{4+} co-doping concentrations below 0.09 mol of Ti^{4+} and remained reasonably constant through this range as illustrated in Figure 5.4.

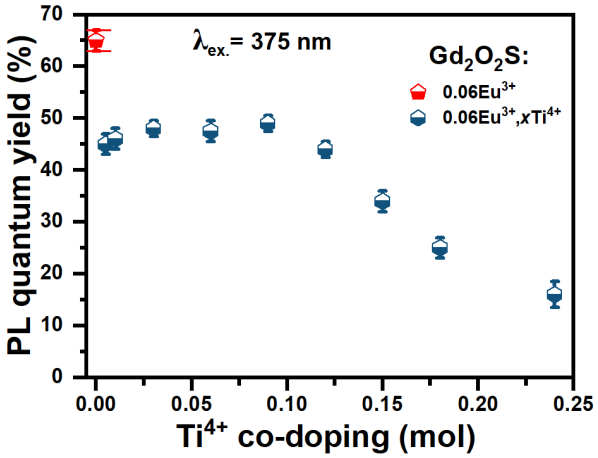

Figure 5.4. Absolute PLQY values of the Gd_2O_2S: $0.06Eu^{3+}$, xTi^{4+} phosphors for ($0 < x < 0.24$ mol) under 375 nm excitation. The Ti^{4+} co-doping leads to relatively constant PLQY for co-doping concentrations up to 0.09 mol. Beyond 0.09 mol of Ti^{4+} co-doping the PLQY gradually decreases. Reproduced from Katumo et al. [11]. CC BY-ND 4.0 license.

Beyond 0.09 mol, the PLQY drastically reduced with the Gd_2O_2S: $0.06Eu^{3+}$, $0.24Ti^{4+}$ registering a relatively low PLQY value of 16 ± 3%. This gradual reduction beyond 0.09 mol of Ti^{4+} co-doping is presumably due to concentration quenching of the charge carriers being populated in the instantaneous emission.

5.3 PersL Lifetimes of Gd_2O_2S: Eu^{3+}, xTi^{4+}

The PersL lifetime of Gd_2O_2S: $0.06Eu^{3+}$, xTi^{4+} for x = 0 - 24 mol were acquired and fitted similarly as in the previous case of Gd_2O_2S: Eu^{3+} [8]. In brief, the temporal intensity of the videos at ROI is acquired using a smartphone from which PersL decay curves are realized. Since the smartphone acquires videos at 30 fps, only the PersL emission can be fitted, and the fluorescence (the fast component) of emission is neglected. As such, the initial fitting region starts at t_1 = 2 s post excitation and the endpoint of the fitting t_2 is the time at which the phosphor has emitted 90% of its emission intensity when computed from t_1. This endpoint is experimentally determined by computing the integral area of the emission and identifying the 90% point in the time axis. A representative procedure for determining the fitting region is depicted in Figure 5.5 using the Gd_2O_2S: $0.06Eu^{3+}$, $0.03Ti^{4+}$ phosphor. Figure 5.5a shows the PersL emission integrated area of Gd_2O_2S: $0.06Eu^{3+}$, $0.03Ti^{4+}$ indicating three points of interest in the fitting region. From the t_1 (2s), starting point, the area increases, and plateaus as the integrated emission decay grow smaller and smaller such that the accumulative addition is quite small. Note that since for each Ti^{4+} co-doping the PersL lifetime is different, t_2 must be computed for every unique phosphor. The value of t_2 ideally decreased as the PersL decreased.

The PersL lifetime is fitted in the region of interest (ROI) using a single exponential function of the form:

$$I = I_0 + A_1 exp\left(\frac{-\tau}{t}\right) \tag{5.20}$$

where I_0 is an offset, and τ is the PersL lifetime determined by the fitting region. An example of the PersL lifetime fitting is shown in Figure 5.5b for the Gd_2O_2S: 0.06 Eu^{3+}, $0.03Ti^{4+}$ phosphor whose ROI has been identified in Figure 5.5a. The determined PersL lifetime is 4.51 ± 0.03 s.

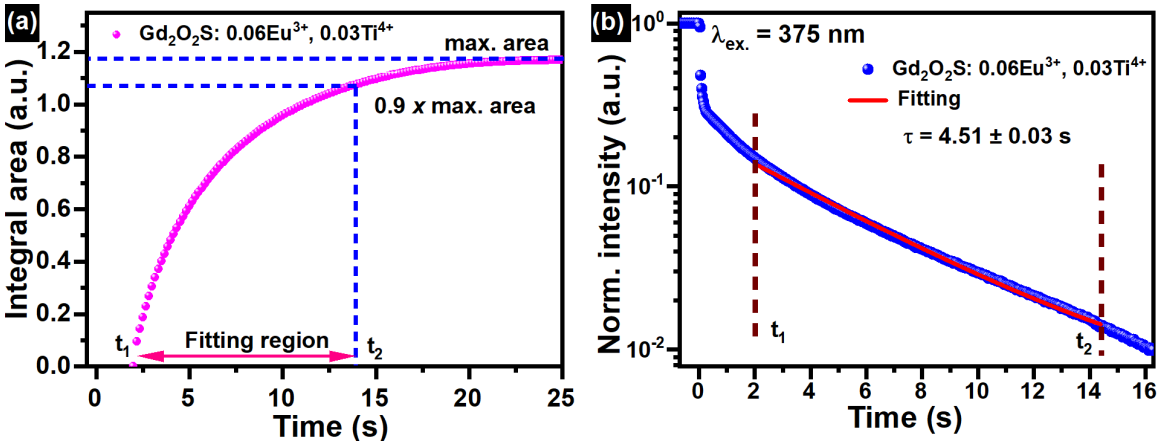

Figure 5.5. a) Computed emission integrated of the PersL as a function of time from 2 s for Gd_2O_2S: 0.06 Eu^{3+}, 0.03Ti^{4+}. The fitting region as determined by t_2, the time in which 90% of the emission has decayed after excitation is removed. (b) The PersL lifetime of Gd_2O_2S: 0.06 Eu^{3+}, 0.03Ti^{4+} with a fit in the defined fitting region t_1-t_2 using a single exponential fit. Reproduced from Katumo et al. [11]. CC BY-ND 4.0 license.

Figure 5.6 illustrates the PersL lifetime plots of the other samples, that is, Gd_2O_2S: 0.06 Eu^{3+}, x Ti^{4+} for x = 0 - 21 mol. In Figure 5.6a, the PersL lifetime is demonstrated to increase as the Ti^{4+} co-doping is increased up to 0.09 mol. This is unlike the PLQY which remained relatively constant in this regime (see Figure 5.4). The PersL lifetime increases from 1.17 ± 0.03 - 5.95 ± 0.07 s as the co-doping of Ti^{4+} is increased up to 0.09 mol. Interestingly, beyond 0.09 mol of Ti^{4+} co-doping, the PersL lifetime began to decrease with increasing Ti^{4+} co-doping, analogously to the PLQY. A PersL lifetime of 2.90 ± 0.03 s is registered for the highest Ti^{4+} co-doped sample, Gd_2O_2S: 0.06 Eu^{3+}, 0.24 Ti^{4+} as illustrated in Figure 5.6b and summative in Figure 5.6c. A qualifying argument for the gradual decrease in PLQY and PersL lifetime beyond 0.09 mol Ti^{4+} co-doping is concentration quenching.

Figure 5.6c shows a summary of the PersL lifetime, depicting the initial increase and decrease of PersL as the Ti^{4+} co-doping is increased. The PersL lifetime trend deviates from that of the PLQY at lower Ti^{4+} doping as it increases whereas in that region the PLQY relatively remains constant. For anti-counterfeiting applications, only the phosphors co-doped with Ti^{4+} up to 0.09 mol were of interest as a higher concentration of co-doping only led to the replication of the already established

PersL lifetimes albeit with relatively low PLQYs. The constant PLQY in the regime below 0.09 mol Ti^{4+} is an attractive catch for tunable PersL lifetime-based applications as the phosphors have extremely high uniform initial brightness. Note that even at higher Ti^{4+} co-doping, the initial brightness of the phosphor saturates the red channel of the smartphone camera (detector). This is also important as the PersL lifetime fitting occurs 2 s after the UV excitation has been switched off.

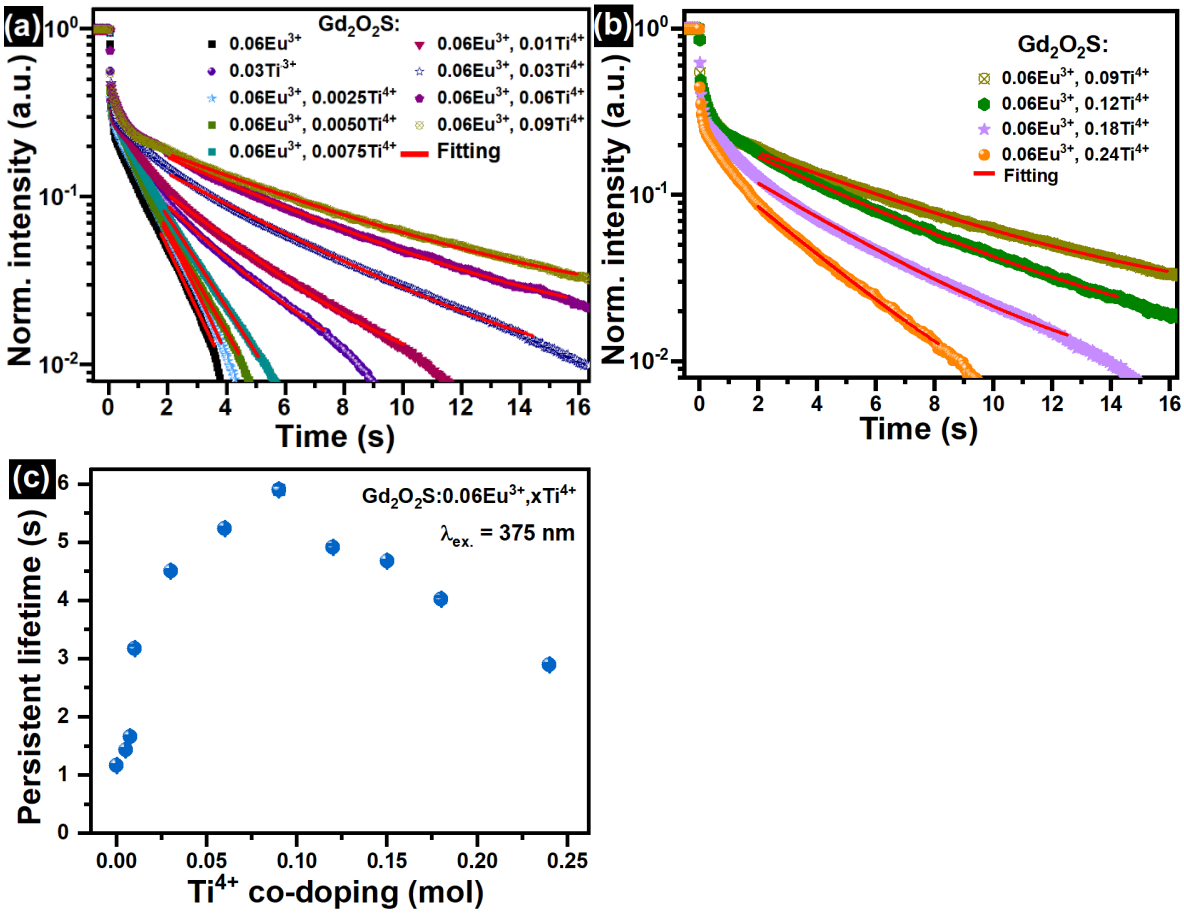

Figure 5.6. Normalized PersL emission as a function of time extracted from smartphone-acquired videos of Gd_2O_2S: $0.06Eu^{3+}$, xTi^{4+} emissions after pulsed UV-LED excitation (375 nm). a) The Ti^{4+} concentrations $0 \leq x \leq 0.09$ mol and b) $0.09 \leq x \leq 0.24$ mol. The persistent emission is fitted using a single exponential in the ROI and is tunable in the 1.17 ± 0.02 to 5.95 ± 0.07 s range. Adapted from Katumo et al. [11]. CC BY-ND 4.0 license.

5.4 PersL Mechanism of $Gd_2O_2S: Eu^{3+}, Ti^{4+}$

Universally, PersL occurs due to the thermal release of trapped charge carriers [17]. The process of charge carrier release is dependent on the nature of the host material involved, the excitation band, and energy transfer mechanisms within the host to the emitting center. In light of this, and for reasons of clarity to better understand the role played by Ti ions, we explore the PersL mechanism by exploring the photophysical effect of co-doping the $Gd_2O_2S: Eu^{3+}$ with Ti^{4+} ions.

5.4.1 Prompt Vs Delayed Emission in $Gd_2O_2S: Eu^{3+}, Ti^{4+}$

Before turning to a detailed discussion on the mechanism responsible for the PersL, and for clarity reasons the emitters centers in the prompt and delayed (PersL) are first investigated. Figure 5.7 shows the prompt and delayed PersL of $Gd_2O_2S: Eu^{3+}, Ti^{4+}$ at 3 and 6 s after the 375 nm excitation is ceased. Figure 5.7a reveals that the Eu^{3+} is the dominant emitting center for both the prompt and delayed emission in the case of $Gd_2O_2S: Eu^{3+}$. Similarly, as shown in Figure 5.7b, the Eu^{3+} remains the dominant emitter center in the steady-state and delayed PersL after 375 nm excitation.

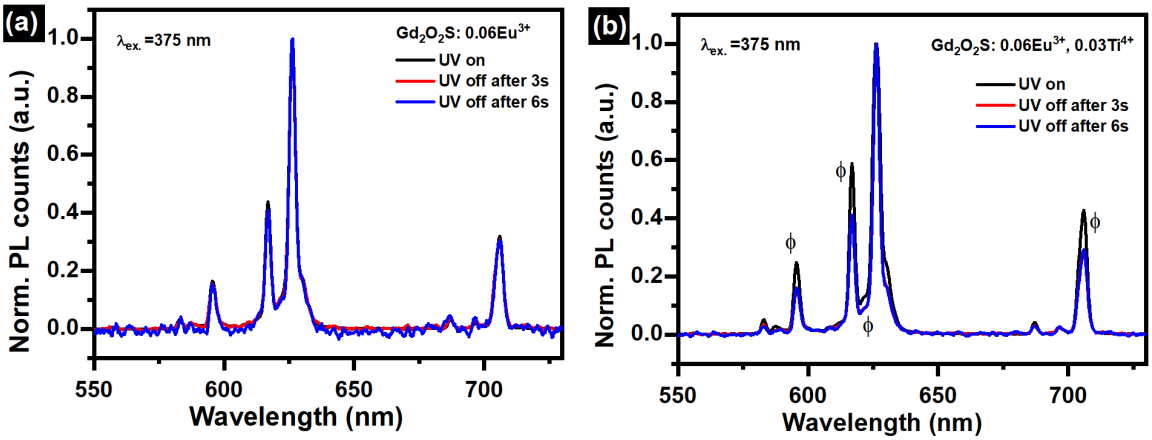

Figure 5.7. The normalized prompt and delayed (3 s and 6 s) photoluminescence spectrum after 375 nm LED excitation for (a) $Gd_2O_2S: 0.06Eu^{3+}$; (b) $Gd_2O_2S: 0.06Eu^{3+}, 0.03Ti^{4+}$. The phosphors were first excited for 10 s, then a 100 ms integration time spectra was taken 1 s before the excitation ceased, or a 500 ms integration time spectrum taken 3 or 6 s after the excitation had ceased. Reproduced from Katumo et al. [11]. CC BY-ND 4.0 license.

The data is provided when the 375 nm LED is on and the spectra after 3 and 6 s after the excitation is turned off. By normalizing the emission spectra, it is clear that the emission during excitation and the PersL have the same spectrum and come from the $^5D_0$ state of the Eu^{3+}. No emission comes from the Ti^{3+} center that has a broadband emission (see Figure 5.3). Despite the spectra having the same trend and emanating from the same Eu^{3+} state, there are slight differences in the delayed emission peak ratios marked with ϕ in the delayed emission shown in Figure 5.7b. This could be due to the slight alterations between the Eu^{3+} level transitions and the Ti^{4+} co-doped samples.

These findings deviate from the results of most materials that usually have a major component of the Ti ion emission in the PersL. This is demonstrated in the work of Bingfu *et al.* on PersL of rare-earth ion-doped oxysulphide phosphors [253]. Bingfu and colleagues demonstrated that except for Eu^{3+} that maintained its characteristic emission in the PersL, the PersL for samples doped with Ce^{3+}, Pr^{3+}, Nd^{3+}, Sm^{3+}, Tb^{3+}, Dy^{3+}, Tm^{3+}, Ho^{3+}, Er^{3+}, and Yb^{3+} as the emitting centers have a major component of the Ti ion emission in their PersL spectra [253]. Having the Eu^{3+} ion remain as the dominant emitting center after Ti ions introduction is highly beneficial to the straightforward realization of the PersL lifetime with a smartphone after UV excitation. This is also among the reasoning behind the use of Gd_2O_2S: Eu^{3+}, Ti^{4+} phosphor for anti-counterfeiting applications. On the contrary, if the PersL contained the Ti^{3+} persistent emission, the determination of the PersL using a smartphone would be frustrated as differentiating the two components of persistent emission (Eu^{3+} and Ti^{3+}) would not be straightforward.

Up to now, a consensus that Ti ions are particularly not involved in the prompt and delayed emission, and that their incorporation in the host affects the PersL lifetime of the Eu^{3+} ions is established. As already noted, the PersL lifetime first increases with a rise in Ti^{4+} doping from 1.17 ± 0.02 to 5.95 ± 0.07 s before gradually decreasing due to concentration quenching effects. In comparison, a similar increase in PersL lifetime due to Ti ions co-doping has been observed in Re_2O_2S: Eu^{3+}, Ti^{4+}, Mg^{4+} for Re = (Gd, La, Y) [253, 255-257]. The lack of Ti^{4+} broadband emission in the PersL of Gd_2O_2S: Eu^{3+}, Ti^{4+} coupled with the increased PersL tunable via the Ti^{4+} co-doping points to the Ti^{4+} ions transferring their energy to the Eu^{3+} emitting center. This property forms the basis under which the PersL decay is

tuned via controlling the Ti^{4+} co-doping for applications in luminescence anti-counterfeiting.

5.4.2 Proposed PersL Mechanism in Gd_2O_2S: Eu^{3+}, Ti^{4+}

With a special focus on the work of Luo *et al.* on the nature of PersL in this class of materials, a procedural description of the PersL mechanism is proposed herein. Luo *et al.* showed that charge transfer excitation can lead to a Ti^{3+} or Eu^{2+} along with a hole on the host using the Vacuum Referred Binding Energy (VRBE) [17]. The VRBE is defined as the energy required to extract an electron from the diagram to the outside vacuum. Position-wise, in the VRBE diagram, the $Eu^{3+/2+}$ ion is lower in energy than the $Ti^{3+/4+}$ ion in the Gd_2O_2S host [17]. Due to this, electron transfer from Ti^{3+} to Eu^{2+} occurs, leading to Eu^{3+} being the dominant emitting center for the prompt luminescence and PersL.

To test the above hypothesis, temperature-dependent PersL lifetime for Gd_2O_2S: $0.06Eu^{3+}$ and Gd_2O_2S: $0.06Eu^{3+}$, $0.03Ti^{4+}$ samples in the 175 - 350 K range were undertaken following 375 nm excitation. The results are illustrated in Figure 5.8. The Gd_2O_2S: $0.06Eu^{3+}$ registered a maximum PersL lifetime of 2.01 ± 0.03 s at 253 K while the Gd_2O_2S: $0.06Eu^{3+}$, $0.03Ti^{4+}$ registered a maximum PersL lifetime of 4.9 ± 0.03 s at the room temperature 293 K.

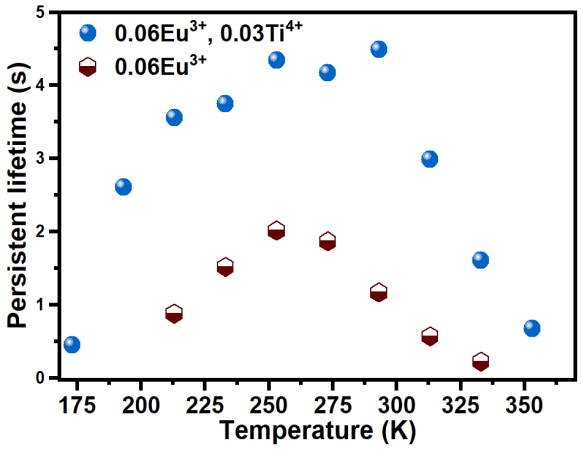

Figure 5.8. Temperature dependent persistent lifetime for Gd_2O_2S: $0.06Eu^{3+}$ and Gd_2O_2S: $0.06Eu^{3+}$, $0.03Ti^{4+}$ in the 175 - 350 K temperature range. Reproduced from Katumo et al. [11]. CC BY-ND 4.0 license.

Quantitatively, the Gd_2O_2S: $0.06Eu^{3+}$, $0.03Ti^{4+}$ PersL lifetime is roughly a factor of two longer than that of the Gd_2O_2S: $0.06Eu^{3+}$ at any temperature. However, a similar trend of the temperature-dependent PersL lifetime suggests that the changes are dominated by the position of the temperature-dependent CTB relative to the $^5D_0$ level of Eu^{3+}, and by the rate of non-radiative deactivation of the CTB. With these results, it is hypothesized that the extension of the PersL of Gd_2O_2S: Eu^{3+} emission by Ti^{4+} co-doping is due to delayed filling of the CTB by the Ti^{4+} slowing the release of the hole on the host (potentially due to charge imbalance effects) and by sometimes necessitating electron transfer between the Ti and Eu before emission. Although further work/data is needed to solidify the mechanistic understanding of PersL, the current system excellently satisfies all the nontrivial requirements for a persistent phosphor with a tunable lifetime for smartphone-based lifetime determination.

Since these phosphors are used for anti-counterfeiting with a smartphone as the device used for capturing the PersL, maintaining narrowband emissions, such as the one demonstrated from the Eu^{3+} is desirable [8]. Maintaining the narrowband emission for the prompt and delayed emission guarantees high spectral brightness that also allows for the use of band-pass filters to minimize spectral interferences [8].

5.5 Smartphone - Readable Labels based on Gd_2O_2S: Eu^{3+}, Ti^{4+}

To demonstrate the anti-counterfeiting potential of the persistent phosphors, three kinds of labels are developed, namely; 1) seven-segment display labels, 2) inkjet-printed labels**,** and 3) drop-casted labels. For these labels, informed selection of the PersL lifetime determines the level of security of the anti-counterfeiting features. For instance, labels developed with persistent phosphors having a large difference in their PersL lifetimes allowed the use of naked eyes for authentication/verification. On the other hand, labels developed using persistent phosphors with close PersL lifetimes were hard to decode by naked eyes but could be decoded from the analysis of the smartphone-acquired video after excitation. Alternatively, binarization of the video frames at various timestamps could also reveal the covert patterns. These PersL-based anti-counterfeiting labels are discussed hereafter.

5.5.1 Seven-Segment Display Labels

Anti-counterfeiting labels based on a 4-digit 7-segment display were developed by embedding phosphors with specific PersL in the segments as outlined in Figure 5.9a. The phosphor embedded in segments ① and ② was Gd_2O_2S: $0.06Eu^{3+}$, in ③ and ④, was Gd_2O_2S: $0.06Eu^{3+}$, $0.01Ti^{4+}$, and that in segments ⑤, ⑥ and ⑦ was Gd_2O_2S: $0.06Eu^{3+}$, $0.09Ti^{4+}$ respectively. The dimensions of each segment are 10 x 3 x1 mm for the length, width, and depth, respectively. Figure 5.9b shows the dynamic transitions of the anti-counterfeiting label following UV excitation. During and immediately after the excitation is ceased, the dynamic pattern displays '8 8 8 8', in red that remains up to 2.5 s post excitation.

The display then changes to '3 3 3 3' after the two left-side segments marked ① and ② of each digit containing the shortest PersL Gd_2O_2S: $0.06Eu^{3+}$ is exhausted. Next, the two lower horizontal segments marked ③ and ④ containing Gd_2O_2S:$0.06Eu^{3+}$, $0.01Ti4^{+}$ fade away after 7.5 s leading to a '7 7 7 7' display. Segments displaying '7 7 7 7' at are those that contain the longest PersL phosphors Gd_2O_2S: $0.06Eu^{3+}$, $0.09Ti4^{+}$ and the pattern are observable even after 10 s.

The above analysis is an overt feature of the labels that are also directly observable by the naked eye following 375F nm UV excitation. The transition would ideally be clear to an observer that upon 375 nm excitation the anti-counterfeiting label changes from a '8 8 8 8' to '3 3 3 3' and finally to a '7 7 7 7' display in red. This could be easily counterfeited, as only three sets of different phosphors are needed to clone the labels. However, by covertly identifying the PersL lifetime from the analysis of the smartphone-acquired videos at various segments of the label, the security level of the label is highly enhanced. Note that in this case, a simple dynamic model with repeatable phosphors in each segment has intentionally been selected; each segment can ideally have a unique persistent phosphor.

Figure 5.9c displays the lifetimes of the phosphors in the segments indicated in the inset picture of one of the seven-segment numbers. These lifetimes are 1.16 ± 0.02, 3.18 ± 0.04, and 5.93 ± 0.07 s for Gd_2O_2S: $0.06Eu^{3+}$, Gd_2O_2S: $0.06Eu^{3+}$, $0.01Ti4^{+}$ and Gd_2O_2S: $0.06\ Eu^{3+}$, $0.09Ti^{4+}$, respectively and agree well with the PersL lifetime of the phosphors shown in Figure 5.6c.

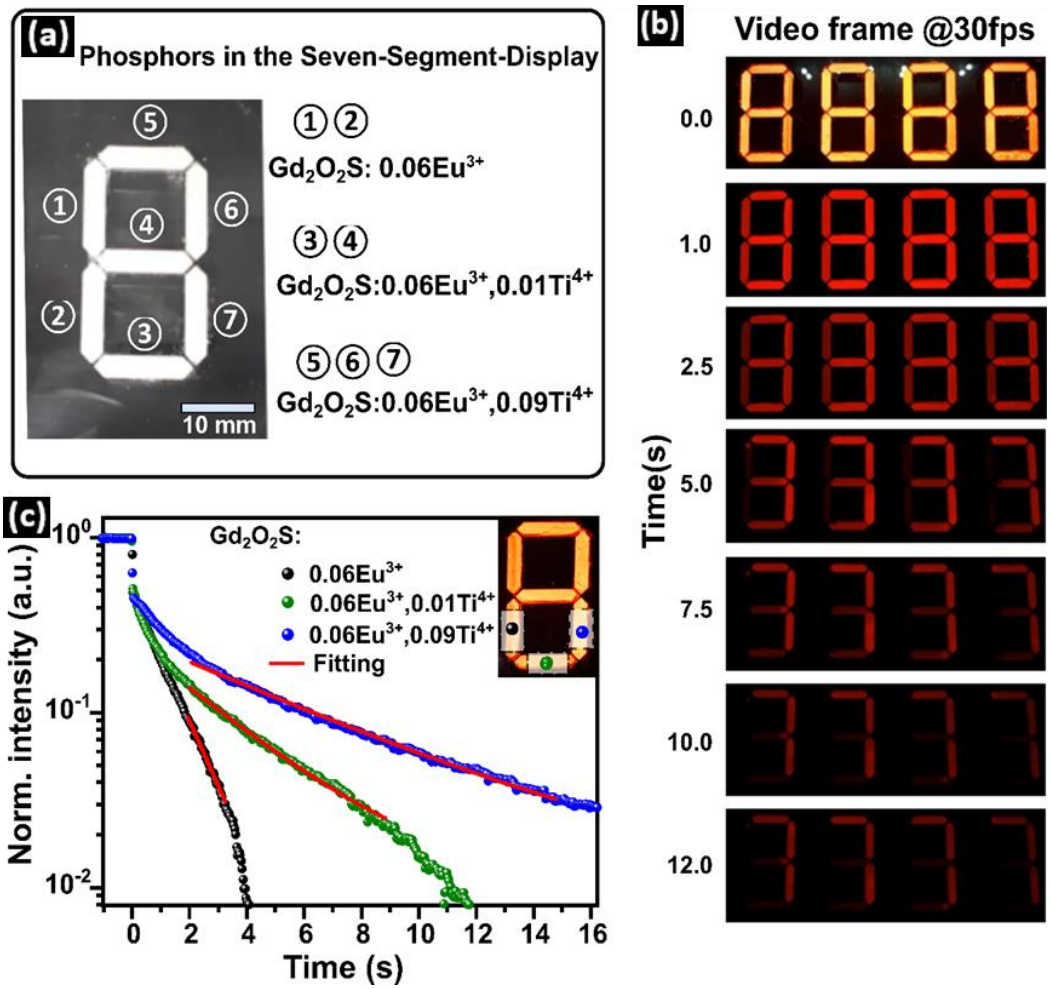

Figure 5.9. a) Information indicating the specific phosphors pressed on each of the seven-segment four-digit display. b) Video frames of interest extracted from smartphone-acquired videos of Gd_2O_2S: $0.06Eu^{3+}$, xTi^{4+} for (x = 0, 0.01 and 0.09 mol) demonstrating dynamic luminescence for anti-counterfeiting applications in a seven-segment four-digit display filled with the phosphors. Upon UV excitation, a "8 8 8 8" pattern is displayed and it changes to "3 3 3 3" after the PersL of Gd_2O_2S: $0.06Eu^{3+}$ is completely exhausted after ~5 s. The display later transitions to "7 7 7 7" when the Gd_2O_2S: $0.06Eu^{3+}$, $0.01Ti^{4+}$ exhausts its luminescence. The final displayed "7 7 7 7" comes from the PersL of the Gd_2O_2S: $0.06Eu^{3+}$, $0.09Ti^{4+}$ that has the longest PersL. c) PersL lifetime of the three phosphors as extracted from the first digit in segments ②, ③, and ⑦ as mapped in the inset figure with the legend colors after excitation with UV (375 nm) LED. Reproduced from Katumo et al. [11]. CC BY-ND 4.0 license.

By extending the quantitative authentication possibilities to utilize the PersL lifetimes, the security of the anti-counterfeiting labels, and their difficulty to clone are enhanced. In a broader perspective, the authentication process using a smartphone allows the determination of the PersL lifetimes in selected ROI to confirm the authenticity of the tagged product. An extension to this is the use of a smartphone app, such as the one demonstrated by Ramalho *et al.* for anti-counterfeiting and product tracing [37].

5.5.2 Inkjet-Printed Labels

In a bid to explore mass reproduction possibilities, inkjet printing of the label was explored. To start, inks consisting of 20mg/mL solution of Gd_2O_2S: 0.06 Eu^{3+}, 0.03Ti^{4+}, Gd_2O_2S: 0.06 Eu^{3+}, 0.06Ti^{4+} and Gd_2O_2S: 0.06Eu^{3+}, 0.09 Ti^{4+} in Terpineol were developed. An SEM representative phosphor image of Gd_2O_2S: 0.06 Eu^{3+}, 0.06Ti^{4+} depicting the size of the phosphor particles is shown in Figure 5.10. The zoomed-in image alongside is from the marked rectangle. The SEM images show that the phosphors particles are loosely clustered and have quasi-spherical shapes with a broad distribution of ~0.2 to 5 µm. To avoid clogging in the Dimatix DMP-2831 inkjet printer cartridges, the inks are filtered with 10, 5, and then 2.7 µm syringes.

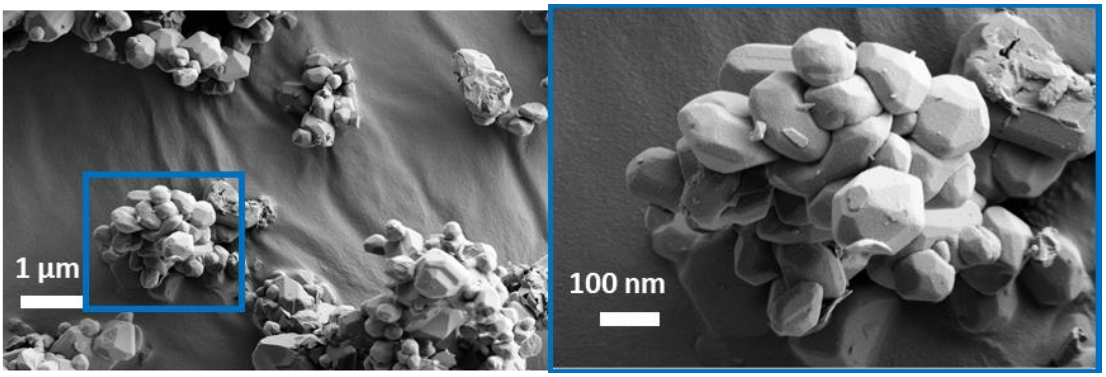

Figure 5.10. Representative Scanning electron Microscope (SEM) images of Gd_2O_2S: 0.06Eu^{3+}, 0.06Ti^{4+} showing loosely clustered quasi-spherical shaped particles with a broad distribution of ~ 0.2 – 5 µm. The zoomed-in image is from the mapped small rectangle. Reproduced from Katumo et al. [11]. CC BY-ND 4.0 license.

Figure 5.11 shows the SEM images of the dried-sieved ink. From the SEM images, it is clear that the sieved particles of Gd_2O_2S: Eu^{3+}, Ti^{4+} phosphors dispersed in the Terpineol clustered together. This is clearer in the zoomed-in image marked by the rectangle. To avoid clustering, and subsequent clogging of the printing cartridge, the inks were ultra-sonicated for 1 h before inkjet printing the patterns.

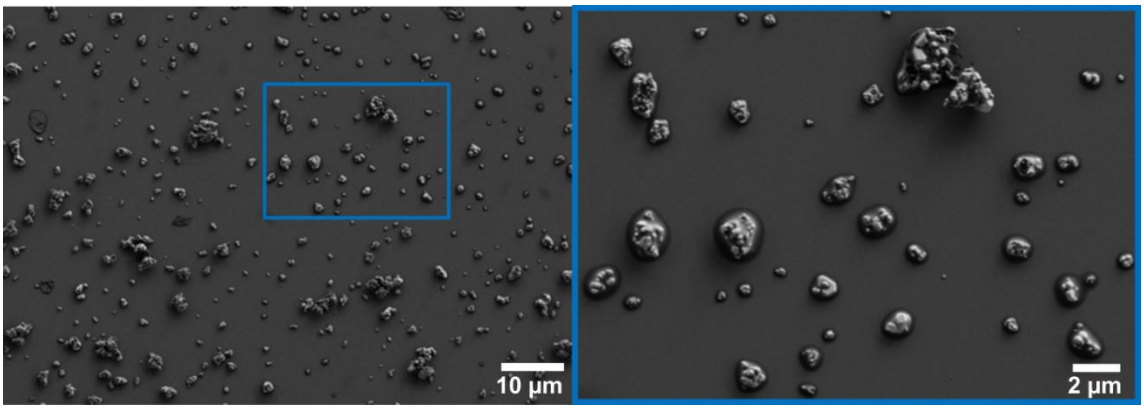

Figure 5.11. The SEM images of the dried ink, containing the Gd_2O_2S: $0.06Eu^{3+}$, $0.09Ti^{4+}$ showing the distribution of the phosphor particles in the ink. Particle agglomeration of the phosphors is observed in the dried clusters of the zoomed-in region. Reproduced from Katumo et al. [11]. CC BY-ND 4.0 license.

Figure 5.12 illustrates the inkjet printing process of developing the labels. The representative label is a pattern containing the concealed information 'IMT'. The labels are printed on plasma-treated glass. The 'IMT' pattern is first printed using the first cartridge with the Gd_2O_2S: 0.06 Eu^{3+}, $0.09Ti^{4+}$ based ink. To conceal the pattern, a masking pattern is then printed using a second cartridge containing the Gd_2O_2S: 0.06 Eu^{3+}, $0.03Ti^{4+}$ based ink. Note that the Gd_2O_2S: 0.06 Eu^{3+}, $0.09Ti^{4+}$ based ink here has a longer PersL lifetime compared to the Gd_2O_2S: 0.06 Eu^{3+}, $0.03Ti^{4+}$ based ink. After printing, the labels are allowed to dry on the Dimatix DMP-2831 inkjet printer plate that is maintained at 65°C to speed up the ink drying process and avoid the printed ink from spreading. In the absence of UV excitation, i.e., in normal lighting conditions, the patterns are observed as a batch of white dots. However, upon 375 nm excitation, these dots emit bright red.

When the excitation source is removed, the pattern formed by the Gd_2O_2S: 0.06 Eu^{3+}, 0.03Ti^{4+} based ink fades away faster than the ones based on the Gd_2O_2S: 0.06 Eu^{3+}, 0.09Ti^{4+} based ink leading to the 'IMT' pattern being observed as shown in Figure 5.12b. For authentication, binarization of the still frames at the targeted timestamp reveals the hidden feature of the anti-counterfeiting pattern as shown in the binarized image.

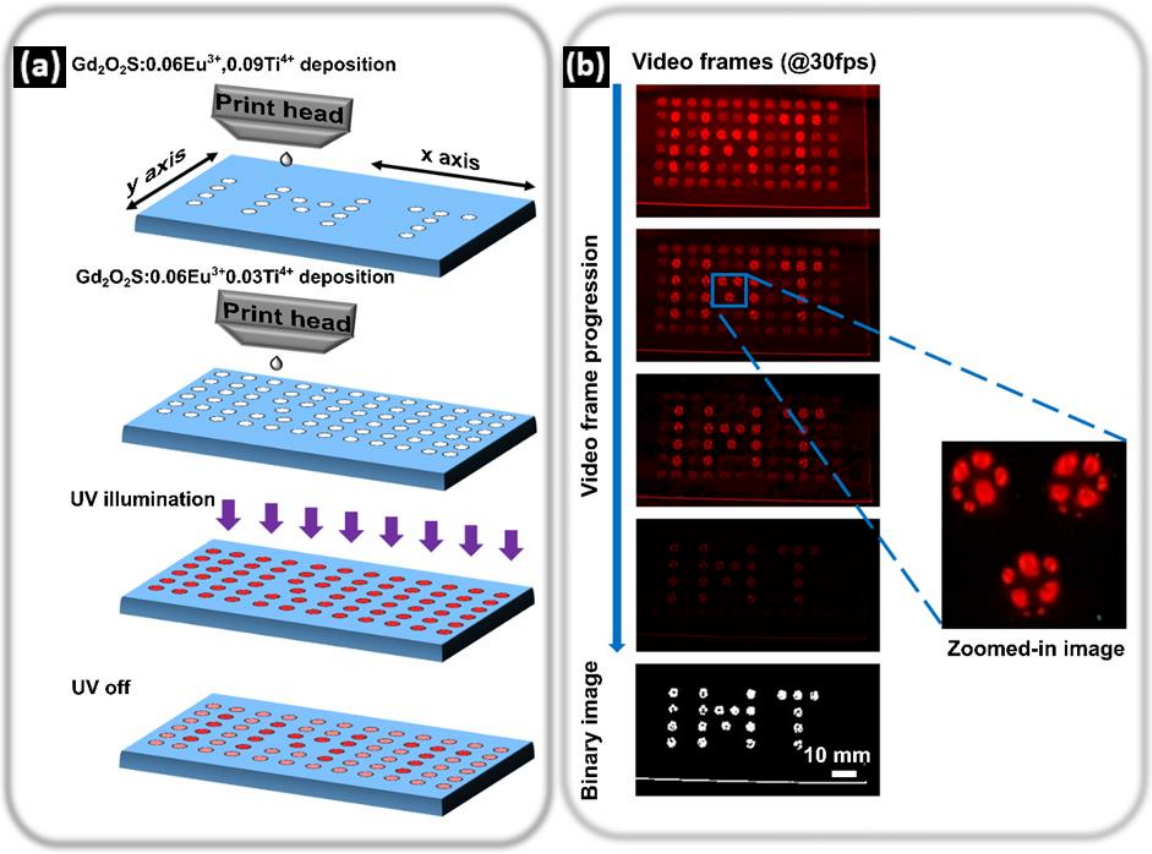

Figure 5.12. a) Schematic of the process of inkjet-printing "I M T" patterns using Gd_2O_2S: 0.06Eu^{3+}, 0.09Ti^{4+} and Gd_2O_2S: 0.06Eu^{3+}, 0.03Ti^{4+} persistent phosphor inks b) Frames of video progression of the label after UV illumination showing initial brightness of the prints followed by subsequent different rate PL lifetime decay that reveals the "I M T" label. A binary image visualizing the "I M T" logo representing the Gd_2O_2S: 0.06Eu^{3+}, 0.09Ti^{4+} phosphor. The zoomed-in image shows the possibility of having unique physical architectures (cat-like-footprints) for enhanced physical masking of the anti-counterfeiting label. Reproduced from Katumo et al. [11]. CC BY-ND 4.0 license.

Therefore, the printed dots are unique, as demonstrated using the zoomed-in image, further revealing the possibility to integrate the smartphone-readable temporal anti-counterfeiting labels with other anti-counterfeiting technologies such as those utilizing PUFs [59, 258]. Nevertheless, inkjet printing of the micron-sized particles is challenging and alternative printing methods for such particles should be sought.

5.5.3 Drop-Casted Labels

The authenticity of the labels presented in the last two sections can be read either by the naked eye or from the location-dependent PersL lifetime analysis determined from the acquired videos. To enhance the level of security of the labels, such that it is hard to distinguish them by the naked eye, phosphors with close PersL lifetimes are used to develop the labels using a drop-casting technique. The set of three phosphors used for this demonstration is Gd_2O_2S: $0.06Eu^{3+}$, $0.0025Ti^{4+}$, Gd_2O_2S: $0.06Eu^{3+}$, $0.005Ti^{4+}$ and Gd_2O_2S: $0.06Eu^{3+}$,$0.005Ti^{4+}$ and their PersL lifetimes are 1.27 ± 0.02 s, 1.41 ± 0.02 s and 1.65 ± 0.02 s, respectively. To drop cast the phosphors into patterns, they are dispersed in polyvinylpyrrolidone (PVP) solution containing 70% ethanol and 30% water.

Figure 5.13a shows the drop-casted schemes of the dynamic anti-counterfeiting labels. For each label, two sets of phosphors that exhibit similar short PersL lifetimes are utilized to make flower-like anti-counterfeiting labels. The labels are drop-casted on glass slides that are maintained at 65 °C in order to accelerate the drying process and minimize the spreading effect of the dropped suspension. In Figure 5.13b, (label A) only Gd_2O_2S: $0.06Eu^{3+}$, $0.005Ti^{4+}$ phosphor is used to make the label. For label B, the phosphors with the longest PersL lifetime Gd_2O_2S: $0.06Eu^{3+}$, $0.0075Ti^{4+}$ are drop-casted to form a ‘G’ pattern with the other dots being camouflaged with the Gd_2O_2S: $0.06Eu^{3+}$, $0.005Ti^{4+}$ based ink. In Label C, the Gd_2O_2S: $0.06Eu^{3+}$, $0.0025Ti^{4+}$, shortest PersL phosphor is used in the ‘G’, position, while Gd_2O_2S: $0.06Eu^{3+}$, $0.005Ti^{4+}$ is used to form the other dots.

Upon excitation with 375 nm, it is quite difficult to detect the concealed pattern in label C by eye and distinguish it from label A. This is unlike label B in which the pattern is observable through a direct eye examination. The time evolution of label

C is not only difficult to resolve by eye but also difficult to distinguish from label A. Apart from the pattern being concealed in the short-lived phosphor, it is also natural for the eye to neglect the few dim points forming the pattern and focus on the bright points leading to label confusion with label A.

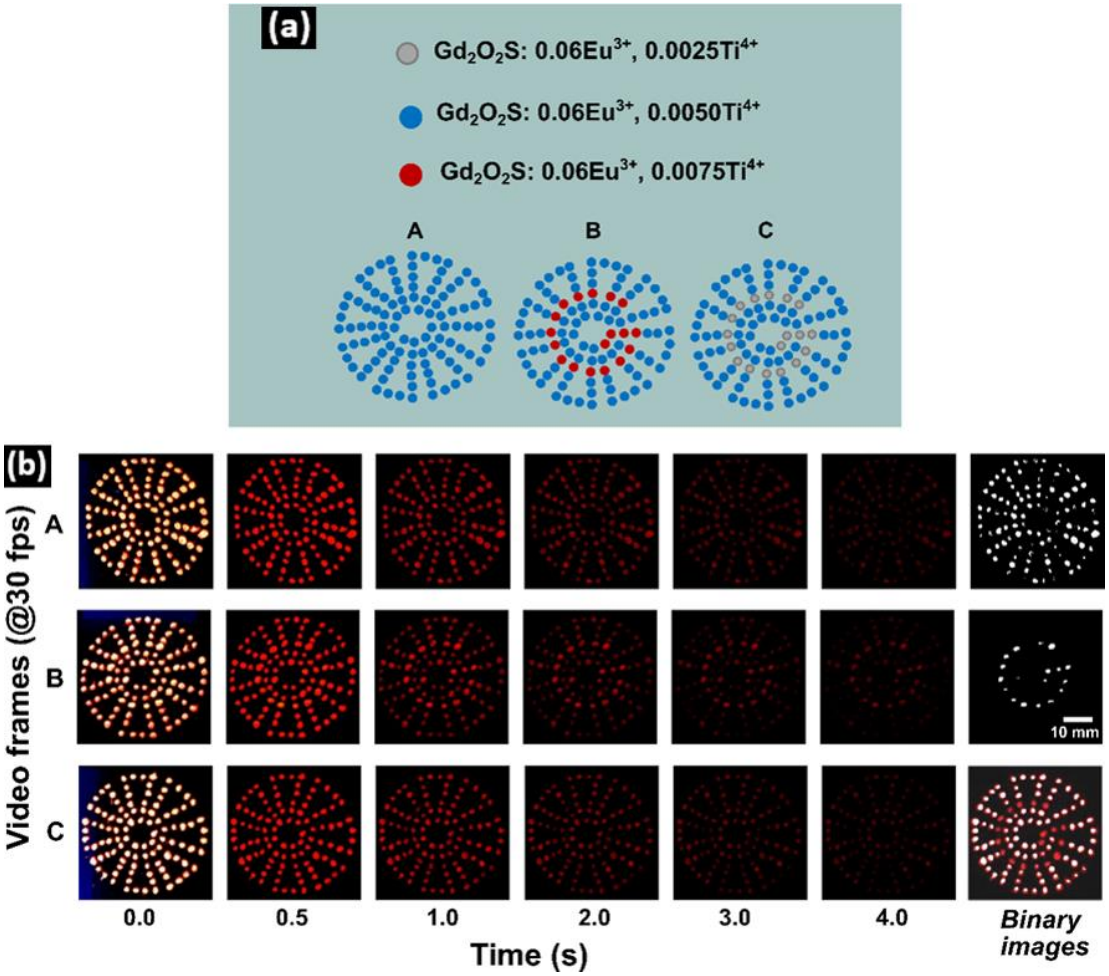

Figure 5.13. Dynamic anti-counterfeiting labels based on analysis of still images from smartphone acquired videos. a) Schematic of the three label patterns created indicating the persistent phosphors contained in the patterns depicting dynamic anti-counterfeiting. b) Frames extracted from smartphone videos of each label, the hidden image is obtained by making a binary image with an appropriate threshold from the 4 s image (label "B"), or using such a binary image to mask the image collected at 0.5 s (label "C"). Reproduced from Katumo et al. [11]. CC BY-ND 4.0 license.

However, by analyzing the still-frames of a video acquired using a smartphone, it is possible to determine and distinguish the three patterns accurately as shown in their binary images. The G pattern in label B is clear after the video frame at 4 s is binarized. For label C, the binarization creates a mask that reveals the pattern when applied to the still image during excitation.

The labels herein indicate that tunable persistent emission has the potential to provide high-level intricacy for anti-counterfeiting applications. For these labels, the dynamic change of the patterns can ideally be made impossible to observe by the naked eye. However, it is easy to read the patterns from the analysis of the smartphone acquired videos. The analysis is accomplished through either determining the point-based PersL lifetimes or broadly comparing the still images at various time stamps via a binarization process. Taken together, the three patterns demonstrate the uniqueness of using the time evolution of the PersL for anti-counterfeiting.

5.6 Effect of Temperature on the Anti-Counterfeiting Labels

The PersL lifetimes of the phosphors have already been shown to decrease for temperatures above 250 K. A similar situation is therefore expected to surface when the labels are subjected to different temperature conditions. Figure 5.14 shows video frames of interest extracted from smartphone-acquired videos after the seven-segment display after UV excitation at 273, 293, and 313 K respectively. Recall that this label is based on the Gd_2O_2S: $0.06Eu^{3+}$, Gd_2O_2S: $0.06Eu^{3+}$, $0.01Ti^{4+}$, and Gd_2O_2S: $0.06Eu^{3+}$, $0.09Ti^{4+}$ PersL phosphors.

In general, all the patterns show ‘8 8 8 8’ in red for the first one-second post UV excitation. The display then changes to ‘3 3 3 3’ after the PersL of the short-lived Gd_2O_2S: $0.06Eu^{3+}$ is exhausted. Afterward, the ‘3 3 3 3’ changes to ‘7 7 7 7’ after the Gd_2O_2S: $0.06Eu^{3+}$, $0.01Ti^{4+}$ stops its emission. All these changes occur first in the label maintained at 313 K obviously due to the faster rates of decay. In fact, at 7.5 s the label only shows ‘7 7 7 7’ with no traces of the horizontal bars leading to the ‘3 3 3 3’ display. This is contrary to the other bars at 273 K and 293 K which, although showing ‘7 7 7 7’, have a minute trace display of the two horizontal bars forming the ‘3 3 3 3’. Therefore, as expected, at higher temperatures the dynamic changes occur at a faster rate.

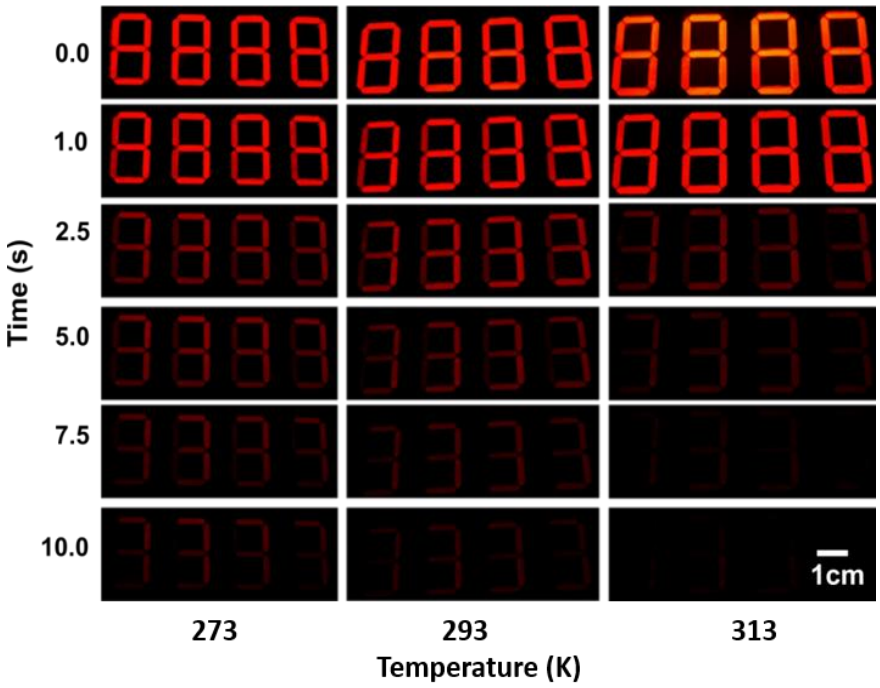

Figure 5.14. Video frames of interest extracted from smartphone-acquired videos of Gd_2O_2S: $0.06Eu^{3+}$, xTi^{4+} for (x = 0, 0.01 and 0.09 mol) demonstrating dynamic luminescence for anti-counterfeiting applications in a seven-segment four-digit display filled with the phosphors excited at 273, 293 and 313 K. Reproduced from Katumo et al. [11]. CC BY-ND 4.0 license.

The data displayed from the three temperature regimes indicate that the patterns are usable throughout the annual and regional temperatures globally. This is of course true if the authenticator has to map the PersL lifetime at the right temperature, else the visual inspection of the dynamic change in the pattern can be relied on.

5.7 Ultraviolet Photostability Studies

Photostability of luminescent anti-counterfeiting labels is a key parameter in measuring their shelf life. For UV excitable labels, stability against UV excitation is vital. To have an insight into the UV stability of the phosphors, three samples: Gd_2O_2S: $0.06Eu^{3+}$, $0.001Ti^{4+}$, Gd_2O_2S: $0.06Eu^{3+}$, $0.03Ti^{4+}$ and Gd_2O_2S: $0.06Eu^{3+}$, $0.09Ti^{4+}$ were continuously illuminated with a 365 nm UV light (Herolab GmbH, Type NU-8, 8 W, emission: 365 nm) at 500 µW/cm^2 irradiation. During the continuous illumination, the PersL lifetime is checked periodically by turning off the UV light source and video recording the PersL decay with a smartphone.

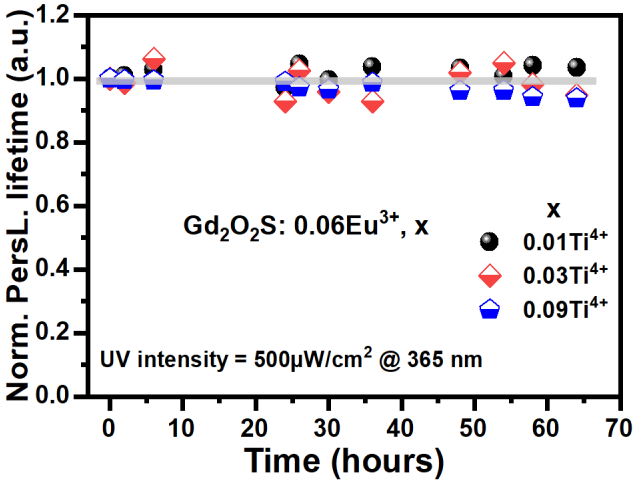

Figure 5.15. The normalized lifetimes of Gd_2O_2S: 0.06Eu^{3+}, 0.01Ti^{4+}, Gd_2O_2S: 0.06Eu^{3+}, 0.03Ti^{4+} and Gd_2O_2S: 0.06Eu^{3+}, 0.09Ti^{4+} under continuous UV illumination (365 nm lamp, power density 500 μW/cm²) as a function of time. No photo-degradation is observed from the UV exposure over time. The grey line is a guide to the eye. Reproduced from Katumo et al. [11]. CC BY-ND 4.0 license.

From the analysis of the PersL lifetime, no alteration of the PersL lifetime over the 70 hours was observed as shown in Figure 5.15 [259]. Due to their stability, they also have wide applications in cathodoluminescence, scintillation, bioimaging, security, and now anti-counterfeiting applications [11, 227, 259-263].

5.8 Summary

This chapter explored the use of Gd_2O_2S: 0.06Eu^{3+}, *x*Ti^{4+} persistent phosphors for dynamic anti-counterfeiting following UV excitation. The chapter began by covering the photophysical properties of Gd_2O_2S: 0.06Eu^{3+}, *x*Ti^{4+} that include the PL, PLE, DRS, and its PersL behavior following Ti^{4+} co-doping. By varying the Ti^{4+} co-doping concentration up to 0.09 mol, the PersL lifetime could be tuned from 1.17 ± 0.02 to 5.95 ± 0.07 s. In the same co-doping regime, the PLQY remained above 46%, maintaining a good emission efficiency for the persistent luminescent palette. This property made the persistent phosphor attractive for smartphone-based dynamic anti-counterfeiting applications. The PersL lifetime was also in a 'sweet spot' region of 100 ms - 6 s range for which smartphones cameras could precisely determine it. Such a possibility guaranteed that anyone with a smartphone could easily authenticate tagged products at POS terminals.

Two sets of anti-counterfeiting labels were realized using these phosphors, ones with more significant PersL lifetime differences and others with close PersL lifetimes. For anti-counterfeiting labels based on persistent phosphors with large differences in the PersL lifetime, the dynamic pattern changes of the PersL after 375 nm excitation were visible by the naked eye. Their security was enhanced by having to decode the point-specific PersL from ROI on the labels using the smartphone acquired videos. For the anti-counterfeiting labels developed with a close PersL lifetime, it was almost impossible to resolve the dynamic patterns by the naked eye but they were authenticated from the analysis of smartphone acquired video frames. The use of smartphones for authentication directly added onboard covert features in addition to the overt features verifiable by the naked eyes. While these results are interesting and inspiring as far as PersL for smartphone-based anti-counterfeiting is concerned, developing labels which need only the smartphone as single hardware for excitation, detection, and authentication of the labels would be more promising for POS terminal applications. This approach is explored in the next chapter.

6

Smartphone Authentication of Dual-Color Dynamic Anti-Counterfeiting Labels

This chapter presents the results of dual-color dynamic anti-counterfeiting labels that are excited with a smartphone flashlight and authenticated from smartphone acquired videos. The anti-counterfeiting labels are based on green-emitting $SrAl_2O_4$: Eu^{2+}, Dy^{3+} (SAED), and red-emitting CaS: Eu^{2+} and SrS: Eu^{2+} persistent phosphors. The results discussed herein are based on the following first author publication and co-authored patent.

***Katumo, N.**, Li, K., Richards, B. S., & Howard, I. A. (2022). Dual-color dynamic anti-counterfeiting labels with persistent emission after visible excitation allowing smartphone authentication. Scientific Reports, 12(1), 1-14 [35].*

*Kai L., **Katumo, N.**, Howard, I. A.**,** Richards, B. S., Busko, D., Turshatov, A., Photonic markers enabling security marking, product identification, and material sorting using low frame rate cameras' 102021003206.3 (Patent Pending).*

The research concept was conceived by the first author in conjunction with Dr. Ian Howard as a continuation of the previous work on smartphone-based anti-counterfeiting applications. The core objective was to develop anti-counterfeiting labels based on persistent phosphors that could be excited with a smartphone flashlight and have the dynamic patterns video-recorded using its camera. This then would bring on board labels that compete with 2D barcodes and holograms as only the smartphone would act as the authenticating hardware.

6.1 Introduction

Anti-counterfeiting systems that allow the use of a smartphone device as the only hardware component in the authentication process are attractive and convenient [8, 11, 36, 68, 187, 191]. The reason is their simplicity of use, availability, and ease of integration to POS terminals. As a result, most of the luminescence-based approaches in anti-counterfeiting, are aimed at using the smartphone as the authentication device for their labels [11, 35, 264].

However, to realize smartphone-only authentication on luminescence-based anti-counterfeiting labels, as already discussed, the phosphors used in developing these labels have to absorb and emit in the visible region. More so, to achieve a dynamic shift in the emission pattern of the anti-counterfeiting labels, the labels should contain phosphors with varied persistent lifetimes that remain bright enough during the persistent process. Three of the phosphors used here that meet these criteria are SAED, CaS: $Eu^{2+,}$ and SrS: Eu^{2+}.

For anti-counterfeiting applications, rather than having a fixed PersL character of the phosphor, a pallet of PersL lifetime is created to ensure dynamic patterns are realized post excitation. For the SAED persistent phosphors, this was realized by annealing the commercial phosphor in the air at various temperatures to intentionally distort the trap density and depth and tune the PersL for dynamic anti-counterfeiting applications. Throughout this work, the SAED phosphor samples used are labeled according to the annealing in air temperature (in units of ^{o}C). For

instance, SAED phosphors annealed at 700 °C, 800 °C, 810 °C, 820 °C, and 830 °C are named SAED (700), SAED (800), SAED (810), SAED (820), and SAED (830), respectively. Representative phosphor images from smartphone-acquired video frames following smartphone flashlight excitation are shown in Figure 6.1. For SAED, the three phosphor materials demonstrated are SAED (810), SAED (830), and SAED (850). Increasing the annealing temperature leads to reduced persistent luminescence. Due to the high annealing temperature, the initial brightness of SAED (850) does not reach saturation and is dim from the start.

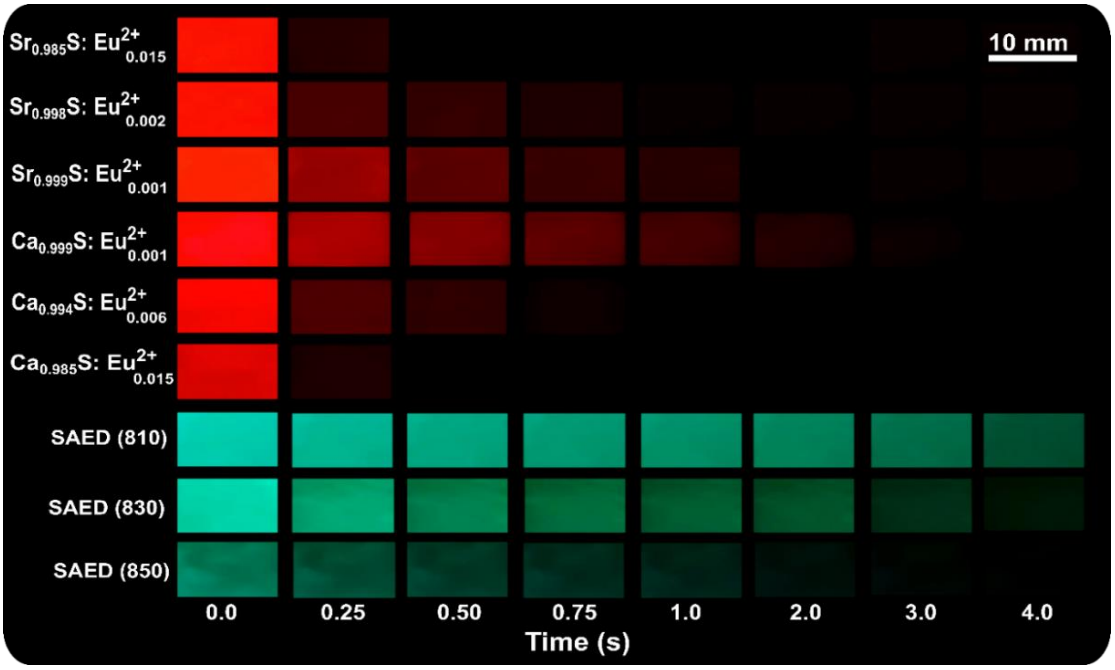

Figure 6.1. Still frames acquired at indicated times after smartphone flashlight excitation is stopped for red phosphors $Ca_{0.999}S: Eu^{2+}_{0.001}$, $Ca_{0.994}S: Eu^{2+}_{0.006}$, $Ca_{0.985}S: Eu^{2+}_{0.015}$ and $Sr_{0.999}S: Eu^{2+}_{0.001}$, $Sr_{0.992}S: Eu^{2+}_{0.002}$ and $Sr_{0.985}S: Eu^{2+}_{0.015}$ and green phosphors SAED (810), SAED (830) and SAED (850) visually demonstrating the change in persistent lifetime.

The red-emitting phosphors are based on $Ca_{1-x}S: Eu^{2+}_{x}$ and $Sr_{1-x}S: Eu^{2+}_{x}$ persistent phosphors and their PersL lifetime could be varied from 0.1 – 0.6 s and 0.15 – 0.377 s respectively by varying the Eu^{2+} dopant concentration. Representative still frames of the various phosphors following smartphone excitation are shown in Figure 6.1. The representative red emission for the CaS sample is based on

$Ca_{0.999}S: Eu^{2+}_{0.001}$, $Ca_{0.994}S: Eu^{2+}_{0.006}$ $Ca_{0.985}S: Eu^{2+}_{0.015}$. The SrS samples demonstrated include the $Sr_{0.999}S: Eu^{2+}_{0.001}$, $Sr_{0.998}S: Eu^{2+}_{0.002}$ and $Sr_{0.985}S: Eu^{2+}_{0.015}$ samples. Further, by increasing the Eu^{2+} doping concentration the PersL decreased.

6.2 Smartphone Authentication Process

Keeping in mind that the prerequisites of smartphone-only authentication are fulfilled, label authentication would proceed as illustrated in Figure 6.2. For this demo, a four-digit seven-segment anti-counterfeiting label that has dual-color dynamic anti-counterfeiting patterns based on SAED, CaS: $Eu^{2+,}$ and SrS: Eu^{2+} phosphor blends is used. Before the authentication process, the authenticating parameters are preset, to which the label results have to agree, otherwise, the label is not authentic.

The authentication process starts with the tuning of the video recording function of the smartphone, followed by illumination with a smartphone flashlight for 5 s with continuous video capture of the emission for another10 s. The acquired PersL patterns show a ‘8 8 8 8’ initially observed in red for the raw video, with the segments transitioning to green at various times of the persistent emission leading finally to a ‘7 7 7 7’ on the display. In this case, the authenticating patterns are set for the pattern at zero and 0.75 s for the red channel and 3 s for the green channel. Now, when the red and green channels are split, the channel transitions are observed to have different transitions with the red channel still frames displaying the observed ‘8 8 8 8’ at the beginning and ‘3 3 3 3’ at 0.75 s after the flashlight is extinguished. This is in agreement with the verification parameters.

On the other hand, the green channel also confirms the verification pattern at 3 s, a green ‘7 7 7 7’ display. Notice that the green channel ‘8 8 8 8’ is concealed at time zero and this would also be an authenticating parameter. Alternatively, other timestamps could also be chosen to widen the verification library. In a practical setting, the complete authentication process would take approximately 15 s to accomplish, making it realistic for product authentication at point of sale (POS) terminals.

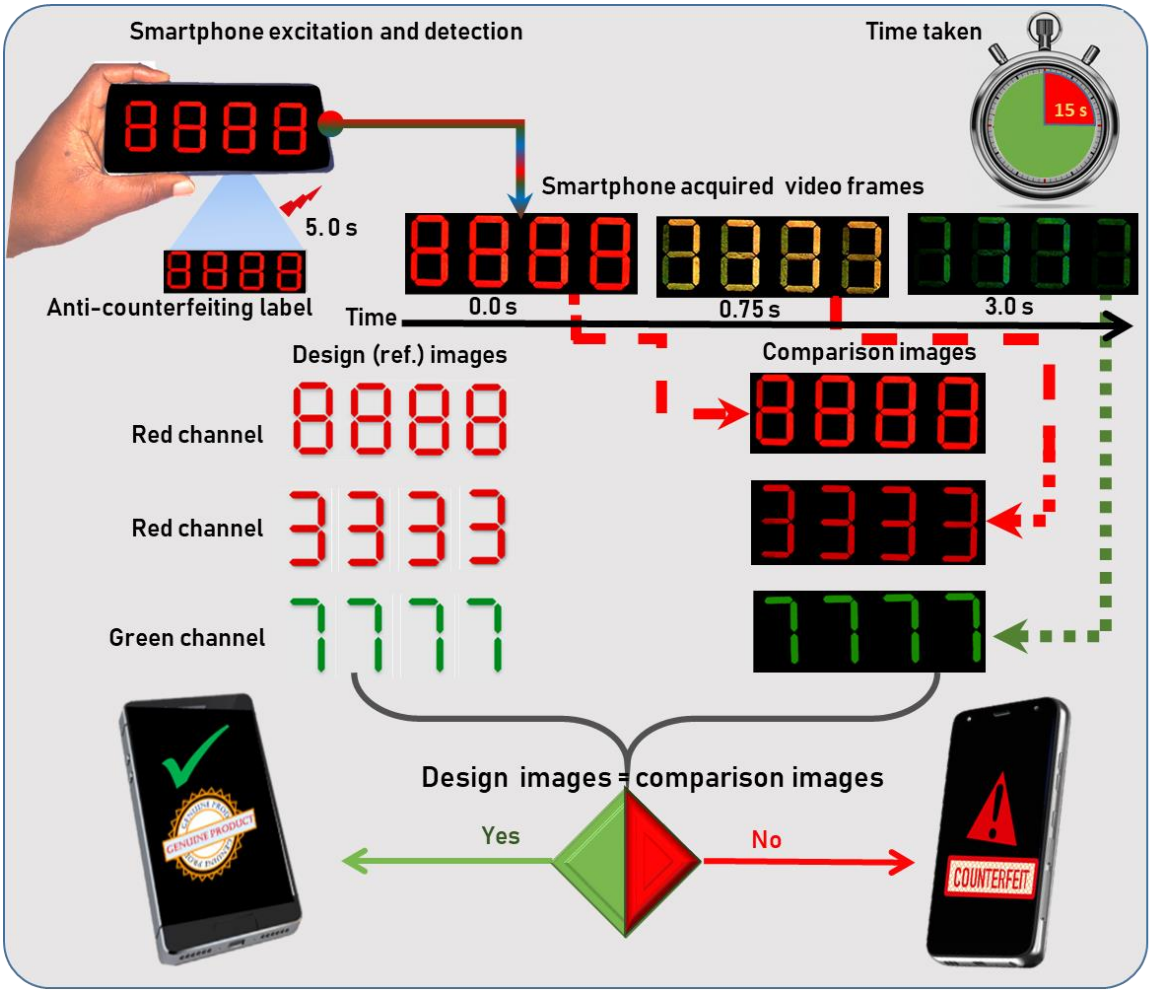

Figure 6.2. Schematic illustration of smartphone-based authentication of dual-color dynamic anti-counterfeiting labels. The smartphone-flashlight first illuminates the label for 5 s and then the persistent emission is video-recorded with the smartphone's camera. The acquired raw video is then split at into the red and green channel and the frames at various timestamps (for red 0.0 and 0.75 s and for green 3.0 s) are compared to the intended design images. If the images of the split frames match with the designed image the product is genuine, else counterfeit. The total time taken for the authentication is less than 15s. Reproduced with permission from Katumo et al. [35]. CC-BY 4.0 License.

6.3 Photophysical Properties of SAED

In this section, the steady-state spectroscopic properties and PersL properties of SAED are discussed. The PL, PLE, DRS, and PLQY for the various samples annealed in the air for SAED are explored and finally, the mechanism of PersL is discussed.

6.3.1 Steady-State PL Studies of SAED

The SAED phosphor is characterized by a strong UV-Vis absorption band that extends beyond 475 nm (monitored at 514 nm) as illustrated in Figure 6.3. The commercial phosphor, defined as SAED (Reference) and abbreviated as SAED (Ref.) has the strongest absorption. Annealing the SAED (Ref.) phosphor in the air led to a narrowing of the absorption band. It is postulated that the narrowing of the absorption band is due to the oxidation of the Eu^{2+} ion to Eu^{3+} ion during the re-annealing of the commercial phosphor in the air [265, 266]. This narrowing leads to a reduced excitation band when a smartphone flashlight excitation component is used for illumination. The strong absorption band in all the samples is due to the electric dipole that allowed the $4f^{6}5d \rightarrow 4f^{7}$ transition of the Eu^{2+} ions [267].

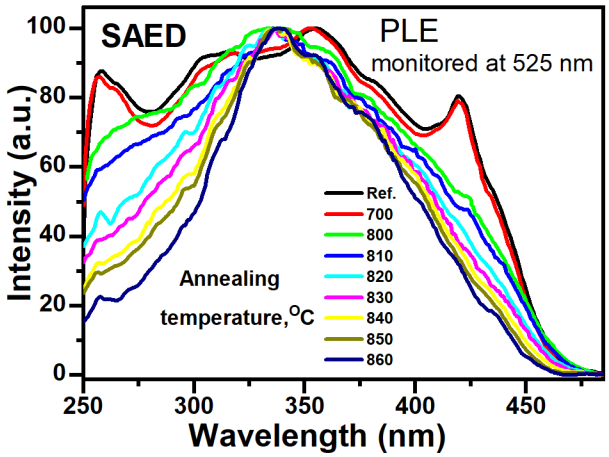

Figure 6.3. The PLE of SAED 250-500 nm showing the narrowing of the absorption band as the annealing in air temperature is increased from 700 to 860 °C. Reproduced from Katumo et al. [35]. CC-BY 4.0 License.

The SAED phosphors are excited using a smartphone flashlight leading to the broadband emission as illustrated in Figure 6.4. Cutting across the absorption and emission spectra of SAED are the smartphone flashlight spectra that has two peaks, one centered at 450 nm and the other centered at 580 nm. In the majority of smartphones, the flashlight is based on an indium gallium nitride (InGaN) or gallium nitride (GaN) LED with an emission peak at 450 nm whose blue light is converted to longer wavelengths by downshifting phosphors (YAG: Ce^{3+}) incorporated in the LED coating [246].

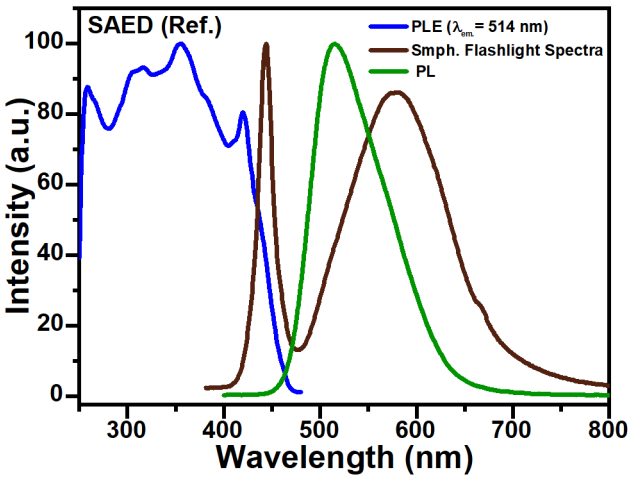

Figure 6.4. The PLE spectrum (monitored at 514 nm) of SAED (Ref.) alongside the spectrum of a smartphone-flashlight (Smph. Flashlight Spectra.) (Brown line) and the PL emission spectra after smartphone flashlight excitation. The overlap of the smartphone flashlight spectra with the absorption is just sufficient to allow smartphone excitation of the SAED persistent phosphors. Reproduced from Katumo et al. [35]. CC-BY 4.0 License.

Notice that the smartphone flashlight spectra coincide with the tail of the SAED phosphors (monitored at 514 nm) that extends from 250 to 450 nm due to the $4f^7 \rightarrow 4f^65d^1$ transition of Eu^{2+} ion [267]. The observed broadband emission, centered at 514 nm is due to the $4f^7 – 4f^65d^1$ transition of the Eu^{2+} ion (green line in Figure 6.4).

The PLQY values of the SAED persistent phosphors are illustrated in Figure 6.5. The SAED (Ref.), SAED (700), SAED (800), SAED (810), and SAED (820) registered PLQY values above 11 ± 0.5 %. Annealing the SAED phosphor beyond 810 ^oC led to a gradual decrease in the PLQY with the SAED phosphors annealed at 860 ^oC registering a low PLQY of 2 %. The mechanism of the gradual decrease in PLQY due to annealing in the air for the SAED is discussed in the next section.

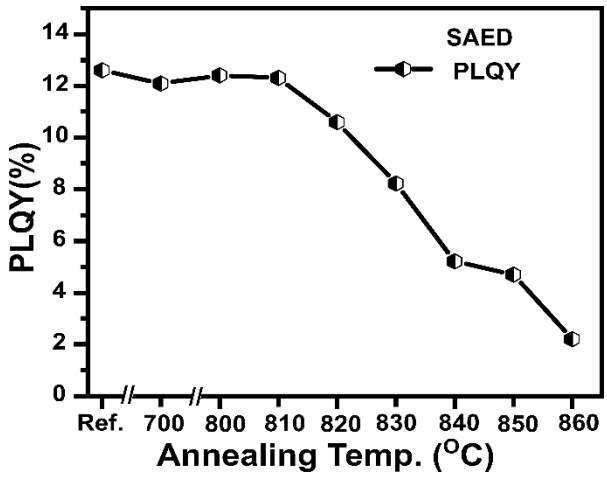

Figure 6.5. The steady state PL quantum yield (PLQY) following 450 nm excitation and persistent lifetime values of SAED samples that are annealed in air for one hour.

6.3.2 PersL Lifetime of SAED

The PersL lifetime was determined from the analysis of acquired smartphone videos after smartphone flashlight excitation for 5 s. For each fitting, a time boundary was defined. A representative procedure using SAED (820) is presented herein for which boundaries t_1 and t_2 are shown in Figure 6.6a.

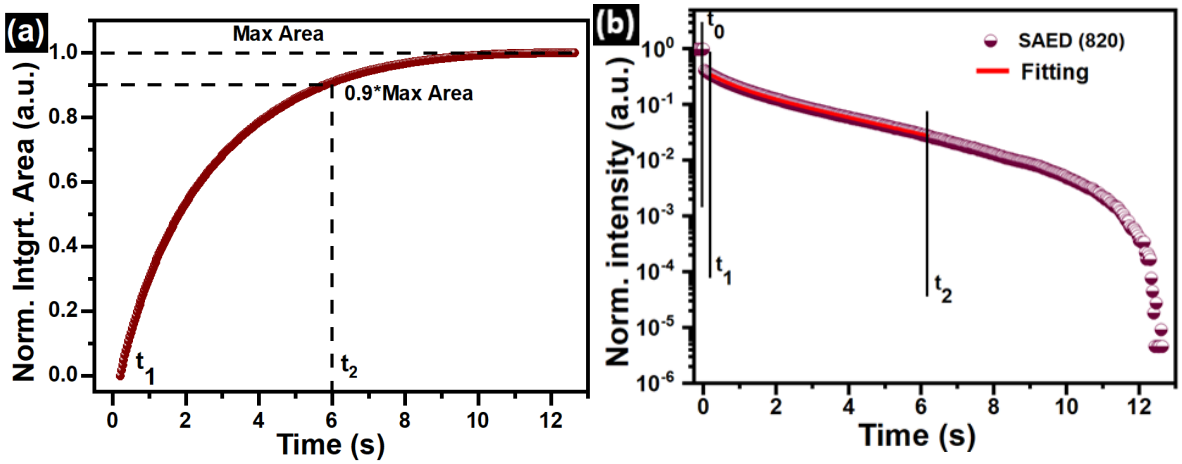

Figure 6.6. PersL lifetime fitting. (a) The computed integrated area of the persistent luminescence of SAED (820) as a function of time to identify boundary time t_2 at 90 % exhaustion of the emission. (b) Representative fitting in the t_1 and t_2 region for SAED (820).

The first boundary t_1 is globally taken to be 0.2 s after the excitation ceased, while the second boundary t_2 is taken to be the time coinciding with the point at which the phosphor has exhausted 90 % of its emission. In this particular case, this t_2 is 6.06 s. For this determined fitting region, a double exponential fitting for the SAED (820) progresses as illustrated in Figure 6.6b. Note that the endpoint of the fitting t_2 keeps changing for each phosphor with a different PersL lifetime.

For the SAED phosphors annealed below 830 °C, a double exponential fit is used in the fitting while those annealed at 840 °C and above are fitted using a single exponential equation given in the following equation:

$$I = I_o + \sum_{i=1}^{2} A_i \exp\left(-t/\tau_i\right) \tag{6.1}$$

where τ_i are the characteristic lifetimes, A_i are their respective coefficients and I_o is an offset. The average persistent lifetime $\bar{\tau}$ was estimated using:

$$\bar{\tau} = \sum_{i=1}^{2} A_i \times \tau_i^2 \Big/ \sum_{i=1}^{2} A_i \times \tau_i \tag{6.2}$$

The persistent lifetime of the SAED phosphors gradually decreases with an increase in annealing-in-air temperature as illustrated in Figure 6.7a. The gradual decrease in the persistent emission provides the desired PersL lifetime palette for realizing dynamic patterns. The obtained PersL lifetime of the various SAED phosphors is shown in Figure 6.7b. For purposes of discussion, the PLQY from Figure 6.5 is superimposed on Figure 6.7b**.** The SAED (ref.) registered a persistent lifetime of 11.7 s and this gradually decreased up to 0.5 s for the SAED (860). While the annealing in the air led to a gradual decrease in the persistent luminescence, the PLQY first remained relatively flat, registering values above 10 % for up to SAED (820) before drastically reducing to a low of 2 % for the SAED (860). By annealing the SAED(Ref.) phosphor in air, non-radiative Eu^{3+} ions are formed that effectively reduce the trap density and depth coordination thereby reducing the emission intensity (see Figure 6.1) and PersL lifetime.

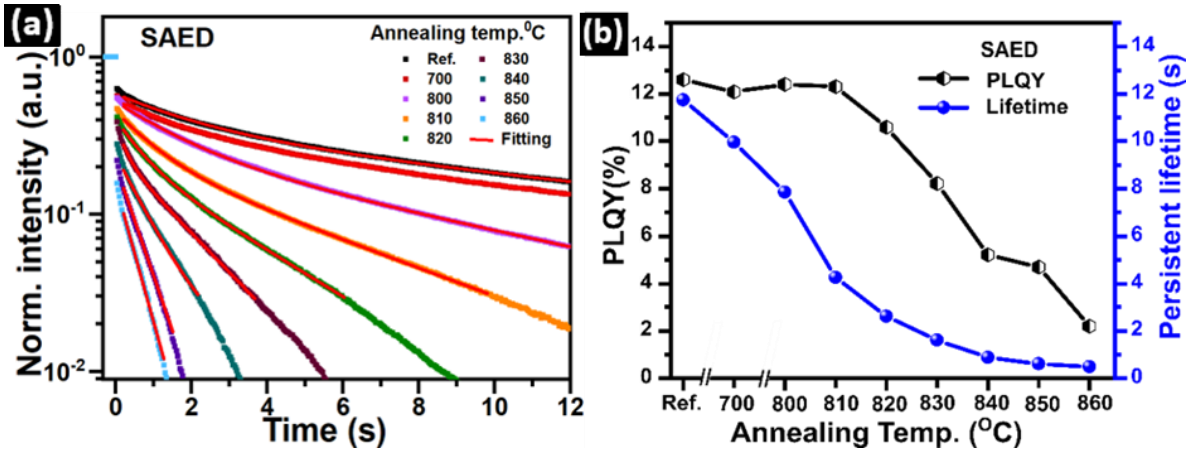

Figure 6.7. a) Persistent decay of SAED phosphors annealed at 700 - 860 ^{o}C for one hour in air. Re-firing the phosphors in air decreases the persistent luminescence decay of the SAED phosphors. For phosphors annealed at 820 ^{o}C and below, a double exponential fitting is used while for phosphors annealed in air at 820 ^{o}C and above the persistent decays are fitted using a single exponential. b) The steady state PL quantum yield (PLQY) following 450 nm excitation and persistent lifetime values of SAED samples that are annealed in air for one hour. Reproduced with permission from Katumo et al. [35]. CC-BY 4.0 License.

6.3.3 Proposed SAED PersL Mechanism

The spectroscopic data on SAED presented so far indicate that annealing the SAED phosphor in the air gradually led to reducing PLQY, decreasing PersL, and decreasing absorption band. For all the SAED phosphors, the Eu^{2+} remained the active optical emitter center. With a special focus on the current literature on the nature of PersL in this class of materials, the PersL mechanism can be explained in the following fashion.

Following, 450 nm excitation, a part of the excitons are trapped in the trap centers. After the excitation is ceased, these trapped excitons are thermally promoted and recombine Eu^{2+} center sites leading to PersL [268]. Note that the trapping centers are either Dy^{3+} mediated or the oxygen vacancies centers [268-270]. Now, when the SAED (Ref.) is annealed in air, the oxygen vacancies and trap density are reduced due to oxidation of the Eu^{2+} to a non-radiative Eu^{3+} as the temperature is increased. This process then leads to the observed decline in emission and PersL

[265, 271]. In addition, if the formed Eu^{3+} centers were to be radiative, we would expect that during excitation part of the energy at the Eu^{3+} centers is funneled towards the Dy^{3+} ion leading to NIR emission [272]. However, as observed in Figure 6.8, this is not the case as the NIR emission following 450 nm excitation for SAED (820) is much less than that of SAED (ref.) under the same excitation conditions. Nevertheless, due to the lack of sufficient experimental data, it is still acknowledged that the precise mechanism of PersL in SAED is still lacking [16, 270]. While this proposal is not conclusive, the tuning mechanism sufficiently allows the creation of a persistent lifetime palette for dynamic anti-counterfeiting applications.

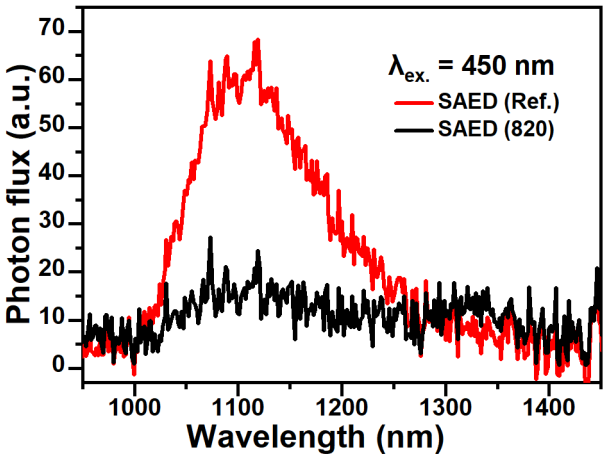

Figure 6.8. Near-infrared PL emission spectra of SAED (Ref.) and SAED (820) following 450 nm excitation. The NIR emission is low for the annealed SAED (820) phosphor. Reproduced from Katumo et al. [35]. CC-BY 4.0 License.

6.4 Photophysical Properties of CaS: Eu^{2+}

Alkaline earth sulfides doped with Eu^{2+} have closely related spectroscopic properties. In this section, the steady-state and temporal PL properties of $Ca_{1-x}S:Eu_x^{2+}$ are discussed. In addition, the temperature-dependent PL and PersL behavior are explored with a focus on understanding the underlying mechanism of varying the PersL lifetime by varying the Eu^{2+} doping.

6.4.1 Steady-State PL Studies of CaS: Eu^{2+}

The PL excitation and emission spectra of $Ca_{1-x}S: Eu_x^{2+}$ showing UV to visible broad absorption (denoted in blue) and broad emission centered at 650 nm is illustrated in Figure 6.9. Alongside is also the smartphone flashlight spectra that efficiently excite the phosphors. As illustrated, the PLE (monitored at 650 nm) extends beyond 600 nm from 300 nm. The most intense absorption however occurs beyond 400 nm and coincides well with the 450 nm excitation of the smartphone flashlight. The Eu^{2+} emission centered at 650 nm is due to the $^4F_6{}^5D_1 \rightarrow {}^4F_7$ allowed electrostatic dipole transition [26].

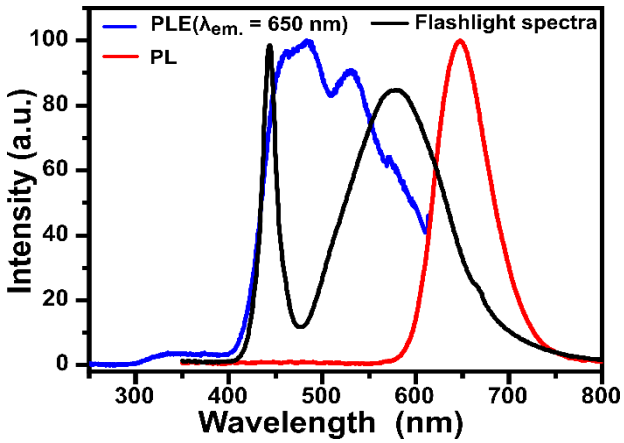

Figure 6.9. The PL excitation spectrum (monitored at 650 nm) and PL emission of CaS: Eu^{2+} alongside that of the exciting smartphone-flashlight. There is substantial overlap of the PL excitation spectra (absorption) with the exciting smartphone flashlight spectra that ensures sufficient phosphor excitation. Excitation with the smartphone flashlight leads to the deep red broad-band PL emission centered at 650 nm. Reproduced from Katumo et al. [35]. CC-BY 4.0 License.

The PLQY of the CaS: Eu^{2+} phosphors for the various Eu^{2+} doping concentrations is shown in Figure 6.10. At first, the PLQY slightly increases from 32 ± 1 % up to 39 ± 1 % for $Ca_{0.9995}S: Eu_{0.0005}^{2+}$ and $Ca_{0.998}S: Eu_{0.002}^{2+}$ respectively after which it gradually decreases, with the highest doped sample, $Ca_{0.085}S: Eu_{0.015}^{2+}$ registering the lowest PLQY of 18 ± 1%. The initial increase in PLQY is in agreement with previous observation of the phosphor in which the PLQY first reaches an optimum doping concentration upon which further Eu^{2+} doping leads to a gradual decrease due to concentration doping [26, 273]. The initial increase is usually due to

optimization of the Eu^{2+}– Eu^{2+} ionic distances in the absorption matrix. The gradual decrease in PLQY is attributed to concentration quenching effects.

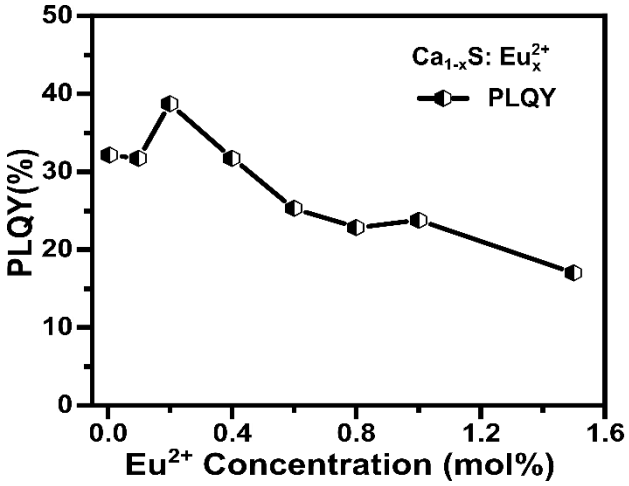

Figure 6.10. The steady state PL quantum yield (PLQY) following 450 nm excitation and persistent lifetime values of CaS: Eu^{2+} samples that are annealed in air for one hour.

6.4.2 TDPL of CaS: Eu^{2+}

Temperature-dependent photoluminescence (TDPL) performed on $Ca_{0.999}S: Eu^{2+}_{0.0001}$, $Ca_{0.996}S: Eu^{2+}_{0.004}$ and $Ca_{0.992}S: Eu^{2+}_{0.008}$ to provide insights into why the PersL lifetime and PLQY decrease with an increase in Eu^{2+} doping concentration. The TDPL results for the 100 – 823 K range are shown in Figure 6.11a-c. The integrated emission decreases with an increase in temperature and is accompanied by a blue shift and an increase in the full-width half maximum (FWHM) of the emission spectra. At lower temperatures, 113 K to 153K, there is a slight increase in the intensity of persistent emission. Throughout the temperature range, the emission remains in the 5d - 4f transition of Eu^{2+}.

A possible explanation for the blue shift is thermally active phonon-assisted tunneling from the excited state of the low energy emission band in Eu^{2+} to one of higher energy. This thermal back transfer of excited states is of course inefficient, and usually weak relative to the dominating thermal quenching process at a higher temperature. A similar case of a blue shift was reported on $Ca_2SiO_4: Eu^{2+}$ and $Ba_2SiO_4:Eu^{2+}$ persistent phosphors [274]. The summary of the integral emission of the three phosphors is shown in Figure 6.11d and indicates that a higher Eu^{2+}

doping concentration enhances the thermal quenching of the luminescence. The more significant quenching suggests more easily activated non-radiative rates for the higher Eu^{2+} concentrations that could act to also deactivate the traps responsible for the PersL.

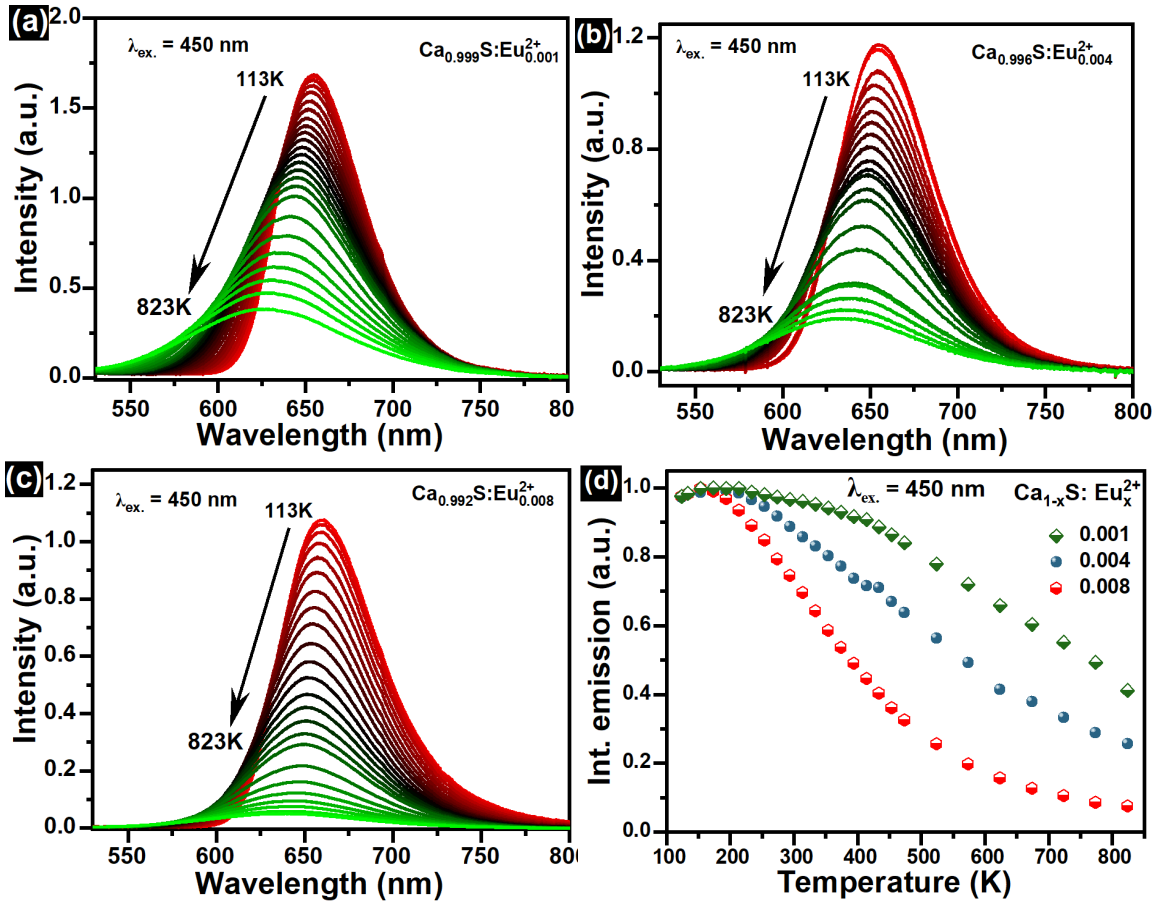

Figure 6.11. Temperature dependent photoluminescence (TDPL) emission in the 100 - 823 K range under 450 nm excitation. (a) The $Ca_{0.999}S: Eu^{2+}_{0.001}$ phosphor. (b) The $Ca_{0.996}S: Eu^{2+}_{0.004}$ phosphor. (c) The $Ca_{0.992}S: Eu^{2+}_{0.008}$ phosphor. (d) Summary of the integral emission of the phosphors in the 100-823 K range. Reproduced from Katumo et al. [35]. CC-BY 4.0 License.

Figure 6.12 shows that the normalized FWHM of the temperature specific spectra and the integrated emission decrease as the temperature is increased for $Ca_{0.9995}S: Eu^{2+}_{0.0005}$. This is expected, since as the temperature is increased, phonon density increases. Therefore, at high temperatures, the electron-phonon

density dominates which leads to the broadening of the FWHM of the emission spectrum.

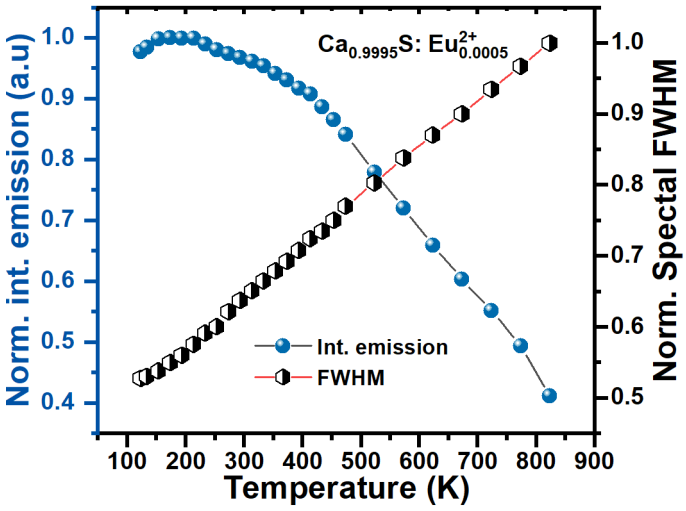

Figure 6.12 The normalized integral emission and normalized spectral FWHM of as a function of temperature in the range 100 – 823 K for $Ca_{0.9995}S: Eu^{2+}_{0.0005}$ phosphor.

6.4.3 PersL Lifetime of CaS: Eu^{2+}

The PersL lifetime of $Ca_{1-x}S: Eu^{2+}_{x}$ for x = 0.0005 - 0.015mol, after smartphone flashlight excitation is as illustrated in Figure 6.13a. The fitting shown in Figure 6.13a was carried out similarly as demonstrated in Figure 6.6 and accomplished using a single exponential fit function shown in equation 6.1. Figure 6.13b shows a summary of the fitted PersL lifetime. Also plotted alongside are the PLQY values for discussion purposes. The PersL lifetime gradually decreases with an increase in Eu^{2+} doping from 590 ms for $Ca_{0.9995}S: Eu^{2+}_{0.0005}$ to 125 ms for $Ca_{0.985}S: Eu^{2+}_{0.015}$. This is as opposed to the initial increase in PLQY for low concentrations before the gradual decrease due to concentration quenching set in.

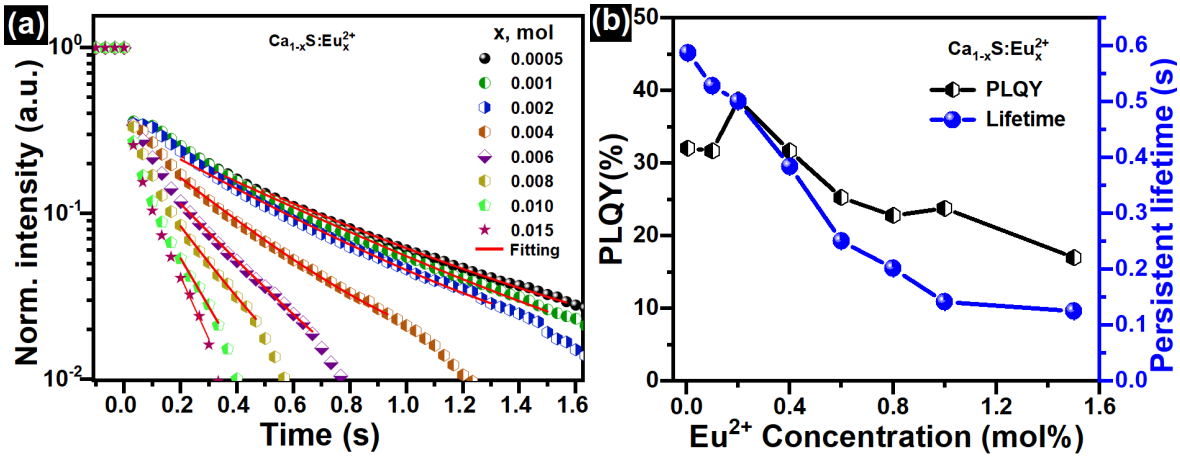

Figure 6.13 a) Persistent luminescence decay lifetime of $Ca_{1-x}S: Eu_x^{2+}$ phosphors extracted from the analysis of videos acquired using a smartphone following 5 s excitation with the smartphone-flashlight. b) The persistent luminescence lifetime and steady state PLQY of $Ca_{1-x}S: Eu_x^{2+}$ samples for $0.0005 \leq x \leq 0.015$ mol. after 450 nm excitation. Reproduced from Katumo et al. [35]. CC-BY 4.0 License.

6.4.4 Temperature-Dependent PersL Lifetimes of CaS: Eu^{2+}

The temperature-dependent PersL lifetime of $Ca_{0.999}S: Eu_{0.001}^{2+}$, $Ca_{0.996}S: Eu_{0.004}^{2+}$ and $Ca_{0.992}S: Eu_{0.008}^{2+}$ in the 233 – 473 K range are shown in Figure 6.14a-c. The samples show that the PersL starts around 213 K, reaches a maximum at 233 K, and then begins to decrease. This maps the 233 K temperature as the activation temperature for the PersL in the CaS: Eu^{2+} samples. Similar to the TDPL, the lowest Eu^{2+} doped sample maintained its persistent emission longer than the highly doped samples as shown in the summarized PersL lifetime data in Figure 6.14d. The PersL decay was fitted using a single exponential fit (equation 6.1) and the persistent lifetime as a function of temperature is estimated within a simple Arrhenius model as:

$$\tau\,(T) = A * \exp(-E_a/k_B T) \tag{6.3}$$

Where τ is the measured lifetime, A is a constant, k_B is Boltzmann constant and E_a is the activation energy corresponding to the trap depth. The apparent activation energy was estimated to be 0.07 eV and slightly reduced to 0.05 eV for $Ca_{0.999}S: Eu_{0.001}^{2+}$ and $Ca_{0.992}S: Eu_{0.008}^{2+}$ respectively.

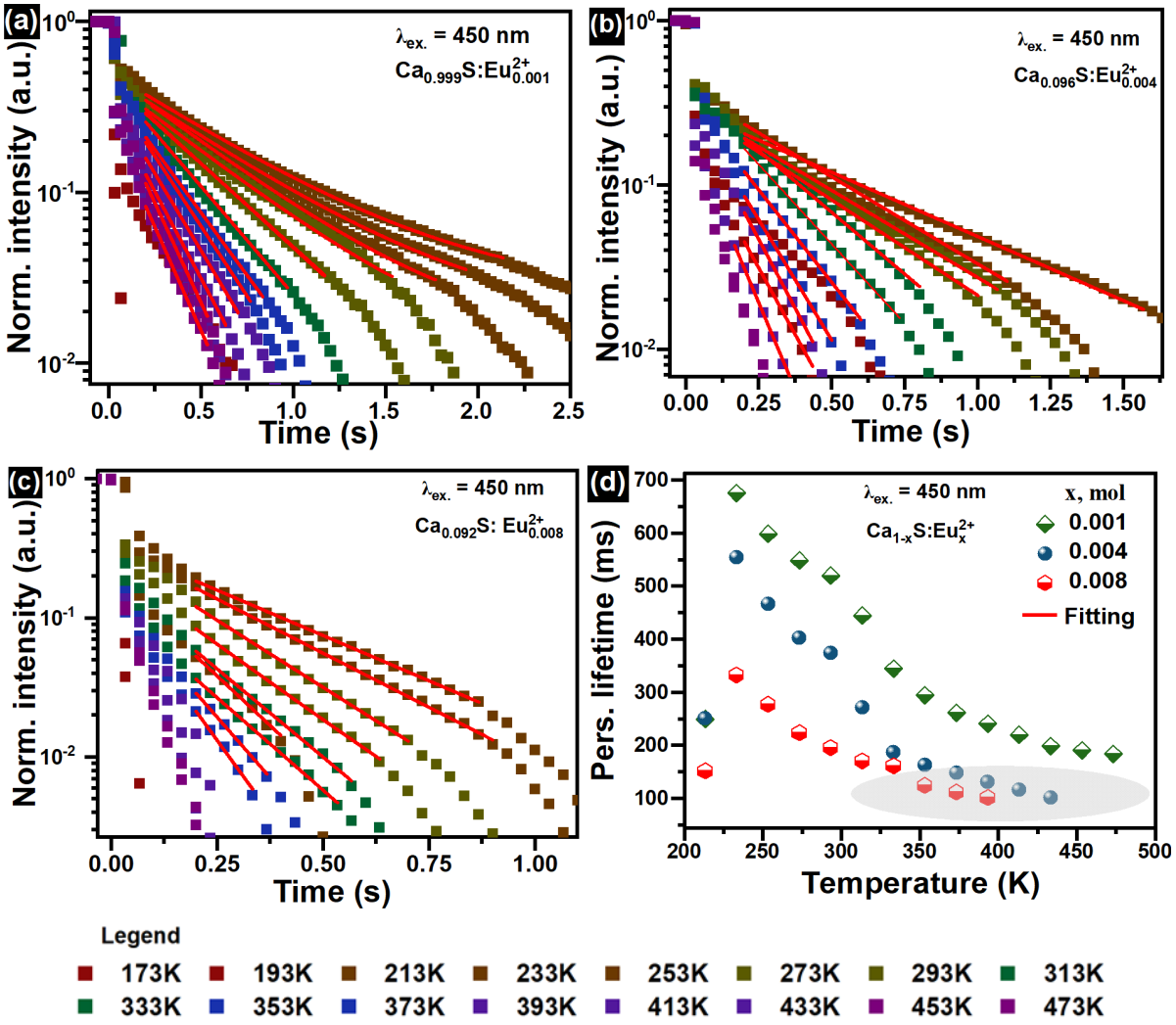

Figure 6.14. The temperature dependent PersL lifetime of $Ca_{1-x}S: Eu^{2+}_x$ phosphors (x = 0.001, 0.004 and 0.08) at various temperatures following 450 nm excitation. (a) The PersL lifetime of $Ca_{0.999}S: Eu^{2+}_{0.001}$ in the 193- 473 K. (b) The PersL lifetime $Ca_{0.996}S: Eu^{2+}_{0.004}$ in the 193- 473 K and (c) The PersL lifetime of $Ca_{0.992}S: Eu^{2+}_{0.008}$ phosphor for the 173 - 473 K. Each temperature dependent PersL lifetime in a - c can be differentiated using the legend. (d) Summary of the integral emission of the phosphors in the 193 - 473 K range. Adapted from Katumo et al. [35]. CC-BY 4.0 License.

The trap depth thus stays relatively constant across all the Eu^{2+} concentrations leading to a change in the PersL lifetime as a function of Eu^{2+} doping concentration is due to the non-radiative deactivation of the trapped states. More so, the temperature-dependent PersL lifetime of $Ca_{0.996}S: Eu^{2+}_{0.004}$ and $Ca_{0.992}S: Eu^{2+}_{0.008}$ starts to plateau in the 350 K region (oval-mapped) meaning that the non-radiative

deactivation process becomes dominant early for the highly doped samples as the temperature is increased.

6.5 Photophysical Properties of SrS: Eu^{2+}

The SrS: Eu^{2+} exhibits similar photophysical properties as its CaS: Eu^{2+} counterparts are in the same class of Eu^{2+} alkaline earth sulfides. This section reports on the steady-state and temporal behavior of SrS: Eu^{2+} together with the temperature-dependent PL.

6.5.1 Steady-state PL Studies of SrS: Eu^{2+}

The PL excitation and emission spectra of SrS: Eu^{2+} is shown in Figure 6.15. The PLE (monitored at 614 nm) has a broadband absorption according to Laporte's rule allowing $4f^6 5d^1 \rightarrow 4f^7$ transition of the Eu^{2+} ion. The absorption band has a maximum at 475 nm, and another relatively weak absorption centered at 275 nm.

The broad excitation bands monitored at 614 nm peaking at 275 nm and 475 nm can be attributed to the e_g and t_{2g} field splitting 5d bands of the Eu^{2+} respectively [26, 275]. Excitation of the broadband absorption of SrS: Eu^{2+} with a smartphone flashlight (flashlight spectra shown alongside) leads to the observed broadband red emission centered at 614 nm region due to the $4f^6 5d^1 \rightarrow 4f^7$ transition of the Eu^{2+} ion.

Figure 6.16 shows the PLQY SrS: Eu^{2+} samples as the doping concentration is varied from 0.001 to 0.015 mol. The maximum registered PLQY is 39 % for the $Sr_{0.999}S: Eu^{2+}_{0.001}$ sample and gradually reduces to 28 % in case of the $Sr_{0.985}S: Eu^{2+}_{0.015}$ sample. The PLQY remains above 35 % for samples doped with 0.08 mol of Eu^{2+} or less. The gradual decrease with increasing Eu^{2+} doping concentration is usually attributed to concentration quenching [26].

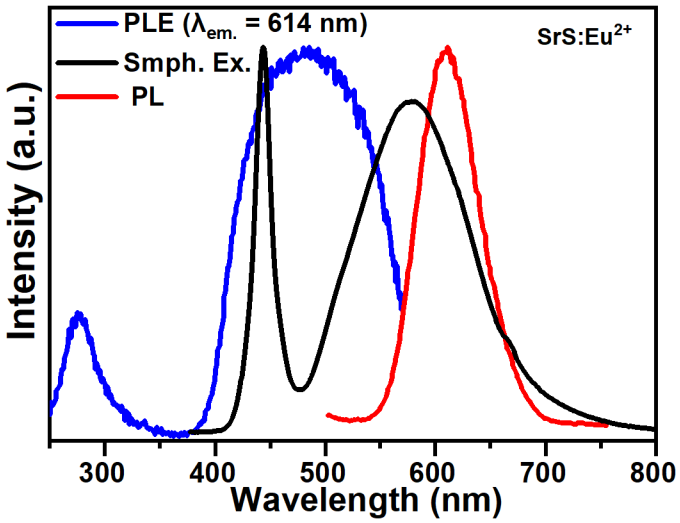

Figure 6.15. Photoluminescence (PL) properties of SrS: Eu^{2+}. The phosphor shows a broad band absorption (PL excitation spectra) extending beyond 550 nm from the 250 nm UV region. It is more pronounced in the 375 - 550 nm region. Exciting the broadband with a smartphone flash leads to the observed broadband PL emission centered at 614 nm. A representative smartphone flashlight spectrum (black) is presented alongside to demonstrate the excitation cross-section covered in the PLE spectra.

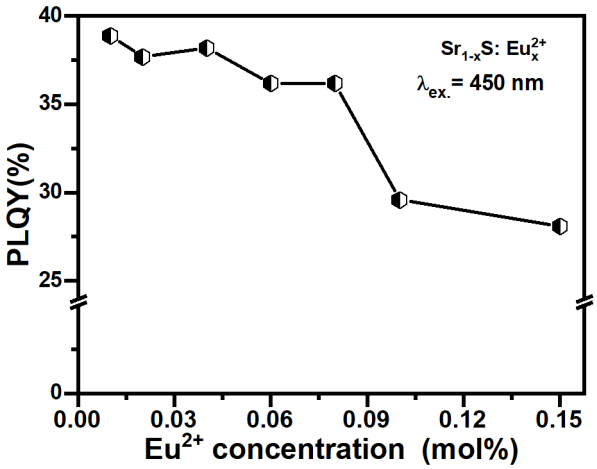

Figure 6.16. The PLQY of $Sr_{1-x}S: Eu_x^{2+}$ as a function of Eu^{2+} doping concentration. The PLQY has a maximum at of 39 % at 0.01 mol doping of Eu^{2+} and gradually decreases with increasing Eu^{2+} doping.

6.5.2 TDPL of SrS: Eu^{2+}

Figure 6.17a shows the TDPL emission of $Sr_{0.998}S: Eu^{2+}_{0.002}$ following 450 nm excitation in the 153 – 823 K range. The emission intensity gradually decreases with an increase in temperature. The decrease is characterized by a blue shift and FWHM increase of the spectra similar to the case of CaS: Eu^{2+} as shown in Figure 6.17b. The increase in FWHM and decrease in emission intensities are due to thermal quenching at higher temperatures. This is possibly due to thermally active phonon-assisted tunneling from the excited state of the low energy emission band to one of higher energy [274]. No special peaks arise from the Eu^{2+}spectra.

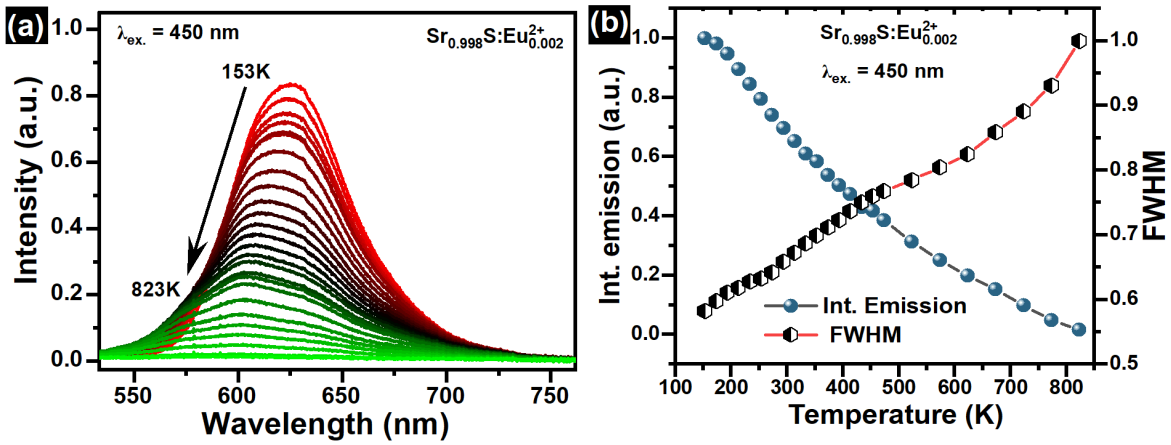

Figure 6.17. a) The temperature dependent PL emission of $Sr_{0.998}S: Eu^{2+}_{0.002}$ in the 153-823 K range. b) The normalized integral emission and spectral FWHM of as a function of temperature in the range for $Sr_{0.998}S: Eu^{2+}_{0.002}$ phosphor.

6.5.3 PersL Lifetime of SrS: Eu^{2+}

The PersL lifetime of $Sr_{1-x}S: Eu^{2+}_{x}$ (x = 0.001 to 0.015 mol.) decreases with Eu2+ doping concentration increase following smartphone flashlight excitation as shown in Figure 6.18a. A single exponential fit according to equation 6.1 is used to fit the PersL. The $Sr_{0.999}S: Eu^{2+}_{0.001}$sample shows the maximum PersL lifetime that gradually decreases to 150 ms for the $Sr_{0.985}S: Eu^{2+}_{0.015}$ sample as summarized in Figure 6.18b. The PLQY values are also plotted alongside for trend comparison. Both the PLQY and the PersL of all the phosphors provided meet the requirements for excitation and detection with a smartphone (bright and having a PersL lifetime greater than 100 ms).

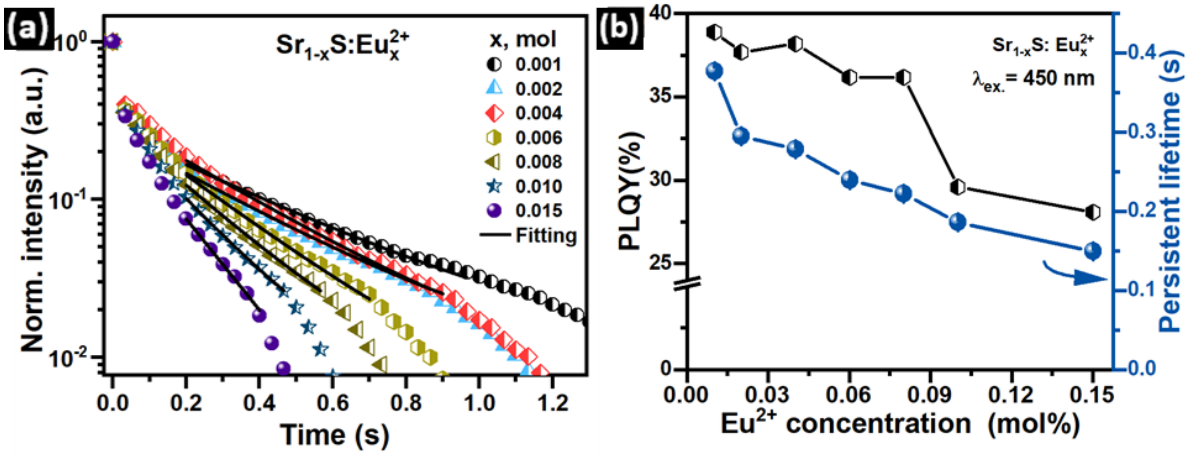

Figure 6.18. a) The PersL decay curves of $Sr_{1-x}S: Eu^{2+}_x$ samples for $0.001 \leq x \leq 0.015$ mol after 450 nm LED excitation. b) The persistent luminescence decay data of $Sr_{1-x}S: Eu^{2+}_x$. The PLQY data is also provided alongside. Reproduced from Katumo et al. [35]. CC-BY 4.0 License.

6.5.4 Proposed PersL Lifetime Tuning Mechanism

The similarity of spectroscopic properties of the SrS: Eu^{2+} and CaS: Eu^{2+} points to the same mechanism under which the PersL lifetime is tuned via increasing the Eu^{2+} doping concentration. Although not fully explored, it is hypothesized that the decrease in PersL in SrS: Eu^{2+} and CaS: Eu^{2+} phosphors with respect to the increase in Eu^{2+} doping is due to the increase in the non-radiative deactivation process of the trapped states [35]. It is narrowed to this conclusion after excluding the radiative channels from being contributors to the change in persistent luminescence.

The radiative rates depend on the activation energy required for the trapped state to be stimulated back to the Eu^{2+} emitter center. Now, if this were to contribute to the decrease in the PersL as Eu^{2+} doping is increased, the temperature-dependent PersL lifetime would indicate it. This is however not the case as observed in the temperature-dependent PersL lifetime of CaS: Eu^{2+} phosphors in the 230 - 450 K region (see Figure 6.14). Across the phosphors with various doping concentrations of Eu^{2+}, the activation energy remains in the 0.05 – 0.1 eV range and almost constant as Eu^{2+} doping is changed. Therefore, the non-radiative channels are the ones responsible for the reduction in PersL as the Eu^{2+} doping is increased. This inference agrees well with the gradual decrease in PLQY at higher Eu^{2+}

concentrations and the integrated temperature-dependent PL data (see Figure 6.11 and Figure 6.17).

6.6 Dynamic Color Tuning

To realize dual-mode color tunability, we blended the SAED persistent phosphor with either CaS: Eu^{2+} or SrS: Eu^{2+} to form SAED: CaS: Eu^{2+} and SAED: SrS: Eu^{2+} phosphor-blends as shown in Figure 6.19. The figure represents still video frames at various times after smartphone excitation. As illustrated, the color transitions from the initially observed red to green at different times for the various phosphors after the smartphone excitation is ceased. These blended phosphors are composed of SAED (820): $Ca_{0.9995}S: Eu^{2+}_{0.0005}$ for (i), SAED (820): $Ca_{0.994}S: Eu^{2+}_{0.006}$ for (ii), SAED (820): $Sr_{0.992}S: Eu^{2+}_{0.008}$ for (iii) SAED (820): $Sr_{0.985}S: Eu^{2+}_{0.015}$ for (iv) and SAED (850): $Ca_{0.985}S: Eu^{2+}_{0.015}$ for (v) at a ratio of 95:5 wt% of SAED to the red phosphors. For clarity purposes, half of each frame image has been saturated. The high SAED blending ratio of 95 wt% to the red phosphors was optimally selected to balance the transitional change from red to green post excitation.

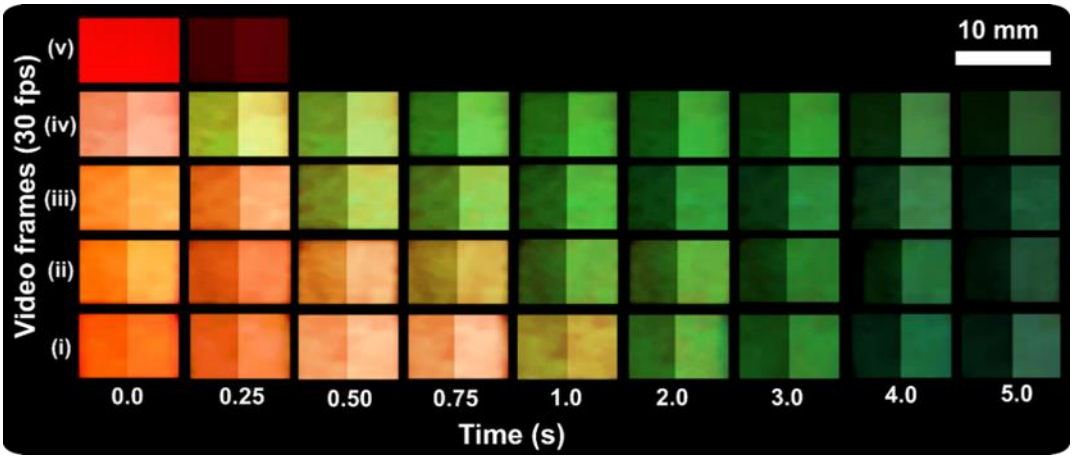

Figure 6.19. Illustration of dual-mode dynamic color tuning of persistent luminescence enabling red to green transitions using SAED, CaS: Eu^{2+} and SrS: Eu^{2+} blended phosphors. The left half of each video frame-image shows the raw video frame (change in color and intensity), the right half highlights the color change only by normalizing to a constant intensity. Reproduced from Katumo et al. [35]. CC-BY 4.0 License.

In addition, as already demonstrated in Figure 6.3 on SAED PLE spectra, only the tail of absorption coincides with the smartphone flashlight, unlike in the red phosphors in which the flashlight spectra are fully immersed in the absorption spectra. Due to this excitation difference, a higher weight ratio of SAED was necessary. More so, due to the high PLQY and higher initial emission intensity of the red phosphors relative to the SAED phosphors, only red to green transition could be realized.

The longer the PersL lifetime of the red-emitting phosphor blended with SAED (820) the longer the red to green transitional time and vice versa. For the SAED (820): $Ca_{0.9995}S: Eu^{2+}_{0.0005}$ phosphor blend, the red emission remains beyond 0.75 s after which it turns yellowish and finally changes to green after 1 s. As the PersL lifetime of the red phosphors is decreased, the red to green transitions occur faster. A failed color transition, in which only the red is observable post excitation with no green transition is also shown using the SAED (850): $Ca_{0.985}S: Eu^{2+}_{0.015}$ phosphor blend. Color transition failed due to the weak absorption (see Figure 6.3) of SAED (850) and weak PersL intensity after excitation. Regarding this failure, only phosphor blends annealed below 830 ^{o}C were used. To enhance the intricacy level of labels created with the blended phosphors, the PersL lifetime of the independent colors (red and green) was retrieved from the blended phosphors as illustrated in Figure 6.20a – d.

The SAED (820) phosphors show a persistent lifetime of 2.55 ± 0.01 s across the four samples. This causes a 2.3 % decline in the average PersL lifetime registered by the unblended SAED (820) phosphor. The decline is attributed to the re-absorption of the emission by the red-emitting phosphors as the SAED emission coincides with their absorption spectra. Due to this spectral overlap, the PersL lifetime of the red-emitting phosphors is slightly enhanced to 0.60 s, 0.40 s, 0.27 s, and 0.16 s representing a 2, 4, 4.5, and 7 % PersL lifetime increase for $Ca_{0.9995}S: Eu^{2+}_{0.0005}$, $Ca_{0.996}S: Eu^{2+}_{0.004}$, $Sr_{0.992}S: Eu^{2+}_{0.008}$, $Sr_{0.985}S: Eu^{2+}_{0.015}$, respectively.

The slight alteration in PersL lifetime following blending due to the ‘crosstalk’ mediated reabsorption does not pose a problem when designing color-tunable anti-counterfeiting labels. It is also worth noting herein that the crosstalk can be eliminated by exploiting printing techniques that allow the spatial distribution of the

particles. The next section demonstrates dual-mode color-tunable dynamic anti-counterfeiting labels using these phosphors with the smartphone acting as the exciting and detecting hardware.

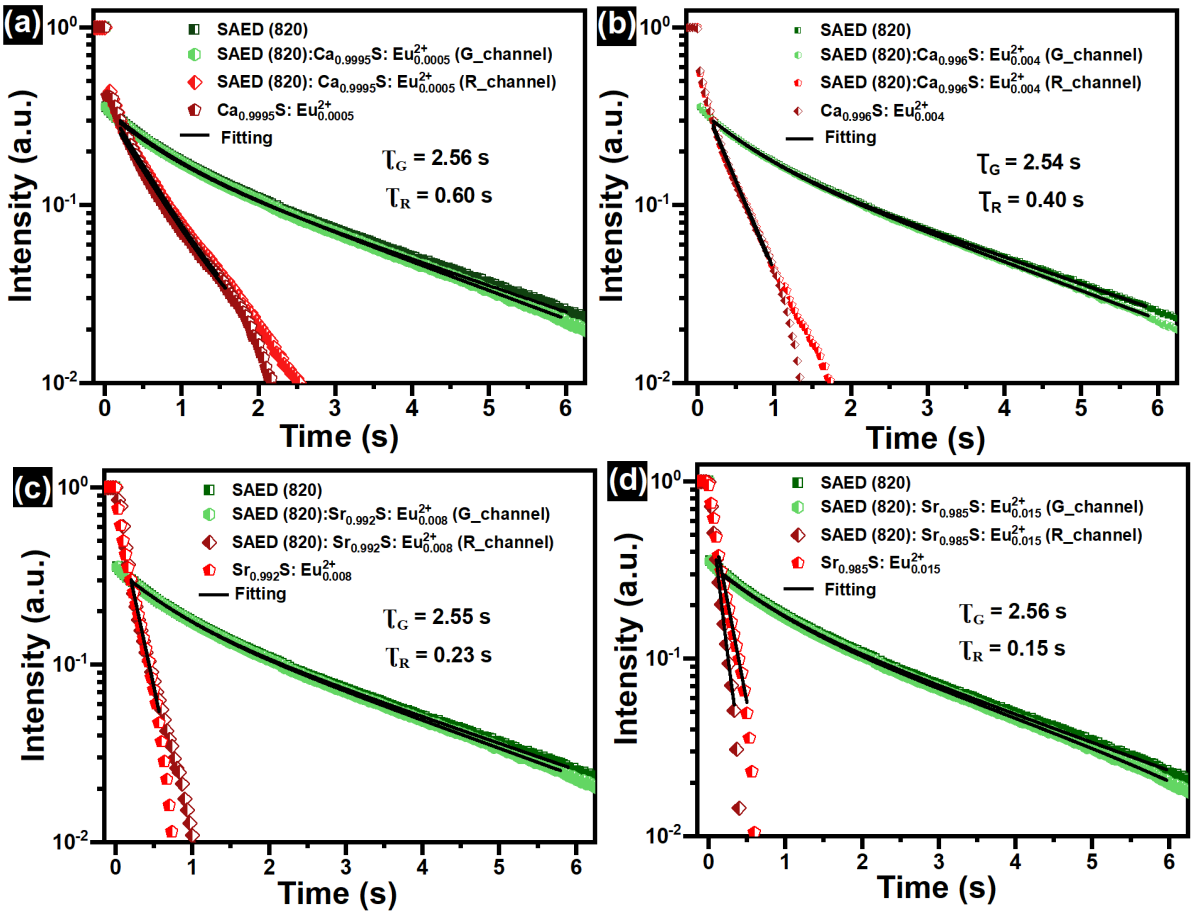

Figure 6.20. The PersL lifetime of split red and green channels of blended phosphors after smartphone flashlight excitation;(a) SAED (820): $Ca_{0.9995}S: Eu^{2+}_{0.0005}$ (b) SAED (820): $Ca_{0.996}S: Eu^{2+}_{0.004}$ (c) SAED (820): $Sr_{0.992}S: Eu^{2+}_{0.008}$ and (d) SAED (820): $Sr_{0.985}S: Eu^{2+}_{0.015}$ alongside the persistent lifetime of the pure phosphors. Adapted from Katumo et al. [35]. CC-BY 4.0 License.

6.7 Smartphone Excitable and Readable Anti-Counterfeiting Labels

The pure and blended phosphors were used to develop dynamic and color-tunable anti-counterfeiting labels that allow the use of a smartphone as the exciting source and detecting device. The three sets of labels developed are based on a seven-segment display, 2D barcodes, and customizable aesthetic labels.

6.7.1 Seven-Segment Labels

For the seven-segment color-tunable dynamic anti-counterfeiting labels, the blended phosphors are embedded on segments ① - ⑦ of a custom-designed four-digit label as shown in Figure 6.21a. The label is then excited using a smartphone flashlight and the PersL video-recorded. Figure 6.21b shows the extracted video frames of interest (raw) and the red and green split channels, at various timestamps illustrating the dynamic and color tunability of the anti-counterfeiting labels after smartphone flashlight excitation. The raw video frames show that the pattern changes from the observed '8 8 8 8' to a yellowish '3 3 3 3' display at 0.5s after which it changes again to a green '7 7 7 7' after 1 s respectively.

The yellowish '3 3 3 3' display occurs when segments ① and ② exhaust their red emission. Afterward, the red emission in segments ③ and ④ is also exhausted leading to the '7 7 7 7' display after 2 s. Covertness of the labels, which also serve as the authentication parameters, is realized when the raw video frames are split into the red and green channels. The phosphors in each segment are designed such that the red channel transitions from the red display of '8 8 8 8' to a '3 3 3 3' at 0.5 s. This occurs as a result of exhaustion of the red emission of $Sr_{0.985}S:Eu^{2+}_{0.015}$ in segments ① and ②. The transition then proceeds to a '7 7 7 7' display after the red emission of $Ca_{0.994}S:Eu^{2+}_{0.006}$ from segments ③ and ④ in each digit gets exhausted.

On the other hand, the green channel is concealed at the beginning of the excitation, obviously due to the strong red emission of the CaS: Eu^{2+} and SrS: Eu^{2+} phosphors. This is a very potent anti-counterfeiting approach as the hidden anti-counterfeiting pattern is hidden in the low-intensity, channel. Unlike the red channels that exhibit three transitions, the green channel only transitions from the concealed '8 8 8 8' directly to a '7 7 7 7' after 0.5 s. This is because only two green phosphors were utilized in the phosphor blends as shown in Figure 6.21a.

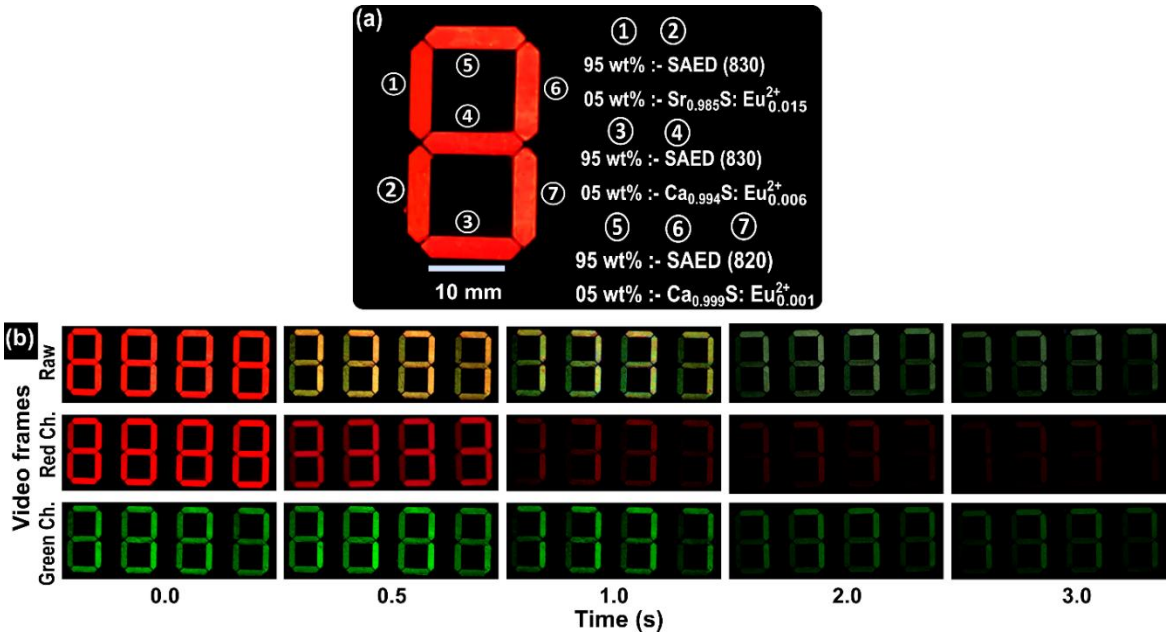

Figure 6.21. (a) Schematic representation detailing the phosphors placed in each of the seven - segment anti- counterfeiting display. (b) Smartphone acquired video frames of interest for four digits of the 7-segment display described in (a) after 5 s excitation with smartphone-flashlight showing the raw video-frames and split red and green channel frames of interests of the dual-color dynamic label. Reproduced from Katumo et al. [35]. CC-BY 4.0 License.

To further enhance the intricacy of the labels, the PersL lifetime at each segment could also act as a covert anti-counterfeiting verification parameter. Figure 6.22 shows the extracted PersL lifetime (s) of the labels. The data are similar to the PersL labels of the phosphor blends in segments ① - ④. For segments ⑤ - ⑦, containing the SAED (820): $Ca_{0.999}S: Eu^{2+}_{0.001}$ phosphor blend, the PersL decay is as shown in Figure 6.20.

The PersL lifetime of the blended phosphors extracted from the red channel for the $Sr_{0.985}S: Eu^{2+}_{0.015}$ and $Ca_{0.994}S: Eu^{2+}_{0.006}$, were 0.16 s and 0.27 s, respectively. A slight decrease of 3.7 % was registered in the green channel for the SAED (830) phosphor which registered a persistent lifetime of 1.56 s. This slight variation due to reabsorption is however insignificant and can always be factored in during the label development process.

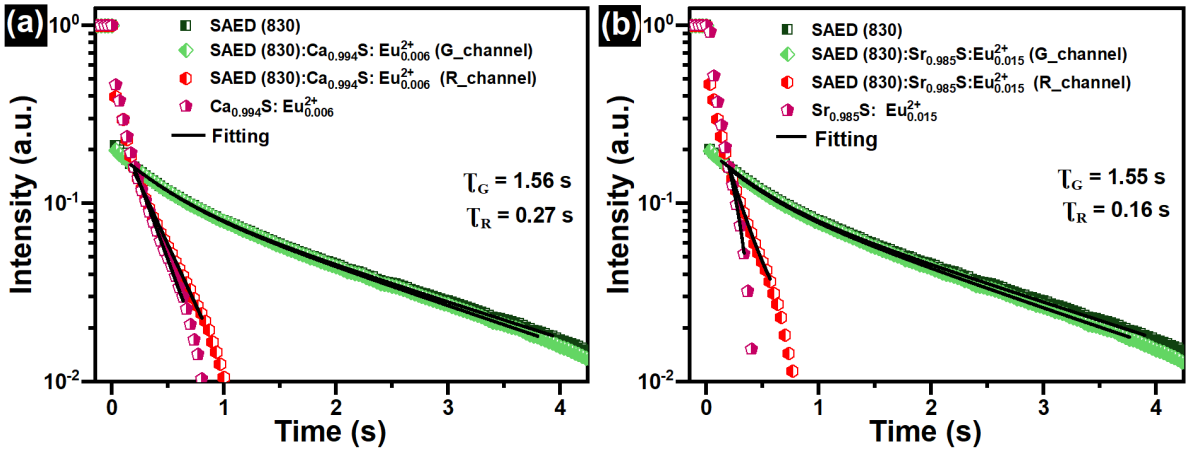

Figure 6.22. Extracted persistent luminescence lifetime of the red and green channels persistent lifetime of SAED (830): $Ca_{0.994}S: Eu^{2+}_{0.006}$ and SAED (830): $Sr_{0.985}S: Eu^{2+}_{0.015}$ phosphors blend after smartphone flashlight excitation. The persistent lifetime decays are plotted alongside the lifetimes of the pure phosphors. Reproduced from Katumo et al. [35]. CC-BY 4.0 License.

6.7.2 2D Barcodes

In this section, single color and dual-color dynamic anti-counterfeiting labels with advanced optical coding parameters in the temporal domain are demonstrated. Their covertness is guaranteed through either the pixel decay cross-referencing at various times after excitation or their PersL lifetime. The barcode labels developed using the pure SAED and CaS: Eu^{2+} and SrS: Eu^{2+} phosphors are shown in Figure 6.23.

The phosphor utilized in each bar, from left to right is as described in the caption. Alongside the split, barcodes are also binarized frames of the split channels and reference barcodes computed from the analysis of the persistent lifetime of each phosphor material. If the pixels for a channel fall below 12 % (~30 pixels out of 255 possible pixels per channel) then the barcode transition from one (bright white lines) to zero (transition to black) for that channel. The same pixel threshold of 12 % is used to compute the expected barcode from the analysis of persistent luminescence decay videos.

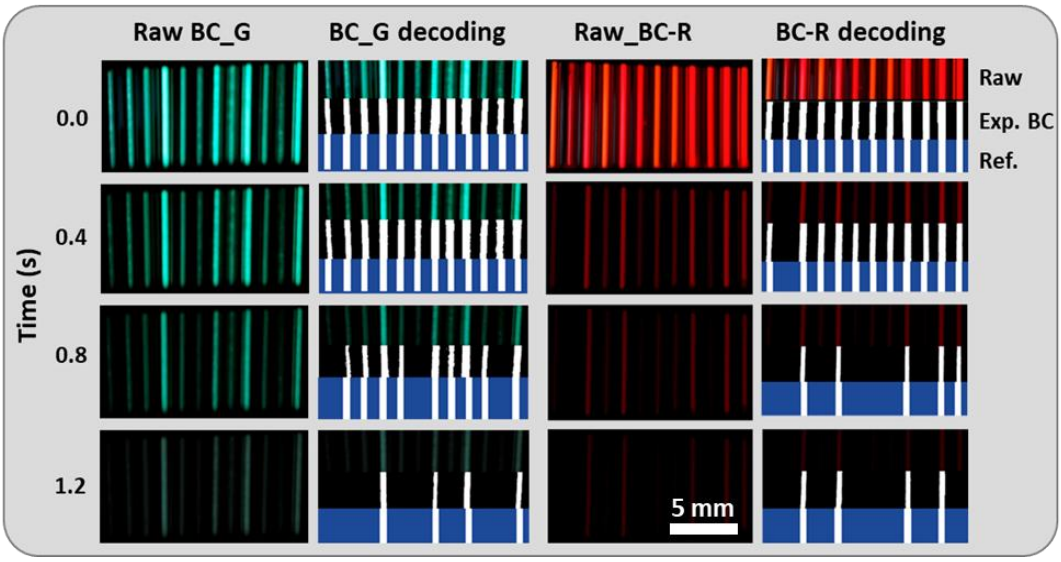

Figure 6.23. Single-color-coded 12-line dynamic barcodes made from SAED, CaS: Eu^{2+} and SrS: Eu^{2+} persistent phosphors showing progression of PersL after smartphone flashlight excitation. The dynamic barcodes agree well with the reference barcode of obtained from analysis of persistent luminescence of the phosphors. For the green barcode from left to right each bar contains the following phosphor SAED (850) (lines 2 & 11), SAED (840) (lines 1 & 6), SAED (830) (lines 3,5, 8 and 10), SAED (820) (line 7) and SAED (810) (lines 4, 9 and 12). For the red barcodes counting from left to right the barcode-line materials are $Ca_{0.999}S:Eu^{2+}_{0.001}$ (lines 3, 5,9 and 11), $Ca_{0.985}S:Eu^{2+}_{0.015}$ (lines 2), $Ca_{0.992}S:Eu^{2+}_{0.008}$ (line 6), $Ca_{0.99}S:Eu^{2+}_{0.01}$ (line 10), $Ca_{0.998}S:Eu^{2+}_{0.002}$ (line 12), $Sr_{0.998}S:Eu^{2+}_{0.002}$ (line 1), $Sr_{0.996}S:Eu^{2+}_{0.004}$ (line 4), and $Sr_{0.994}S:Eu^{2+}_{0.006}$ (lines 7 & 8). The various timestamps therefore register different barcodes depending on the exhausted persistent emission of the phosphors in the bars.

The green channel timestamps change from '1 1 1 1 1 1 1 1 1 1 1 1' at 4s to '0 1 1 1 1 0 1 1 1 1 0 1' at 0.8 s and finally to '0 0 0 1 0 0 1 0 1 0 0 1' at 1.2 s. Notice that due to the strong persistent emission of SAED phosphors all the emission signal is strong at 0.4 s such that the barcode is similar to the time of excitation. The authentication time post excitation should also be selected such that it does not coincide with the boundary under the signal and would give either a false positive. For the red phosphors, the initial '1 1 1 1 1 1 1 1 1 1 1 1' display during excitations changes to '1 0 1 1 1 1 1 1 1 1 1 1' then to '0 0 1 0 1 0 0 0 1 0 1 1' and '0 0 1 0 1 0 0 0 1 0 1 0' at 0.4, 0.8 and 1.2 s

respectively and agree well with the confirmation reference data for authentication. The experimental barcodes are all in agreement with the reference signatures derived from the phosphors. Dynamic and color-tunable barcodes were also realized using the SAED, CaS: Eu^{2+}, SrS: Eu^{2+}, and the respective phosphor blends as shown in Figure 6.24.

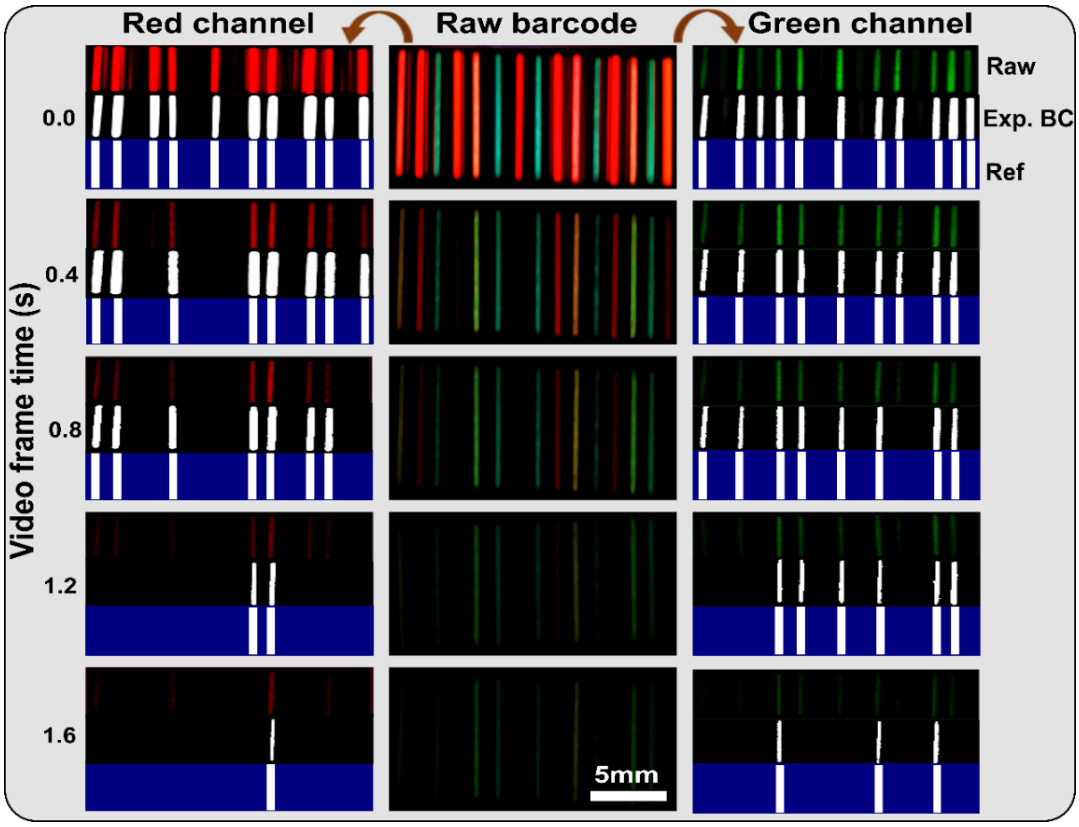

Figure 6.24. Multi-color-tunable 15-line dynamic barcode registering different dynamic codes following evaluation of the red and green channel of the emission after smartphone excitation. From left to right the raw barcode lines have the following samples SAED (850) in line 11, SAED (840) in line 3, SAED (830) lines 6, 8 and 14, $Ca_{0.999}S: Eu^{2+}_{0.001}$ (lines 9), $Ca_{0.996}S: Eu^{2+}_{0.004}$, (lines 2 and 12), $Ca_{0.9}S: Eu^{2+}_{0.01}$ (lines 7), and $Sr_{0.99}S: Eu^{2+}_{0.01}$, in line 4, and $Sr_{0.994}S: Eu^{2+}_{0.006}$, line 15. Blended phosphors shown in Figure 6.19 include phosphors (i) in line 10, phosphor (ii) in lines 1, 5 and 13. For each barcode, the raw barcode is shown alongside the processed barcode and the reference barcode for authentication at the various time stamps. Reproduced from Katumo et al. [35]. CC-BY 4.0 License.

Again, the phosphor utilized in each bar, from left to right is as described in the caption. The raw video frames are shown in the middle following smartphone flashlight excitation. The split channels are shown alongside, with the green channel on the left and the red channel on the right. Alongside the split channels are also binary frames of the raw videos split to the respective channels and reference/expected barcode computed from the analysis of the PersL lifetime. Again, the binarization and selection of either a positive bar (one) or a zero (black) are based on the 12 % threshold (~30 pixels out of 255 possible pixels for a channel). Unlike in the single-color codes where all the bars were positive (ones) at the beginning, with color-dynamic barcodes, the initial of the split channels are usually a combination of zeros and ones.

For example, at zero time the red channel barcode reads '1 1 0 1 1 0 1 0 1 1 1 1 1 0 1' and then transitions to '1 1 0 0 1 0 0 0 1 1 1 1 1 0 1' then to '1 1 0 0 1 0 0 0 1 1 0 1 1 0 0' then '0 0 0 0 0 0 0 0 1 1 0 0 0 0 0' and finally to '0 0 0 0 0 0 0 0 0 1 0 0 0 0 0' at 0.4, 0.8, 1.2, and 1.6 s respectively. The green channel barcode at time zero is '1 0 1 1 1 1 0 1 0 1 1 0 1 1 1' and transitions to '1 0 1 0 1 1 0 1 0 1 1 0 1 1 0' then to '1 0 1 0 1 1 0 1 0 1 0 0 1 1 0' then to '0 0 0 0 1 1 0 1 0 1 0 0 1 1 0' and finally to '0 0 0 0 1 0 0 0 0 1 0 0 1 0 0' at times 0.4, 0.8, 1.2, and 1.6 s respectively. The green and red barcode readings and transitions are therefore completely different, and due to their temporal nature of verification, provide a high intricacy level. Higher timestamps of verification would increase the intricacy level of the labels further.

6.7.3 Customizable Aesthetic Labels

Custom-made labels that can be embedded in the product's logo labels are desirable in maintaining classical brand features while at the same time preventing counterfeiting. In this direction, anti-counterfeiting labels ought to aesthetically blend with existing product specifications. To explore this dimension, color-tunable dynamic anti-counterfeiting labels with emoji patterns were developed using two phosphor blends as shown in Figure 6.25. These emoji labels were developed using SAED (820): $Ca_{0.999}S: Eu^{2+}_{0.0001}$ and SAED (900): $Ca_{0.992}S: Eu^{2+}_{0.008}$ phosphor blends. The blends are made by forming a colloidal of the phosphors with PVP containing 70 % ethanol and 30 % deionized water. Three

faces, a ‘wow’, ‘smiley’, and ‘sad’ emoji are developed but only reveal themselves post excitation transitions. During and immediately after excitation, all the emojis show the ‘wow’ face. The first emoji labeled (a) remains a ‘wow’ emoji and only transitions from red to green as it is only based on the SAED (820): SAED (820): $Ca_{0.999}S$: $Eu^{2+}_{0.0001}$ phosphor blend only. The transition occurs when the red emission of SAED (820): $Ca_{0.999}S$: $Eu^{2+}_{0.0001}$ is exhausted and only the persistent emission of SAED (820) is visible. In the second emoji labeled (b), the ‘wow’ emoji changes to a green smiley face.

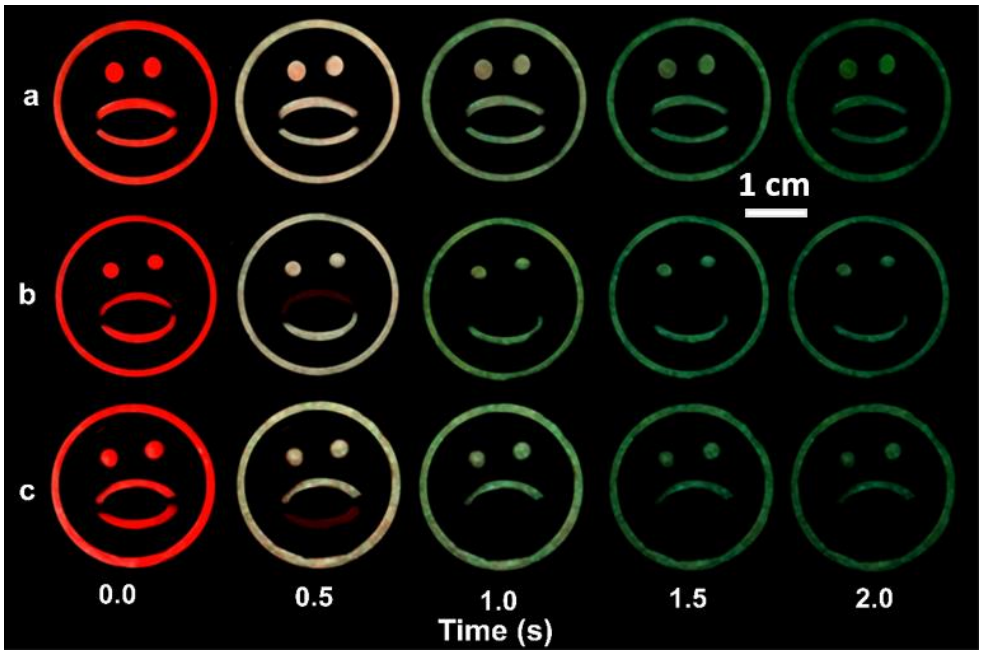

Figure 6.25. Color tunable emoji-patterns extracted from smartphone-video-acquired frames after 10 s of flashlight excitation. Immediately after the excitation is ceased, the labels show a ‘wow’ emoji in red. This then transitions to a green wow emoji in label a, a smiley green emoji in label b and finally a sad emoji in label c. The external diameter of the emoji is 3.0 cm. Adapted with permission from Katumo et al. [35]. CC-BY 4.0 License.

To realize this transition, the upper lip of the emoji is replaced with a SAED (900): $Ca_{0.992}S$: $Eu^{2+}_{0.008}$ phosphor blend colloidal that has a shorter PersL. The SAED (900) in the blends is used as a camouflaging matrix since it does not have persistent emission. Its purpose is to guarantee the same color for the

unexcited label in all the regions. Similarly, by using the same approach we can realize a sad emoji face as shown in label (c). For this label, the lower lip of the emoji is replaced with a blend of SAED (900): $Ca_{0.992}S$: $Eu^{2+}_{0.008}$ phosphor. These labels demonstrate that it is possible to develop customizable labels befitting already existing markings in product labels.

6.8 Effect of Temperature on the Labels

It is expected that the authentication process of the anti-counterfeiting labels would occur in POS terminals. The temperature in POS terminals would ideally vary all year round. In addition, the verification would also take place in different global regions that have significantly different temperature levels. For this reason, the influence of temperature on the pattern change of the emoji labels was investigated. Figure 6.26 shows the smiley emoji pattern transitions that have been taken at 278 K, 298 K, and 318 K. While the color transitions remain similar, they are fastest at 318 K and slow at 278 K.

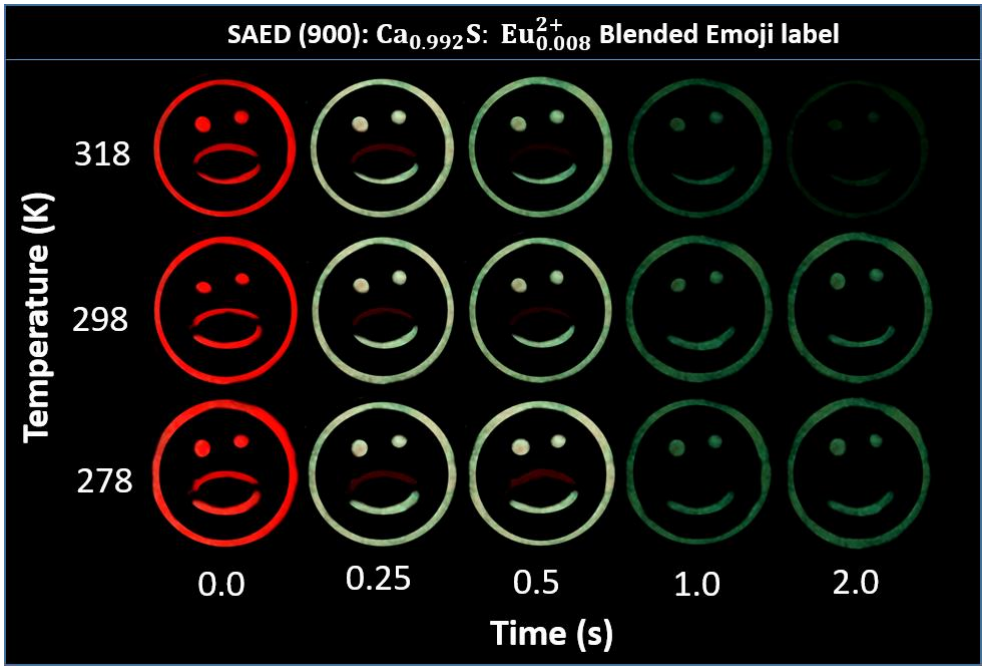

Figure 6.26. Transitions of the wow emoji from red to green after smartphone excitation for 10 s at three different temperature settings. As the temperature is increased, the transitions occurs faster but the same transitional patter is realized in the three temperature settings.

The higher the temperature the faster the transitions, as they mimic the temperature-dependent PersL lifetime of the phosphors. The transitions, albeit changing faster for the labels maintained at 317 K maintain the dynamic and color changes. These results prove the opportunity to not only customize the dynamic labels but to realize the desired changes at various temperatures as well. Meaning the possible application of this technology in various parts of the world.

6.9 Summary

In this chapter, dual-color dynamic anti-counterfeiting that allows the use of a smartphone as an exciting and authenticating device is presented. To use a smartphone for the excitation and subsequent authentication, it is demonstrated that the phosphors have to meet several conditions. Firstly, they need to absorb in the visible region to be excited with the visible light of the smartphone flashlight. Secondly, the persistent emission had to be in the visible region as well for the smartphone camera to capture it. This limitation is due to the NIR filter in the cameras. Finally, to have dynamic pattern change, the persistent emission has to be varied and bright enough to be captured by the smartphone camera in a darkened environment.

The three phosphors that meet the aforementioned criteria and are used herein include SAED, CaS: Eu^{2+} and SrS: Eu^{2+} persistent phosphors. For green-emitting SAED phosphors, the PersL lifetime was tuned from 11.7 s to 0.5 s by annealing the commercial phosphors in the air at various temperatures between 700 - 860 ^{o}C. On the other hand, the PersL lifetime of the red emission CaS: Eu^{2+} and SrS: Eu^{2+} persistent phosphors are tuned by varying the Eu^{2+} doping concentration. For CaS: Eu^{2+} the PersL could be varied from 590 ms to 150 ms by increasing the Eu^{2+} doping concentration from 0.0005 to 0.015 mol. Similarly, for SrS: Eu^{2+} the PersL decreases from 377 ms to 150 ms as the Eu^{2+} doping concentration from 0.001 to 0.015 mol.

To demonstrate this concept, seven-segment display labels, 2D barcodes, and aesthetic labels are used. The authentication process involves exciting the phosphors and subsequently recording the emission with a smartphone. Thereafter, the video channels of the labels are split to reveal the covert patterns in the red or green channel. The verification methods used involved observing the

pattern in the split channels after excitation or determining the persistent lifetime or the number of pixels at various locations and cross-referencing the obtained values to the already known established data sets. These results present the proof of concept that indeed the temporal domain of PersL can be utilized for anti-counterfeiting applications in a far superior manner than the steady-state counterpart.

7

Conclusions and Outlook

This thesis demonstrated the potential for smartphone-based luminescence thermometry and anti-counterfeiting applications using persistent phosphors. Before the applications, the photophysical behavior (PL, PLQY, PersL lifetime, and TDPL) of the persistent phosphors was explored. The phosphors used include SAED, $Gd_2O_2S: Eu^{3+}$, $Gd_2O_2S: Eu^{3+}, Ti^{4+}$, $CaS: Eu^{2+}$, and $SrS: Eu^{2+}$. Of these PersL phosphors, SAED was the only commercial material, the others were synthesized as part of this thesis. In the following section, the most important results in each of the investigated applications are summarized and an outlook is provided.

7.1 Towards Smartphone-Based PersL Sensing Systems

Over the last decade, there has been increased interest in smartphone-based applications that previously required expensive and complicated hardware to

accomplish. Some of the interesting smartphone-based applications include bio-sensing [276], chemical sensing [277], anti-counterfeiting [11], water quality monitoring [278], e-health and IoT [279], and the work presented herein on luminescence thermometry [8], besides many other applications. The success of these applications owes to low-cost, readily available, international connectivity, and easy-to-use smartphones that provide economical means of accomplishing otherwise expensive applications.

In the first results section of this thesis, non-contact temperature determination using a smartphone was accomplished by exploiting the temperature-dependent PersL lifetime of Gd_2O_2S: Eu^{3+} phosphor. The phosphor emits in the visible region after 375 nm excitation and has a temperature-dependent PersL lifetime that decreases with an increase in temperature due to thermal promotion of the excitons held in long-lived CTB to the $^5D_0$ level of the Eu^{3+} ion. While the lifetime of phosphor ideally decreases as temperature increases according to the Arrhenius model, the behavior depicted by Gd_2O_2S: Eu^{3+} phosphor is a little different. For this phosphor, PersL emanates from the CTB-based pathways, (composed of radiative and non-radiative pathways) and as the temperature is increased, the PersL decreases but the PLQY is reduced at a lesser magnitude than it would be if only the non-radiative channels were activated. This is necessitated by the shifting of the CTB to lower energy as the temperature is increased that also enhances the $^5D_0$ state feeding. This leads to a relatively less decrease in PLQY, consistently allowing a smartphone to video-record the PersL as the temperature is varied from 270 K to 338 K as the PersL remains bright. As the temperature is increased from 270 K to 338 K, the PersL lifetime gradually reduces from 1107 ms to 100 ms, providing a thermometric calibration curve. The persistent phosphors' lifetime was first calibrated in a lab setting using a smartphone where its temperature-dependent PersL lifetime was mapped to the indicative temperature. Afterward, the phosphors could be applied in other varied settings where its PersL lifetime after appropriate excitation would give an indicative temperature. The phosphors had a respectable PLQY of 65% and were thus bright enough to be captured by the smartphone camera. Interestingly, the thermometer could work in the ambient lighting of up to 1500 lm/m^2 since the lifetime property is insignificantly affected by background radiation. Even under background illumination, the thermometer had

a high precision of 2 K and a high relative sensitivity of 4.5%K^{-1} at 270 K reduced to 3.1%K^{-1} at 333 K. The smartphone-based thermometer is a worthy competitor of the near-infrared thermometers that are several orders more expensive.

7.2 Smartphone-Based Anti-Counterfeiting

Anti-counterfeiting technologies provide tools that determine whether a product is original or fake by tagging the products with anti-counterfeiting markers or by making the markers part of the product. While the overt anti-counterfeiting features are usually observable by naked eyes, covert anti-counterfeiting features must be authenticated using a dedicated authenticating device. Ideally, the authenticating devices ought to consume the least resources possible for the anti-counterfeiting technology to be economically feasible. This is always never the case, especially for complicated covert features in luminescence-based labels. In this thesis, persistent luminescence-based anti-counterfeiting labels whose covert features are authenticated from the analysis of videos acquired using a smartphone are presented. This significantly reduces the cost factor of authenticating the device while at the same time benefiting from the ubiquitous distribution and international presence of smartphones.

The first section on anti-counterfeiting extended the work of $Gd_2O_2S: Eu^{3+}$ by creating a palette of lifetimes at room temperature that could be used for dynamic anti-counterfeiting using a smartphone following UV excitation. By co-doping, the $Gd_2O_2S: Eu^{3+}$ persistent phosphors with Ti^{4+} varying concentrations up to 0.09 mol, the PersL lifetime could be tuned from 1.17 ± 0.02 to 5.95 ± 0.07 s. An interesting feature about the $Gd_2O_2S: Eu^{3+}$, Ti^{4+} is that while the PersL lifetime drastically increased as the Ti^{4+} co-doping increased up to 0.09 mol, the PLQY remained relatively constant in this region, at 46% ± 3% giving the phosphors uniform initial brightness after excitation. Using these phosphors, four-digit seven-segment patterns embedded on PMMA were developed with large differences in their PersL lifetime. For these labels, authentication could directly be observed with the naked eye. In addition, covert features, herein the persistent lifetimes at specified regions of interest, could be retrieved from the analysis of smartphone acquired videos following 375 nm UV excitation. In a further experiment, the phosphors were inkjet-printed to form a pattern that changed post excitation and uniquely had PUF

functionalities. These again could easily be verified from the analysis of smartphone acquired videos after excitation. When the patterns were developed with phosphors with comparable lifetimes, (0.20 s PersL lifetime difference) the dynamic changes post excitation were hard to observe with the naked eyes but could be easily decoded from the analysis of 30 fps acquired using a smartphone video. The complete authentication system in this work thus required a UV source, the anti-counterfeiting label, and a smartphone for successful authentication.

It would however be more interesting if the complete authentication of the labels only required a smartphone as the authenticating hardware for both exciting (using the smartphone's flashlight) and detection (using the smartphone camera). Hither, dual-color dynamic anti-counterfeiting labels whose covert features could directly be authenticated by comparing still images from the red and green-split channels of smartphone acquired videos after smartphone flashlight excitation were demonstrated. Smartphone-only authentication was possible since the persistent phosphors used not only absorbed and emitted in the visible region, but also their PersL was long enough to be captured by the 30 fps smartphone camera. The phosphors used for this demonstration included the green-emitting (SAED), red-emitting CaS: $Eu^{2+,}$ and SrS: Eu^{2+}. For the green-emitting SAED persistent phosphors, the PersL lifetime was tunable in the 0.5 - 11.7 s via annealing the commercial phosphor in air. By annealing the phosphors in the air at different temperatures up to 860^0C the trap density could be intentionally distorted to provide tunable persistent lifetimes. On the other hand, for the red-emitting phosphors, PersL lifetime was tunable in the 0.1 to 0.6 s range and 150 ms to 377 ms range for CaS: Eu^{2+} and SrS: Eu^{2+} respectively by increasing the Eu^{2+} doping concentration from 0.0005 - 0.015 mol. Dynamic color tuning was realized by blending the SAED phosphors with CaS: Eu^{2+} or SrS: Eu^{2+}. For these blends, only the red to green transition could be realized as the PLQY of the red-emitting phosphors was high relative to the SAED phosphors besides the SAED weakly absorbing the smartphone flashlight excitation. Dynamic color-tunable anti-counterfeiting was demonstrated using a seven-segment display, a barcode, and aesthetic emojis, for customizable labels. The three main approaches used to authenticate the labels included; 1) determination of the PersL lifetime at a specified region of interest in the label, 2) binarization of the still frames at various

timestamps, and 3) extraction of concealed patterns through channel splitting in the case of dual-color labels at various time stamps post smartphone excitation. The main contribution of this work is the proof of concept that a smartphone-only authentication of luminescence-based anti-counterfeiting labels utilizing the temporal domain is possible. This brings the use of smartphones authentication of luminescence-based anti-counterfeiting to the same level as other anti-counterfeiting technologies that use only a smartphone for authentication.

7.3 Outlook

The findings on smartphone-based luminescence thermometry laid the grounds under which PersL lifetime could be explored to provide thermal images from which the temperature is determined. Luckily, the phosphor Gd_2O_2S is also used for multimodal bio-imaging [280, 281]. Taken together with the current advancements in smartphone photography, such as having dedicated NIR camera features, it would be possible to realize a combined bio-imaging and real-time temperature monitoring in biological systems using a smartphone. In the same line of thought, the system can easily exploit smartphone capabilities and be integrated into IoT systems.

PersL and PL of materials, in general, respond to various environmental factors including, but not limited to, chemical, temperature, humidity, and pressure. Consequently, it is possible to realize sensors for each of the responses and integrate a smartphone as the detecting device. Along this line of thought for example, in 1988, a fiber-optic humidity was developed exploiting fluorescence quenching of perylene silica-gel-adsorbed dyes [282]. For this sensor, a monochromator, a PMT, and integrated A/D converters and using a computer had to be implemented [282]. Presently, there are several publications on smartphone-based fluorescence detection of moisture, using the same concept but only realizing tasks using only a smartphone [283-285]. Following this, smartphone-based sensors have taken the center stage of applications leaving a gap in realizing/developing phosphors and materials that easily integrate with smartphone sensors for diversified applications. There is thus a need to accelerate the development of special phosphors to enable smartphone-based detection that complements other analytical techniques.

Additional work should first focus on expanding the library of persistent phosphors with absorption and emission in the visible to NIR boundary for the development of luminescence-based anti-counterfeiting labels authenticable with smartphones only. Some of the promising candidates include YAG: Ce^{3+}, Pr^{3+} (excitation band at 430 nm) [286], $K_2NaAlF_6:Mn^{4+}$ (excitation at 460 nm) [287], $Ba_2MgSi_2O_7:Eu^{2+}$ (excitation 420 nm) [288], $Zn_3Ga_2Ge_2O_{10}$: Cr^{3+} (excitation at 450 - 500 nm) [15], $CaAlSiN_3$: Eu^{2+} (excitation 450 nm) [289], along with other Eu^{2+},Dy^{3+} doped aluminates and silicates [4]. Theoretically, it would be interesting to develop single phosphors that change their color after excitation. This would alternatively complement the phosphor blending aspect and even enhance the intricacy level of the luminescence-based labels. Although not in the desired excitation region of 420 - 450 nm, the $Gd_{1.5}Y_{1.5}Ga_3Al_2O_{12}:Tb^{3+}$ demonstrates color-tunable emission post excitation and would be an interesting starting point for the development of such phosphors [290].

The second area of improvement would entail implementing strategies for effectively printing the labels. In this thesis, the major anti-counterfeiting label development techniques used included, embedding the phosphors in pattern-designed PMMA sheets, drop-casting the inks into patterns, and inkjet printing. Embedding the phosphor is easily accomplished, but this utilized a lot of phosphor content. Similarly, drop-casting also utilizes lots of phosphor content. While inkjet printing is promising, the particle size of the phosphors was a major drawback as they led to clogging of the cartridge. Alternative and more efficient methods for printing the labels include screen printing and offset or flexo printing which tolerates the large phosphor particle sizes.

Finally, the use of smartphones opens other possibilities to exploit beyond the anti-counterfeiting aspects. If an app were to be developed for anti-counterfeiting applications, onboarding other functions such as tracking/tracing tagged products [291] and also tracer-based-sorting when the products reach the end of use for recycling [292] would easily be integrated. This would contribute positively to the circular economy and sustainability in end-of-life products management.

References

[1] D. Poelman, D. Van der Heggen, J. Du, E. Cosaert, and P.F. Smet, “Persistent phosphors for the future: Fit for the right application.” *J. Appl. Phys.*, 2020. **128**(24): p. 240903.

[2] J. Ueda, S. Miyano, J. Xu, P. Dorenbos, and S. Tanabe, “Development of white persistent phosphors by manipulating lanthanide ions in gadolinium gallium garnets.” *Adv. Photonics Res.*, 2021. **2**(3): p. 2000102.

[3] J. Hölsä, “Persistent luminescence beats the afterglow: 400 years of persistent luminescence.” *Electrochem. Soc. Interface*, 2009. **18**(4): p. 42.

[4] K. Van den Eeckhout, P.F. Smet, and D. Poelman, “Persistent luminescence in Eu^{2+}-doped compounds: a review.” *Materials*, 2010. **3**(4): p. 2536-66.

[5] F. Kang, G. Sun, P. Boutinaud, H. Wu, F.-X. Ma, J. Lu, J. Gan, H. Bian, F. Gao, and S. Xiao, “Recent advances and prospects of persistent luminescent materials as inner secondary self-luminous light source for photocatalytic applications.” *Chem. Eng. J.*, 2021. **403**: p. 126099.

[6] M.D. Dramićanin, “Trends in luminescence thermometry.” *J. Appl. Phys.*, 2020. **128**(4): p. 040902.

[7] C. Brites, A. Millán, and L. Carlos, Lanthanides in luminescent thermometry, in *Handbook on the Physics and Chemistry of Rare Earths*. 2016, Elsevier. p. 339-427.

[8] N. Katumo, G. Gao, F. Laufer, B.S. Richards, and I.A. Howard, “Smartphone-based luminescent thermometry via temperature-sensitive delayed fluorescence from Gd_2O_2S: Eu^{3+}.” *Adv. Opt. Mater.*, 2020. **8**(19): p. 2000507.

[9] S.W. Allison, “A brief history of phosphor thermometry.” *Meas. Sci. Technol.*, 2019. **30**(7): p. 072001.

[10] L. Chavarria, Q. Walker, and D. Bahamon, “Illicit trade in times of coronavirus.” *euromonitor international. August*, 2020. URL: https://www.cnc.cl/wp-content/uploads/2020/09/wpIllicitTrade20.pdf.

[11] N. Katumo, L.A. Ruiz-Preciado, V. Kumar, G. Hernandez-Sosa, B.S. Richards, and I.A. Howard, “Anticounterfeiting labels with smartphone-readable dynamic luminescent patterns based on tailored persistent lifetimes in Gd_2O_2S: Eu^{3+}/Ti^{4+}.” *Adv. Mater. Technol.*, 2021: p. 2100047.

[12] J.W. Leem, M.S. Kim, S.H. Choi, S.-R. Kim, S.-W. Kim, Y.M. Song, R.J. Young, and Y.L. Kim, “Edible unclonable functions.” *Nat. Commun.*, 2020. **11**(1): p. 1-11.

[13] J.-C. Krupa and N.A. Kulagin, Physics of laser crystals. Vol. 126. 2003: Springer Science & Business Media.

[14] N. Liu, X. Chen, X. Sun, X. Sun, and J. Shi, “Persistent luminescence nanoparticles for cancer theranostics application.” *J. Nanobiotechnology*, 2021. **19**(1): p. 1-24.

[15] Z. Pan, Y.-Y. Lu, and F. Liu, “Sunlight-activated long-persistent luminescence in the near-infrared from Cr3+-doped zinc gallogermanates.” *Nat. Mater.*, 2012. **11**(1): p. 58-63.

[16] V. Vitola, D. Millers, I. Bite, K. Smits, and A. Spustaka, “Recent progress in understanding the persistent luminescence in $SrAl_2O_4$: Eu, Dy.” *Mater. Sci. Technol.*, 2019. **35**(14): p. 1661-77.

[17] H. Luo, A.J. Bos, and P. Dorenbos, “Charge carrier trapping processes in RE_2O_2S (RE= La, Gd, Y, and Lu).” *J. Phys. Chem. C*, 2017. **121**(16): p. 8760-69.

[18] J. Kong, W. Zheng, Y. Liu, R. Li, E. Ma, H. Zhu, and X. Chen, “Persistent luminescence from Eu^{3+} in SnO_2 nanoparticles.” *Nanoscale*, 2015. **7**(25): p. 11048-54.

[19] Y. Liang, F. Liu, Y. Chen, X. Wang, K. Sun, and Z. Pan, “Extending the applications for lanthanide ions: efficient emitters in short-wave infrared persistent luminescence.” *J. Mater. Chem. C*, 2017. **5**(26): p. 6488-92.

[20] D. Dutczak, Eu^{2+} activated persistent luminescent materials. 2013, Ph.D. dissertation, University Utrecht.

[21] K. Binnemans, “Interpretation of europium (III) spectra.” *Coord. Chem. Rev.*, 2015. **295**: p. 1-45.

[22] J. Zhang, Z. Zhang, Z. Tang, and T. Wang, “A new method to synthesize long afterglow red phosphor.” *Ceram. Int.*, 2004. **30**(2): p. 225-28.

[23] J.M. de Carvalho, C.C.S. Pedroso, I.P. Machado, J. Hölsä, L.C.V. Rodrigues, P. Głuchowski, M. Lastusaari, and H.F. Brito, “Persistent luminescence warm-light LEDs based on Ti-doped RE_2O_2S materials prepared by rapid and energy-saving microwave-assisted synthesis.” *J. Mater. Chem. C.*, 2018. **6**(33): p. 8897-905.

[24] T. Matsuzawa, Y. Aoki, N. Takeuchi, and Y. Murayama, “A new long phosphorescent phosphor with high brightness, $SrAl_2O_4$: Eu^{2+}, Dy^{3+}.” *J. Electrochem. Soc.*, 1996. **143**(8): p. 2670.

[25] S. Gedam, P. Thakre, and S. Dhoble, “Luminescence and spectroscopic studies of halosulfate phosphors: a review.” *Luminescence*, 2015. **30**(2): p. 187-97.

[26] D. Game, N. Ingale, and S. Omanwar, “Synthesis and photoluminescence properties of Eu 2+ doped CaS and SrS phosphor for phosphor converted white light emitting diodes.” *J. Mater. Sci. Mater. Electron.,* 2017. **28**(1): p. 915-22.

[27] D.O.A. Dos Santos, L. Giordano, M.A.S.G. Barbará, M.C. Portes, C.C.S. Pedroso, V.C. Teixeira, M. Lastusaari, and L.C.V. Rodrigues, “Abnormal co-

doping effect on the red persistent luminescence SrS: Eu^{2+}, RE^{3+} materials." *Dalton Trans.*, 2020. **49**(45): p. 16386-93.

[28] S. Wu, Z. Pan, R. Chen, and X. Liu, Long afterglow phosphorescent materials. 2017: Springer International Publishing.

[29] N. Scott. "Dutch test glow-in-the-dark road of the future." 2014 URL: https://www.npr.org/sections/thetwo-way/2014/04/14/302987616/dutch-test-glow-in-the-dark-road-of-the-future?t=1645521935992. [Accessed 02. 22. 2022].

[30] Y. Zhuang, D. Chen, W. Chen, W. Zhang, X. Su, R. Deng, Z. An, H. Chen, and R.-J. Xie, "X-ray-charged bright persistent luminescence in $NaYF_4$:Ln^{3+}@$NaYF_4$ nanoparticles for multidimensional optical information storage." *Light Sci. Appl.*, 2021. **10**(1): p. 132.

[31] B.S. Richards, "Luminescent layers for enhanced silicon solar cell performance: Down-conversion." *Sol. Energy Mater Sol. Cells, 2006.* ***90****(9): p. 1189-207.*

[32] C. Chen, H. Li, J. Jin, X. Chen, Y. Cheng, Y. Zheng, D. Liu, L. Xu, H. Song, and Q. Dai, "Long-lasting nanophosphors applied to UV-resistant and energy storage perovskite solar cells." *Adv. Energy Mater., 2017.* ***7****(20): p. 1700758.*

[33] A. Abdukayum, J.-T. Chen, Q. Zhao, and X.-P. Yan, "Functional Near Infrared-Emitting Cr^{3+}/Pr^{3+} Co-doped zinc gallogermanate persistent luminescent nanoparticles with superlong afterglow for in vivo targeted bioimaging." *J. Am. Chem. Soc.*, 2013. **135**(38): p. 14125-33.

[34] B.-Y. Wu, H.-F. Wang, J.-T. Chen, and X.-P. Yan, "Fluorescence resonance energy transfer inhibition assay for α-fetoprotein excreted during cancer cell growth using functionalized persistent luminescence nanoparticles." *J. Am. Chem. Soc.*, 2011. **133**(4): p. 686-88.

[35] N. Katumo, K. Li, B.S. Richards, and I.A. Howard, "Dual-color dynamic anti-counterfeiting labels with persistent emission after visible excitation allowing smartphone authentication." *Sci. Rep.*, 2022. **12**(1): p. 1-14.

[36] J.F. Ramalho, L.D. Carlos, P.S. André, and R.A. Ferreira, "mOptical sensing for the internet of things: A smartphone-controlled platform for temperature monitoring." *Adv. Photonics Res.*, 2021. **2**(6): p. 2000211.

[37] J.F. Ramalho, S.F. Correia, L. Fu, L.L. António, C.D. Brites, P.S. André, R.A. Ferreira, and L.D. Carlos, "Luminescence Thermometry on the Route of the Mobile-Based Internet of Things (IoT): How Smart QR Codes Make It Real." *Adv. Sci.*, 2019. **6**(19): p. 1900950.

[38] P. Kumbhakar, A.R. Karmakar, G.P. Das, J. Chakraborty, C.S. Tiwary, and P. Kumbhakar, "Reversible temperature-dependent photoluminescence in semiconductor quantum dots for the development of a smartphone-based optical thermometer." *Nanoscale*, 2021. **13**(5): p. 2946-54.

[39] J. Turner, A.V. Parisi, D.P. Igoe, and A. Amar, “Detection of ultraviolet B radiation with internal smartphone sensors.” *Instrum. Sci. Technol.,* 2017. **45**(6): p. 618-38.

[40] Y. Wang, S. Zhang, and Q. Wei, “Smartphone videoscopy: Recent progress and opportunities for biosensing.” *Adv. Opt. Technol.,* 2021.

[41] I. Hussain and A.K. Bowden, “Smartphone-based optical spectroscopic platforms for biomedical applications: a review.” *Biomed. Opt. Express.* 2021. **12**(4): p. 1974-98.

[42] J.F. Ramalho, L.M. Dias, L. Fu, A.M. Botas, L.D. Carlos, A.N. Carneiro Neto, P.S. André, and R.A. Ferreira, “Customized luminescent multiplexed quick-response codes as reliable temperature mobile optical sensors for eHealth and Internet of Things.” *Adv. Photonics Res.*, 2021: p. 2100206.

[43] L. Lu, Z. Jiang, Y. Hu, H. Zhou, G. Liu, Y. Chen, Y. Luo, and Z. Chen, “A portable optical fiber SPR temperature sensor based on a smartphone.” *Opt. Express.* 2019. **27**(18): p. 25420-27.

[44] A. Saleheen, B.M. Campbell, R.A. Prosser, and C.A. Baker, “Estimation of available epinephrine dose in expired and discolored autoinjectors via quantitative smartphone imaging.” *Anal. Bioanal. Chem.*, 2020. **412**(12): p. 2785-93.

[45] D. Igoe, A. Parisi, and B. Carter, “Characterization of a smartphone camera's response to ultraviolet A radiation.” *Photochem. Photobiol.*, 2013. **89**(1): p. 215-18.

[46] L.-P. Boivin, “Spectral responsivity of various types of silicon photodiode at oblique incidence: comparison of measured and calculated values.” *Appl. Opt.*, 2001. **40**(4): p. 485-91.

[47] Stemmer Imaging, “The imaging & vision handbook.” *Stemmer Imaging, Germany*, 2010.

[48] P. Nguyen, N.T. Le, and Y.M. Jang. Challenges issues for OCC based android camera 2 API. in *2017 Ninth International Conference on Ubiquitous and Future Networks (ICUFN)*. 2017. IEEE. Milan, Italy.

[49] Z. Zhu, “Smartphone-based apparatus for measuring upconversion luminescence lifetimes.” *Anal. Chim. Acta*, 2019. **1054**: p. 122-27.

[50] M.D. Dramićanin, “Sensing temperature via downshifting emissions of lanthanide-doped metal oxides and salts. A review.” *Methods Appl. Fluoresc.*, 2016. **4**(4): p. 042001.

[51] K.D. Sattler, 21st Century Nanoscience–A Handbook: Exotic Nanostructures and Quantum Systems (Volume Five). 2020: CRC Press.

[52] T. Sun, B. Xu, B. Chen, X. Chen, M. Li, P. Shi, and F. Wang, “Anti-counterfeiting patterns encrypted with multi-mode luminescent nanotaggants.” *Nanoscale*, 2017. **9**(8): p. 2701-05.

[53] L. Li, “Technology designed to combat fakes in the global supply chain.” *Bus. Horiz.*, 2013. **56**(2): p. 167-77.

[54] K.L. Wlodarczyk, M. Ardron, N.J. Weston, and D.P. Hand, “Holographic watermarks and steganographic markings for combating the counterfeiting practices of high-value metal products.” *J. Mater. Process. Technol.*, 2019. **264**: p. 328-35.

[55] Z.C. Kennedy, D.E. Stephenson, J.F. Christ, T.R. Pope, B.W. Arey, C.A. Barrett, and M.G. Warner, “Enhanced anti-counterfeiting measures for additive manufacturing: coupling lanthanide nanomaterial chemical signatures with blockchain technology.” *J. Mater. Chem. C*, 2017. **5**(37): p. 9570-78.

[56] Y. Cui, R.S. Hegde, I.Y. Phang, H.K. Lee, and X.Y. Ling, “Encoding molecular information in plasmonic nanostructures for anti-counterfeiting applications.” *Nanoscale*, 2014. **6**(1): p. 282-88.

[57] Y. Liu, F. Han, F. Li, Y. Zhao, M. Chen, Z. Xu, X. Zheng, H. Hu, J. Yao, and T. Guo, “Inkjet-printed unclonable quantum dot fluorescent anti-counterfeiting labels with artificial intelligence authentication.” *Nat. Commun.*, 2019. **10**(1): p. 1-9.

[58] Y. Gu, C. He, Y. Zhang, L. Lin, B.D. Thackray, and J. Ye, “Gap-enhanced Raman tags for physically unclonable anticounterfeiting labels.” *Nat. Commun.*, 2020. **11**(1): p. 1-13.

[59] R. Arppe and T.J. Sørensen, “Physical unclonable functions generated through chemical methods for anti-counterfeiting.” *Nat. Rev. Chem.,* 2017. **1**(4): p. 1-13.

[60] J. Andres, R.D. Hersch, J.E. Moser, and A.S. Chauvin, “A new anti-counterfeiting feature relying on invisible luminescent full color images printed with lanthanide-based inks.” *Adv. Funct. Mater.*, 2014. **24**(32): p. 5029-36.

[61] Authentic Vision. “Protect, Engage, Inspire: Protect your products, revenue Stream and Brand value.” 2022- URL: https://www.authenticvision.com/. [Accessed on 02.15. 2022].

[62] Systech. “Optimized packaging solutions.” 2022. URL: https://www.systechone .com/ [Accessed on 02.15. 2022].

[63] Zortag. “Technologies: Authenticate anytime anywhere.” 2019. URL: https: //www.zortag.com/ Technologies. [Accessed on 02.15. 2022].

[64] Bosch. “Anti-counterfeiting: Protecting value and securing revenue. ” 2022. URL: https://bosch.io/use-cases/cross-industry/anti-counterfeiting/. [Accessed 02.15. 2022].

[65] A.D. Furasova, V. Ivanovski, A.V. Yakovlev, V.A. Milichko, V.V. Vinogradov, and A.V. Vinogradov, “Inkjet fabrication of highly efficient luminescent Eu-doped ZrO_2 nanostructures.” *Nanoscale*, 2017. **9**(35): p. 13069-78.

[66] X. Yu, H. Zhang, and J. Yu, “Luminescence anti-counterfeiting: From elementary to advanced.” *Aggregate*, 2021. **2**(1): p. 20-34.

[67] M. Arapinis, M. Delavar, M. Doosti, and E. Kashefi, “Quantum physical unclonable functions: Possibilities and impossibilities.” *Quantum*, 2021. **5**: p. 475.

[68] R. Arppe-Tabbara, M. Tabbara, and T.J. Sørensen, “Versatile and validated optical authentication system based on physical unclonable functions.” *ACS Appl. Mater. Interfaces*, 2019. **11**(6): p. 6475-82.

[69] D. Zhang, W. Zhou, Q. Liu, and Z. Xia, “CH3NH3PbBr3 perovskite nanocrystals encapsulated in lanthanide metal–organic frameworks as a photoluminescence converter for anti-counterfeiting.” *ACS Appl. Mater. Interfaces,* 2018. **10**(33): p. 27875-84.

[70] J. Liu, N. Wang, Y. Yu, Y. Yan, H. Zhang, J. Li, and J. Yu, “Carbon dots in zeolites: A new class of thermally activated delayed fluorescence materials with ultralong lifetimes.” *Sci. Adv.*, 2017. **3**(5): p. e1603171.

[71] C. Shi, X. Shen, Y. Zhu, X. Li, Z. Pang, and M. Ge, “Excitation wavelength-dependent dual-mode luminescence emission for dynamic multicolor anticounterfeiting.” *ACS Appl. Mater. Interfaces,* 2019. **11**(20): p. 18548-54.

[72] X. Han, E. Song, B. Zhou, and Q. Zhang, “Color tunable upconversion luminescent perovskite fluoride with long-/short-lived emissions toward multiple anti-counterfeiting.” *J. Mater. Chem. C,* 2019. **7**(27): p. 8226-35.

[73] S.K.B. Mane, Y. Mu, E. Ubba, Z. Yang, J. Zhao, and Z. Chi, “Tuning the organic persistent room-temperature phosphorescence through aggregated states.” *J. Mater. Chem. C*, 2019. **7**(48): p. 15219-24.

[74] J. Chen, T. Yu, E. Ubba, Z. Xie, Z. Yang, Y. Zhang, S. Liu, J. Xu, M.P. Aldred, and Z. Chi, “Achieving Dual-Emissive and Time-Dependent Evolutive Organic Afterglow by Bridging Molecules with Weak Intermolecular Hydrogen Bonding.” *Adv. Opt. Mater.,* 2019. **7**(7): p. 1801593.

[75] Y. Lu, J. Zhao, R. Zhang, Y. Liu, D. Liu, E.M. Goldys, X. Yang, P. Xi, A. Sunna, and J. Lu, “Tunable lifetime multiplexing using luminescent nanocrystals.” *Nat. Photonics,* 2014. **8**(1): p. 32-36.

[76] M. Tan, F. Li, X. Wang, R. Fan, and G. Chen, “Temporal Multilevel Luminescence Anticounterfeiting through Scattering Media.” *ACS Nano*, 2020.

[77] C. Cao, Q. Liu, M. Shi, W. Feng, and F. Li, “Lanthanide-doped nanoparticles with upconversion and downshifting near-infrared luminescence for bioimaging.” *Inorg. Chem.,* 2019. **58**(14): p. 9351-57.

[78] J. Sang, J. Zhou, J. Zhang, H. Zhou, H. Li, Z. Ci, S. Peng, and Z. Wang, “Multilevel Static–Dynamic Anticounterfeiting Based on Stimuli-Responsive Luminescence in a Niobate Structure.” *ACS Appl. Mater. Interfaces*, 2019. **11**(22): p. 20150-56.

[79] L. Bai, N. Xue, Y. Zhao, X. Wang, C. Lu, and W. Shi, “Dual-mode emission of single-layered graphene quantum dots in confined nanospace: Anti-counterfeiting and sensor applications.” *Nano Res.*, 2018. **11**(4): p. 2034-45.

[80] J. Song, Q. Ma, Y. Liu, Y. Guo, F. Feng, and S. Shuang, “Novel single excitation dual-emission carbon dots for colorimetric and ratiometric fluorescent dual mode detection of Cu^{2+} and Al^{3+} ions.” *RSC Adv.*, 2019. **9**(66): p. 38568-75.

[81] Y. Liu, K. Ai, and L. Lu, “Designing lanthanide-doped nanocrystals with both up-and down-conversion luminescence for anti-counterfeiting.” *Nanoscale*, 2011. **3**(11): p. 4804-10.

[82] P. Kumar, K. Nagpal, and B.K. Gupta, “Unclonable security codes designed from multicolor luminescent lanthanide-doped Y_2O_3 nanorods for anticounterfeiting.” *ACS Appl. Mater. Interfaces,* 2017. **9**(16): p. 14301-08.

[83] L. Ji, J. Zhou, J. Zhang, Z. Zhang, Z. Ma, W. Wang, H. Li, and C. Wu, “A multicolor persistent luminescent phosphor $Sr_2Ga_2GeO_7$: Pr^{3+} for dynamic anticounterfeiting.” *J. Am. Ceram. Soc.*, 2019. **102**(9): p. 5465-70.

[84] H. Yang, W. Zhao, E. Song, R. Yun, H. Huang, J. Song, J. Zhong, H. Zhang, Z. Nie, and Y. Li, “Highly flexible dual-mode anti-counterfeiting designs based on tunable multi-band emissions and afterglow from chromium-doped aluminates.” *J. Mater. Chem. C, 2020*. **8**(46): p. 16533-41.

[85] J.C. Zhang, C. Pan, Y.F. Zhu, L.Z. Zhao, H.W. He, X. Liu, and J. Qiu, “Achieving thermo-mechano-opto-responsive bitemporal colorful luminescence via multiplexing of dual lanthanides in piezoelectric particles and its multidimensional anticounterfeiting.” *Adv. Mater.*, 2018. **30**(49): p. 1804644.

[86] Y.W. Hu, T.P. Zhang, C.F. Wang, K.K. Liu, Y. Sun, L. Li, C.F. Lv, Y.C. Liang, F.H. Jiao, and W.B. Zhao, “Flexible and biocompatible physical unclonable function anti-counterfeiting label.” *Adv. Funct. Mater.*, 2021. **31**(34): p. 2102108.

[87] T. Fukuoka, Y. Mori, T. Yasunaga, K. Namura, M. Suzuki, and A. Yamaguchi, “Physically unclonable functions taggant for universal steganographic prints.” *Sci. Rep.*, 2022. **12**(1): p. 1-8.

[88] H.J. Bae, S. Bae, C. Park, S. Han, J. Kim, L.N. Kim, K. Kim, S.H. Song, W. Park, and S. Kwon, “Biomimetic microfingerprints for anti-counterfeiting strategies.” *Adv. Mater.*, 2015. **27**(12): p. 2083-89.

[89] M.R. Carro-Temboury, R. Arppe, T. Vosch, and T.J. Sørensen, “An optical authentication system based on imaging of excitation-selected lanthanide luminescence.” *Sci. Adv.*, 2018. **4**(1): p. e1701384.

[90] S. Kalytchuk, Y. Wang, K.i. Poláková, and R. Zbořil, “Carbon dot fluorescence-lifetime-encoded anti-counterfeiting.” *ACS Appl. Mater. Interfaces,* 2018. **10**(35): p. 29902-08.

[91] V. Kumar, S. Dottermusch, A. Chauhan, B.S. Richards, and I.A. Howard, “Expanding the angle of incidence tolerance of unclonable anticounterfeiting

labels based on microlens arrays and luminescent microparticles." *Adv. Photonics Res.*, 2022: p. 2100202.

[92] J.-C.G. Bünzli and S.V. Eliseeva, Basics of lanthanide photophysics, in Lanthanide Luminescence. 2010, Springer. p. 1-45.

[93] M. Silberberg, Chemistry: the molecular nature of matter and change with advanced topics. 2017: McGraw-Hill Education.

[94] P. Hänninen and H. Härmä, Lanthanide luminescence: photophysical, analytical and biological aspects. Vol. 7. 2011: Springer Science & Business Media.

[95] G.W. Drake, Springer handbook of atomic, molecular, and optical physics. 2006: Springer Science & Business Media.

[96] Maschen, L-S Coupling, in Wikimedia Commons. 2019. Wikimedia. URL: https://commons.wikimedia.org/wiki/File:LS_coupling.svg. [Acessed 05.11.2021].

[97] A. de Bettencourt-Dias, Luminescence of lanthanide ions in coordination compounds and nanomaterials. 2014: John Wiley & Sons.

[98] D.J. Newman, "Theory of lanthanide crystal fields." *Adv. Phys.,* 1971. **20**(84): p. 197-256.

[99] W. Martin and W. Wiese, " *Springer handbook of atomic, molecular and optical physics* 2006: p. 175. Springer International Publishing.

[100] S.K. Gupta, R. Kadam, and P. Pujari, "Lanthanide spectroscopy in probing structure-property correlation in multi-site photoluminescent phosphors." *Coord. Chem. Rev., 2020.* ***420****: p. 213405.*

[101] G. Deng, "Terbium glows green." *Nat.Chem.,* 2018. **10**(1): p. 110-10.

[102] A. de Bettencourt-Dias, "Lanthanides: electronic structure." *Encyclopedia of Inorganic and Bioinorganic Chemistry*, 2011.

[103] T. Moeller, The chemistry of the lanthanides: pergamon texts in inorganic chemistry. Vol. 26. 2013: Elsevier.

[104] J.-C.G. Bunzli and V.K. Pecharsky, Handbook on the physics and chemistry of rare earths: including actinides. 2016: Elsevier.

[105] R. Reisfeld, "Optical properties of lanthanides in condensed phase, theory and applications." *AIMS Mater. Sci.*, 2015. **2**(2): p. 37-60.

[106] P. Dorenbos, "The Eu^{3+} charge transfer energy and the relation with the band gap of compounds." *J. Lumin.*, 2005. **111**(1-2): p. 89-104.

[107] M. Hatanaka and S. Yabushita, "Theoretical Study on the f− f Transition Intensities of Lanthanide Trihalide Systems." *J. Phys. Chem. A*, 2009. **113**(45): p. 12615-25.

[108] G.H. Dieke, “Spectra and Energy Levels of Rare Earth Ions in Crystals.” 1968. *Phys. Bull.* **20** 525.

[109] P. Dorenbos, “The 4fn↔ 4fn− 15d transitions of the trivalent lanthanides in halogenides and chalcogenides.” *J. Lumin.*, 2000. **91**(1-2): p. 91-106.

[110] P.S. Peijzel, A. Meijerink, R. Wegh, M. Reid, and G.W. Burdick, “A complete 4fn energy level diagram for all trivalent lanthanide ions.” *J. Solid State Chem.*, 2005. **178**(2): p. 448-53.

[111] W. Carnall, G. Goodman, K. Rajnak, and R. Rana, “A systematic analysis of the spectra of the lanthanides doped into single crystal LaF_3.” *J. Chem. Phys.*, 1989. **90**(7): p. 3443-57.

[112] G.B. Jean-claude, “The europium (III) ion as spectroscopic probe in bioinorganic chemistry.” *Inorg. Chim. Acta*, 1987. **139**(1-2): p. 219-22.

[113] A. Hooda, S. Khatkar, A. Khatkar, R.K. Malik, S. Devi, J. Dalal, and V. Taxak, “Combustion synthesis, Judd–Ofelt parameters and optical properties of color-tunable $Ba_3Y_4O_9$: Eu^{3+} nanophosphor for near-UV based WLEDs.” *J. Mater. Sci.: Mater. Electron.*, 2019. **30**(9): p. 8751-62.

[114] P. Goldner, “Accuracy of the Judd—Ofelt theory.” *Mol. Phys., 2003. **101**(7): p. 903-08*.

[115] M.P. Hehlen, M.G. Brik, and K.W. Krämer, “50th anniversary of the Judd–Ofelt theory: An experimentalist's view of the formalism and its application.” *J. Lumin.*, 2013. **136**: p. 221-39.

[116] S. Constantin and M. Stanciu, “Calculation Of The Judd-Ofelt Parameters Of The $ZnAl_2O_4$: Eu^{3+}.” *Ann. West Univ. Timisoara-Phys*, 2012. **56**: p. 127-31.

[117] B.M. Walsh, Judd-Ofelt theory: Principles and practices, in advances in spectroscopy for lasers and sensing. 2006, Springer. p. 403-33.

[118] A.K. Soni and B.P. Singh, Luminescent materials in lighting, display, solar cell, sensing, and biomedical applications, in luminescence-oled technology and applications. 2019, IntechOpen.

[119] R.E. Joseph, “Photophysics of upconversion: towards application in upconversion displays.” 2021. Ph.D. Dissertation, Karlsruhe Institute of Technology.

[120] H. Dong, L.-D. Sun, and C.-H. Yan, “Basic understanding of the lanthanide related upconversion emissions.” *Nanoscale*, 2013. **5**(13): p. 5703-14.

[121] A. Nadort, J. Zhao, and E.M. Goldys, “Lanthanide upconversion luminescence at the nanoscale: fundamentals and optical properties.” *Nanoscale*, 2016. **8**(27): p. 13099-130.

[122] N. Menyuk, K. Dwight, and J. Pierce, “NaYF4: Yb, Er—an efficient upconversion phosphor.” *Appl. Phys. Lett.*, 1972. **21**(4): p. 159-61.

[123] J. Suyver, A. Aebischer, D. Biner, P. Gerner, J. Grimm, S. Heer, K. Krämer, C. Reinhard, and H.-U. Güdel, "Novel materials doped with trivalent lanthanides and transition metal ions showing near-infrared to visible photon upconversion." *Opt. Mat.*, 2005. **27**(6): p. 1111-30.

[124] M.K. Mahata, H.C. Hofsäss, and U. Vetter, "Photon-upconverting materials: advances and prospects for various emerging applications." *luminescence - An outlook on the phenomena and their applications; intech: Rijeka, Croatia*, 2016: p. 109-31.

[125] K.W. Krämer, D. Biner, G. Frei, H.U. Güdel, M.P. Hehlen, and S.R. Lüthi, "Hexagonal sodium yttrium fluoride based green and blue emitting upconversion phosphors." *Chem. Mater.,* 2004. **16**(7): p. 1244-51.

[126] X. Chen, Y. Liu, and D. Tu, Lanthanide-doped luminescent nanomaterials. 2016: Springer.

[127] D. Dexter, "Possibility of luminescent quantum yields greater than unity." *Physical Review*, 1957. **108**(3): p. 630.

[128] J. Sommerdijk, A. Bril, and A. De Jager, "Two-photon luminescence with ultraviolet excitation of trivalent praseodymium." *J. Lumin.*, 1974. **8**(4): p. 341-43.

[129] R.T. Wegh, H. Donker, K.D. Oskam, and A. Meijerink, "Visible quantum cutting in $LiGdF_4$: Eu^{3+} through downconversion." *Science*, 1999. **283**(5402): p. 663-66.

[130] R. Wegh, E. Van Loef, and A. Meijerink, "Visible quantum cutting via downconversion in $LiGdF_4$: Er^{3+}, Tb^{3+} upon Er^{3+} $^4f_{11} \rightarrow {}^4f_{10}{}^5d$ excitation." *J. Lumin.*, 2000. **90**(3-4): p. 111-22.

[131] P. Vergeer, T. Vlugt, M. Kox, M. Den Hertog, J. Van der Eerden, and A. Meijerink, "Quantum cutting by cooperative energy transfer in $Yb_xY_{1-x}PO_4$: Tb^{3+}." *Phy. Rev. B*, 2005. **71**(1): p. 014119.

[132] X. Luo, T. Ding, X. Liu, Y. Liu, and K. Wu, "Quantum-cutting luminescent solar concentrators using ytterbium-doped perovskite nanocrystals." *Nano Lett.,* 2018. **19**(1): p. 338-41.

[133] D. Timmerman, I. Izeddin, P. Stallinga, I. Yassievich, and T. Gregorkiewicz, "Space-separated quantum cutting with silicon nanocrystals for photovoltaic applications." *Nature Photonics*, 2008. **2**(2): p. 105-09.

[134] C. Strümpel, M. McCann, G. Beaucarne, V. Arkhipov, A. Slaoui, V. Švrček, C. Del Cañizo, and I. Tobias, "Modifying the solar spectrum to enhance silicon solar cell efficiency—An overview of available materials." *Sol. Energy Mater. Sol. Cells*, 2007. **91**(4): p. 238-49.

[135] B. Liu, Y. Chen, C. Shi, H. Tang, and Y. Tao, "Visible quantum cutting in BaF2: Gd, Eu via downconversion." *J. Lumin.*, 2003. **101**(1-2): p. 155-59.

[136] A. Solodovnyk, K. Forberich, E. Stern, J. Krč, M. Topič, M. Batentschuk, B. Lipovšek, and C.J. Brabec, "Highly transmissive luminescent down-shifting layers filled with phosphor particles for photovoltaics." *Opt. Mater. Express*, 2015. **5**(6): p. 1296-305.

[137] B. Richards, "Enhancing the performance of silicon solar cells via the application of passive luminescence conversion layers." *Sol. Energy Mater. Sol. Cells,*, 2006. **90**(15): p. 2329-37.

[138] W.H. Weber and J. Lambe, "Luminescent greenhouse collector for solar radiation." *Appl. Opt.,* 1976. **15**(10): p. 2299-300.

[139] H. Hovel, R. Hodgson, and J. Woodall, "The effect of fluorescent wavelength shifting on solar cell spectral response." *Sol. Energy Mater.,* 1979. **2**(1): p. 19-29.

[140] C. Wang, T. Xuan, J. Liu, H. Li, and Z. Sun, "Long Afterglow $SrAl_2O_4$: Eu^{2+}, Dy^{3+} phosphors as luminescent down-shifting layer for crystalline silicon solar cells." *Int. J. Appl. Ceram. Technol.,* 2015. **12**(4): p. 722-27.

[141] B. Richards and K. McIntosh, "Overcoming the poor short wavelength spectral response of CdS/CdTe photovoltaic modules via luminescence down-shifting: ray-tracing simulations." *Prog. Photovolt.: Res. Appl.*, 2007. **15**(1): p. 27-34.

[142] E. Klampaftis, D. Ross, S. Seyrling, A.N. Tiwari, and B.S. Richards, "Increase in short-wavelength response of encapsulated CIGS devices by doping the encapsulation layer with luminescent material." *Sol. Energy Mater. Sol. Cells,* 2012. **101**: p. 62-67.

[143] H. Lian, Z. Hou, M. Shang, D. Geng, Y. Zhang, and J. Lin, "Rare earth ions doped phosphors for improving efficiencies of solar cells." *Energy*, 2013. **57**: p. 270-83.

[144] B. Shao, J. Huo, and H. You, "Prevailing strategies to tune emission color of lanthanide-activated phosphors for WLED applications." *Adv. Opt. Mater.,* 2019. **7**(13): p. 1900319.

[145] A.G. Bispo-Jr, L.F. Saraiva, S.A. Lima, A.M. Pires, and M.R. Davolos, "Recent prospects on phosphor-converted LEDs for lighting, displays, phototherapy, and indoor farming." *J. Lumin.*, 2021: p. 118167.

[146] P. Singh, R.S. Yadav, P. Singh, and S.B. Rai, "Upconversion and downshifting emissions of Ho^{3+}-Yb^{3+} co-doped ATiO3 perovskite phosphors with temperature sensing properties in Ho^{3+}-Yb^{3+} co-doped $BaTiO_3$ phosphor." *J. Alloys Compd.,* 2021. **855**: p. 157452.

[147] I. Suryawanshi, S. Srinidhi, S. Singh, R. Kalia, R.K. Kunchala, S.L. Mudavath, and B.S. Naidu, "Downshifting and upconversion dual mode emission from lanthanide doped $GdPO_4$ nanorods for unclonable anti-counterfeiting." *Mater. Today Commun.*, 2021. **26**: p. 102144.

[148] H. Lin, T. Yu, M.-K. Tsang, G. Bai, Q. Zhang, and J. Hao, "Near-infrared-to-near-infrared down-shifting and upconversion luminescence of KY_3F_{10} with single dopant of Nd^{3+} ion." *Appl. Phys. Lett.*, 2016. **108**(4): p. 041902.

[149] Q. Xiao, H. Zhu, D. Tu, E. Ma, and X. Chen, "Near-infrared-to-near-infrared downshifting and near-infrared-to-visible upconverting luminescence of Er^{3+}-doped In_2O_3 nanocrystals." *J. Phys. Chem. C.* 2013. **117**(20): p. 10834-41.

[150] P. Dorenbos, "A review on on how lanthanide impurity levels change with chemistry and structure of inorganic compounds." *ECS J Solid State Sci Technol.,* 2012. **2**(2): p. R3001.

[151] H.F. Brito, J. Hölsä, T. Laamanen, M. Lastusaari, M. Malkamäki, and L.C. Rodrigues, "Persistent luminescence mechanisms: human imagination at work." *Opt. Mater. Express*, 2012. **2**(4): p. 371-81.

[152] C. Chiatti, C. Fabiani, and A.L. Pisello, "Long Persistent Luminescence: A road map toward promising future developments in energy and environmental science." *Annu. Rev. Mater. Res.,* 2021. **51**.

[153] M. Lastusaari, T. Laamanen, M. Malkamäki, K.O. Eskola, A. Kotlov, S. Carlson, E. Welter, H.F. Brito, M. Bettinelli, and H. Jungner, " The Bologna Stone: history's first persistent luminescent material." *Eur. J. Mineral.*, 2012. **24**(5): p. 885-90.

[154] P.F. Smet, K. Van den Eeckhout, O.Q. De Clercq, and D. Poelman, Persistent phosphors, in Handbook on the physics and chemistry of rare earths, including actinides. 2015, Elsevier. p. 1-108.

[155] J. Xu and S. Tanabe, "Persistent luminescence instead of phosphorescence: History, mechanism, and perspective." *J. Lumin.*, 2019. **205**: p. 581-620.

[156] H.S. Virk. History of luminescence from ancient to modern times. in *Defect and Diffusion Forum*. 2015. Trans Tech Publ.

[157] E.N. Harvey, A history of luminescence from the earliest times until 1900. Vol. 44. 1957: Am. Philos. Soc.

[158] Y. Li, M. Gecevicius, and J. Qiu, "Long persistent phosphors—from fundamentals to applications." *Chem. Soc. Rev.*, 2016. **45**(8): p. 2090-136.

[159] L. Wang, Z. Shang, M. Shi, P. Cao, B. Yang, and J. Zou, "Preparing and testing the reliability of long-afterglow $SrAl_2O_4$: Eu^{2+}, Dy^{3+} phosphor flexible films for temperature sensing." *RSC Adv.*, 2020. **10**(19): p. 11418-25.

[160] B. Smets, "Phosphors based on rare-earths, a new era in fluorescent lighting." *Mater. Chem. Phys.*, 1987. **16**(3-4): p. 283-99.

[161] V. Abbruscato, "Optical and Electrical Properties of $SrAl_2O_4$: Eu^{2+}." *J. Electrochem. Soc.*, 1971. **118**(6): p. 930.

[162] I. Bite, G. Krieke, A. Zolotarjovs, K. Laganovska, V. Liepina, K. Smits, K. Auzins, L. Grigorjeva, D. Millers, and L. Skuja, "Novel method of

phosphorescent strontium aluminate coating preparation on aluminum." *Mater. & Des.*, 2018. **160**: p. 794-802.

[163] J. Vuojola and T. Soukka, "Luminescent lanthanide reporters: new concepts for use in bioanalytical applications." *Methods Appl. Fluoresc.*, 2014. **2**(1): p. 012001.

[164] E. Finley, Structure-Composition Relationships and Their Influence on Long Luminescent Lifetimes in Persistent Luminescent Phosphors. 2019. Ph.D. Dissertation, University of Houston.

[165] J. Hölsä, T. Aitasalo, H. Jungner, M. Lastusaari, J. Niittykoski, and G. Spano, "Role of defect states in persistent luminescence materials." J. Alloys Compd., 2004. **374**(1-2): p. 56-59.

[166] D. Gourier, A. Bessière, S.K. Sharma, L. Binet, B. Viana, N. Basavaraju, and K.R. Priolkar, "Origin of the visible-light-induced persistent luminescence of Cr^{3+}-doped zinc gallate." *J Phys. Chem. Solids*, 2014. **75**(7): p. 826-37.

[167] P. Smet, N. Avci, and D. Poelman, "Red persistent luminescence in Ca_2SiS_4: Eu, Nd." *J. Electrochem. Soc.*, 2009. **156**(4): p. H243.

[168] K. Van den Eeckhout, A.J. Bos, D. Poelman, and P.F. Smet, "Revealing trap depth distributions in persistent phosphors." *Phys. Rev. B,* 2013. **87**(4): p. 045126.

[169] H. Guo, Y. Wang, G. Li, J. Liu, P. Feng, and D. Liu, "Insights into excellent persistent luminescence and detecting trap distribution in $BaHfSi_3O_9$: Eu^{2+}, Pr^{3+}." *J. Mater. Chem. C*, 2017. **5**(46): p. 12090-96.

[170] J. Wang, H. Zhang, Y. Liu, H. Dong, B. Lei, M. Zheng, Y. Xiao, M. Peng, and J. Wang, "Insights into luminescence quenching and detecting trap distribution in in $Ba_2Si_5N_8$: Eu^{2+} phosphor with comprehensive considerations of temperature-dependent luminescence behaviors." *J. Mater. Chem. C*, 2015. **3**(37): p. 9572-79.

[171] G. Gao, D. Busko, N. Katumo, R. Joseph, E. Madirov, A. Turshatov, I.A. Howard, and B.S. Richards, "Ratiometric luminescent thermometry with excellent sensitivity over a broad temperature range utilizing thermally-assisted and multiphoton upconversion in triply-doped La_2O_3: $Yb^{3+}/Er^{3+}/Nd^{3+}$." *Adv. Opt. Mater.*, 2021. **9**(5): p. 2001901.

[172] A. Ćirić, T. Gavrilović, and M.D. Dramićanin, "Luminescence intensity ratio thermometry with Er^{3+}: Performance overview." *Crystals*, 2021. **11**(2): p. 189.

[173] C.D. Brites, S. Balabhadra, and L.D. Carlos, "Lanthanide-based thermometers: at the cutting-edge of luminescence thermometry." *Adv. Opt. Mater.*, 2019. **7**(5): p. 1801239.

[174] C.D. Brites, P.P. Lima, N.J. Silva, A. Millán, V.S. Amaral, F. Palacio, and L.D. Carlos, "Thermometry at the nanoscale." *Nanoscale*, 2012. **4**(16): p. 4799-829.

[175] F. Jahanbazi and Y. Mao, “Recent advances on metal oxide-based luminescence thermometry.” *J. Mater. Chem. C,* 2021.

[176] V. Lojpur, S. Ćulubrk, M. Medić, and M. Dramicanin, “Luminescence thermometry with Eu^{3+} doped $GdAlO_3$.” *J. Lumin.*, 2016. **170**: p. 467-71.

[177] M.G. Nikolić, Ž. Antić, S. Ćulubrk, J.M. Nedeljković, and M.D. Dramićanin, “Temperature sensing with Eu^{3+} doped TiO_2 nanoparticles.” *Sens. & Actuators B: Chem.*, 2014. **201**: p. 46-50.

[178] G. Särner, M. Richter, and M. Aldén, “Investigations of blue-emitting phosphors for thermometry.” *Meas. Sci. Technol.,* 2008. **19**(12): p. 125304.

[179] M. Dramićanin, Ž. Antić, S. Ćulubrk, S.P. Ahrenkiel, and J. Nedeljković, “Self-referenced luminescence thermometry with Sm^{3+} doped TiO_2 nanoparticles.” *Nanot.*, 2014. **25**(48): p. 485501.

[180] K. He, L. Zhang, Y. Liu, B. Xu, L. Chen, and G. Bai, “Lanthanide ions doped nonhygroscopic $La_2Mo_3O_{12}$ microcrystals based on multimode luminescence for optical thermometry.” *J. Alloys Compd.,* 2022. **890**: p. 161918.

[181] M.D. Dramićanin, B. Milićević, V. Đorđević, Z. Ristić, J. Zhou, D. Milivojević, J. Papan, M.G. Brik, C.G. Ma, and A.M. Srivastava, “Li_2TiO_3: Mn^{4+} deep-red phosphor for the lifetime-based luminescence thermometry.” *ChemistrySelect*, 2019. **4**(24): p. 7067-75.

[182] F. Chi, B. Jiang, Z. Zhao, Y. Chen, X. Wei, C. Duan, M. Yin, and W. Xu, “Multimodal temperature sensing using Zn_2GeO_4: Mn^{2+} phosphor as highly sensitive luminescent thermometer.” *Sens. Actuators B Chem.,* 2019. **296**: p. 126640.

[183] K. Suhling, L.M. Hirvonen, J.A. Levitt, P.-H. Chung, C. Tregido, A.l. Marois, D.A. Rusakov, K. Zheng, S. Ameer-Beg, and S. Poland, Fluorescence lifetime imaging (flim): basic concepts and recent applications, in advanced time-correlated single-photon counting applications. 2015, Springer. p. 119-88.

[184] H. Gao, C. Kam, T.Y. Chou, M.-Y. Wu, X. Zhao, and S. Chen, “A simple yet effective AIE-based fluorescent nano-thermometer for temperature mapping in living cells using fluorescence lifetime imaging microscopy.” *Nanoscale Horiz.*, 2020. **5**(3): p. 488-94.

[185] T.H. Chia and M.J. Levene, “Detection of counterfeit US paper money using intrinsic fluorescence lifetime.” *Opt. Express*, 2009. **17**(24): p. 22054-61.

[186] S. Yakunin, J. Chaaban, B.M. Benin, I. Cherniukh, C. Bernasconi, A. Landuyt, Y. Shynkarenko, S. Bolat, C. Hofer, and Y.E. Romanyuk, “Radiative lifetime-encoded unicolour security tags using perovskite nanocrystals.” *Nat. Commun.*, 2021. **12**(1): p. 1-8.

[187] Y. Zhou, W. Qin, C. Du, H. Gao, F. Zhu, and G. Liang, “Long-lived room-temperature phosphorescence for visual and quantitative detection of oxygen.” *Angew. Chem.*, 2019. **131**(35): p. 12230-34.

[188] V. Kumar, S. Dottermusch, N. Katumo, A. Chauhan, B.S. Richards, and I.A. Howard, "Unclonable Anti-Counterfeiting Labels Based on Microlens Arrays and Luminescent Microparticles." *Adv. Opt. Mater.*, 2021: p. 2102402.

[189] Q. Li, F. Chen, J. Kang, J. Su, F. Huang, P. Wang, X. Yang, and Y. Hou, "Physical Unclonable Anticounterfeiting Electrodes Enabled by Spontaneously Formed Plasmonic Core–Shell Nanoparticles for Traceable Electronics." *Adv. Funct. Mater.*, 2021. **31**(18): p. 2010537.

[190] J.V. Rival, P. Mymoona, R. Vinoth, A.V. Mohan, and E.S. Shibu, "Light-emitting atomically precise nanocluster-based flexible QR codes for anticounterfeiting." *ACS Appl. Mater. Interfaces*, 2021. **13**(8): p. 10583-93.

[191] W. Ren, G. Lin, C. Clarke, J. Zhou, and D. Jin, "Optical nanomaterials and enabling technologies for high-security-level anticounterfeiting." *Adv. Mater.*, 2020. **32**(18): p. 1901430.

[192] V. Blahnik and O. Schindelbeck, "Smartphone imaging technology and its applications." *Adv. Opt. Technol.*, 2021. **10**(3): p. 145-232.

[193] S. Melumad and M.T. Pham, "The smartphone as a pacifying technology." *J. Cons. Res.*, 2020. **47**(2): p. 237-55.

[194] J. Cartwright, "Technology: smartphone science." *Nature*, 2016. **531**(7596): p. 669-71.

[195] S.K. Thio, S. Lee, S. Bae, and S.-Y. Park. Lab on a Smartphone (LOS): A low-cost portable platform for real-time on-site water quality detection. in *2018 International Conference on Optical MEMS and Nanophotonics (OMN)*. 2018. IEEE. Lausanne, Switzerland.

[196] X. Huang, D. Xu, J. Chen, J. Liu, Y. Li, J. Song, X. Ma, and J. Guo, "Smartphone-based analytical biosensors." *Analyst*, 2018. **143**(22): p. 5339-51.

[197] D. Xu, X. Huang, J. Guo, and X. Ma, "Automatic smartphone-based microfluidic biosensor system at the point of care." *Biosens. Bioelectron.,* 2018. **110**: p. 78-88.

[198] Y.H. Johary, J. Trapp, A. Aamry, H. Aamri, N. Tamam, and A. Sulieman, "The suitability of smartphone camera sensors for detecting radiation." *Sci. Rep.*, 2021. **11**(1): p. 1-12.

[199] H.G. Kang, J.-J. Song, K. Lee, K.C. Nam, S.J. Hong, and H.C. Kim, "An investigation of medical radiation detection using CMOS image sensors in smartphones." *Nucl. Instrum. Methods. Phys. Res. A.,* 2016. **823**: p. 126-34.

[200] C. Danakis, M. Afgani, G. Povey, I. Underwood, and H. Haas. Using a CMOS camera sensor for visible light communication. in *2012 IEEE Globecom Workshops. 2012. Anaheim, CA, USA*.

[201] Edmund Optics. "Imaging Electronics 101: Understanding Ca,era Sensors for Machine Vision Applications." 2020, URL: https://www.edmundoptics.com

/knowledge-center/application-notes/imaging/understanding-camera-sensors-for-machine-vision-applications/#properties. [Accessed 2021 13.12.2021].

[202] Samsung Electronics. “Mobile Image Sensor: Capture a Moment as you feel it.“ 2021, URL: https://www.samsung.com/semiconductor/image-sensor/mobile-image-sensor. [Accessed 21.10.2021].

[203] S. Nasrazadani and S. Hassani, “Modern analytical techniques in failure analysis of aerospace, chemical, and oil and gas industries.” *Handbook of Materials Failure Analysis with Case Studies from the Oil and Gas Industry*, 2016: p. 39-54.

[204] Carl Zeiss, ''Division, Operator’s User Guide: ΣIGMA™ field emission scanning electron microscope (FESEM).'' 2011.

[205] V. Mishra, M.K. Warshi, A. Sati, A. Kumar, V. Mishra, A. Sagdeo, R. Kumar, and P.R. Sagdeo, “Diffuse reflectance spectroscopy: an effective tool to probe the defect states in wide bandgap semiconducting materials.” *Mater. Sci. Semicond. Process, 2018. **86**: p. 151-56.*

[206] PerkinElmer, “High-performance lambda spectroscopy accessories.” 2007. URL:https://www.s4science.at/wordpress/wp-content/uploads/2019/04/L60500 0 7 _ Getting-Started-Guide_en-US.pdf. [Accessed 02.02.2022]

[207] Agilent Technologies, “Cary Eclipse fluorescence spectrophotometer".” 2016. URL: https://www.agilent.com/cs/library/brochures/5990-7788EN_Cary_Eclipse Brochure.pdf. [Accessed 03.02.2022].

[208] C. Würth, M. Grabolle, J. Pauli, M. Spieles, and U. Resch-Genger, “Relative and absolute determination of fluorescence quantum yields of transparent samples.” *Nat. Protoc.*, 2013. **8**(8): p. 1535-50.

[209] S. Fery-Forgues and D. Lavabre, “Are fluorescence quantum yields so tricky to measure? A demonstration using familiar stationery products.” *J. Chem. Educ.,* 1999. **76**(9): p. 1260.

[210] D.O. Faulkner, J.J. McDowell, A.J. Price, D.D. Perovic, N.P. Kherani, and G.A. Ozin, “Measurement of absolute photoluminescence quantum yields using integrating spheres–Which way to go?” *Laser & Photonics Rev.*, 2012. **6**(6): p. 802-06.

[211] K. Carr, “Integrating sphere theory and applications Part I: integrating sphere theory and design.” *Surf. Coat. Int.,* 1997. **80**(8): p. 380-85.

[212] K. Carr, “Integrating sphere theory and applications Part II: integrating sphere applications.” *Surf. Coat. Int.,* 1997. **80**(10): p. 485-90.

[213] J.C. de Mello, H.F. Wittmann, and R.H. Friend, “An improved experimental determination of external photoluminescence quantum efficiency.” *Adv. Mater.*, 1997. **9**(3): p. 230-32.

[214] R.E. Joseph, C. Jiménez, D. Hudry, G. Gao, D. Busko, D. Biner, A. Turshatov, K. Krämer, B.S. Richards, and I.A. Howard, “Critical power density: a metric to compare the excitation power density dependence of photon upconversion in different inorganic host materials.” *J. Phys. Chem. A*, 2019. **123**(31): p. 6799-811.

[215] PicoQuant, “TCSPC and Time Tagging Electronics ” 2020. URL: https://www.picoquant.com/products/category/tcspc-and-time-tagging-modules. [Accessed 12.12.2021]

[216] U. Ortmann, M. Wahl, and P. Kapusta, Time-resolved fluorescence: novel technical solutions, in Standardization and quality assurance in fluorescence measurements I. 2008, Springer. p. 259-75.

[217] L.H. Pham, D.N.-N. Tran, C.H. Rhie, and J.W. Jeon. Analysis of the Smartphone Camera Exposure Effect on Laser Extraction. in *2021 International Conference on Electronics, Information, and Communication (ICEIC)*. 2021. IEEE. Jeju, Korea (South).

[218] S.R. Teli, S. Zvanovec, and Z. Ghassemlooy. The first tests of smartphone camera exposure effect on optical camera communication links. in *2019 15th International Conference on Telecommunications (ConTEL)*. 3 - 5th July 2019. IEEE. Graz, Austria.

[219] H. Dzieciol, H. Le Minh, Z. Ghassemlooy, P.T. Dat, and S.T. Tran. Comparative Study of Image Processing Performance of Camera-Based Visible Light Communication Using Android Acceleration Frameworks. in *2018 11th International Symposium on Communication Systems, Networks & Digital Signal Processing (CSNDSP)*. 18 - 20th July 2018. IEEE. Budapest, Hungary.

[220] D.C. Mukunda, V.K. Joshi, and K.K. Mahato, “Light emitting diodes (LEDs) in fluorescence-based analytical applications: a review.” *Appl. Spectrosc. Rev., 2020: p. 1-38.*

[221] Y. Kim, J. Oh, S.-H. Choi, A. Jung, J.-G. Lee, Y.S. Lee, and J.K. Kim, “A Portable Smartphone-Based Laryngoscope System for High-Speed Vocal Cord Imaging of Patients With Throat Disorders: Instrument Validation Study.” *JMIR mHealth and uHealth*, 2021. **9**(6): p. e25816.

[222] B. Xiong and Q. Fang, “Luminescence lifetime imaging using a cellphone camera with an electronic rolling shutter.” *Optics Lett.*, 2020. **45**(1): p. 81-84.

[223] Y. Liu, A.M. Rollins, R.M. Levenson, F. Fereidouni, and M.W. Jenkins, “Pocket MUSE: an affordable, versatile and high-performance fluorescence microscope using a smartphone.” *Commun. Biol., 2021. **4**(1): p. 1-14.*

[224] P. Cheremkhin, V. Lesnichii, and N. Petrov. Use of spectral characteristics of DSLR cameras with Bayer filter sensors. *J. Phys. Conf. Ser.* 2014. IOP Publishing.

[225] Throlabs. “Compact CCD Spectrometers.“ URL: https://www.thorlabs.de/newgrouppage9.cfm?objectgroup_id=3482&pn=CCS200. [Accessed 10.10.2021].

[226] Hamamatsu, Photomultiplier tubes: Basics and applications, ed. E. 3a. 2007, UK:Hamamatsu. URL: https://www.hamamatsu.com/content/dam/hamamatsu-photonics/sites/documents/99_SALES_LIBRARY/etd/PMT_handbook_v3aE.pdf

[227] N. Katumo, I. Howard, D. Busko, G. Gao, and B. Richards, Photonic markers enabling temperature sensing and/or security marking using low frame rate cameras. 2021, EP patent EP. No. 3 842 505 a1.

[228] D. Avram, I. Porosnicu, A. Patrascu, and C. Tiseanu, "Real-Time Thermal Imaging based on the Simultaneous Rise and Decay Luminescence Lifetime Thermometry." *Adv. Photonics Res.,* 2021: p. 2100208.

[229] S. Som, A. Choubey, and S. Sharma, "Spectral and trapping parameters of Eu^{3+} in Gd_2O_2S nanophosphor." *J. Exp. Nanosci.,* 2015. **10**(5): p. 350-70.

[230] S.A. Osseni, S. Lechevallier, M. Verelst, C. Dujardin, J. Dexpert-Ghys, D. Neumeyer, M. Leclercq, H. Baaziz, D. Cussac, and V. Santran, "New nanoplatform based on Gd_2O_2S: Eu^{3+} core: synthesis, characterization and use for in vitro bio-labelling." *J. Mater. Chem.,* 2011. **21**(45): p. 18365-72.

[231] J. Bang, M. Abboudi, B. Abrams, and P.H. Holloway, "Combustion synthesis of Eu-Tb and Tm-doped Ln_2O_2S (Ln= Y, La, Gd) phosphors." *J. Lumin.*, 2004. **106**(3-4): p. 177-85.

[232] G. Zhu, Z. Ci, Y. Shi, M. Que, Q. Wang, and Y. Wang, "Synthesis, crystal structure and luminescence characteristics of a novel red phosphor $Ca_{19}Mg_2(PO4)_{14}$: Eu^{3+} for light-emitting diodes and field emission displays." *J. Mater. Chem.*, 2013. **1**(37): p. 5960-69.

[233] M.T. Berry, P.S. May, and H. Xu, "Temperature dependence of the Eu3+ 5D0 lifetime in europium tris (2, 2, 6, 6-tetramethyl-3, 5-heptanedionato)." *J. Phys. Chem.,* 1996. **100**(22): p. 9216-22.

[234] Y. An, G.E. Schramm, and M.T. Berry, "Ligand-to-metal charge-transfer quenching of the Eu^{3+} (5D1) state in europium-doped tris (2, 2, 6, 6-tetramethyl-3, 5-heptanedionato) gadolinium (III)." *J. Lumin.*, 2002. **97**(1): p. 7-12.

[235] J. Wang, H. Song, X. Kong, W. Xu, and H. Xia, "Temperature dependence of the fluorescence of Eu 3+-ion doped in various silicate glasses." *J. Appl. Phys.,* 2002. **91**(12): p. 9466-70.

[236] M. Chambers and D. Clarke, "Doped oxides for high-temperature luminescence and lifetime thermometry." *Annu. Rev. Mater. Res., 2009. **39**: p. 325-59.*

[237] W. Yuan, R. Pang, T. Tan, H. Wu, S. Wang, J. Su, J. Wang, S. Jiao, C. Li, and H. Zhang, "Tuning emission color and improving the warm-white persistent luminescence of phosphor $BaLu_2Al_2Ga_2SiO_{12}$: Pr^{3+} via Zn^{2+} co-doping." *Dalton Trans*., 2021. **50**(35): p. 12137-46.

[238] S. Gharouel, L. Labrador-Páez, P. Haro-González, K. Horchani-Naifer, and M. Férid, "Fluorescence intensity ratio and lifetime thermometry of praseodymium phosphates for temperature sensing." *J. Lumin.,* 2018. **201**: p. 372-83.

[239] Y. Fu, L. Zhao, Y. Guo, and H. Yu, "Up-conversion luminescence lifetime thermometry based on the $^1G_4$ state of Tm^{3+} modulated by cross-relaxation processes." *Dalton Trans*., 2019. **48**(42): p. 16034-40.

[240] V. Bachmann, A. Meijerink, and C. Ronda, "Luminescence properties of $SrSi_2AlO_2N_3$ doped with divalent rare-earth ions." *J. Lumin.*, 2009. **129**(11): p. 1341-46.

[241] S.M. Bruno, D. Ananias, F.A.A. Paz, M. Pillinger, A.A. Valente, L.D. Carlos, and I.S. Gonçalves, "Crystal structure and temperature-dependent luminescence of a heterotetranuclear sodium–europium (III) β-diketonate complex." *Dalton Trans.,* 2015. **44**(2): p. 488-92.

[242] X. Liu, A. Skripka, Y. Lai, C. Jiang, J. Liu, F. Vetrone, and J. Liang, "Fast wide-field upconversion luminescence lifetime thermometry enabled by single-shot compressed ultrahigh-speed imaging." *Nat. Commun.*, 2021. **12**(1): p. 1-9.

[243] V. Lojpur, Ž. Antić, and M. Dramićanin, "Temperature sensing from the emission rise times of Eu^{3+} in SrY_2O_4." *Phys. Chem. Chem. Phys.*, 2014. **16**(46): p. 25636-41.

[244] J. Zhou, R. Lei, H. Wang, Y. Hua, D. Li, Q. Yang, D. Deng, and S. Xu, "A new generation of dual-mode optical thermometry based on ZrO_2: Eu^{3+} nanocrystals." *Nanophotonics*, 2019. **8**(12): p. 2347-58.

[245] C. Wang, Y. Jin, L. Yuan, H. Wu, G. Ju, Z. Li, D. Liu, Y. Lv, L. Chen, and Y. Hu, "A spatial/temporal dual-mode optical thermometry platform based on synergetic luminescence of Ti^{4+}-Eu^{3+} embedded flexible 3D micro-rod arrays: High-sensitive temperature sensing and multi-dimensional high-level secure anti-counterfeiting." *Chem. Eng. J.*, 2019. **374**: p. 992-1004.

[246] A. Griffiths, J. Herrnsdorf, J. McKendry, M. Strain, and M. Dawson, "Gallium nitride micro-light-emitting diode structured light sources for multi-modal optical wireless communications systems." *Philos. Trans. Royal Soc. A*, 2020. **378**(2169): p. 20190185.

[247] Z. Long, Y. Wen, J. Zhou, J. Qiu, H. Wu, X. Xu, X. Yu, D. Zhou, J. Yu, and Q. Wang, "No-interference reading for optical information storage and ultra-multiple anti-counterfeiting applications by designing targeted recombination in charge carrier trapping phosphors." *Adv. Opt. Mater.*, 2019. **7**(10): p. 1900006.

[248] P. Pei, P. DuanMu, B. Wang, X. Miao, C. Zhang, and W. Liu, "An advanced color tunable persistent luminescent $NaCa_2GeO_4F$: Tb^{3+} phosphor for multicolor anti-counterfeiting." *Dalton Trans.*, 2021. **50**(9): p. 3193-200.

[249] T. Hang, Q. Liu, D. Mao, and C. Chang, "Long lasting behavior of Gd_2O_2S: Eu^{3+} phosphor synthesized by hydrothermal routine." *Mater. Chem. & Phys.*, 2008. **107**(1): p. 142-47.

[250] S.A. Osseni, S. Lechevallier, M. Verelst, P. Perriat, J. Dexpert-Ghys, D. Neumeyer, R. Garcia, F. Mayer, K. Djanashvili, and J.A. Peters, "Gadolinium oxysulfide nanoparticles as multimodal imaging agents for T 2-weighted MR, X-ray tomography and photoluminescence." *Nanoscale*, 2014. **6**(1): p. 555-64.

[251] P. Rodnyĭ, “Energy levels of rare-earth ions in Gd_2O_2S.” *Opt. Spectrosc.*, 2009. **107**(2): p. 270-74.

[252] Z.Q. Zheng and X.P. Zhou, “Reduction of Ti^{4+} to Ti^{3+} in Boron-Doped BaTiO 3 at Very Low Temperature.” *J. Am. Ceram. Soc.*, 2013. **96**(11): p. 3504-10.

[253] B. Lei, Y. Liu, J. Zhang, J. Meng, S. Man, and S. Tan, “Persistent luminescence in rare earth ion-doped gadolinium oxysulfide phosphors.” *J. Alloys Compd.*, 2010. **495**(1): p. 247-53.

[254] Y. Tang, S. Dai, and Y. Fang, “Electron structure and photoluminescence behavior of $Ti_{0.09}Y_{1.91}O_2S$.” *J. Appl. Phys.,* 2009. **105**(3): p. 033101.

[255] X. Wang, Z. Zhang, Z. Tang, and Y. Lin, “Characterization and properties of a red and orange Y_2O_2S-based long afterglow phosphor.” *Mater. Chem. Phys.*, 2003. **80**(1): p. 1-5.

[256] Z. Hong, P. Zhang, X. Fan, and M. Wang, “ Eu^{3+} red long afterglow in Y_2O_2S: Ti, Eu phosphor through afterglow energy transfer.” *J. Lumin.*, 2007. **124**(1): p. 127-32.

[257] X. Zhou, M. Xing, T. Jiang, Y. Fu, Y. Peng, H. Wang, and X. Luo, “Afterglow performance enhancement and mechanism studies on Y_2O_2S: Eu, Mg, Ti prepared via cold isostatic pressing.” *J. Alloys Compd.,* 2014. **585**: p. 376-83.

[258] J. Guajardo, B. Škorić, P. Tuyls, S.S. Kumar, T. Bel, A.H. Blom, and G.-J. Schrijen, “Anti-counterfeiting, key distribution, and key storage in an ambient world via physical unclonable functions.” *Inf. Syst. Front.,* 2009. **11**(1): p. 19-41.

[259] E. Gorokhova, V. Demidenko, O. Khristich, S. Mikhrin, and P. Rodnyi, “Luminescence properties of ceramics based on terbium-doped gadolinium oxysulfide.” *J. Opt. Technol.*, 2003. **70**(10): p. 693-98.

[260] J. Santelli, S. Lechevallier, H. Baaziz, M. Vincent, C. Martinez, R. Mauricot, A. Parini, M. Verelst, and D. Cussac, “Multimodal gadolinium oxysulfide nanoparticles: a versatile contrast agent for mesenchymal stem cell labeling.” *Nanoscale*, 2018. **10**(35): p. 16775-86.

[261] T.T. Farman, R.H. Vandre, J.C. Pajak, S.R. Miller, A. Lempicki, and A.G. Farman, “Effects of scintillator on the modulation transfer function (MTF) of a digital imaging system.” *Oral Surg. Oral Med. Oral Pathol. Oral Radiol., 2005. **99**(5): p. 608-13.* 2005. **99**(5): p. 608-13.

[262] S.J. Duclos, “Scintillator phosphors for medical imaging.” *Electrochem. Soc. Interface, 1998. **7**(2): p. 34.*

[263] T. Guo, Y. Lin, Z. Li, S. Chen, G. Huang, H. Lin, J. Wang, G. Liu, and H.-H. Yang, “Gadolinium oxysulfide-coated gold nanorods with improved stability and dual-modal magnetic resonance/photoacoustic imaging contrast enhancement for cancer theranostics.” *Nanoscale*, 2017. **9**(1): p. 56-61.

[264] A.S. Omar and O. Basir, “Decentralized Identifiers and Verifiable Credentials for Smartphone Anticounterfeiting and Decentralized IMEI Database.” *Canadian J. Electr. Comput. Eng.,* 2020. **43**(3): p. 174-80.

[265] E. Karacaoglu and B. Karasu, “The effects of re-firing process under oxidizing atmosphere and temperatures on the properties of strontium aluminate phosphors.” *Mater. Res. Bull.,* 2013. **48**(10): p. 3702-06.

[266] V. Havasi, D. Tátrai, G. Szabó, E. Varga, A. Erdőhelyi, G. Sipos, Z. Kónya, and Á. Kukovecz, “On the effects of milling and thermal regeneration on the luminescence properties Eu^{2+} and Dy^{3+} doped strontium aluminate phosphors.” *J. Lumin.*, 2020. **219**: p. 116917.

[267] D. Van der Heggen, J.J. Joos, D.C. Rodríguez Burbano, J.A. Capobianco, and P.F. Smet, “Counting the photons: Determining the absolute storage capacity of persistent phosphors.” *Materials*, 2017. **10**(8): p. 867.

[268] R. Khattab, H. Sadek, H. Badr, F. Abd-El-Raoof, H. Abo-Almaged, and Y. Hamdy, “Preparation of strontium aluminate: Eu^{2+} and Dy^{3+} persistent luminescent materials based on recycling alum sludge.” *Ceram. Int.*, 2020. **46**(9): p. 12955-64.

[269] T. Delgado, J. Bierwagen, N. Gartmann, B. Walfort, I. Kinski, M. Pollnau, and H. Hagemann. Characterization and afterglow of $SrAl_2O_4$: Eu, Dy for various phosphor applications. in *Fiber Lasers and Glass Photonics: Materials through Applications II*. 2020. SPIE.

[270] J. Botterman, J.J. Joos, and P.F. Smet, “Trapping and detrapping in $SrAl_2O_4$: Eu, Dy persistent phosphors: Influence of excitation wavelength and temperature.” *Phys. Rev. B*, 2014. **90**(8): p. 085147.

[271] V. Havasi, D. Tátrai, G. Szabó, E. Varga, A. Erdőhelyi, G. Sipos, Z. Kónya, and Á. Kukovecz, “On the effects of milling and thermal regeneration on the luminescence properties of Eu^{2+} and Dy^{3+} doped strontium aluminate phosphors.” *J. Lumin.*, 2020. **219**.

[272] C.-J. Liang and H.-Y. Siao, “Luminescence behaviors of Eu-and Dy-codoped alkaline earth metal aluminate phosphors through potassium carbonate coprecipitation.” *Mater. Chem. Phys.*, 2016. **177**: p. 429-36.

[273] Y. Tamura, T. Okuno, Y. Suda, and Y. Nanai, “Red persistent luminescence excited by visible light in CaS: Eu^{2+}, Tm^{3+}.” *J. Phys. D: Appl. Phys.*, 2020. **53**(15): p. 155101.

[274] J.S. Kim, Y.H. Park, S.M. Kim, J.C. Choi, and H.L. Park, “Temperature-dependent emission spectra of M_2SiO_4: Eu^{2+} (M= Ca, Sr, Ba) phosphors for green and greenish white LEDs.” *Solid State Commun.*, 2005. **133**(7): p. 445-48.

[275] K. Suresh, K. Murthy, A. Rao, and N. Poornachandra Rao, “Rare earth doped alkali earth sulfide phosphors for white-light LEDs.” *Int. Sch. Res. Notices,* **2011**.

[276] A. Roda, E. Michelini, M. Zangheri, M. Di Fusco, D. Calabria, and P. Simoni, “Smartphone-based biosensors: A critical review and perspectives.”*Trends Anal. Chem.*, 2016. **79**: p. 317-25.

[277] P.E. Araque, I.M.P. de Vargas Sansalvador, N.L. Ruiz, M.M. Erenas, M.A.C. Rodríguez, and A.M. Olmos, “Non-invasive oxygen determination in intelligent packaging using a smartphone.” *IEEE Sens. J.*, 2018. **18**(11): p. 4351-57.

[278] K.E. McCracken, S.V. Angus, K.A. Reynolds, and J.-Y. Yoon, “Multimodal imaging and lighting bias correction for improved μPAD-based water quality monitoring via smartphones.” *Sci. Rep.*, 2016. **6**(1): p. 1-13.

[279] J.F. Ramalho, A.N.C. Neto, L.D. Carlos, P.S. André, and R.A. Ferreira, “Lanthanides for the new generation of optical sensing and Internet of Things.” *Handbook on the physics and chemistry of rare-earths*. 2022. *Elsevier.*

[280] J. Santelli, C. Lepoix, S. Lechevallier, C. Martinez, D. Calise, Q. Zou, S. Moyano, D. Cussac, M. Verelst, and R. Mauricot, “Custom NIR Imaging of New Up-Conversion Multimodal Gadolinium Oxysulfide Nanoparticles.” *Part.& Part. Syst. Charact.,* 2021. **38**(4): p. 2000216.

[281] C. Rosticher, B. Viana, M.-A. Fortin, J. Lagueux, L. Faucher, and C. Chanéac, “Gadolinium oxysulfide nanoprobes with both persistent luminescent and magnetic properties for multimodal imaging.” *RSC Adv.*, 2016. **6**(60): p. 55472-78.

[282] H.E. Posch and O.S. Wolfbeis, “Optical sensors, 13: fibre-optic humidity sensor based on fluorescence quenching.” *Sens. Actuators*, 1988. **15**(1): p. 77-83.

[283] R. Kaushik, R. Sakla, N. Kumar, A. Ghosh, V.D. Ghule, and D.A. Jose, “Multianalytes sensing probe: fluorescent moisture detection, smartphone assisted colorimetric phosgene recognition and colorimetric discrimination of Cu^{2+} and Fe^{3+} ions ions.” *Sens. Actuators B: Chem.*, 2021. **328**: p. 129026.

[284] A.G. Leal-Junior, A. Prado, A. Frizera, and M.J. Pontes, “Smartphone integrated polymer optical fiber humidity sensor: Towards a fully portable solution for healthcare.” *IEEE Sens. Lett.*, 2019. **3**(8): p. 1-4.

[285] H. Rao, W. Liu, K. He, S. Zhao, Z. Lu, S. Zhang, M. Sun, P. Zou, X. Wang, and Q. Zhao, “Smartphone-based fluorescence detection of Al3+ and H2O based on the use of dual-emission biomass carbon dots.” *ACS Sustain. Chem. Eng.,* 2020. **8**(23): p. 8857-67.

[286] B. Wang, H. Lin, Y. Yu, D. Chen, R. Zhang, J. Xu, and Y. Wang, “ Ce^{3+}/Pr^{3+}: YAGG: A long persistent phosphor activated by blue-light.” *J. Am. Ceram. Soc.*, 2014. **97**(8): p. 2539-45.

[287] Y. Wang, Y. Zhou, H. Ming, Y. Zhao, E. Song, and Q. Zhang, “Luminescence Enhancement of Mn^{4+}-activated fluorides via a heterovalent co-doping strategy for monochromatic multiplexing.” *ACS Appl. Mater. Interfaces,* 2021. **13**(43): p. 51255-65.

[288] T. Aitasalo, J. Holsa, T. Laamanen, M. Lastusaari, L. Lehto, J. Niittykoski, and F. Pelle, “Luminescence properties of Eu^{2+} doped dibarium magnesium disilicate, $Ba_2MgSi_2O_7$: Eu^{2+}.” *Ceram. - Silik.*, 2005. **49**(1): p. 58-62.

[289] Y. Xia, H. Ou, W. Li, G. Han, and Z. Li, “Efficient blue to red afterglow tuning in a binary nanocomposite plastic film.” *Nanomaterials*, 2018. **8**(4): p. 260.

[290] T. Ma, H. Li, S. Zhang, W. Sun, Z. Cheng, R. Pang, J. Feng, L. Jiang, D. Li, and C. Li, “Study of a color-tunable long afterglow phosphor $Gd_{1.5}Y_{1.5}Ga_3Al_2O_{12}$: Tb_{3+}: luminescence properties and mechanism.” *RSC Adv.,* 2020. **10**(47): p. 28049-58.

[291] P. Lei, F. Claret-Tournier, C. Chatwin, and R. Young. A secure mobile track and trace system for anti-counterfeiting. in *2005 IEEE International Conference on e-Technology, e-Commerce and e-Service*. 2005. IEEE. Hong Kong China.

[292] J. Gasde, J. Woidasky, J. Moesslein, and C. Lang-Koetz, “Plastics recycling with tracer-based-sorting: challenges of a potential radical technology.” *Sustainability*, 2021. **13**(1): p. 258.